University of Latvia
Faculty of Physics and Mathematics
Department of Physics

Modelling of the Floating Zone Growth of Silicon Single Crystals with Diameter up to 8 Inch

Ph.D. Thesis
by
Gundars Ratnieks

Advisor :
Prof. Dr.-Phys. A. Muižnieks

2007

Anotācija

Šajā darbā tiek piedāvāta noslēgta aksiālsimetrisku matemātisku modeļu sistēma stacionārai peldošās zonas (FZ) kristāla augšanai, kas piemērota peldošo zonu aprēķinam liela diametra (piem., 8 collu) kristāliem. Fāzu robežu aprēķinu sērija 8 collu peldošajai zonai vispirms tiek veikta, neievērojot kausējuma plūsmu tajā, tad 8, 4 un 2 collu peldošajām zonām aprēķini tiek veikti, ņemot vērā arī kausējuma plūsmu. Tiek noskaidrots, ka aprēķini, kuros nav ņemta vērā kausējuma kustība, dod tikai fāzu robežu pirmo tuvinājumu, kurpretim konvektīvās siltuma pārneses ievērošana noved pie ļoti labas aprēķinu rezultātu atbilstības eksperimentāliem datiem. Tiek analizēta arī kausējuma plūsmas tiešā ietekme uz kausējuma brīvās virsmas formu. Darba otra daļa veltīta induktora novirzes no aksiālās simetrijas ietekmei uz kausējuma 3D kustību peldošajā zonā un uz īpatnējās pretestības sadalījumu izaudzētajā kristālā. Rotācijas joslu (angļu val.: *rotational striations*) parādīšanās FZ kristālos tiek pētīta skaitliski, un aprēķini tiek salīdzināti ar eksperimenta rezultātiem.

Abstract

A closed system of axisymmetric mathematical models for steady-state FZ crystal growth is proposed as applicable for calculation of floating zones with large crystal diameters, e.g., 8 inch. Parametric studies of the phase boundaries for an 8 inch floating zone are performed first by neglecting the melt flow, then calculations for 8-, 4- and 2 inch floating zones are performed with account for the melt flow as well. It is found that the calculations neglecting the melt motion yield only a first approximation of the phase boundaries, whereas accounting for the convective heat transfer brings a very good agreement with experiments. The direct influence of the melt flow on the free melt surface shape is analysed as well. Another part of the work is devoted to the effect of the three-dimensionality of the inductor on the 3D melt flow in the floating zone and on the resistivity distribution in the grown crystal. The phenomenon of rotational striations in FZ crystals is examined numerically and the calculation results are compared to experiment.

Acknowledgements

The present work has been carried out partly at the University of Latvia, partly while working as research associate at the Institute for Electrothermal Processes, University of Hanover, and finished during my work at Siltronic AG, Burghausen.

First I would like to thank Prof. A. Muižnieks, my thesis advisor, and Prof. B. Nacke, director of the Institute for Electrothermal Processes, for making my work on the interesting topic about modelling floating zone possible. I am also greatly indebted to Prof. A. Mühlbauer, the former director of the Institute for Electrothermal Processes (then Institute for Electroheat), who, unfortunately, left us too early.

I would like to thank Prof. A. Muižnieks also for his support, advice and the many interesting discussions we had.

I owe much to my colleagues at the University of Latvia, especially A. Rudevičs, for his valuable help in objected-oriented programming during the elaboration of the code `FZONE`, and K. Dadzis, for his patience with some very time-consuming computations. My thanks go also to Prof. L. Buligins for his kind support with respect to the CFD package `FLUENT`.

Thesis on modelling of the industrial floating zone growth would not have been possible without the permanent interest in FZ research by the present and former co-workers at Siltronic AG. Especially I would like to thank Dr. W. v. Ammon, L. Altmannshofer, Dr. J. Virbulis, Dr. M. Grundner, Dr. R. Knobel, K. Niederer and Dr. Th. Wetzel.

For supplying photo-scanning measurements, I am greatly indebted to Dr. A. Lüdge and Dr. H. Riemann from the Institute for Crystal Growth (IKZ), Berlin.

Last but not least, I would like to express my gratitude to my mother Ligita and sister Inese for their kind support and understanding during the times I worked on my thesis in Rīga.

Contents

1 Introduction

Hyper-pure single-crystalline silicon wafers are the usual substrate to the semiconductor devices and integrated circuit (IC) chips for the state-of-the-art micro-electronics industry. Single crystal silicon is used instead of poly-crystalline silicon since the former does not have defects associated with grain boundaries found in polysilicon and limiting the lifetimes of minority carriers. The silicon substrates must also have a high degree of chemical purity and a high degree of crystalline perfection. The silicon wafers presenting thin discs of small thickness (e.g. 0.70 to 0.75 mm) and relatively large diameter (e.g. 76 to 300 mm) are obtained by slicing single crystal ingots, which are grown carefully from molten polysilicon. The silicon wafer market is nowadays the largest materials market in the semiconductor materials industry and obeys the extreme dynamics of the semiconductor branch. An illustration can be seen on the basis of data published by *Gartner, Inc.* Due to a major slump of semiconductor chip demand, the worldwide silicon wafer market revenue in year 2001 totaled $ 5.4 billion in U.S. dollars, a 31% decline from 2000 revenue of $ 7.8 billion. The industry returned to positive growth in 2002. Wafer demand on surface area basis surged 19% in 2002 to ca. 4,700 millions of square inches (ca. 30 billions of square centimeters) and produced a total revenue of $ 5.7 billion, an increase of ca. 5% from 2001. The wafer market continued to grow with uneven growth rates in the next years, topping the revenue of the year 2000 first in 2004 and reaching $ 10.2 billion market volume in 2006, a 24% growth in revenues and 21% rise in area-based demand over 2005, according to *Gartner*. In view of this market dynamics, a hard competition takes place and an extreme flexibility of the participants is essential. The first and most critical step in the manufacturing of silicon wafers is the growth of single crystal silicon ingots. The high expenses of the single-crystalline silicon wafer production and the competition among several main players in the branch have been a strong push for an intensive research and development in the field of crystal growth over the last decade.

The single crystal silicon ingots are grown either by Czochralski or floating zone process. Czochralski (CZ) crystal growth, the idea of which was first invented by Czochral-

ski already in 1917, involves the crystal pulling from the melt sustained in a crucible and heated by the infrared radiation of a resistance heater. Since the silica crucibles used for silicon growth add oxygen to the melt, CZ technique only permits growth of silicon crystals having relatively low resistivity, which is alright for application in substrates of IC chips. The floating zone (FZ) crystal growth technique, the basic idea of which was patented by Theuerer [1] in 1952, is in contrast crucible-free and more complicated than CZ technique. The principle of FZ growth is shown schematically in Fig. 1.1. The polysilicon feed rod is pushed continuously from above and melted by a high-frequency induction coil. The molten silicon makes a liquid bridge between the feed rod and the single crystal, which is pulled downwards as it grows. The melt mass on top of the growing crystal is stabilized by the surface tension of the liquid. The crystal and feed rods are rotated to ensure a better thermal symmetry and melt mixing. A sketch of a modern FZ puller after [2] is shown in Fig. 1.2.

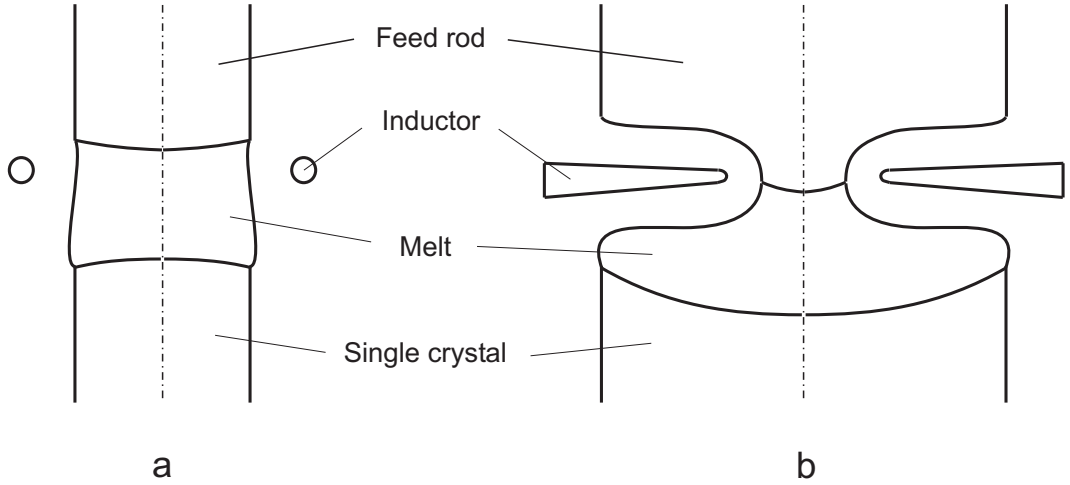

Figure 1.1: Schematic picture of the bottom-seeded floating zone process for small crystal diameters (a) and for large crystal diameters (b). The first one is the classical FZ process, the last one is the so-called needle-eye process. In the classical process, there is often a radiative heater instead of the inductor.

Featuring low oxygen content in a crystal, FZ method is suitable for obtaining single crystals with high resistivity that is not available by CZ method. Furthermore, by intentional introduction of electrically active elements (dopants) during the growth process, the resistivity of FZ silicon can be varied in a very wide range from few mΩ·cm to several thousand Ω·cm to cover the most different industry needs. The common substitutional dopants are boron as p-type dopant and phosphorus as n-type dopant.

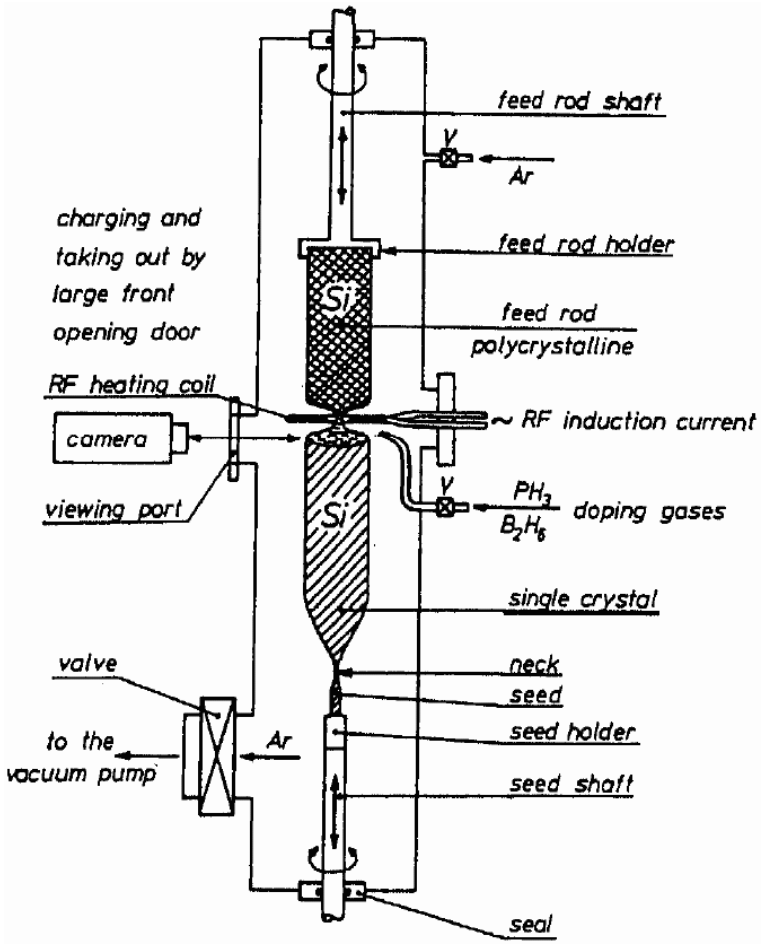

Figure 1.2: Schematic sketch of a modern FZ-Si puller for the growth of large crystals (after [2]).

The introduction of the dopants is usually carried out by gas doping[1] through nozzles built in the coil which direct the gas jet onto the melt surface. The dopants are hence transported with the fluid through the liquid zone toward the crystallization interface, and consequently the resistivity homogeneity in the crystal is much dependent on the melt flow pattern. An important issue for the crystal growers is to obtain the resistivity distribution as homogeneous as possible both in the radial and axial direction of silicon ingot to meet the increasing quality requirements of the semiconductor device industry. As an alternative to the doping during the growth process, for a better resistivity homogeneity, the grown silicon ingot can be doped later through the neutron transmutation doping process in which silicon isotopes ^{30}Si are converted in phosphorous ^{31}P leading to an n-type material. Nevertheless, since the neutron trans-

[1] As a doping gas, B_2H_6 is used for doping with boron and PH_3, for doping with phosphorus.

mutation doping technique is rather expensive and there is no suitable reaction for a p-type dopant available, the early dopant incorporation during the growth process is the usual approach.

FZ wafers are used primarily for applications in which very high resistivity or superior purity (particularly the absence of oxygen) are necessary for good device performance. Such applications include discrete power, MOS power, high efficiency solar cells and RF/wireless communication chips. FZ wafers make approximately 5% of the total silicon wafer market, the other 95% are CZ wafers [2]. Provided that there is success in producing FZ silicon significantly cheeper, the FZ share has a strong potential to grow, e.g., due to the solar application segment [3].

Beside the crystal purity and resistivity homogeneity, the crystalline quality is of utmost importance for the device industry. So crystals with dislocations do not satisfy the modern technological needs. Fortunately by the seed necking technique invented by Dash [4, 5, 6], it is possible to grow fully dislocation-free crystals, which are now standard in the silicon semiconductor industry. The Dash technique, however, only ensures that the crystal is free of dislocations at the initial stage of the growth process. The appearance of dislocations during the whole process must be avoided by the crystal grower self. It is believed (see e.g. [7]) that a certain kind of disturbance at the growth interface is enough to release the dislocation production by the high thermal stress in the crystal. The disturbance can be a strong local change of temperature and crystallization rate or small external particle reaching the growth interface. In many cases the degree of probability of occurrence of such perturbations can be substantially influenced by altering the puller configuration or growth parameters.

The crystalline quality of the single crystals is determined also by the intrinsic point defects, i.e., vacancies and Si interstitial atoms, which are incorporated during the growth process. While single point defects are normally not critical to the semiconductor device performance, their aggregation to large clusters during the cool-down phase of the crystal can lead to significant deterioration of the material. So the so-called A-swirls or L-pit defects are related to self-interstitial aggregates and result in damage to devices owing to their large size of several μm. The voids or vacancy aggregates, named also crystal originated particles (COP), have a smaller size of ca. 150 nm but make also effect on device functionality. It is well established that the pull rate V and the local axial temperature gradient G at the growth interface of the growing crystal have a dominant influence on the defect types that develop in the crystal and

their spatial as well as their density/size distribution. If V/G exceeds a critical value, vacancy aggregates develop, and if V/G is less than the critical value, self-interstitial related defects are built (it was noticed first by Voronkov in 1982 [8]). The change of the local value of $V/G(r)$ along the crystal radius determine the concentric defect regions in the grown crystal. A region free of significant defect agglomerates is found where V/G is close to the critical value. The radial extension of the defect-free ring is, however, determined by how homogeneous the radial distribution of V/G is. An appropriate control of the pull rate and the thermal field in the crystal helps to increase the area of the defect-free region and even to extend the region along the whole crystal radius. The latter is a necessary condition to be met for the growth of the so-called *perfect* or *ultimate* silicon, which is produced by the Czochralski method. With regard to the FZ crystals, the aggregation of single point defects is fortunately suppressed by the nitrogen, which is introduced in the atmosphere to avoid the arcing between the electrodes of the inductor. Hence the FZ crystals grown in presence of nitrogen are free of COP's and L-pits but contain nitrogen atoms, which are usually of no relevance for device production.

Another important issue is the size of the wafers. The semiconductor industry is currently experiencing a changeover from 150 mm to 200 mm diameter for FZ crystals and from 200 mm to 300 mm diameter for CZ crystals. Many semiconductor devices, or chips, are made from the same wafer, and all chips from a particular wafer are manufactured and processed simultaneously at each stage in the device manufacturing process. Because of this, larger-sized wafers allow for a greater throughput from the same semiconductor manufacturing process and allow semiconductor manufacturers to spread their fixed costs of production over a larger volume of finished products. Meanwhile the growing demand for larger and larger chips for the integration of higher-density semiconductor circuits tends to reduce the number of chips that can be made from one wafer. Hence the large-diameter crystal growth gets increasingly important.

Whereas the 8 inch (200 mm) FZ wafer has appeared not so long ago as a new market product, the 6 inch (150 mm), 5 inch (125 mm) and 4 inch (100 mm) FZ wafers keep significant industrial importance. FZ crystals of that large diameters are grown by the so-called needle-eye technique [9, 10], which differs from the classical FZ technique used for the growth of thin crystals up to ca. 15 mm in diameter. The problem with the classical inductor (see Fig. 1.1a) is the inability to maintain the liquid bridge between the polysilicon feed rod and the growing crystal if the diameter gets large. The needle-eye inductor (see Fig. 1.1b) is therefore a pancake-shaped one-turn coil

with a central hole (the needle eye) smaller than the feed rod and crystal, in order to allow the melting of the feed rod in its full thickness.

With regard to the diameter increase, the FZ technology meets several challenges due to the high complexity of FZ process. One of them is that the induction coil must be designed to melt off uniformly the polysilicon rod and, simultaneously, supply the right distribution of heat to the melt in a way that ensures a round shaped and dislocation free growth of the crystal despite the thermal stresses augmented with its size. Meanwhile the radial resistivity distribution must stay homogeneous enough, which fortunately is a minor problem for 8 inch crystal growth in contrast to 4 inch case, due to a better melt mixing in a larger melt volume. To mention the other difficulties of the FZ technology at large crystal diameter, the necessary voltage between the two electrodes of the inductor reaches a level where arcing can hardly be avoided. Furthermore, the polysilicon rod must meet certain specifications, e.g., a smooth surface and the absence of cracks, which are increasingly difficult to achieve with a larger diameter.

Due to the importance of the large-diameter crystal growth and, on the other hand, the challenges associated with it, the research and development and hence also the numerical modelling of the crystal growth processes gets increasingly relevant. The present work focuses on the numerical modelling (in frame of the mechanics of continuous media) of the needle-eye floating zone growth of silicon crystals of large diameter.

The work consists of the following parts. A short historical overview on the evolution of the floating zone method with references to the relevant patents and other publications as well as a survey of literature sources considering the modelling of the floating zone process is given in Chapter 2, at the end of which also the objectives of the present work can be found. The important physical features of a floating zone process with selected derivations and equations used in the following parts are provided in Chapter 3. The main part of the work is described in Chapters 4 and 5, which deal with axisymmetric modelling of phase boundaries in FZ process. This is accomplished by analysis of some three-dimensional effects in Chapter 6. Summary and conclusions are provided in Chapter 7.

2 Historical and literature survey

2.1 Short history of the floating zone method

With the beginning of the transistor technology era in 1947/1948, there emerged a need for semiconductor materials such as germanium or silicon with impurity concentration as small as 10^{14} cm^{-3} or even less, which seemed unrealistic in those years. The first solution was proposed in 1952 by US-American engineer William G. Pfann working at Bell Laboratories and inventing the zone refining process for purifying germanium [11]. The multiple-pass purification process took advantage of the concentration change by segregation for most impurities during the liquid–solid transition: the melt will sustain a higher level of impurity concentration than the crystal itself. Pfann was apparently unaware that a single pass purification technique had been proposed in a paper published in 1928 by Russian physicist Peter Kapitza working for Rutherford at Manchester University. The Pfann process involved localized melting by induction, or other, heating the germanium ingot supported in a graphite boat inside a tube. By moving the heater along the tube the molten zone passes down the ingot melting the impure solid at its forward edge and leaving a wake of purer material solidified behind it. In this way the impurities concentrate in the melt, and with each pass are moved to one end of the ingot. After multiple passes the impure end of the ingot is cut off.

Unfortunately, while Pfann's method worked well for refining germanium with a melting point of 937°C, it did not work for silicon whose melting point is 1414°C because no suitable boat material could be found to withstand the high temperatures without contaminating the melt. The problem was solved in 1953 by Bell Laboratories metallurgist Henry C. Theuerer with the development of the floating zone method [1]. He was able to create a molten zone in silicon by holding the ingot in a vertical position and moving it relative to the heating element. In this vertical configuration the surface tension of the molten silicon was sufficient to keep it from coming apart.

P. H. Keck and M. J. E. Golay (Bell Laboratories, [12]) grew the first silicon crystal with this new method, still without rotating the crystal. R. Emeis [13] independently

invented and initiated the development of the floating-zone process at Siemens, Germany. He rotated the growing crystal, thus producing straight cylindrical crystals with diameters up to 10 mm. The high-frequency induction heating instead of the radiation heating of the floating zone was introduced by S. Müller [14] and P. H. Keck with coworkers [15]. By the end of 1954, the basic techniques for the floating-zone growth of industrial high purity silicon had been established. Further development (see the historical survey and description of technical aspects in [16]) was directed mainly toward automation of the process control, improving the crystalline perfection (reducing dislocations) as well as increasing the diameter of the grown crystals.

Figure 2.1: The worldwide first dislocation-free 200 mm FZ silicon crystal (courtesy of Siltronic AG).

In 1956, Wolfgang Keller (Siemens) introduced a slim seed to reduce the dislocation density. The first fully dislocation-free crystals, both float-zone and Czochralski, were however grown by William C. Dash from General Electric, USA, during the late fifties. Dash used a special seeding technique with an extremely thin tapered seed, tip etched down to 0.25 mm [4, 5, 6]. In 1960, G. Ziegler (Siemens) simplified the seeding by transforming the Dash's method to the so-called bottle-neck technique. Ziegler used an untapered thin seed and made a bottle-neck at the fusion point of seed crystal and supply rod by means of rapid pulling [17]. This method established in the industrial scale growth of dislocation-free float-zoned (FZ) silicon crystals.

Until the end of the 1950s the crystal diameter size did not exceed 20 mm, whereas during the 60s and beginning of 70s a dramatic increase to 50 mm and 75 mm was achieved. One of the most important improvements that enabled the growth of large diameter dislocation-free silicon crystals was the bottom-seeded needle-eye floating-zone technique (invented first by Keller [9], then also by US-American researchers [10]) with application of a flat one-turn pancake coil having the inner hole diameter smaller than the diameter of both, the crystallizing single crystal and the feed rod. In the last decades a further increase of crystal diameter has taken place: the 100 mm crystal appears at the end of the 1970s, the 125 mm one in 1986, and the 150 mm one at the end of the 1980s. The worldwide first dislocation-free 200 mm silicon crystal was grown at Wacker Siltronic in September 2000 (Fig. 2.1).

Although the silicon crystals of large diameters are always grown by the needle-eye FZ process and modelling of that is in the focus of the current work, the modelling of the classical FZ process will be touched in the following literature survey as well, due to the similarity of both processes and the common issues in modelling them. The survey is, however, limited according to the content of the work to the macroscopic (continuous media) theoretical investigations of FZ growth.

2.2 Modelling of floating zone growth

Separate theoretical aspects of the floating zone growth were considered already in the 1950s. So Heywang [18] analysed the stability of the free melt surface during FZ growth. Neglecting the electromagnetic forces, the so-called Heywang limit for the zone height in case of equal diameters of the grown crystal and feed rod was found approximately at $2.84\sqrt{\frac{\gamma}{\rho_l g}}$ where ρ_l stands for the density of liquid silicon, γ is the surface tension coefficient, and g, the gravity. Later, in the 1970s, more precise numerical calculations by Coriell and Cordes [19] corrected this result to $2.67\sqrt{\frac{\gamma}{\rho_l g}}$, which corresponds to ca. 15 mm for silicon. Heywang had also found an estimation to the maximum zone length if the crystal and feed rod diameters are strongly different. His result, $(2+\sqrt{2})\sqrt{\frac{\gamma}{\rho_l g}} \approx 3.41\sqrt{\frac{\gamma}{\rho_l g}}$, which corresponds to ca. 19–20 mm[1], shows agreement with the maximum zone limit that can be found also numerically in the asymptotic case when both diameters are large keeping strong difference between them.

[1] It depends on the chosen surface tension of silicon, whose experimentally measured values are distributed in a wide range, see the references mentioned below Table 3.1.

With realistic crystal and melting interface diameters, as applicable for the calculation of typical needle-eye processes, the Heywang limit is, however, a bit too high because the diameter of the melting interface is not large enough for the asymptotic estimation to work well.

In the late eighties, Riahi and Walker [20] studied the shape stability of a small floating zone under the influence of electromagnetic pressure in case of the classical shape inductor and Lie et al. [21] extended the study to a needle-eye inductor.

Till the mid-1990s, numerous two-dimensional (i.e. axisymmetric) computational studies including heat conduction with Stefan problem and fluid flow had been made to investigate the classical optically heated floating zone process (in a mirror furnace) for oxide crystals of small diameters [22, 23, 24, 25, 26, 27, 28, 29]. So in [24] Lan and Kou (Taiwan) considered melt convection and calculated the convex interfaces induced by the Marangoni flow. In [25] they considered also the effect of rotation and compared with experimental observations. Further in [29], Lan considered the effects of magnetic fields on dopant transport and investigated multiple steady states.

In the second half of the 1990s, Lan et al. [30, 31] extended their model to three dimensions, first without melt convection. The 3D heat transfer in a double-ellipsoid mirror furnace was considered. Later also the 3D melt flow and particularly its stability was analysed by several authors [32, 33].

In the beginning years of the century, the models developed by Lan et al. for the classical optically heated FZ process included already the whole coupling of the 3D shape of phase interfaces with the 3D time-dependent Marangoni-driven melt convection [34, 35].

Also the group of Benz (Germany) had worked intensively on the modelling of the classical FZ process. So in [36] Kaiser and Benz use the commercial program package `FIDAP` to study numerically the melt flow, temperature- and dopant distribution with a fixed geometry of the liquid zone and under the influence of different magnetic fields. The heat sources due to the optical heater were approximated by a parabolic function. It was shown that the Marangoni convection is in general three-dimensional but can be reduced to axisymmetric under an axial magnetic field. A more general study of the influence of different magnetic fields in the classical FZ process has been performed in the Ph.D. thesis of Kaiser [37]. Rotating magnetic fields have been considered later by Dold et al. in [38] showing their symmetrizing influence on the 3D flow structure.

Beside the numerous studies on the magnetic fields as means of altering the fluid flow in the floating zone, also e.g. the influence of axial vibrations has been investigated numerically by Lyubimova et al. (Russia), see [39] and references therein.

As seen above, the numerical studies of the classical FZ process usually consider an optical heater. The classical FZ process for a crystal of diameter 10 mm with a radio-frequency inductor has been investigated by Munakata and Tanasawa (Japan) at the end of the nineties. In [40] they use a two-dimensional model to calculate the time-dependent melt flow numerically and compare it with experimental results. The influence of an axial magnetic field on the flow is considered and a reduction of the flow oscillations is detected.

For the modelling of the classical FZ growth of small-diameter crystals several simplifications are typically possible: the zone shape can be assumed cylindrical or quasi-cylindrical, which makes it easy to use structured finite volume grids, and the heat sources or the heat flux on the free surface may be approximated by a predefined coordinate function. These simplifications are normally not applicable in case of the more complex needle-eye process calculations because of the specific shape of the molten zone, the forming of the open melting front above the inductor, and the strong dependence of the induced heat sources on the shape of the high-frequency inductor and phase boundaries. The first numerical calculations for the needle-eye configuration were though made in a simplified way by Mühlbauer et al. (Germany) [41] already in the 1980s. They calculated the induced current distribution at the free melt surface and the electromagnetically driven fluid flow in the floating zone with a presumed free surface shape.

In the 1990s, Lie et al. [42] calculated the melt motion in the floating zone under strong axial magnetic field. The influence of the inductor slit on the distribution of the electromagnetic (EM) field has been analysed by Mühlbauer et al. [43, 44] by means of 3D (i.e. three-dimensional) calculations of the EM field.

In the following publication by the international team of Mühlbauer in 1995 [45] and in the Ph.D. thesis of Virbulis (Latvia) [46] an axisymmetric model was presented for calculation of the phase boundaries and global heat transfer with melt convection in a needle-eye FZ process for growth of large crystals of diameter e.g. 4 inch (ca. 100 mm). Their model considered most of the physical features possible to consider in a 2D model, even including the large open part of the melting front, which is characteristic to the needle-eye process. Meantime Riemann et al. [47] performed calculations

of the interface shape and heat transfer by a more limited model, without melt convection and open melting front calculation, and analysed the thermal stress inside the crystal. Later Mühlbauer, Muižnieks and Virbulis [48, 49] completed their model with axisymmetric calculation of the time-dependent dopant transport in the melt, derived the resistivity variation in the grown crystal from the time-dependent dopant distribution, and compared the theoretical results with resistivity measurements performed by Riemann and Lüdge. A good agreement of the calculation model with laboratory experiment was achieved with regard to the interface shape and the radial resistivity profile. An overview of the full model is given in [50]. Raming et al. used the above model to study the influence of different magnetic fields on the resistivity distribution of FZ-grown crystals [51] (see also the Ph.D. thesis of Raming [7]).

Also Japanese researchers have developed axisymmetric calculation models of the needle-eye FZ process and compared the results to crystal resistivity measurements. Togawa et al. [52] calculate the global heat transfer and the liquid zone shape, a time-dependent melt flow and the dopant transport, and they obtain the radial resistivity distribution in the crystal. The work of Togawa et al. is complemented with better radiation heat transfer models by Guo et al. in [53]. The effect of the vertical magnetic field on the FZ growth process has been investigated by Kimura et al. [54, 55]. Their calculations, however, have been performed for a very simplified shape of the molten zone.

The approximation of the radiation heat transfer is an important issue of the modelling of the phase boundaries in FZ growth of large crystals. Regarding the references mentioned above, only Guo et al. [53] have considered the view factors associated with surface of the sample including crystal, melt and feed rod, with the inductor and with the casing. They also study the importance of the consideration of the specular property of the crystal and melt surfaces instead of treating all of them as diffuse. Guo et al. conclude that the specular property is important. It can however be seen in Fig. 8 of [53] that the corrections made by accounting the specular character of the free melt surface and crystal are rather small from the practical point of view.

Togawa et al. and Guo et al., as well as Riemann et al. before, do not calculate the shape of the open melting front and the position of the inner triple point (the melt/feed/gas trijunction where the wetting of the feed rod by the bulk melt begins) but take it from experimental observations. Virbulis and Mühlbauer et al. [45, 46] do calculate the open front, but they meet two problems with it [56]: 1) the calculated position of the open

front near the feed rim tends to lie lower than that at the middle radius due to the insufficiency of the semi-empirical model used (see the empirical constant ξ in [45]); and 2) the calculation of the position of the inner triple point (ITP) is a bit handwork because of lack of a reliable automated calculation procedure. Another point is that the model of the electromagnetic field calculation does not include the influence of the main inductor slit. They also use the simplest model for the radiation heat transfer, i.e., the T^4-radiation to ambience neglecting view factors, which lowers the precision of results, particularly in case of large crystal growth where the temperature differences at the radiating surfaces are higher. Hence the models described in [45, 46] loose their applicability with larger crystal diameters (like 8 inch).

Excepting the works by Mühlbauer et al. [43, 44], where the influence of the inductor slit on the distribution of the EM field has been analysed by means of 3D calculations of the EM field, the rest of publications before year 1999 that were considering the needle-eye FZ process treated the system in frame of a 2D model as axisymmetric.

2.3 Objectives and publications of the present work

Motivated by the industrial needs on the one hand (see Chapter 1) and the above-mentioned limitations of the floating zone modelling on the other hand, the objectives of the present work have been set as follows:

- Development of a fully closed system of mathematical models for axisymmetric calculations of steady-state phase boundaries for large floating zones up to 8 inch diameter and implementing the models into a computation code.
- Investigation of the phase boundaries with the developed computation code and verification of the results by comparison to experimental data.
- Going beyond the axisymmetric model by studying the influence of the inductor's three-dimensionality in order to see the 3D structure of the melt flow and the resulting rotational striations in the grown crystal.

Significant part of this work has already been published. Here a short outline follows.

To overcome the disadvantages with respect to 8 inch crystal growth modelling inherent in the phase boundary calculation model by Virbulis and Mühlbauer et al. [45, 46] and

to proceed with modelling transient processes like cone growth, we developed our own calculation model as published in [57, 58]. The content of these publications can be found in a more complete form in Chapters 4 and 5, which contain also recent unpublished work concerning parametric studies of the phase boundaries for 8 inch crystal growth and modelling of the melt flow effect on the crystallization interface shape, as well as the experimental verification of the predicted phase boundaries.

Usually it is enough to consider a steady-state floating zone by assuming that the process parameters like pulling rate and crystal diameter stay approximately unchanged. For modelling inherently transient stages of the growth process like cone growth, additional enhancement of the above model has been done in collaboration with Rudevičs et al., see publications [59, 60, 61]. These model developments, however, stay outside the scope of the present work, which is fully devoted to the steady-state floating zone.

In [62] we presented for the first time a coupled 3D model for the melt flow-, temperature- and dopant concentration fields in the floating zone under influence of a 3D EM field created by a pancake-shaped one-turn inductor with a slit and current suppliers. The calculation results demonstrated the generation of the rotational striations in the crystal, assuming the EM field as the single source of asymmetry. The study was extended in our further publications [63, 64, 65, 66], three of which are included in Chapter 6, as well as in the project report for the VW-foundation [67]. The results of the work are reviewed also in the articles [68, 69].

3 Physical features of FZ-Si process

Here we consider the main characteristic features of large floating zone silicon growth processes: the physical properties of silicon, the distribution of the magnetic field, the forces acting in the melt, the melt flow and the free surface of the melt. The aim is to put down the background assumptions and equations that are common for the two-dimensional and three-dimensional models in Chapters 4 and 6. The more specific parts of the models are not considered here but postponed instead to the respective sections where the models are developed.

At the end of this chapter, a more detailed analysis is devoted to the influence of the fluid motion on the free surface of the melt, since it seems that this aspect has not been considered in previous works about FZ modelling.

3.1 Properties of silicon

In the temperature region about the melting point of silicon, not all physical properties of silicon are known precisely enough. Hence some of the properties assumed for the floating zone modelling and summarized in Table 3.1 are just a choice between different values in literature. Not shown in the table is the temperature dependence of the thermal conductivity and emissivity of solid silicon, which is assumed, after [45, 46], as follows:

$$\lambda_{\mathrm{s}}(T) = \lambda_{\mathrm{s}}(T_0) \cdot \left[4.495 - 7.222 \cdot (T/T_0) + 3.728 \cdot (T/T_0)^2\right],$$

$$\varepsilon_{\mathrm{s}}(T) = \begin{cases} \varepsilon_{\mathrm{s}}(T_0) \cdot 1.39, & \text{if} \quad T/T_0 < 0.593, \\ \varepsilon_{\mathrm{s}}(T_0) \cdot \left[1.96 - 0.96 \cdot (T/T_0)\right], & \text{if} \quad T/T_0 \geq 0.593, \end{cases}$$

where the designations correspond to those in Table 3.1.

Some of the silicon properties used in the 3D flow calculations in Chapter 6, which have been performed earlier, have values differing from the ones listed in Table 3.1. They can be found together with the calculations in Chapter 6.

Silicon property	Symbol	Value
Melting point	T_0	1687 K
Density of liquid	ρ_l	2580 kg/m^3
Density of solid	ρ_s	2329 kg/m^3
Heat capacity	c_p	1000 J/(kg·K)
Latent heat of fusion	Q	$1.8 \cdot 10^6$ J/kg
Electric conductivity of liquid	σ_l	$1.2 \cdot 10^6$ S/m
Electric conductivity of solid	σ_s	$5.0 \cdot 10^4$ S/m
Thermal conductivity of liquid	λ_l	67 W/(m·K)
Thermal conductivity of solid at T_0	$\lambda_\mathrm{s}(T_0)$	22 W/(m·K)
Emissivity of liquid	ε_l	0.27
Emissivity of solid at T_0	$\varepsilon_\mathrm{s}(T_0)$	0.46
Surface tension	γ	0.88 N/m
Thermal gradient of γ	$\partial\gamma/\partial T$	$-2.5 \cdot 10^{-4}$ N/(m·K)
Growth angle	ϕ_0	11 deg
Thermal expansion coefficient of liquid	β	$1.0 \cdot 10^{-4}$ K^{-1}
Dynamic viscosity	η	$8.6 \cdot 10^{-4}$ kg/(m·s)

Table 3.1: Physical properties of silicon, after [45, 46, 70, 71, 72, 73].

3.2 High-frequency EM field

Let us consider the alternating harmonic electromagnetic (EM) field created by the inductor in a typical FZ growth system. The frequency of the field is $f \approx 3$ MHz. Since the typical size of the puller is much smaller than the wavelength of the field ($c/f \approx$ 100 m), the EM field is quasi-stationary and we neglect the displacement currents. There are no ferromagnetic materials in the FZ growth system under consideration, i.e., $\mu = 1$.

Due to the high frequency, the EM field penetrates only in a thin skin layer of the silicon sample and inductor itself, the latter being made of copper or silver. The penetration depth of the field is calculated by (see e.g. [74])

$$\delta = \frac{1}{\sqrt{\pi \mu_0 f \sigma}}, \tag{3.1}$$

where σ is the electrical conductivity of silicon or inductor material. Values of δ for the materials usually relevant in case of FZ growth are listed in Table 3.2.

material	σ, S/m	δ, mm
Si (solid)	$5 \cdot 10^4$ [45]	1.3
Si (liquid)	$1.2 \cdot 10^6$ [45]	0.27
Cu, Ag	$5 \cdot 10^7$— $6 \cdot 10^7$	0.041— 0.038

Table 3.2: The penetration depth of EM field of frequency 3 MHz in different materials.

Since the penetration depth δ is small in comparison to the characteristic length scales of the floating zone, the equivalent integrated quantities such as the surface density of electric current, Joulean heat flux density on silicon surfaces and surface density of EM force are used instead of the volume current density, volume power density and volume force density, respectively.

In order to write the relations between these quantities, we introduce local orthogonal coordinates (ξ_1, ξ_2, ξ_3) with ξ_1 and ξ_2 along the surface of the conductor and ξ_3 directed into the material and normal to the surface. Due to the distinct skin-effect, we can assume that the magnetic field $\mathbf{B}$ and the current volume density $\mathbf{j}$ in the skin layer are parallel to the surface, i.e.

$$\mathbf{B} = \mathbf{e}_1 B_1 + \mathbf{e}_2 B_2, \qquad B_3 = 0, \tag{3.2}$$

$$\mathbf{j} = \mathbf{e}_1 j_1 + \mathbf{e}_2 j_2, \qquad j_3 = 0, \tag{3.3}$$

where $\mathbf{e}_1$ and $\mathbf{e}_2$ are unity vectors in the directions ξ_1 and ξ_2, respectively.

The change of the electromagnetic field in the normal direction ξ_3 is much steeper as in the directions ξ_1 and ξ_2. Under these circumstances, the solution of the Maxwell's equations (see [74]) and the material relation between the electric field intensity and volume current density (the Ohm's law[1]),

$$\mathbf{j} = \sigma \mathbf{E}, \tag{3.4}$$

yield

$$\mathbf{j} = \mathbf{j}^a \cdot \exp(-\xi_3/\delta) \cdot \cos(\omega t - \xi_3/\delta + \pi/4), \tag{3.5}$$

where $\mathbf{j}^a$ designates the amplitude of $\mathbf{j}$ at the surface, and $\omega = 2\pi f$. The reference point of time t is chosen in order to reduce the expressions following below.

The surface current density is defined by

$$\mathbf{i} = \int_0^\infty \mathbf{j}\, \mathrm{d}\xi_3 \tag{3.6}$$

and with account of (3.5) we have

$$\mathbf{i} = \mathbf{i}^a \cdot \cos(\omega t), \tag{3.7}$$

where $\mathbf{i}^a$, the amplitude of $\mathbf{i}$, is related to $\mathbf{j}^a$ by

$$\mathbf{i}^a = \mathbf{j}^a \cdot \frac{\delta}{\sqrt{2}}. \tag{3.8}$$

The corresponding effective value of the time-dependent surface current, i_{ef}, is defined as follows (line above variable stands for averaging in time):

$$i_{\mathrm{ef}}^2 = \overline{i^2} \qquad \text{or} \qquad i_{\mathrm{ef}} = \frac{i^a}{\sqrt{2}}\,. \tag{3.9}$$

From the current density distribution (3.5) and the Maxwell's equation for the quasi-stationary EM field, neglecting the displacement currents,

$$\mu_0 \mathbf{j} = \mathrm{rot}\mathbf{B}, \tag{3.10}$$

[1] At that high frequencies, the second part in the Ohm's law $\mathbf{j} = \sigma(\mathbf{E} + \mathbf{u} \times \mathbf{B})$, i.e., the cross-product of fluid velocity and magnetic field, is much smaller than the electric field $\mathbf{E}$ that is induced by the change of $\mathbf{B}$. Indeed, one can show that $u \cdot B \ll E$ will be true if $u/L \ll f$, where L is the characteristic length (radius). In our case, $f \approx 3 \cdot 10^6$ Hz, $u \approx 0.1$ m/s, $L \approx 0.1$ m, and the above inequality is satisfied.

with account of (3.2), (3.3) and (3.8), we get the distribution of the magnetic field in the skin layer:

$$\mathbf{B} = \mathbf{B}^a \cdot \exp(-\xi_3/\delta) \cdot \cos(\omega t - \xi_3/\delta), \tag{3.11}$$

$$\mathbf{B}^a = \mu_0 \cdot \mathbf{e}_3 \times \mathbf{i}^a, \tag{3.12}$$

$$B_{\text{ef}} = \mu_0 i_{\text{ef}} \cdot \exp(-\xi_3/\delta), \tag{3.13}$$

where $\mathbf{B}^a$ is the amplitude of $\mathbf{B}$ at the surface and the effective value B_{ef} is defined like that of $\mathbf{i}$, cf. (3.9).

Comparing (3.7) and (3.11) we see that there is no phase shift between the surface current $\mathbf{i}$ and the magnetic field near the surface of the conductor, $\mathbf{B}|_{\xi_3=0}$. Since the EM field is quasi-stationary (i.e., no wave process has to be taken into account), the $\mathbf{B}$–field has a constant phase in the whole atmosphere between the inductor and the silicon body. The above conclusion about the phases of $\mathbf{B}|_{\xi_3=0}$ and $\mathbf{i}$ holds for silicon surface as well as for the surface of the inductor. As a consequence, we have no phase shift other than 0° or 180° between the surface currents on inductor and silicon parts[2]. That brings a simplification for the calculation procedures both in 3D and 2D models: the surface currents may be treated as real vectors and the mathematical formalism in complex numbers, which is often used in harmonic EM field analysis, becomes redundant (as stated in [75]).

The above thesis about no phase shift between the surface currents and magnetic field is based on the used high-frequency approximation: it works if the skin layer depth is sufficiently small and the magnetic field has no normal component to the conducting surface, see (3.2). The applicability of this approximation for the FZ system with field frequency about 3 MHz has been tested and found appropriate in [46].

3.3 Joulean power and EM force in HF approximation

In the high-frequency approximation, the induction heating effect can be described by the Joulean heat flux density at the conducting surface, q^{EM}, called also the surface power density, which can be expressed via surface current $\mathbf{i}$ by using expressions (3.5),

[2] If the system is close to axisymmetric, the surface currents on inductor are oriented opposite to the surface currents on the other parts. That is why one speaks about a phase shift of 180°, although there is no principal difference to the phase shift of 0°.

(3.8) and (3.9):

$$q^{\mathrm{EM}} = \int_0^\infty \frac{\overline{j^2}}{\sigma}\,\mathrm{d}\xi_3 = \frac{{i_{\mathrm{ef}}}^2}{\delta \cdot \sigma}. \tag{3.14}$$

This formula is only valid if the thickness of the conducting body is large compared to the EM field penetration depth δ, otherwise the high-frequency approximation would not be applicable.

The melt flow in the floating zone is strongly influenced by the EM force. From the expression for the force volume density $\mathbf{f}$,

$$\mathbf{f} = \mathbf{j} \times \mathbf{B}, \tag{3.15}$$

and from the Maxwell's equation (3.10) it follows that

$$\mathbf{f} = -\frac{1}{2\mu_0}\,\mathrm{grad}(B^2) + \frac{1}{\mu_0}(\mathbf{B}\nabla)\mathbf{B}. \tag{3.16}$$

In the high-frequency approximation, from the equations (3.2), (3.3) and (3.10) we also have $\partial B_2/\partial\xi_1 = \partial B_1/\partial\xi_2$, and consequently

$$(\mathbf{B}\nabla)\mathbf{B} = \frac{1}{2}\left(\mathbf{e}_1\frac{\partial B^2}{\partial\xi_1} + \mathbf{e}_2\frac{\partial B^2}{\partial\xi_2}\right) \equiv \frac{1}{2}\,\mathrm{grad}_{1,2}(B^2).$$

With respect to the fluid flow in the melt and the shape of the free melt surface, the time-averaged value of the force (3.16) is relevant:

$$\overline{\mathbf{f}} = -\,\mathrm{grad}\left[\frac{B_{\mathrm{ef}}^2}{2\mu_0}\right] + \mathrm{grad}_{1,2}\left[\frac{B_{\mathrm{ef}}^2}{2\mu_0}\right]. \tag{3.17}$$

It can be seen that the first part of the expression (3.17) is a potential force and we denote it by $\mathbf{f}_{\mathrm{p}} = -\,\mathrm{grad}\,p^{\mathrm{EM}}$. The second part is a tangential force having no normal component, we denote this part by $\mathbf{f}_\tau$. Both the expression denoted by p^{EM} and $\mathbf{f}_\tau$ decay to zero with $\xi_3 \to \infty$. It can be shown that the splitting up of the total force in two parts having the above properties,

$$\overline{\mathbf{f}} = \mathbf{f}_{\mathrm{p}} + \mathbf{f}_\tau \;= -\,\mathrm{grad}\,p^{\mathrm{EM}} + \mathbf{f}_\tau, \tag{3.18}$$

is unique[3], and that the potential part $\mathbf{f}_{\mathrm{p}}$ has no direct influence on the solution of the

[3] Let us assume that $\overline{\mathbf{f}} = -\,\mathrm{grad}(p_1 + p_2) + \mathbf{f}_\tau$ and that there is another way of splitting up, namely $\overline{\mathbf{f}} = -\,\mathrm{grad}\,p_1 + (\mathbf{f}_\tau - \mathrm{grad}\,p_2)$, such that the normal component of $(\mathbf{f}_\tau - \mathrm{grad}\,p_2)$ is zero. The latter means that $\partial p_2/\partial\xi_3 = 0$, i.e., p_2 depends only on the tangential coordinates. According to the condition that the EM pressure in both expressions of $\overline{\mathbf{f}}$ decays to zero deep in the conducting body, we have $(p_1 + p_2)|_{\xi_3\to\infty} = 0$ and $p_1|_{\xi_3\to\infty} = 0$. Consequently $p_2|_{\xi_3\to\infty} = 0$ must be fulfilled for all tangential coordinates. Recalling the previous constraint on p_2, we have $p_2 \equiv 0$. Hence both ways of splitting up of $\overline{\mathbf{f}}$ are identical.

Navier-Stokes equations[4] and hence is only responsible for the equilibrium shape of the free surface of the liquid, whereas the tangential part $\mathbf{f}_\tau$ influences solely the fluid motion. The influence on the shape of the free surface by the fluid motion itself must not be considered at this point and is postponed to Section 3.5.

The above splitting up of $\overline{\mathbf{f}}$ defines a unique coordinate function p^{EM} that decays to zero at $\xi_3 \to \infty$. We call it the electromagnetic pressure and have the expression

$$p^{\mathrm{EM}} = \frac{B_{\mathrm{ef}}^2}{2\mu_0}.$$

We will not consider the values of the electromagnetic pressure inside the skin layer, hence we keep the designation p^{EM} for the electromagnetic pressure at the free surface of the liquid. With account of (3.13) we have on the surface $\xi_3 = 0$:

$$p^{\mathrm{EM}} = \frac{\mu_0 {i_{\mathrm{ef}}}^2}{2}. \tag{3.19}$$

For the tangential part $\mathbf{f}_\tau$ we have with account of (3.13):

$$\mathbf{f}_\tau = \frac{\mu_0}{2}\,\mathrm{grad}_{1,2}({i_{\mathrm{ef}}}^2) \cdot \exp(-2\xi_3/\delta). \tag{3.20}$$

The tangential force volume density $\mathbf{f}_\tau$ is integrated over the skin layer to get the force surface density, called also the tangential shear stress:

$$\mathbf{F}^{\mathrm{EM}} = \int_0^\infty \mathbf{f}_\tau \,\mathrm{d}\xi_3 \;= \frac{1}{4}\mu_0\delta \cdot \mathrm{grad}_{1,2}({i_{\mathrm{ef}}}^2). \tag{3.21}$$

3.4 Melt flow in the floating zone

In the high-frequency approximation, there are no volume forces except the gravity acting in the bulk of melt. We consider the silicon melt flow as an incompressible Newtonian fluid flow described by the Navier-Stokes equation (see e.g. [76]):

$$\tilde{\rho}_{\mathrm{l}} \left[\frac{\partial \mathbf{u}}{\partial t} + (\mathbf{u}\nabla)\mathbf{u} \right] = -\nabla p + \eta \Delta \mathbf{u} + \tilde{\rho}_{\mathrm{l}}\, \mathbf{g}, \tag{3.22}$$

where $\mathbf{u}$ and p are the velocity- and pressure fields, respectively, $\mathbf{g}$ is the gravity, η, the dynamic viscosity, which is assumed constant, and $\tilde{\rho}_{\mathrm{l}}$ is the melt density (the

[4] Writing the modified pressure $p' = p + p^{\mathrm{EM}}$ instead of the fluid pressure p in the Navier-Stokes equations of an incompressible fluid flow allows to account for the potential force $\mathbf{f}_{\mathrm{p}} = -\nabla p^{\mathrm{EM}}$ without changing the velocity field of the fluid.

subscript l stands for liquid). The assumption of incompressibility means that the density change due to the changes in pressure may be neglected. The temperature dependence of the density, however, has to be taken into account at least for the gravity term, in order to allow for the buoyancy effect. In the other terms of the equation, the density variation may be neglected (the Boussinesq approximation, see e.g. [77]). The temperature dependence of density is expressed using the coefficient of volume expansion, $\beta = -(1/\tilde{\rho}_\mathrm{l})(\partial\tilde{\rho}_\mathrm{l}/\partial T)_p$, as follows:

$$\tilde{\rho}_\mathrm{l} = \rho_\mathrm{l} \times [1 - \beta(T - T_0)],$$

where T is the temperature and ρ_l is the density of liquid at the melting point T_0. It is, of course, assumed that $\beta|T - T_0| \ll 1$ overall in the liquid volume.

Consequently, the original equation (3.22) transforms to:

$$\rho_\mathrm{l}\left[\frac{\partial \mathbf{u}}{\partial t} + (\mathbf{u}\nabla)\mathbf{u}\right] = -\nabla p + \rho_\mathrm{l}\,\mathbf{g} + \eta\Delta\mathbf{u} - \rho_\mathrm{l}\,\beta(T - T_0)\mathbf{g}.$$

Since $\rho_\mathrm{l}\,\mathbf{g}$ is a potential force, it is balanced exactly by a pressure equal to

$$p^\mathrm{HS} = \rho_\mathrm{l}\,\mathbf{g}\mathbf{z} + \mathrm{const} = -\rho_\mathrm{l}\,gz + \mathrm{const}, \tag{3.23}$$

i.e., the hydrostatic pressure of fluid in rest and equilibrium ($\mathbf{u} = 0$, $T = T_0$). In the above expression $g = |g_z|$ and the constant depends on the reference point of the coordinate z being measured vertically upwards.

The rest of the absolute pressure p can be named the hydrodynamic pressure,

$$p^\mathrm{HD} = p - p^\mathrm{HS}, \tag{3.24}$$

and is the only part of pressure left in the above Navier-Stokes equation after elimination of the hydrostatic part: $-\nabla p + \rho_\mathrm{l}\,\mathbf{g} = -\nabla(p - p^\mathrm{HS}) = -\nabla p^\mathrm{HD}$.

The system of equations for the fluid flow in the floating zone consists of the continuity equation, the Navier-Stokes equation transformed as shown before, and the temperature equation neglecting viscous dissipation [77]:

$$\nabla\mathbf{u} = 0, \tag{3.25}$$

$$\frac{\partial \mathbf{u}}{\partial t} + (\mathbf{u}\nabla)\mathbf{u} = -\frac{1}{\rho_\mathrm{l}}\nabla p^\mathrm{HD} + \frac{\eta}{\rho_\mathrm{l}}\Delta\mathbf{u} - \beta(T - T_0)\mathbf{g}, \tag{3.26}$$

$$\frac{\partial T}{\partial t} + (\mathbf{u}\nabla)T = \frac{\lambda_\mathrm{l}}{\rho_\mathrm{l} c_p}\,\Delta T, \tag{3.27}$$

where λ_l is the thermal conductivity and c_p, the specific heat of the liquid.

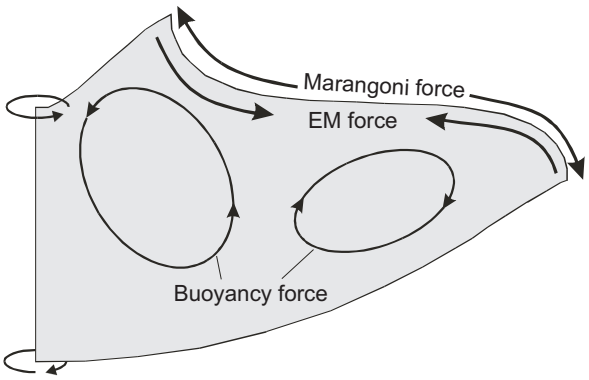

Figure 3.1: Schematic sketch of the action of forces in the floating zone.

As boundary condition for the temperature on the melting and crystallization interfaces, the melting point temperature is used. On the free melt surface, both the radiation heat transfer and the heat flux corresponding to the electromagnetic power surface density (3.14) have to be accounted. For considering boundary conditions for the fluid flow in the molten zone, a cylindrical coordinate system (r, φ, z) with the symmetry axis coinciding with the crystal and feed rod rotation axis and the cylindrical components of the velocity vector $\mathbf{u}$, i.e., u_r, u_φ and u_z, are practical.

The boundary conditions for the velocity field consider the rotation of the feed rod and melting process at the melting interface:

$$u_r = 0, \quad u_z = -V_\mathrm{S}, \quad u_\varphi = 2\pi r\,\Omega_\mathrm{F}, \tag{3.28}$$

where V_S is the supply velocity of molten silicon from feed rod and Ω_F, the rotation rate of feed rod. It is a simplification to assume that V_S is constant over the melting interface. On the growth interface, the crystallization process and the rotation of the crystal are considered:

$$u_r = 0, \quad u_z = -V_\mathrm{Cr}, \quad u_\varphi = 2\pi r\,\Omega_\mathrm{Cr}, \tag{3.29}$$

where V_Cr is the pull rate of the single crystal and Ω_Cr, its rotation rate.

Due to the small penetration depth of the EM field in the melt, the free surface of the melt is considered as a boundary with tangential shear stress, or the so-called surface force $\mathbf{F}$. For the total value of $\mathbf{F}$, both the electromagnetic force (3.21) and Marangoni force (see Fig. 3.1) are accounted:

$$\mathbf{F} = \mathbf{F}^\mathrm{EM} + \frac{\partial \gamma}{\partial T}\,\mathrm{grad}_{1,2}\,T, \tag{3.30}$$

where γ is the surface tension of the melt.

The precise flow boundary conditions at the free surface and the equation of the free surface shape are described later in Section 3.5. Here, let us first consider the dimensionless numbers characterizing the flow in the floating zone. For this purpose we introduce the characteristic length scale L as a half of crystal radius R_{Cr} and the characteristic azimuthal velocity $U_\varphi = 2\pi L\Omega_{\mathrm{Cr}}$, and take the characteristic meridional velocity $U_{rz} = 0.01$ m/s and the characteristic melt temperature difference $\Theta = 30$ K from numerical calculations of 4 to 8 inch floating zones. We also assume the characteristic values of crystal rotation rate Ω_{Cr} being 5 rpm for 4 inch crystals and 2 rpm for 8 inch crystals.

The ratio of inertial to viscous forces and the stability of the flow is characterized by the Reynolds number. Since the flow structure could have certain anisotropy due to the crystal rotation, it is meaningful to consider two Reynolds numbers: the meridional Reynolds number $\mathrm{Re}_{rz} = LU_{rz}/\nu$ and the azimuthal Reynolds number $\mathrm{Re}_\varphi = LU_\varphi/\nu$, where we use the kinetic viscosity $\nu = \eta/\rho_{\mathrm{l}}$. Other important dimensionless numbers are: the Prandtl number $\mathrm{Pr} = \nu/\chi$, i.e., the ratio of momentum diffusivity (viscosity) and thermal diffusivity $\chi = \lambda_{\mathrm{l}}/(\rho_{\mathrm{l}} c_p)$; the Grashof number $\mathrm{Gr} = g\beta\Theta L^3/\nu^2$, which approximates the ratio of the buoyancy to viscous force acting on the liquid; the Rayleigh number $\mathrm{Ra} = \mathrm{Gr}\cdot\mathrm{Pr}$, which characterizes whether conduction or free convection dominates the heat transfer; and the Péclet number $\mathrm{Pe} = \mathrm{Re}\cdot\mathrm{Pr}$ relating the rate of advection of a flow to its rate of thermal diffusion.

The estimated values of the dimensionless numbers are shown in Table 3.3. The values of Reynolds number show that the transition to turbulence, which could be expected occurring in Reynolds number region 2000—3000, is not yet achieved even with the large 8 inch zone. The Rayleigh number, however, is high, which indicates to a significant presence of buoyancy.

3.5 Free surface of the floating zone

To obtain the boundary conditions at the free surface we use the equation for the jump in stress across the interface between gas (g) and liquid (l), see e.g. [76], with adding the contributions (3.19) and (3.30) caused by the high-frequency electromagnetic field

Characteristic quantity	Units	FZ 4”	FZ 8”
R_{Cr}	m	0.050	0.100
$L = R_{\mathrm{Cr}}/2$	m	0.025	0.050
U_{rz}	m/s	0.010	0.010
Θ	K	30	30
Ω_{Cr}	1/s	0.083	0.033
$U_\varphi = 2\pi L \Omega_{\mathrm{Cr}}$	m/s	0.013	0.010
$\nu = \eta/\rho_{\mathrm{l}}$	m^2/s	$3.3 \cdot 10^{-7}$	$3.3 \cdot 10^{-7}$
$\chi = \lambda_{\mathrm{l}}/(\rho_{\mathrm{l}} c_p)$	m^2/s	$2.6 \cdot 10^{-5}$	$2.6 \cdot 10^{-5}$
$\mathrm{Pr} = \nu/\chi$	1	0.013	0.013
$\mathrm{Re}_{rz} = LU_{rz}/\nu$	1	750	1500
$\mathrm{Re}_\varphi = LU_\varphi/\nu$	1	980	1500
$\mathrm{Gr} = g\beta\Theta L^3/\nu^2$	1	$4.1 \cdot 10^6$	$3.3 \cdot 10^7$
$\mathrm{Ra} = g\beta\Theta L^3/(\nu\chi)$	1	$5.3 \cdot 10^4$	$4.2 \cdot 10^5$
$\mathrm{Pe} = LU_{rz}/\chi$	1	9.6	19

Table 3.3: The characteristic parameters and estimation of the dimensionless numbers (rounded to two significant digits) for the melt flow in FZ processes.

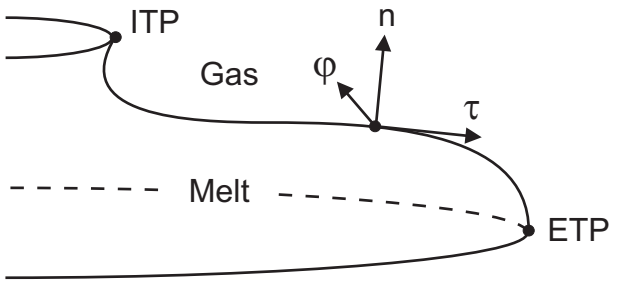

Figure 3.2: Sketch of the local orthogonal coordinates (τ, φ, n) at the free surface of the floating zone. ITP is the inner triple point and ETP, the exterior triple point.

and Marangoni forces:

$$\sum_{\jmath} \sigma^{\mathrm{g}}_{\imath\jmath} n_\jmath - \sum_{\jmath} \sigma^{\mathrm{l}}_{\imath\jmath} n_\jmath = \gamma \mathcal{K} n_\imath + p^{\mathrm{EM}} n_\imath - F_\imath, \tag{3.31}$$

where the normal vector $\mathbf{n}$ points from liquid into gas and $\mathcal{K}$ is the curvature of the interface, being reckoned here as positive when the corresponding center of curvature lies in the liquid region. Since we do not intend to calculate the flow of gas, the stress everywhere in the gas may be approximated (see [76]) by $\sigma^{\mathrm{g}}_{\imath\jmath} = -p^{\mathrm{g}} \delta_{\imath\jmath}$, where p^{g} is a constant gas pressure. The stress in the incompressible Newtonian liquid, however, is considered explicitly: $\sigma^{\mathrm{l}}_{\imath\jmath} = -(p^{\mathrm{HS}} + p^{\mathrm{HD}})\delta_{\imath\jmath} + 2\eta e_{\imath\jmath}$, where p^{HS} and p^{HD} are the hydrostatic pressure (3.23) and hydrodynamic pressure (3.24), respectively, and $e_{\imath\jmath}$ is the rate-of-strain tensor. Consequently, substituting the stresses into (3.31) yields the following boundary condition for the rate of strain of liquid at the free surface:

$$2\eta \sum_{\jmath} e_{\imath\jmath} n_\jmath = \left(p_0 - \rho_{\mathrm{l}} g z - \gamma \mathcal{K} - p^{\mathrm{EM}} + p^{\mathrm{HD}}\right) n_\imath + F_\imath, \tag{3.32}$$

where p_0 is containing constant contributions from p^{HS} and p^{g} and might be named the gauge pressure.

Let us assume now that the liquid zone has an axisymmetric shape. We obtain the local orthogonal coordinate system (τ, φ, n) in each point of the free surface (τ standing for the tangential direction and n, for the normal direction locally at the surface, see Fig. 3.2) by rotation of the local cylindrical coordinates (r, φ, z) about the azimuthal direction φ, which plays now the role of the other tangential direction beside τ.

With the local coordinate system introduced, the sum on the left side of equation (3.32) is interpreted as $e_{\imath n}$, where $\imath$ stands for τ, φ or n. The respective expressions of

the rate-of-strain tensor's components are:

$$\begin{aligned} e_{\tau n} &= \frac{1}{2}\left(\frac{\partial u_n}{\partial \tau} + \frac{\partial u_\tau}{\partial n}\right) \\ e_{\varphi n} &= \frac{1}{2}\left(\frac{1}{r}\frac{\partial u_n}{\partial \varphi} + r\frac{\partial (u_\varphi / r)}{\partial n}\right) \\ e_{nn} &= \frac{\partial u_n}{\partial n} \end{aligned}$$

The expressions of $e_{\tau n}$ and $e_{\varphi n}$ can be simplified by taking into account that for a static free surface

$$u_n = 0, \tag{3.33}$$

which implies that also the gradient of u_n along the free surface vanishes. Consequently, (3.32) yields the following free surface conditions:

$$\frac{\partial u_\tau}{\partial n} = \frac{F_\tau}{\eta} \tag{3.34}$$

$$\frac{\partial u_\varphi}{\partial n} = \frac{u_\varphi}{r}\frac{\partial r}{\partial n} + \frac{F_\varphi}{\eta} \tag{3.35}$$

$$p_0 - \rho_\mathrm{l} g z - \gamma \mathcal{K} - p^{\mathrm{EM}} + p^{\mathrm{HD}} - 2\eta \frac{\partial u_n}{\partial n} = 0 \tag{3.36}$$

The conditions (3.33), (3.34) and (3.35) are the flow boundary conditions at the free surface of the floating zone. The additional equation (3.36) determines the static shape of the free surface. The last two terms on the left side of (3.36) describe the influence of fluid flow on the surface shape.

Let us consider the distribution of the hydrodynamic pressure p^{HD} along the free surface under assumption of an axisymmetric fluid flow. The τ-projection of the Navier-Stokes equation (3.26) with taking into account the continuity (3.25) yields:

$$\frac{\partial u_\tau}{\partial t} + u_\tau \frac{\partial u_\tau}{\partial \tau} + u_n \frac{\partial u_\tau}{\partial n} - \frac{u_\varphi^2}{r}\frac{\partial r}{\partial \tau} = -\frac{1}{\rho_\mathrm{l}}\frac{\partial p^{\mathrm{HD}}}{\partial \tau} + \frac{\eta}{\rho_\mathrm{l} r}\frac{\partial (r\omega)}{\partial n} - g_\tau \beta (T - T_0),$$

where

$$\omega \equiv (\nabla \times \mathbf{u})_\varphi = \frac{\partial u_\tau}{\partial n} - \frac{\partial u_n}{\partial \tau}.$$

Taking into account $u_n = 0$ at the free surface and assuming that the time-dependence of the flow is slow enough, the Navier-Stokes equation simplifies and we have the expression for the gradient of the hydrodynamic pressure along the free surface,

$$\frac{\partial p^{\mathrm{HD}}}{\partial \tau} = \frac{\rho_\mathrm{l} u_\varphi^2}{r}\frac{\partial r}{\partial \tau} - \frac{\rho_\mathrm{l}}{2}\frac{\partial u_\tau^2}{\partial \tau} + \frac{\eta}{r}\frac{\partial (r\omega)}{\partial n} + \rho_\mathrm{l} g \beta (T - T_0)\frac{\partial r}{\partial n},$$

the integration of which yields:

$$p^{\mathrm{HD}}(\tau) = \int_{\tau_0}^{\tau} \frac{\rho_{\mathrm{l}} u_\varphi^2}{r} \frac{\partial r}{\partial \tau}\, \mathrm{d}\tau - \frac{\rho_{\mathrm{l}} u_\tau^2}{2} + \int_{\tau_0}^{\tau} \left(\frac{\eta}{r} \frac{\partial (r\omega)}{\partial n} + \rho_{\mathrm{l}} g \beta (T - T_0) \frac{\partial r}{\partial n} \right) \mathrm{d}\tau, \qquad (3.37)$$

where τ_0 is a reference point where $u_\tau = 0$, so that $p^{\mathrm{HD}}(\tau_0) = 0$. Let us choose as reference point the outmost end-point of the free surface: $\tau_0 = \tau_{\mathrm{ETP}}$.

3.6 Flow influence on the free surface shape

Since it seems that this question has not found place in works on modelling of floating zone before, let us consider the flow influence on the free surface shape in more detail and roughly estimate the comparative order of magnitude of the different flow-related terms in the free surface equation (3.36) with (3.37).

We need for analysis more characteristic quantities than already introduced in Section 3.4. From numerical calculations of 4 to 8 inch floating zones we take the characteristic length scale in the vertical direction, L_z, as a half of the bulk liquid height H_{L}, and the characteristic electric current surface density at the free surface, I_{s}:

$$\begin{aligned} L_z = H_{\mathrm{L}}/2 &= 0.0085 \text{ m}, \\ I_{\mathrm{s}} &= 8000 \text{ A/m}. \end{aligned}$$

To avoid underestimation of the ω-term in (3.37), let us assume that the characteristic flow boundary layer thickness L_n at the free surface is significantly smaller than the length scale L and has the expression: $L_n = L/\sqrt{\mathrm{Re}_{rz}}$.

We use below the following dimensionless numbers beside the ones from Table 3.3:

- Galilei number, $\mathrm{Ga} = g L_z L^2/\nu^2$,
- Laplace number, $\mathrm{La} = \gamma L^2/(\rho_{\mathrm{l}} \nu^2 L_z)$,
- and an electromagnetic number, $\mathrm{Em} = \mu_0 I_{\mathrm{s}}^2 L^2/(\rho_{\mathrm{l}} \nu^2)$.

The equations (3.36) and (3.37) are made dimensionless by dividing them by $\rho_{\mathrm{l}} g L_z$, which is the characteristic value of the hydrostatic pressure p^{HS}. The following list shows the terms of equations and their respective dimensionless representation (a hat

Equation term	FZ 4”	FZ 8”
$\rho g z$-term (3.38)	1	1
$\gamma\mathcal{K}$-term (3.39)	0.5	0.5
p^{EM}-term (3.40)	0.2	0.2
u_φ^2-term (3.41)	$2 \cdot 10^{-3}$	$1 \cdot 10^{-3}$
u_τ^2-term (3.42)	$6 \cdot 10^{-4}$	$6 \cdot 10^{-4}$
ω-term (3.43)	$1 \cdot 10^{-3}$	$1 \cdot 10^{-3}$
T-term (3.44)	$\Lambda \cdot 9 \cdot 10^{-3}$	$\Lambda \cdot 2 \cdot 10^{-2}$
$\partial u_n/\partial n$-term (3.45)	$6 \cdot 10^{-6}$	$3 \cdot 10^{-6}$

Table 3.4: Estimated dimensionless magnitudes $\Upsilon/(\widehat{\Upsilon}\rho_\mathrm{l} g L_z)$ of the terms in the free surface equations (3.36) and (3.37).

over a term denotes that it is dimensionless):

$$p^{\mathrm{HS}} = \mathrm{const} - \rho_\mathrm{l} g z \quad \rightarrow \quad \frac{p^{\mathrm{HS}}}{\rho_\mathrm{l} g L_z} = 1 \cdot \widehat{p}^{\mathrm{HS}} \tag{3.38}$$

$$p^{\mathrm{La}} = -\gamma\mathcal{K} \quad \rightarrow \quad \frac{p^{\mathrm{La}}}{\rho_\mathrm{l} g L_z} = -\mathrm{La}/\mathrm{Ga} \cdot \widehat{p}^{\mathrm{La}} \tag{3.39}$$

$$-p^{\mathrm{EM}} = -\frac{\mu_0 {i_{\mathrm{ef}}}^2}{2} \quad \rightarrow \quad \frac{-p^{\mathrm{EM}}}{\rho_\mathrm{l} g L_z} = -\tfrac{1}{2}\mathrm{Em}/\mathrm{Ga} \cdot \widehat{p}^{\mathrm{EM}} \tag{3.40}$$

$$\Upsilon_1 = \int_{\tau_{\mathrm{ETP}}}^{\tau} \frac{\rho_\mathrm{l} u_\varphi^2}{r}\frac{\partial r}{\partial \tau}\,\mathrm{d}\tau \quad \rightarrow \quad \frac{\Upsilon_1}{\rho_\mathrm{l} g L_z} = -\mathrm{Re}_\varphi^2/\mathrm{Ga} \cdot \widehat{\Upsilon}_1 \tag{3.41}$$

$$\Upsilon_2 = -\frac{\rho_\mathrm{l} u_\tau^2}{2} \quad \rightarrow \quad \frac{\Upsilon_2}{\rho_\mathrm{l} g L_z} = -\tfrac{1}{2}\mathrm{Re}_{rz}^2/\mathrm{Ga} \cdot \widehat{\Upsilon}_2 \tag{3.42}$$

$$\Upsilon_3 = \int_{\tau_{\mathrm{ETP}}}^{\tau} \frac{\eta}{r}\frac{\partial(r\omega)}{\partial n}\mathrm{d}\tau \quad \rightarrow \quad \frac{\Upsilon_3}{\rho_\mathrm{l} g L_z} = \pm\mathrm{Re}_{rz}^2/\mathrm{Ga} \cdot \widehat{\Upsilon}_3 \tag{3.43}$$

$$\Upsilon_4 = \int_{\tau_{\mathrm{ETP}}}^{\tau} \rho_\mathrm{l} g \beta (T - T_0)\frac{\partial r}{\partial n}\mathrm{d}\tau \quad \rightarrow \quad \frac{\Upsilon_4}{\rho_\mathrm{l} g L_z} = -\Lambda \cdot \mathrm{Gr}/\mathrm{Ga} \cdot \widehat{\Upsilon}_4 \tag{3.44}$$

$$\Upsilon_0 = -2\eta\frac{\partial u_n}{\partial n} = 2\eta\left(\frac{\partial u_\tau}{\partial \tau} + \frac{u_\tau}{r}\frac{\partial r}{\partial \tau}\right) \quad \rightarrow \quad \frac{\Upsilon_0}{\rho_\mathrm{l} g L_z} = \pm 4\mathrm{Re}_{rz}/\mathrm{Ga} \cdot \widehat{\Upsilon}_0 \tag{3.45}$$

The factor Λ in (3.44) is the characteristic value of $\partial r/\partial n$ at the free surface and emphasizes that the term Υ_4 can become negligible independently on how large the Grashof number is, if the free surface is horizontal.

Finally, the resulting dimensionless magnitudes, i.e., the dimensionless coefficients of kind $\Upsilon/(\widehat{\Upsilon}\rho_\mathrm{l} g L_z)$, are calculated for all the different terms in Table 3.4. It can be seen that, for the considered 4 inch and 8 inch floating zones, the gravitational, capillary and electromagnetic terms in the free surface equation are some orders of magnitude

larger than any of the flow-related correction terms. Hence it is justified, in these cases, to neglect the flow effect on the shape of the free surface or just to take the largest of the correction terms.

Comparing the flow correction terms, it should be taken into account that the factor Λ in the temperature term is small because of a rather horizontal free surface if the diameter of the crystal is large enough. One of the largest of the flow correction terms is hence the u_φ^2-term (3.41), which represents the effect of the centrifugal forces. An advantage of this flow-related term is that it is possible to account for it even without calculating the melt flow explicitly. If approximating the fluid rotation in the floating zone by a solid-body rotation with the rotation rate of the crystal, then $u_\varphi \approx 2\pi r\,\Omega_{\mathrm{Cr}}$ and integration yields:

$$\int_{\tau_{\mathrm{ETP}}}^{\tau} \frac{\rho_{\mathrm{l}} u_\varphi^2}{r} \frac{\partial r}{\partial \tau}\,\mathrm{d}\tau \;\approx\; 2\pi^2 \rho_{\mathrm{l}}\,\Omega_{\mathrm{Cr}}^2 r^2 + \mathrm{const}, \tag{3.46}$$

where the constant equals $-2\pi^2 \rho_{\mathrm{l}}\,\Omega_{\mathrm{Cr}}^2 R_{\mathrm{Cr}}^2$ and can be eliminated from the final surface equation by a corresponding redefinition of the gauge pressure p_0.

4 Axisymmetric model of phase boundaries

In this chapter, the models and methods of calculation of FZ phase boundaries as implemented in own calculation code `FZONE` are described.

The FZ growth system is assumed to be axisymmetric except the inductor, which may have radial slits according to the industrial practice (Fig. 4.1). The influence of the inductor slits is taken into account in an approximate way and an axisymmetric electromagnetic field is used instead of the real three-dimensional one for the heat generation and phase boundary calculation.

The placement and shape of the phase interfaces between solid and melt is solved by a transient approach (see Section 4.1), meanwhile the free melt surface is treated by a simplified steady-state method without requesting conservation of the melt volume (see Section 4.4). Beside that, the mathematical models contain some other steady-state features. Thus it is altogether a partly transient approach and is usable for obtaining the final stationary growth situation but not the explicit evolution in time.

4.1 Phase interfaces

Starting from an initial phase interface shape, the move rates of each point of the melting and crystallization interfaces are calculated by requesting fulfilment of the local heat balance equation at the respective interface:

$$\lambda_\mathrm{s} \left.\frac{\partial T}{\partial n}\right|_\mathrm{s} = \lambda_\mathrm{l} \left.\frac{\partial T}{\partial n}\right|_\mathrm{l} + \rho_\mathrm{s} Q V_n, \tag{4.1}$$

where the temperature field T in solid and liquid is known after solving the global heat transfer (see Section 4.8.1), Q denotes the latent heat of fusion, ρ, the density, λ, the thermal conductivity, the subscripts s and l stand for solid and liquid, respectively, and V_n is the unknown front's normal rate of solidification in the reference system of the solid phase or, equally, the normal projection of the front's move rate with the

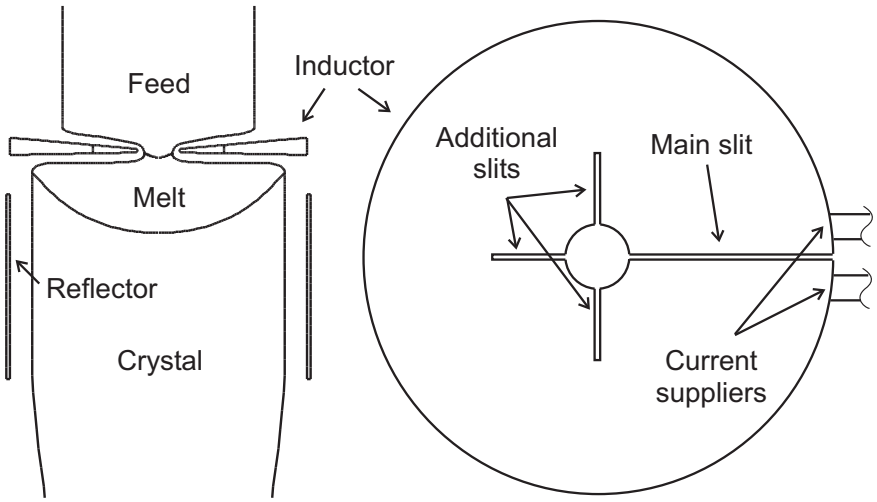

Figure 4.1: FZ growth system and the inductor with radial slits.

positive directions as shown by the vectors **n** in Fig. 4.2 (hence, for example, $V_n < 0$ when melting instead of solidification occurs). The solidification rate V_n is related to the local front's normal velocity v_n in the laboratory reference system (i.e. the reference system of the inductor and the furnace around) by the relation:

$$V_n = V_{\mathrm{s}} n_z + v_n, \tag{4.2}$$

where V_{s} denotes the move rate of the solid silicon in the laboratory reference system, which equals to the move rate of feed, V_{F}, or crystal, V_{Cr}, when considering the melting or crystallization interface, respectively. The value of v_n characterizes how transient the process is (e.g. in a steady-state case $v_n = 0$) and can be calculated from the balance equation (4.1):

$$v_n = \frac{\lambda_{\mathrm{s}}}{\rho_{\mathrm{s}} Q} \left.\frac{\partial T}{\partial n}\right|_{\mathrm{s}} - \frac{\lambda_{\mathrm{l}}}{\rho_{\mathrm{s}} Q} \left.\frac{\partial T}{\partial n}\right|_{\mathrm{l}} - V_{\mathrm{s}} n_z. \tag{4.3}$$

The formula (4.3) applies to the melting and crystallization interfaces. For the open melting front, the velocity expression has to account also the Joulean heat flux q^{EM} and the radiation heat flux q^{rad}:

$$v_n = \frac{\lambda_{\mathrm{s}}}{\rho_{\mathrm{s}} Q} \left.\frac{\partial T}{\partial n}\right|_{\mathrm{F}} + \frac{q^{\mathrm{rad}} - q^{\mathrm{EM}}}{\rho_{\mathrm{s}} Q} - V_{\mathrm{F}} n_z. \tag{4.4}$$

The calculation of the Joulean heat flux q^{EM} at the open front requires assumptions about the open front structure. The fluid film model and the expression for q^{EM} are derived in Section 4.3. The calculation of the radiation heat flux q^{rad} is considered in Section 4.7.

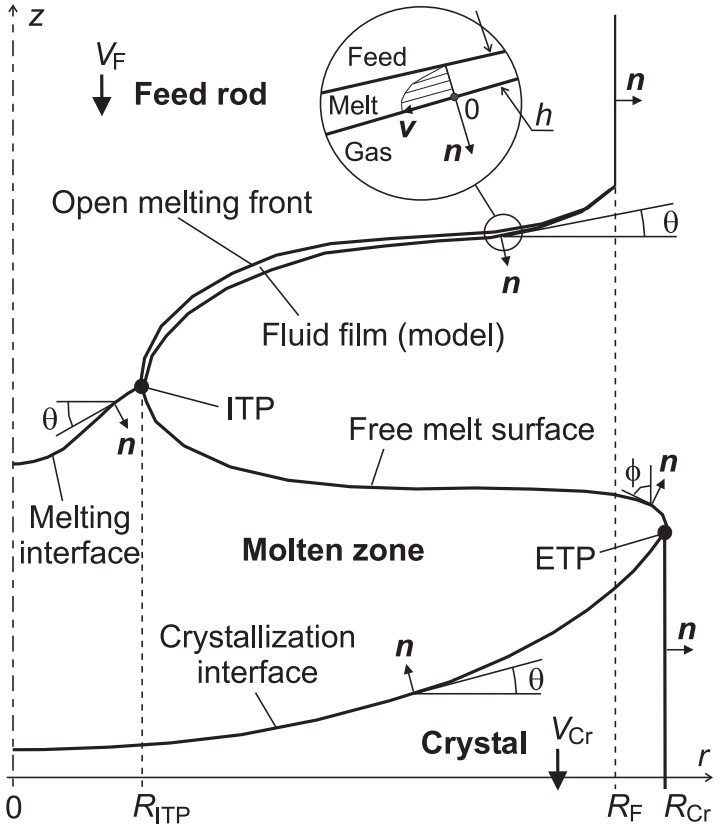

Figure 4.2: Sketch of the model for FZ growth.

For solving the phase boundaries numerically, they are divided into linear elements and the velocities v_n are calculated in the nodes according to the formulas (4.3) and (4.4). All quantities needed for this procedure, including the temperature gradients, electric currents and radiation heat fluxes, are interpolated to the nodes and the normal direction $\mathbf{n}$ is represented locally by the bisector at the respective node (e.g. see Fig. 4.6). Chosen a time step Δt, each node is moved by $v_n \Delta t$ in the direction $\mathbf{n}$.

4.2 Axisymmetric model of high-frequency EM field

In order to obtain the Joulean heat fluxes on all conducting surfaces and the electromagnetic pressure on the free melt surface, the electromagnetic field in the FZ system has to be calculated.

Due to the inductor shape used in FZ process, a 3D EM calculation would actually be necessary in order to take the azimuthal average of the Joulean heat source distribution, for the axisymmetric phase boundary calculation. Since the EM field recalculation

is repeated several times in each calculation step, it costs too much computational resources and must be replaced by effective 2D EM field calculations. It is possible to include the approximate influence of the inductor slits in the axisymmetric EM field model. The method and its physical background for induction furnaces with regularly slitted crucible has been described in [78]. In the present work, the methodology from [78] is adapted to the case of FZ system with a slitted inductor. Additionally, an approximate account of the main slit of the inductor is included.

The boundary lines in the cross-section of the FZ system that are relevant in the electromagnetic part of calculation are shown in Fig. 4.3: the silicon surface (*SilSurf*), the surface of the inductor part that is not slitted if not counting the main slit (*IndSurf*), the surface of the slitted part of the inductor (*IndSlit*), and the end-line of the slits in the middle of inductor (*IndMidd*). The inner plane of the slit is the shaded region in Fig. 4.3. We can attach a local Cartesian coordinate system (x, y) to this (and any other) slit plane. Assuming the axial symmetry is not disturbed much by the slits, the electric current in the high-frequency approximation is going along the surfaces *SilSurf*, *IndSurf* and *IndSlit* only in the azimuthal direction. We will designate, in this section, this azimuthal surface current by $\mathbb{J}$. A part of current is flowing also in the plane of slit and has there some x- and y-component. The slit current will be designated here by $\beth = \{\beth_x, \beth_y\}$.

4.2.1 Equations for the non-slitted parts

The EM field is solved in terms of the magnetic vector-potential $\mathbf{A}$, defined by $\operatorname{rot} \mathbf{A} = \mathbf{B}$. The field is to be found in the space surrounding the conducting bodies by setting boundary conditions at the surfaces of the conductors. The vector-potential in the non-conducting space is governed by the Poisson equation: $\Delta \mathbf{A} = 0$. Only the azimuthal component of $\mathbf{A}$ differs from zero in axisymmetric model, $A \equiv A_\varphi$. Therefore

$$\Delta A(r,z) - \frac{A(r,z)}{r^2} = 0 \quad \text{or} \quad \frac{1}{r}\frac{\partial}{\partial r}\left(r\frac{\partial A}{\partial r}\right) - \frac{A}{r^2} + \frac{\partial^2 A}{\partial z^2} = 0. \tag{4.5}$$

It follows directly from the definition of the magnetic vector-potential that the field lines of $\mathbf{B}$ are as well the isolines of $(r \cdot A)$, in the axisymmetric case. Using the assumption about the magnetic field lines going parallel along the conducting surfaces, it follows for the non-slitted surfaces:

$$\frac{\partial(rA)}{\partial \tau} = 0 \quad \text{at } \textit{SilSurf} \text{ (and } \textit{IndSurf} \text{ without slit)}, \tag{4.6}$$

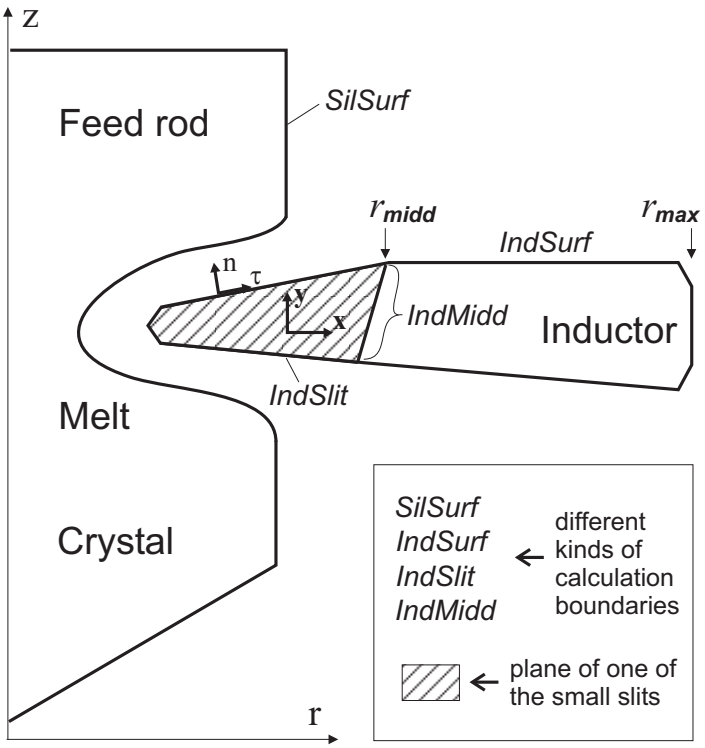

Figure 4.3: The different boundary lines relevant in the calculation.

where τ is the local tangential direction along the boundary lines. For *IndSurf* the condition (4.6) is valid only when not accounting the main slit of the inductor. The modification including the main slit's influence see below.

Since the silicon surface includes points at the symmetry axis and A must have a finite value everywhere, the boundary condition for vector-potential follows from (4.6):

$$A = 0 \qquad \text{at } \mathit{SilSurf}. \tag{4.7}$$

In frame of a model not accounting the main slit's influence, the equation (4.6) yields the boundary condition also for the non-slitted part of inductor:

$$A = \frac{C_0}{r} \qquad \text{at } \mathit{IndSurf} \quad \text{(without the main slit!)} \tag{4.8}$$

4.2.2 Inductor model with m slits

It follows (see [78]) from the Maxwell equations that one can introduce a scalar potential for the slit current $\mathbf{j}$ in the slit plane, $F(x, y)$, such that

$$\mathbf{j} = \nabla F \qquad \text{or} \qquad \mathbf{j}_x = \frac{\partial F}{\partial x}, \quad \mathbf{j}_y = \frac{\partial F}{\partial y}. \tag{4.9}$$

At the line *IndSlit*, the azimuthal current and the normal component of the current in the slit plane are equal: $\mathfrak{J}_n = \mathbb{J}$ (assuming the normal direction as shown in Fig. 4.3). On the other hand, $\mathfrak{J}_n = \frac{\partial \digamma}{\partial n}$, therefore we obtain:

$$\mathbb{J} = \frac{\partial \digamma}{\partial n} \qquad \text{at } \mathit{IndSlit}. \tag{4.10}$$

Taking into account the properties of the magnetic field $\mathbf{B}$ and the definition of the vector-potential $\mathbf{A}$, the relation between the magnetic fields outside and inside the slit is yielding the following condition at the *IndSlit*-line [78]:

$$\frac{\partial (rA)}{\partial \tau} + \frac{mb\mu_0}{2\pi} \frac{\partial \digamma}{\partial \tau} = 0 \qquad \text{at } \mathit{IndSlit}, \tag{4.11}$$

where m – the count of slits, b – the width of each slit, τ – the tangential coordinate along the line *IndSlit* like shown in Fig. 4.3.

From the assumption that the normal component of the high-frequency magnetic field at the conducting surfaces is zero, it follows:

$$\frac{\partial \digamma}{\partial \tau} = 0 \qquad \text{at } \mathit{IndMidd}. \tag{4.12}$$

Since the current satisfies the condition $\mathrm{div}\mathfrak{J} = 0$, we obtain with help of (4.9) the equation for the scalar potential in the slit plane:

$$\Delta \digamma(x, y) = 0 \qquad \text{or} \qquad \frac{\partial^2 \digamma}{\partial x^2} + \frac{\partial^2 \digamma}{\partial y^2} = 0. \tag{4.13}$$

This equation should be solved in the slit plane (the shaded area in Fig. 4.3). For a boundary condition we use (4.12), moreover we may choose zero level for the constant $\digamma$ at *IndMidd*:

$$\digamma = 0 \qquad \text{at } \mathit{IndMidd}. \tag{4.14}$$

We have no other boundary conditions for $\digamma$, but we have the equation (4.11) coupling at *IndSlit* together the fields of scalar potential $\digamma$ and vector-potential A. This can be rewritten in a more convenient form:

$$A + \frac{\mu_0}{2\pi r} mb\digamma = \frac{C_0}{r} \qquad \text{at } \mathit{IndSlit}, \tag{4.15}$$

where the constant C_0 equals that in (4.8) to ensure fitting together of the conditions (4.15), (4.8) and (4.14) in the two common endpoints of the boundary lines *IndSlit*, *IndSurf* and *IndMidd*.

4.2.3 Approximation for the main slit

There are several different possibilities of introducing the main slit in the mathematical model above. However, some of them ask for a considerable increasing in the number of equations for the final numerical problem formulation, which is a disadvantage. Since any of the axisymmetric models can, in principle, produce only a very approximate image of the main slit's effect, we have chosen the most rough of the possible approaches, which asks only one additional equation.

The idea is to replace the constant C_0 in the boundary condition (4.8) by a function $\tilde{C}(r)$ that is changing along *IndSurf* in order to take in account the vertical flux of magnetic field going through the outer part (i.e., the part at the right hand side from *IndMidd*) of the main slit. The inner part of the main slit was already accounted together with the small slits, therefore it is out of interest at this point. So the new boundary condition takes the form

$$A = \frac{\tilde{C}(r)}{r} \qquad \text{at } \textit{IndSurf} \quad \text{(with the main slit!)} \tag{4.16}$$

The shape of the function $\tilde{C}(r)$ must be obtained from physical considerations. The vertical component of the magnetic field near the slit plane, B_y, is coupled with the horizontal current density in the slit, $\mathbb{J}_x$, by the relation $B_y = -\mu_0 \mathbb{J}_x$. Let us introduce an effective dimensionless parameter I_{slit} defined as the ratio between the effective integral current flowing horizontally in the slit plane and the total current I_0 going through the inductor. It is clear that always $I_{\text{slit}} < 1$. Then the approximate expression for the horizontal current density is: $\mathbb{J}_x = I_{\text{slit}} I_0 / H_{\text{av}}$, where H_{av} is the average height of the outer part of the main slit. Consequently, if the length of the outer part of the main slit is L_1 and the width is b_1, then the magnetic flux going through is:

$$\Phi = B \cdot b_1 \cdot L_1 = \mu_0 I_{\text{slit}} I_0 \cdot b_1 L_1 / H_{\text{av}}. \tag{4.17}$$

On the other hand, the same magnetic flux can be expressed also with the vector-potential values at the inner and outer radial positions of the outer part of the main slit:

$$\Phi = 2\pi \left[r_{\max} A(r_{\max}) - r_{\text{mid}} A(r_{\text{mid}}) \right], \tag{4.18}$$

where $r_{\max}$ is the outer radius of the inductor and r_{mid} is the maximum radius of the line *IndMidd* as shown in Fig. 4.3. The previously introduced parameter L_1 equals to

$r_{\max} - r_{\mathrm{mid}}$. Using (4.16), the last expression for the magnetic flux can be transformed in terms of $\tilde{C}$. Together with (4.17) it yields:

$$\tilde{C}(r_{\max}) - \tilde{C}(r_{\mathrm{mid}}) = \frac{\mu_0 I_{\mathrm{slit}} I_0}{2\pi} \cdot b_1 L_1 / H_{\mathrm{av}}. \tag{4.19}$$

Assuming a linear change of the function $\tilde{C}(r)$ between r_{mid} and $r_{\max}$ and recalling that $\tilde{C}(r_{\mathrm{mid}})$ must be equal to C_0 in order to fit the boundary conditions at *IndSlit* and *IndMidd*, we obtain:

$$\tilde{C}(r) = \frac{\mu_0 I_{\mathrm{slit}} b_1}{2\pi H_{\mathrm{av}}} I_0 \cdot \max\{0; r - r_{\mathrm{mid}}\} + C_0. \tag{4.20}$$

The meaning of the "max"-function is to retain consistent boundary conditions also for a case with a slightly sloped *IndMidd*-line, as in the example in Fig. 4.3.

4.2.4 The numerical method

The problem formulated above with the modified boundary condition (4.16) and (4.20) is solved numerically by the Boundary Element Method (BEM). The boundary lines shown in Fig. 4.3 are discretised into boundary elements. The elements are indexed with index k and we can write symbolically $k \in$ *SilSurf, IndSurf, IndSlit, IndMidd*, meaning that the boundary element belongs to one of these surfaces. The vector-potential $A(\imath)$ in some spatial point denoted by $\imath$ (or in the center of the boundary element with index $\imath$) is expressed as a sum of the partial vector-potentials $(A_k(\imath) \cdot \mathbb{J}_k)$ created in the point $\imath$ by the element k (i.e., by the axisymmetric surface ring represented in 2D by the line segment k):

$$A(\imath) = \sum_{k \in \begin{pmatrix} \mathrm{SilSurf} \\ \mathrm{IndSurf} \\ \mathrm{IndSlit} \end{pmatrix}} A_k(\imath) \cdot \mathbb{J}_k. \tag{4.21}$$

Each term $(A_k(\imath) \cdot \mathbb{J}_k)$ is a fundamental solution of the Poisson's equation (4.5) and contains the current density $\mathbb{J}_k$ in the element k. The coefficients $A_k(\imath)$ can be expressed with the elliptic integrals $K(p)$ and $E(p)$:

$$A_k(\imath) = \frac{\mu_0 d_k}{\pi \sqrt{r^* \cdot p}} \cdot \left[K(p) \cdot \left(1 - \frac{p}{2}\right) - E(p) \right], \tag{4.22}$$

with

$$p = \frac{4r^*}{r^{*2} + z^{*2} + 2r^* + 1},$$

$$r^* = \frac{r}{r_k}, \qquad z^* = \frac{z - z_k}{r_k},$$

where d_k is the cross-section length of the boundary element k, while r_k and z_k are the coordinates of its middle point.

The scalar potential F is expressed as a sum of the partial scalar potentials $(P_k(\imath) \cdot \mathbb{K}_k)$ created by the so called "charges" $\mathbb{K}_k$ in the boundary elements k of the slit boundary:

$$F(\imath) = \sum_{k \in \binom{\text{IndSlit}}{\text{IndMidd}}} P_k(\imath) \cdot \mathbb{K}_k. \tag{4.23}$$

The coefficients $P_k(\imath)$ in the fundamental solutions $(P_k(\imath) \cdot \mathbb{K}_k)$ of the equation (4.13) are:

$$P_k(\imath) = d_k \cdot \ln \sqrt{(r - r_k)^2 + (z - z_k)^2}. \tag{4.24}$$

It follows from the relation (4.10) that the azimuthal current density at the boundary of the small slit is:

$$\mathbb{J}(\imath)\Big|_{\imath \in \text{IndSlit}} = \frac{\partial F(\imath)}{\partial n}\Big|_{\imath \in \text{IndSlit}} = \sum_{k \in \binom{\text{IndSlit}}{\text{IndMidd}}} N_k(\imath) \cdot \mathbb{K}_k, \tag{4.25}$$

where

$$N_k(\imath) = \frac{\partial P_k(\imath)}{\partial n}. \tag{4.26}$$

To solve the problem numerically, the equations arising from the boundary conditions (4.14), (4.15), (4.7) and (4.16) by substituting the expressions (4.21), (4.23) and (4.25) are written for each of the boundary elements ($\imath$ running over all the boundaries). The variables to be solved are the currents $\mathbb{J}_k$ ($k \in$ *SilSurf, IndSurf*) and the "charges" $\mathbb{K}_k$ ($k \in$ *IndSlit, IndMidd*). One additional variable, the total inductor current $\mathbb{I}$ renormalized so that $C_0 = 1$, arises because of the accounting of the main slit and implies solving of an additional equation (the first one of the equations below). The equations are as follows:

$\imath = 0$:

$$-\mathbb{I} + \sum_{k \in \text{IndSurf}} d_k \cdot \mathbb{J}_k + \sum_{k \in \binom{\text{IndSlit}}{\text{IndMidd}}} \left[\sum_{\ell \in \text{IndSlit}} d_\ell N_k(\ell) \right] \cdot \mathbb{K}_k = 0 \tag{4.27}$$

$\imath \in$ SilSurf :

$$\sum_{k\in\binom{\text{SilSurf}}{\text{IndSurf}}} A_k(\imath)\cdot\mathbb{J}_k + \sum_{k\in\binom{\text{IndSlit}}{\text{IndMidd}}}\left[\sum_{\ell\in\text{IndSlit}} A_\ell(\imath)N_k(\ell)\right]\cdot\mathbb{K}_k = 0 \tag{4.28}$$

$\imath \in$ IndSurf :

$$-\frac{\mu_0 b_1 I_{\text{slit}}}{2\pi H_{\text{av}}}\cdot\max\left(0;\,1-\frac{r_{\text{mid}}}{r(\imath)}\right)\cdot\mathbb{I} + \sum_{k\in\binom{\text{SilSurf}}{\text{IndSurf}}} A_k(\imath)\cdot\mathbb{J}_k + \sum_{k\in\binom{\text{IndSlit}}{\text{IndMidd}}}\left[\sum_{\ell\in\text{IndSlit}} A_\ell(\imath)N_k(\ell)\right]\cdot\mathbb{K}_k = \frac{1}{r(\imath)} \tag{4.29}$$

$\imath \in$ IndSlit :

$$\sum_{k\in\binom{\text{SilSurf}}{\text{IndSurf}}} A_k(\imath)\cdot\mathbb{J}_k + \sum_{k\in\binom{\text{IndSlit}}{\text{IndMidd}}}\left[\sum_{\ell\in\text{IndSlit}} A_\ell(\imath)N_k(\ell) + \frac{\mu_0 mb}{2\pi r(\imath)}P_k(\imath)\right]\cdot\mathbb{K}_k = \frac{1}{r(\imath)} \tag{4.30}$$

$\imath \in$ IndMidd :

$$\sum_{k\in\binom{\text{IndSlit}}{\text{IndMidd}}} P_k(\imath)\cdot\mathbb{K}_k = 0 \tag{4.31}$$

The system of linear algebraic equations is solved by a direct method (Gauss elimination).

4.3 Open melting front: the "fluid film model"

4.3.1 Fluid film thickness h

The proposed model for the open melting front is an improvement of that used in Ref. [45]. Although in reality the structure is more complicated, we assume that the molten silicon at the open melting front forms a thin fluid film, of which the thickness changes smoothly in the meridional direction but not in the azimuthal direction. Due to gravity, the fluid flow is directed downwards along the front in the meridional direction and obeys the Navier-Stokes equation, which may be written in the specific case as follows:

$$\eta\frac{\mathrm{d}^2 v}{\mathrm{d}n^2} + \rho_{\text{l}} g\sin\theta = 0,$$

where η is the dynamic viscosity, g, the gravity and $v = v(n)$, the flow velocity, which together with the chosen reference of the normal coordinate n and the angle $\theta(r)$ is

depicted in Fig. 4.2. Requiring zero velocity at the melt–solid boundary and zero shear stress at the free surface of the fluid film, we get the parabolic velocity profile in the film:

$$v(n) = \frac{\rho_\mathrm{l} g \sin\theta}{2\eta} \left(h^2 - n^2\right), \tag{4.32}$$

where h denotes the fluid film thickness. The fluid discharge at fixed location r is proportional to the integral of the velocity over n and is related to the melting rate upward from that location. For a stationary process:

$$\rho_\mathrm{l} \cdot 2\pi r \int_{-h}^{0} v(n)\mathrm{d}n = \rho_\mathrm{s} \cdot \pi \left({R_\mathrm{F}}^2 - r^2\right) V_\mathrm{F}, \tag{4.33}$$

where V_F is the constant feed move rate and R_F, the radius of the feed rod. From (4.32) and (4.33), we obtain, in frame of the simplified model, the film thickness distribution along the open melting front:

$$h = \left[\frac{3\eta\rho_\mathrm{s} V_\mathrm{F} \left({R_\mathrm{F}}^2 - r^2\right)}{2{\rho_\mathrm{l}}^2 g \sin\theta(r) \cdot r}\right]^{1/3}. \tag{4.34}$$

4.3.2 Joulean heat flux at the open melting front

The integral surface density of the induced power in the skin layer of the bulk melt or solid can be calculated by the formula (3.14), as shown in Section 3.3. This formula is not applicable in case of the open melting front because of the inhomogeneous material properties along the depth of the skin layer. The total Joulean heat flux density at the open front, q^EM, including both, the power q_M^EM in the molten film of depth h and the power q_F^EM deeper in the solid feed, is expressed as follows:

$$q^\mathrm{EM} \equiv q_\mathrm{M}^\mathrm{EM} + q_\mathrm{F}^\mathrm{EM} = \xi \cdot q_{\mathrm{h}\to\infty}^\mathrm{EM}, \tag{4.35}$$

where $q_{\mathrm{h}\to\infty}^\mathrm{EM}$ is the surface density of a fictitious power calculated for case when the fluid film thickness is much larger than the skin layer depth, and the factor ξ is introduced like in [45] to account how much higher is the power due to the finite depth of the film.

To derive ξ analytically, we consider the penetration of the EM field into the conducting medium near the open front. By neglecting the displacement currents in the Maxwell equation and using the material relation $\mathbf{j} = \sigma\mathbf{E}$ for the volume current density, we have

$$\mathrm{rot}\mathbf{B} = \mu_0 \sigma(n)\mathbf{E},$$

where the change in the normal direction of the conductivity σ is emphasized due to the jump at the melt–feed boundary at $n = -h$ (see the orientation of the n-axis in Fig. 4.2). With help of the other Maxwell equations, we obtain the equation for the azimuthal component E of the electric field,

$$\frac{\partial^2 E(n,t)}{\partial n^2} = \mu_0 \sigma(n) \frac{E(n,t)}{\partial t},$$

where we account for the spatial change only in the normal direction. The solution is sought in the form $E(n,t) = E^{\mathrm{a}}(n)\cos(\omega t + \Delta)$, where $\omega = 2\pi f$, and the field amplitude E^{a} must decrease exponentially with the penetration depth. The solution satisfying the continuity at $n = -h$ is:

$$E(n,t)|_{-h<n<0} = E^{\mathrm{a}}(0) \cdot \mathrm{e}^{n/\delta_{\mathrm{l}}} \cos\left(\omega t + \frac{n}{\delta_{\mathrm{l}}}\right)$$
$$E(n,t)|_{n<-h} = E^{\mathrm{a}}(0)\mathrm{e}^{-h/\delta'} \cdot \mathrm{e}^{n/\delta_{\mathrm{s}}} \cos\left(\omega t + \frac{n}{\delta_{\mathrm{s}}} - \frac{h}{\delta'}\right)$$

with the designation $\delta' = (1/\delta_{\mathrm{l}} - 1/\delta_{\mathrm{s}})^{-1}$ and

$$\delta_{\mathrm{l,s}} = \frac{1}{\sqrt{\pi \mu_0 f \sigma_{\mathrm{l,s}}}}$$

for the skin layer depth in the liquid and solid, respectively.

The relation between the field and the volume current density,

$$j(n,t) = \sigma(n) E(n,t),$$

and the relation between j and the effective surface current i_{ef}, i.e.,

$$i_{\mathrm{ef}}^2 = \overline{\left(\int_{-\infty}^{0} j(n,t)\mathrm{d}n\right)^2},$$

allow to express the amplitude of j at the free surface of the film, $j^{\mathrm{a}}(0) = \sigma_{\mathrm{l}} E^{\mathrm{a}}(0)$, in terms of i_{ef}. The latter is known since calculated by the boundary element method (Section 4.2). The volume current density distribution $j(n,t)$ is hereby determined and yields the Joulean heat flux:

$$q^{\mathrm{EM}} = \int_{-\infty}^{0} \frac{\overline{j^2(n,t)}}{\sigma(n)}\,\mathrm{d}n.$$

This way, the expression (4.35) is evaluated and the coefficient ξ is found:

$$\xi(h) = \frac{1 - (1-\kappa)\,\mathrm{e}^{-2\ell}}{1 - 2(1-\kappa)\,\mathrm{e}^{-\ell}\cos\ell + (1-\kappa)^2\,\mathrm{e}^{-2\ell}}\,, \tag{4.36}$$

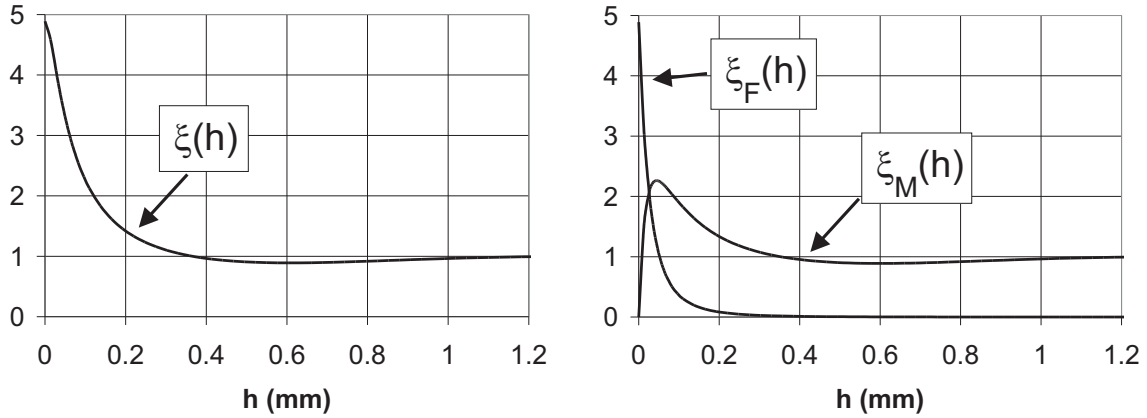

Figure 4.4: Dependence of the dimensionless heat fluxes ξ, ξ_{M} and ξ_{F} on the film thickness h in frame of the "fluid film model" for the open front.

where

$$\ell \equiv \ell(h) = h/\delta_{\mathrm{l}},$$

$$\kappa = \sqrt{\sigma_{\mathrm{s}}/\sigma_{\mathrm{l}}} \equiv \delta_{\mathrm{l}}/\delta_{\mathrm{s}}.$$

The expression for $q^{\mathrm{EM}}_{\mathrm{h}\to\infty}$ in (4.35) is identical to that for the Joulean heat flux at the free surface of the bulk melt, cf. (3.14):

$$q^{\mathrm{EM}}_{\mathrm{h}\to\infty} = \frac{i^2_{\mathrm{ef}}}{\sigma_{\mathrm{l}}\delta_{\mathrm{l}}} \equiv \sqrt{\frac{\pi\mu_0 f}{\sigma_{\mathrm{l}}}}\, i^2_{\mathrm{ef}}. \tag{4.37}$$

Deriving the formula of ξ, respectively, q^{EM}, we obtain by the way also the separate expressions of $q^{\mathrm{EM}}_{\mathrm{M}}$ and $q^{\mathrm{EM}}_{\mathrm{F}}$, which are needed when considering the vicinity of the inner triple point (see Section 4.5.1). The coefficient ξ may be regarded as the dimensionless counterpart of the heat flux q^{EM}. Similarly, we can introduce the coefficients ξ_{M} and ξ_{F} (satisfying $\xi_{\mathrm{M}} + \xi_{\mathrm{F}} = \xi$) as the dimensionless counterparts of the heat fluxes $q^{\mathrm{EM}}_{\mathrm{M}}$ and $q^{\mathrm{EM}}_{\mathrm{F}}$:

$$q^{\mathrm{EM}}_{\mathrm{M}} = \xi_{\mathrm{M}} \cdot q^{\mathrm{EM}}_{\mathrm{h}\to\infty} \quad \text{and} \quad q^{\mathrm{EM}}_{\mathrm{F}} = \xi_{\mathrm{F}} \cdot q^{\mathrm{EM}}_{\mathrm{h}\to\infty}. \tag{4.38}$$

The expressions for ξ_{M} and ξ_{F} are as follow:

$$\xi_{\mathrm{M}}(h) = \frac{1 - \mathrm{e}^{-2\ell}}{1 - 2(1-\kappa)\,\mathrm{e}^{-\ell}\cos\ell + (1-\kappa)^2\,\mathrm{e}^{-2\ell}}\,, \tag{4.39}$$

$$\xi_{\mathrm{F}}(h) = \frac{\kappa \mathrm{e}^{-2\ell}}{1 - 2(1-\kappa)\,\mathrm{e}^{-\ell}\cos\ell + (1-\kappa)^2\,\mathrm{e}^{-2\ell}}\,. \tag{4.40}$$

The shapes of the functions $\xi(h)$, $\xi_{\mathrm{M}}(h)$ and $\xi_{\mathrm{F}}(h)$ corresponding to the conductivities of liquid and solid silicon and to the EM frequency of 2.8 MHz are shown in Fig. 4.4. We see, e.g., that the value $\xi = 1.4$ used in [45] corresponds to a constant thickness of the fluid layer $h = 0.2$ mm. The advantage of the new model is a variable h according to (4.34) and, consequently, a variable ξ along the open front according to (4.36).

4.4 Shape of the free melt surface

The free surface equation has been derived in Section 3.5 and the flow-related terms have been analysed in Section 3.6. Here, a simplified version of equation (3.36), i.e., with neglecting the most of the flow-related terms and keeping just the contribution due to the centrifugal forces, which is integrated by assuming a solid-body rotation as shown in (3.46), is used to derive a practical calculation procedure for the free melt surface. From the above-mentioned equations, it follows that the effective pressure imbalance

$$D = p_0 - \rho_{\mathrm{l}} g z - \gamma \left(\frac{\cos\phi}{r} + \frac{1}{R'} \right) - p^{\mathrm{EM}} + 2\pi^2 \rho_{\mathrm{l}} \Omega_{\mathrm{Cr}}^2 r^2 \tag{4.41}$$

must equal zero in the equilibrium state at every point $(r; z)$ of the free melt surface. The designations in (4.41): ϕ denotes the local surface angle with vertical (see Fig. 4.2), γ is the surface tension of the melt, R', the meridional curvature radius (positive for a convex surface), Ω_{Cr}, the rotation rate of the crystal rod, p_0, the gauge pressure in the melt, and p^{EM}, the EM pressure (3.19), i.e., the integral effective value in the high-frequency approximation as derived in Section 3.3.

For a given gauge pressure p_0, the equality to zero of the imbalance (4.41) allows to determine the shape of the free surface with fixed inner and exterior triple points. The value of p_0 is unknown and its determination needs an additional condition. In frame of the steady-state model, the exterior rim of the crystal grows vertical and the free surface makes a definite angle with the vertical, $\phi_{\mathrm{ETP}} = \phi_0$, at the exterior triple point (ETP). For silicon, the meniscus angle required to keep a constant crystal diameter, $\phi_0 \approx 11°$, is known from the literature.

The free surface is divided into linear elements in order to require zero imbalances (4.41) in every node. The curvature radius R' is approximated in the nodes by the radius of a circle drawn through the node of interest and its two neighbouring nodes. At the inner triple point, the next node of the open melting front is taken as one of the neighbouring nodes. A special approach is used at the exterior triple point.

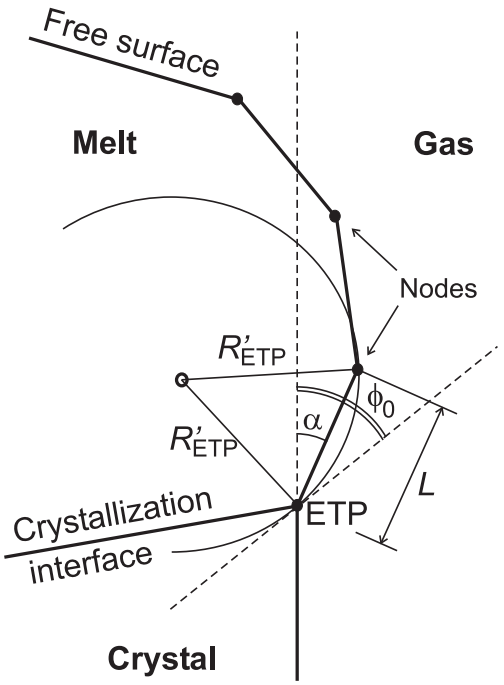

Figure 4.5: The discretized free melt surface and the curvature radius R'_{ETP} at the exterior triple point.

A circle is drawn through ETP and a next node of the free surface and its radius is chosen so that the tangent at ETP makes angle ϕ_0 with the vertical. From geometrical considerations, as shown in Fig. 4.5,

$$\frac{1}{R'_{\mathrm{ETP}}} = \frac{2 \cdot \sin(\phi_0 - \alpha)}{L}, \tag{4.42}$$

where L is the length of the first element and α, the actual angle that the first element makes with the vertical.

The equality to zero of the imbalance at the exterior triple point, $D_{\mathrm{ETP}} = 0$, yields the gauge pressure:

$$p_0 = \rho_{\mathrm{l}} g z_{\mathrm{ETP}} + \gamma \left(\frac{\cos\phi_0}{r_{\mathrm{ETP}}} + \frac{1}{R'_{\mathrm{ETP}}} \right) + p^{\mathrm{EM}}_{\mathrm{ETP}} - 2\pi^2 \rho_{\mathrm{l}} \Omega^2_{\mathrm{Cr}} r^2, \tag{4.43}$$

where the curvature radius at the triple point, R'_{ETP}, is obtained by (4.42). Thus, for a fixed distribution of electric current, the gauge pressure p_0 depends upon the position of the first node next to ETP, i.e. $p_0 = p_0(L, \alpha)$. Due to this reason, the minimization of imbalance begins at this node and the other nodes of the free surface are considered sequentially from ETP to ITP. The shifting of nodes is performed along the bisector between the neighbouring surface elements. By displacing the first node

in the direction of action of the pressure imbalance, the minimum of $|D|$ is searched by putting the actual value (4.43) of p_0 into formula (4.41). At the following nodes, the imbalance is reduced similarly but the gauge pressure is kept constant as known from the last calculation of the first node. The advantage of the described approach is that no special iteration cycle for p_0 is needed to accomplish the angle condition at ETP.

With a fixed EM field, the sweeps through all nodes are repeated many times and the imbalance value at ITP is used to judge about the convergence of the free surface. To couple the free surface and the EM field, some outer iterations are performed. During these iterations, ITP stays fixed but the value of the pressure imbalance at the inner triple point, D_{ITP}, is obtained. It is further used to calculate the location of ITP as described below.

4.5 The inner triple point and related numerical aspects

4.5.1 Inner triple point

The inner triple point is the point in the model where the melting interface, the free surface and the open front are going together. The calculation procedure of ITP is based on the assumption that the transition "melting interface—open front" is smooth. This assumption fits well to the fluid film model of the open front since the transition between the fluid film and the bulk melt must be smooth. The front's normal direction at ITP is calculated like in every other node of the melting interface or open front (see Fig. 4.6) and the distribution of the front velocity v_n is kept continuous at ITP, as described below. Consequently, what concerns the front movement, we treat the melting interface and the open front as one united front. This ensures the first degree of freedom of ITP (denoted by "1" in Fig. 4.6), i.e., the motion due to moving of the melting front.

Another degree of freedom of ITP (denoted by "2" in Fig. 4.6) is the motion due to changing of the free surface shape, which raise the pressure imbalance at the inner triple point, D_{ITP}, as considered in Section 4.4. The location of ITP at the united melting front is chosen in order to minimize the absolute value of the imbalance. Each new trial position of the inner triple point and detection of D_{ITP} requires a recalculation of the free surface shape coupled with the EM field, therefore special algorithms are

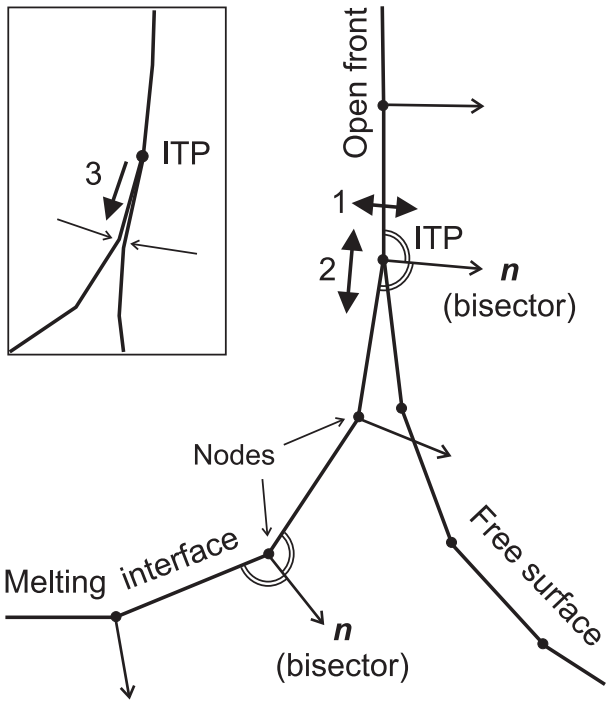

Figure 4.6: The numerical approach to the inner triple point.

used to reduce the count of recalculations needed.

The third possibility of motion of ITP in this model is the one denoted by "3" in Fig. 4.6. When the free surface touches the melting interface below the ITP location, the inner triple point moves downwards in order to eliminate the degenerate bulk melt layer, the thickness of which is vanishing.

The above-mentioned continuity of the front velocity v_n at ITP is essential and is obtained by correcting the expression (4.3) for velocity of the melting interface to take into account that a part of the interface is very close to the free melt surface. If the penetration depth of the EM field is comparable to the depth of the fluid layer covering the feed, a part of the total induced power q^{EM}, namely, $q_{\mathrm{F}}^{\mathrm{EM}}$, is induced in the feed volume and hence should be included in the velocity formula for the melting interface close below ITP:

$$\tilde{v}_n = \left(\frac{\lambda_{\mathrm{s}}}{\rho_{\mathrm{s}} Q} \left. \frac{\partial T}{\partial n} \right|_{\mathrm{F}} - \frac{q_{\mathrm{F}}^{\mathrm{EM}}}{\rho_{\mathrm{s}} Q} \right) - \frac{\lambda_{\mathrm{l}}}{\rho_{\mathrm{s}} Q} \left. \frac{\partial T}{\partial n} \right|_{\mathrm{l}} - V_{\mathrm{F}} n_z, \tag{4.44}$$

where T designates the temperature field calculated under assumption of a small EM skin depth allowing the integral heat flux boundary conditions (4.62) as applied for the temperature calculation in the melt (see Section 4.6). Consequently T does not describe the temperature gradient inside the skin region. The terms in (4.44) that are

grouped in parenthesis correspond to the correct heat flux in feed in the vicinity of the interface. Beside that, since $q_{\mathrm{F}}^{\mathrm{EM}}$ is accounted inside the feed, it is meaningful to use only the heat flux $q_{\mathrm{M}}^{\mathrm{EM}}$, instead of the total $q^{\mathrm{EM}} = q_{\mathrm{M}}^{\mathrm{EM}} + q_{\mathrm{F}}^{\mathrm{EM}}$, as the boundary condition at the free surface of the melt closely below ITP[1]:

$$\lambda_{\mathrm{l}} \frac{\partial T}{\partial n} = q_{\mathrm{M}}^{\mathrm{EM}} - q^{\mathrm{rad}}. \tag{4.45}$$

It can be seen that the open front velocity (4.4) and the corrected melting interface velocity (4.44) are equivalent at the inner triple point if the field T satisfies the boundary condition (4.45) precisely. This condition is, however, not so precisely fulfilled due to the numerical model used and it is thus better to calculate the velocity at ITP by the open front formula (4.4). The accuracy of the melting interface formula (4.44) improves in the next nodes below ITP with increasing distance between the front and the free surface of the bulk melt.

In this context, we introduce a small transition zone, where the formula (4.4) smoothly turns into formula (4.44). The transition zone is that part of the melting interface from where the geometrical distance to the modelled free surface, h^{g}, is less than the fluid film thickness in the triple point, h_{ITP}. The transition zone allows to avoid the contradiction between the modelling of the open front as a single line and ITP as a single point, which means $h_{\mathrm{ITP}}^{\mathrm{g}} \equiv 0$, and considering at the same time a finite fluid film thickness h according to (4.34), i.e., $h_{\mathrm{ITP}} > 0$. The following mixed velocity value is used at the melting interface in the transition zone $h^{\mathrm{g}} < h_{\mathrm{ITP}}$:

$$v_n^{\mathrm{mix}} = \frac{h^{\mathrm{g}}}{h_{\mathrm{ITP}}} \cdot \tilde{v}_n + \frac{h_{\mathrm{ITP}} - h^{\mathrm{g}}}{h_{\mathrm{ITP}}} \cdot v_n^{\mathrm{film}}, \tag{4.46}$$

where $\tilde{v}_n$ is the corrected melting interface velocity (4.44) and v_n^{film} is the velocity calculated according to (4.4) like for the open front under a fluid film of thickness $h^{\mathrm{g}} + h_{\mathrm{ITP}}$.

Under certain circumstances, it may happen that the front actually has a corner at the location of the inner triple point and the respective front velocity undergoes a discontinuity. To maintain the degrees of freedom of ITP in our calculation, the algorithm avoids a sharp corner between neighbouring discretization elements of the front by using a local smoothing in the region of ITP (see Section 4.5.4). The smoothing, however, does not deteriorate the solution in larger scale with multiple elements as it can

[1] Analogical considerations are applicable also to the calculation of the EM pressure on the free surface near ITP.

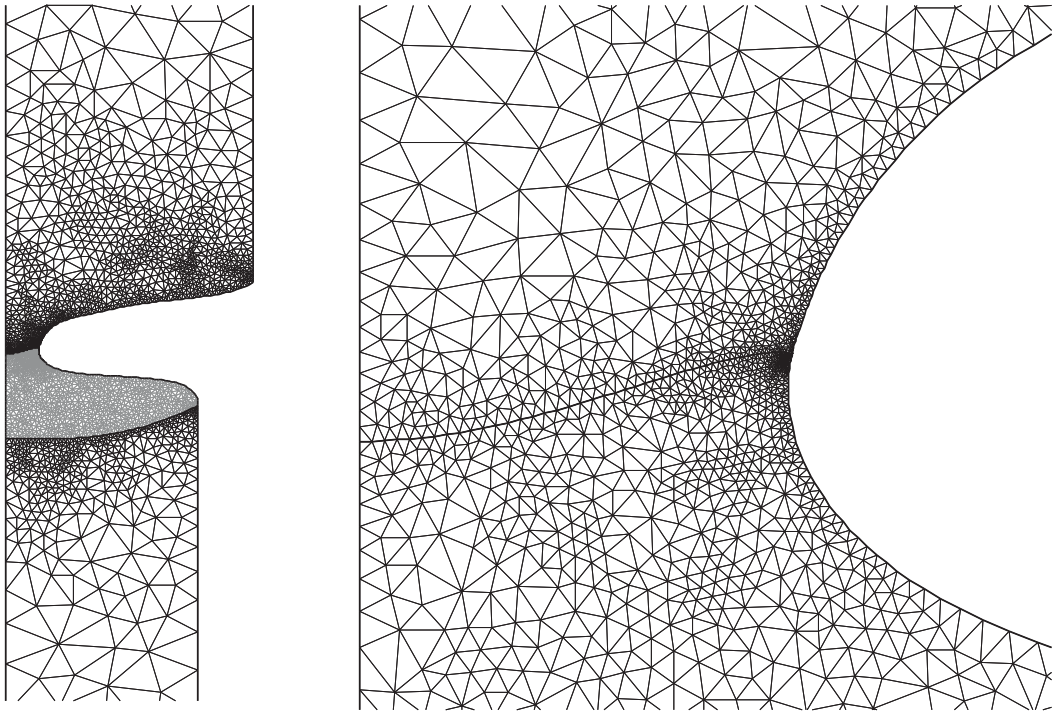

Figure 4.7: Examples of triangulation.

be seen in Fig. 4.6: the uppermost open front element shown and the leftmost melting interface element shown make a corner of 90°. Thus it is enough to use reasonably fine discretization to calculate states with a corner at ITP.

4.5.2 Triangular grid generation with refinement at ITP

The temperature field in the molten zone, feed rod and single crystal as well as the hydrodynamics in the molten zone are calculated in `FZONE` by the Finite Element Method (FEM) as described in further sections. Each of the three calculation domains is discretized in linear finite elements (triangles). Since the domain boundaries are changing during the calculation process, the triangular grid is adjusted at each step in order to fit the respective boundaries.

The grid generator used in `FZONE` is the C code "Triangle" (version 1.2) by Jonathan Richard Schewchuk [79, 80, 81]. It computes Delaunay triangulations and constrained Delaunay triangulations by the exact arithmetic. Quality meshes, i.e. meshes having no small angles are generated using Ruppert's Delaunay refinement algorithm. Among other features of the generator the ones used in `FZONE` are the possibility to set the user-specified constraints on angles and triangle areas and the possibility to put the

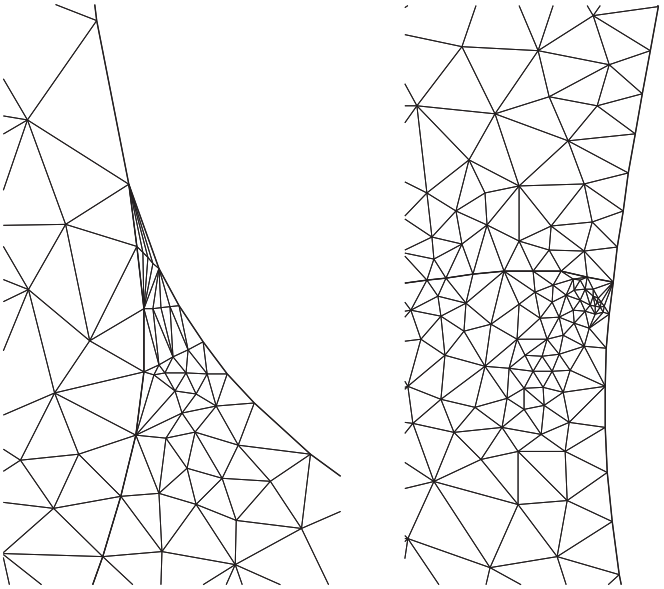

Figure 4.8: Examples of the ITP refinement with forced additional nodes.

obligatory nodes in the inner volume as well as on the boundary.

In the implementation in `FZONE`, the grid generation in each of the calculation domains (melt, feed rod and crystal) is performed separately, one after each other. An example of the mesh is shown in Fig. 4.7. The grid density in the domains is controlled by the density of the elements at the domain boundaries. Hence beside the phase interfaces and the boundaries that are needed for the electromagnetic field calculation by the Boundary Element Method as described in Section 4.2, there are also boundaries defined at the central axis of all three domains. To avoid too big element areas in the middle of domains far from the boundaries, area constraint is imposed on the elements generated. For a domain with maximum boundary element length being equal d_{max}, the area constraint is set to $A_{max} = \sqrt{3}/4 \cdot d_{max}^2$ (the area of a triangle whose each side equals d_{max}). Furthermore an angle constraint of 33° for the minimum inner angle of the triangles is imposed for obtaining a high-quality mesh. This level of mesh quality remains sometimes unachieved due to geometrical reasons like domain boundary with a small inner angle or too big aspect ratio of two neighbouring boundary elements. The first reason, the boundary with a small inner angle, usually takes place in the melt domain closely below the inner triple point. To obtain an optimum grid for the region below ITP, `FZONE` puts additional nodes in the melt volume that forces mesh generator to make a better refinement at this place. Examples of the ITP refinement for two different cases, smooth connection between the open front and melting interface and a corner-like connection, are shown in Fig. 4.8.

4.5.3 Numerical stabilization in case of quasi-vertical melting front

The melting front has often a vertical or nearly vertical part about or below the ITP. The approach to the phase boundary calculation as described in Section 4.1 leads to a numerical problem: the quasi-vertical part of the melting front becomes numerically instable and shows nonphysical wavy shapes that change and even grow with time. The reason of these convergence difficulties is explained in the following way.

Let us first consider v_n, the local normal velocity of the melting front in the laboratory reference system, i.e. the velocity that characterizes the unsteadiness of the process, as described in Section 4.1. The vertical component n_z of the normal vector $\mathbf{n}$, the direction of which at the melting front is depicted in Fig. 4.2, is significantly influencing the value of v_n. Indeed, the equation (4.2) can be rewritten in the form

$$v_n = V_n - V_F n_z$$

with V_n, the normal front velocity in the reference system of the feed rod, i.e. the melting rate from the atomic point of view, and V_F, the feed move rate, which is a positive constant. At the quasi-vertical part of the front we have $V_n \ll V_F$ because little melting occurs in the radial direction if we consider a nearly steady-state shape of the front. Meantime the value of n_z is close to zero at the quasi-vertical part and consequently n_z is changing *relatively* much from node to node and from one calculation step to another due to the numerical character of the solution process. For the purpose of illustration of the numerical problem, we can assume that the fluctuation of n_z brings along the fluctuation of the front velocity v_n in agreement with the relation

$$v_n \approx -V_F n_z. \tag{4.47}$$

Further we consider the discretization of the melting front. The variables in `FZONE` are generally stored at the discretization nodes and, if necessary, the values of the variables inside the boundary elements or triangular finite elements are found by linear interpolation from the node values. This way also the local normal front velocity v_n and the local normal direction $\mathbf{n}$ are considered in the nodes of the front. For defining the front normal direction in a boundary node, a bisector is drawn between the two normal directions of the neighbouring boundary elements found each side from the node. Figure 4.9 illustrates a vertical part of melting front with one node (the node designated by "2") shifted to the right, which can occasionally happen due to the solution process with permanent shifting of the front. The melting front itself is

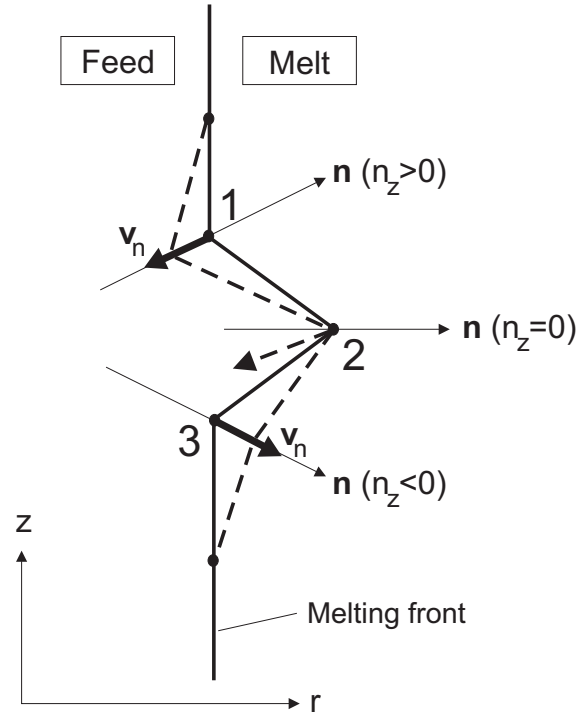

Figure 4.9: Illustration to the mechanism of appearing of numerical instabilities at a quasi-vertical melting front if using the bisectors as normal directions for velocity calculation in the nodes.

drawn by a thick solid line. The thin solid lines and arrows show the bisectors and the corresponding normal vectors in the nodes 1, 2 and 3. The thick arrows are the velocities v_n calculated by the formula (4.47) from the normal vectors. After performing the time step with those velocities, the new shape of the front will be something like the dashed line. At the node 2, the bisector direction will be changed and the corresponding new velocity is shown by the dashed arrow. Meanwhile, the bisectors and the velocities in nodes 1 and 3 preserve their directions. Therefore the following time steps will lead to nodes 1 and 2 shifting considerably to the left and node 3 going to the right and making a sharp corner similar to that the node 2 made at the beginning. Continuing the calculation this way, uncontrolled appearance and motion of a sharp step somewhere at the front can be obtained due to the described numerical effect.

Hence a small numerical fluctuation, like at the node 2 in the above example but smaller, is enough to introduce growing deviations from an even front shape. The issue is that using the bisectors as normal directions work well when those directions are not changing too steep from one node to another, which can take place not only

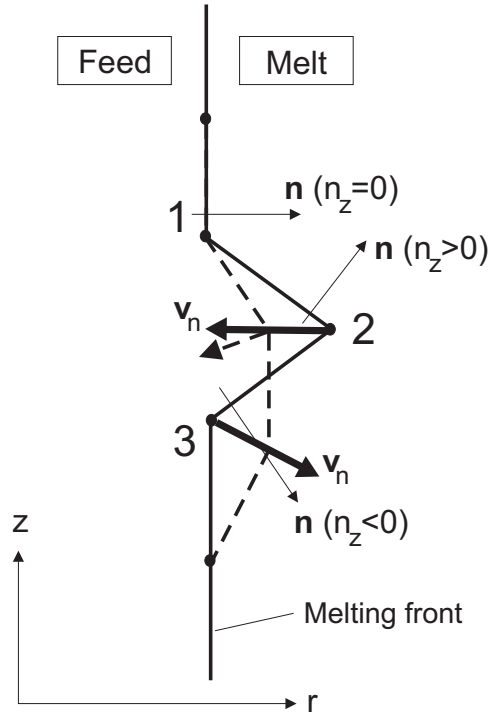

Figure 4.10: Illustration to the calming of numerical fluctuations by a special choice of n_z in the expression of v_n.

due to a fluctuation but also when the discretization is too coarse.

Let us consider the solution of this problem. In principle, the choice of the normal direction at a node can be modified in the limits of the discretization error, i.e., the normal direction can be any direction between the directions of the real normal vectors of the two neighbouring boundary elements. Therefore, to calm down the influence of fluctuations and in the same time not overrun the discretization error, one can choose as the node-normal the one of the element-normals that brings a stabilizing effect on the shape fluctuations.

Following this idea in `FZONE`, the value of the normal velocity v_n at a node of the melting front is calculated by using n_z from the one of the two neighbouring elements that makes a smaller angle by absolute value, in the limits 0°—180°, with a vertical line drawn upwards from the node. Only the value of v_n is modified, while the direction of the velocity vector and therewith the node movement are preserved in the bisector direction as previously. This approach solves the instability problem.

The illustration of how a successful smoothing works in case of the example discussed above is shown in Fig. 4.10. The difference from the previous behaviour (Fig. 4.9)

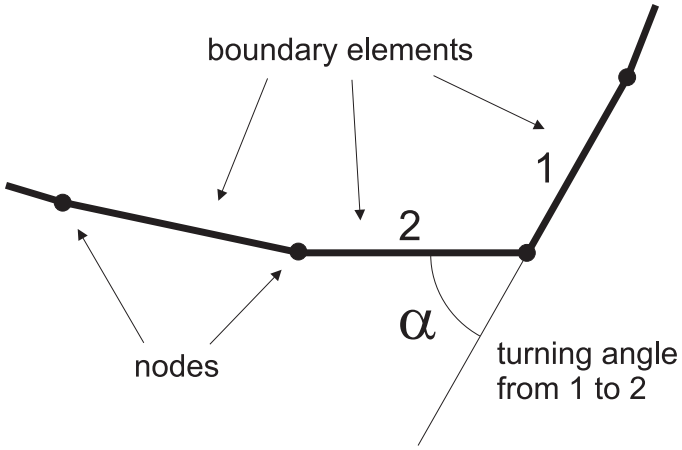

Figure 4.11: Large turning angle α from one boundary element to the next.

is that the moving velocities v_n are converging to zero now, and the shape is getting more smooth with each time step. It should be emphasized that the "smoothness" is relative with respect to the discretization element sizes, therefore also strongly curved melting front shapes can, of course, be solved well if they are discretized fine enough. The method described above works under the threshold of the discretization error and therefore does not cause any additional artificial surface tension at the melting front.

4.5.4 Smoothness control of the discretized melting interface

In order to enable a good performance of the inner triple point moving algorithm described in Section 4.5.1, the melting interface must be smooth enough. Often there arise a problem with the discretized melting interface bending at some nodes, i.e., the turning angle α from one boundary element to the next becomes large (see Fig. 4.11), which leads to big discretization errors when the front is moving. Especially this problem tends to appear in the vicinity of ITP and deteriorates its flexibility needed by the algorithm. A possible way to solve this problem would be simply refining the discretization, however there are times when this does not help if the solution intrinsically contains a corner. Consequently another approach is necessary. The specific method implemented in `FZONE` for avoiding sharp melting interface angles by using what we call "*selective artificial surface tension*" is described below. It is also explained why this works only locally and does not damage the solution as a non-selective artificial surface tension could do.

The main principle of the method of "selective artificial surface tension" is to select

and influence only those turning angles that are "bad", i.e., greater than a predefined critical value α_{crit}. The front moving velocity v at the bad nodes must be corrected so that the correction δv supports the motion towards the center of the front's curvature, which means diminishing the badness of the angle. The value of the velocity correction may be obtained by

$$\delta v = \begin{cases} 0 & \text{if} \quad \alpha < \alpha_{\text{crit}} \\ \gamma \cdot (\alpha - \alpha_{\text{crit}}) & \text{if} \quad \alpha > \alpha_{\text{crit}}, \end{cases} \tag{4.48}$$

where α is assumed positive and γ is the artificial surface tension coefficient, which is unknown and must be determined by the algorithm. The original velocity v may be directed either in the direction of the center of the curvature (the "good" direction) or in the opposite direction (the "bad" direction) in which the movement is increasing the angle α. A large value of γ ensures overcoming the original velocity in case it is directed in the bad direction. On the other hand, a too large γ leads to steep changes in the velocity magnitude from one time step to the next and makes the calculation of the front moving process hard and slow.

The considerations above have led to the following method for the choice of γ. First we introduce a new limiting value of angle, $\alpha_{\max}$, which is greater than α_{crit} and which serves as the maximum allowed value of the turning angle. Let us assume now that among the "bad" nodes there are some "very bad" nodes, i.e., nodes with angles larger or equal to $\alpha_{\max}$. We can find for each of them the minimum γ necessary to ensure that the corrected velocity is not directed in the bad direction. Indeed, for the original velocity in the bad direction, which is assumed the positive direction, the corrected velocity will be reduced to zero or even made negative (see Fig. 4.12), i.e.

$$v_{\text{corr}} \equiv v - \delta v \equiv v - \gamma \cdot (\alpha - \alpha_{\text{crit}}) \leq 0,$$

if the artificial surface tension coefficient for the given node satisfies the inequality

$$\gamma \geq \frac{v}{\alpha - \alpha_{\text{crit}}}.$$

We have to use the same artificial surface tension coefficient for all nodes with bad angles $\alpha > \alpha_{\text{crit}}$. Hence the maximum over the very bad nodes of the minimum necessary γ is taken. If the γ value in the previous step has been larger than the new value, then the old value is retained for the actual step to avoid permanent fluctuations of γ during the calculation. So we determine γ by

$$\gamma = \max_{\imath} \left\{ \frac{v_\imath}{\alpha_\imath - \alpha_{\text{crit}}};\ \gamma_{\text{old}} \right\}, \qquad \imath \in \{\text{nodes} \ \ \imath \ : \ \alpha_\imath \geq \alpha_{\max}\}. \tag{4.49}$$

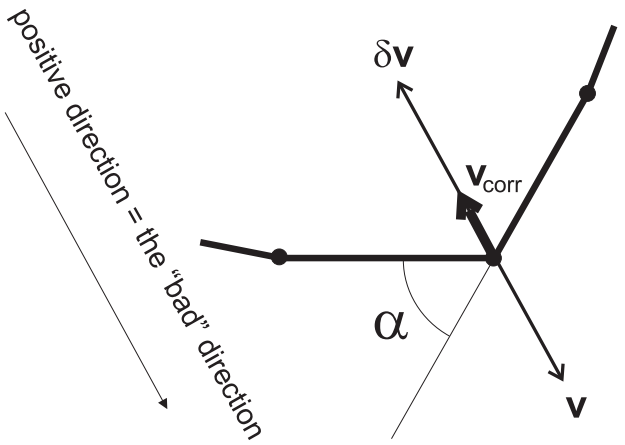

Figure 4.12: The original "bad" velocity v in a node with the turning angle $\alpha \geq \alpha_{\max}$, the correction δv, and the resulting corrected velocity $v_{\text{corr}} \leq 0$.

The calculation is started with $\gamma = 0$ and it is adjusted at each step using the formula (4.49). Only the nodes with $\alpha_i > \alpha_{\text{crit}}$ are touched by the corrections δv_i (see (4.48)) and only in case some angle tends to increase larger than $\alpha_{\max}$ the coefficient γ is increased. As a result, γ increases in the first steps till a certain level, which is the minimum necessary to keep the angles below $\alpha_{\max}$. The influence of the specific value of $\alpha_{\max}$ chosen is illustrated in Fig. 4.13. The selectivity of this "surface tension" is the reason why the effect is local and influences only some nodes, presumed the parameter α_{crit} has been set large enough. We can suppose that the changes in these nodes are not exceeding the actual limits of the discretization error due to the finite length of the discretization elements. By refining the discretization, it is possible to obtain more precise solution and the region of the influence of the selective artificial surface tension becomes more localized.

Figure 4.14 illustrates the local character of the influence of smoothing with $\alpha_{crit} = 30°$ and $\alpha_{max} = 45°$, which are the standard values approved for calculations. The difference in scales in Figs. 4.14(a)–4.14(b) can be seen from the distribution of nodes.

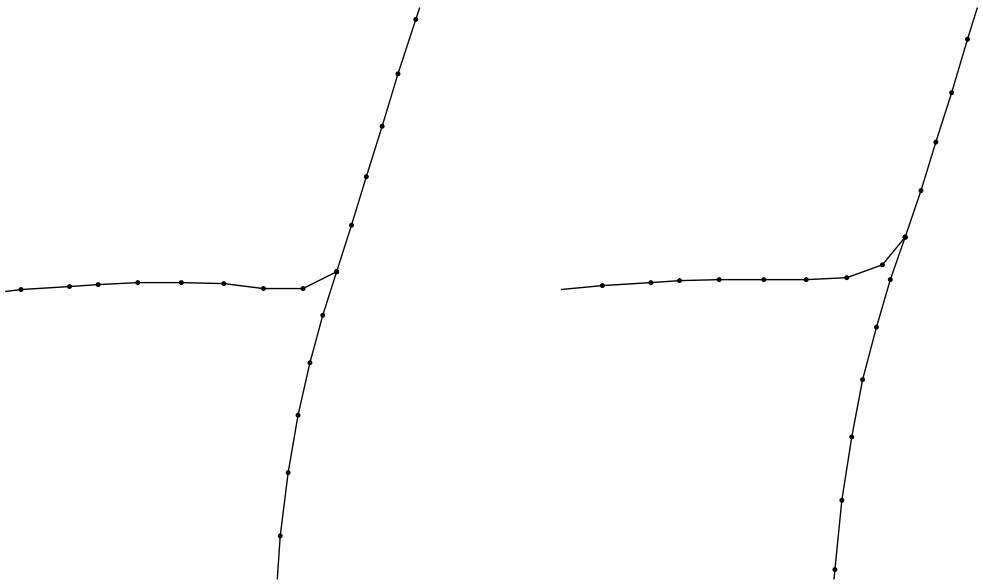

(a) $\alpha_{\text{crit}} = 30°$, $\alpha_{\max} = 45°, n = 2$ (b) $\alpha_{\text{crit}} = 15°$, $\alpha_{\max} = 30°, n = 3$

Figure 4.13: Applying the smoothing algorithm with different parameters $\alpha_{\max}$ and α_{crit}, which results in different number of corrected nodes, n.

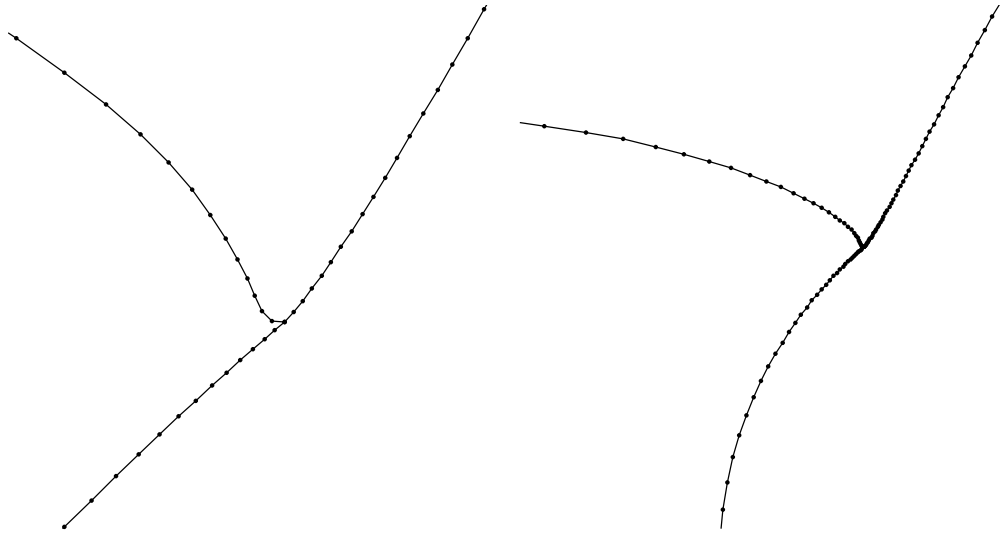

(a) Close view: the rounded corner (b) More global view of the same picture: the influence of smoothing vanishes

Figure 4.14: Local character of the smoothing at ITP ($\alpha_{\text{crit}} = 30°$, $\alpha_{\max} = 45°$).

4.6 Axisymmetric melt flow

4.6.1 The $\psi - \omega$ equations in cylindrical coordinates

To calculate the temperature field in the molten zone, an axisymmetric model of the melt flow and heat transfer is applied. For the incompressible fluid flow, the mass-conservation equation (3.25) and the Navier-Stokes equations with the Boussinesq approximation (3.26) are transformed from the pressure–velocity variables (p^{HD}, u_r, u_φ, u_z) to the variables ψ, ω and u_φ, which brings the advantage that the mass conservation is satisfied automatically and the number of equations to solve is reduced [76, 82]. The stream function ψ and the vorticity ω are defined by

$$u_r = -\frac{1}{r}\frac{\partial\psi}{\partial z}, \qquad u_z = \frac{1}{r}\frac{\partial\psi}{\partial r}, \qquad \omega \equiv (\nabla \times \mathbf{u})_\varphi = \frac{\partial u_r}{\partial z} - \frac{\partial u_z}{\partial r}, \tag{4.50}$$

and the whole set of hydrodynamic equations including the heat transfer equation (3.27) is written in the cylindrical coordinates (r, φ, z) as follows[2]:

$$\frac{\partial}{\partial r}\left(\frac{1}{r}\frac{\partial\psi}{\partial r}\right) + \frac{\partial}{\partial z}\left(\frac{1}{r}\frac{\partial\psi}{\partial z}\right) + \omega = 0 \tag{4.51}$$

$$\frac{\partial T}{\partial t} + u_r\frac{\partial T}{\partial r} + u_z\frac{\partial T}{\partial z} = \frac{1}{r}\frac{\partial}{\partial r}\left(\chi\, r\frac{\partial T}{\partial r}\right) + \frac{\partial}{\partial z}\left(\chi\frac{\partial T}{\partial z}\right) \tag{4.52}$$

$$\frac{\partial u_\varphi}{\partial t} + u_r\frac{\partial u_\varphi}{\partial r} + u_z\frac{\partial u_\varphi}{\partial z} = \frac{\partial}{\partial r}\left(\frac{\nu}{r}\frac{\partial(r u_\varphi)}{\partial r}\right) + \frac{\partial}{\partial z}\left(\nu\frac{\partial u_\varphi}{\partial z}\right) - \frac{u_r}{r}u_\varphi \tag{4.53}$$

$$\frac{\partial\omega}{\partial t} + u_r\frac{\partial\omega}{\partial r} + u_z\frac{\partial\omega}{\partial z} = \frac{\partial}{\partial r}\left(\frac{\nu}{r}\frac{\partial(r\omega)}{\partial r}\right) + \frac{\partial}{\partial z}\left(\nu\frac{\partial\omega}{\partial z}\right) + \frac{u_r}{r}\omega + \frac{2u_\varphi}{r}\frac{\partial u_\varphi}{\partial z} - g\beta\frac{\partial T}{\partial r} \tag{4.54}$$

where χ is the thermal diffusivity of the liquid, $\chi = \lambda_{\mathrm{l}}/(\rho_{\mathrm{l}} c_p)$, ν is the kinematic viscosity, $\nu = \eta/\rho_{\mathrm{l}}$, and $g = |g_z|$. Since the electromagnetic force is treated in the high-frequency approximation as a surface force as well as the Joulean power is approximated by a heat flux through the boundary (see Section 3.3), there are no volume forces beside gravity and no volume heat sources included in these equations.

---

[2] Obviously there has been a mistake in expressing the vorticity equation in cylindrical coordinates in previous works like [45, 46, 7] where the equation (4.54) has been written without the vortex-stretching-related term $u_r\omega/r$, which arises due to the curvature of the coordinate system when taking the φ-component of the vorticity equation

$$\frac{\partial\vec{\omega}}{\partial t} + (\mathbf{u}\nabla)\vec{\omega} = \nu\Delta\vec{\omega} + (\vec{\omega}\nabla)\mathbf{u} + \mathbf{g}\beta \times \nabla T.$$

Here $\vec{\omega} \equiv \nabla \times \mathbf{u}$ while the designation ω as defined by (4.50) always stands for the φ-component of $\vec{\omega} = (\omega_r, \omega, \omega_z)$, with subscript φ just being dropped for convenience.

4.6.2 Boundary conditions

The general flow boundary conditions were considered in Section 3.4 and, particularly for the free surface, in Section 3.5. Here the boundary conditions are rewritten for the $\psi - \omega$ formulation.

Let us choose a vertical cross-section plane going through the symmetry axis of the molten zone and a line in this plane, e.g., a line on the boundary of the melt. From the coordinates (r, z), we can switch everywhere along this line to local coordinates (τ, n), with τ being the tangential- and n, the normal direction locally at each point of the chosen line. This coordinate transformation allows the following recasting of the definitions (4.50):

$$u_\tau = -\frac{1}{r}\frac{\partial \psi}{\partial n}, \qquad u_n = \frac{1}{r}\frac{\partial \psi}{\partial \tau}, \qquad \omega = \frac{\partial u_\tau}{\partial n} - \frac{\partial u_n}{\partial \tau}. \tag{4.55}$$

If neglecting the relatively slow (few millimeters per minute) flow across the solid–melt interfaces occurring due to the crystallization and melting, we can assume $u_n = 0$ at all boundaries of the melt[3]. According to (4.55), we have then a constant value of ψ at all melt boundaries and can choose this value equal to zero. At boundaries with the no-slip condition we get additionally according to (4.55) a zero normal derivative of the stream function.

$$\text{Boundary with } \; u_n = 0 \quad \Rightarrow \quad \psi = 0, \quad \omega = \frac{\partial u_\tau}{\partial n} = \frac{F_\tau}{\eta} \tag{4.56}$$

$$\text{Boundary with } \; u_\tau = 0 \quad \Rightarrow \quad \frac{\partial \psi}{\partial n} = 0 \tag{4.57}$$

F_τ in (4.56) is the tangential stress at the boundary. At the free melt surface, this vorticity boundary condition corresponds to (3.34) and F_τ is created by the action of the electromagnetic and Marangoni forces as given by the expressions (3.30) and (3.21):

$$F_\tau = \frac{\mu_0 \delta}{4}\frac{\partial ({i_{\mathrm{ef}}}^2)}{\partial \tau} + \frac{\partial \gamma}{\partial T}\frac{\partial T}{\partial \tau}. \tag{4.58}$$

At the symmetry axis, which is also one of the melt boundaries in the axisymmetric problem formulation, we can put simply $F_\tau = 0$. At the rigid boundaries, however,

[3] This corresponds to putting $u_z = 0$ in (3.28) and (3.29). Such simplification is favourable for the $\psi - \omega$ formulation, additional measures have, however, to be met if the precise resolution of the flow at interfaces is necessary, e.g., in case of the calculation of dopant concentration, which typically has a very steep boundary layer due to the segregation.

the tangential stress is not explicitly known and a more specific formulation of the boundary condition for the vorticity ω has to be considered:

$$\text{Boundary with } \; u_n = 0, \;\; u_\tau = 0 \quad \Rightarrow \quad \omega = -\frac{1}{r}\frac{\partial^2 \psi}{\partial n^2}.$$

To make this boundary condition of ω suitable for the calculation procedure, we approximate the second order derivative of ψ by lower order derivatives by using the beginning of the Taylor series of the function $\psi(n)$ near the boundary $n = 0$:

$$\psi(n) \approx \psi(0) + n \left.\frac{\partial \psi}{\partial n}\right|_{n=0} + \frac{n^2}{2} \left.\frac{\partial^2 \psi}{\partial n^2}\right|_{n=0}.$$

Due to the boundary conditions for ψ from (4.56) and (4.57), the first two terms on the right-hand side of the approximate equation equal zero. Hence we have the following no-slip boundary condition for ω, which is known as the Thom condition:

$$\text{Boundary with } \; u_n = 0, \;\; u_\tau = 0 \quad \Rightarrow \quad \omega = -\frac{2}{r} \lim_{n \to 0} \frac{\psi(n)}{n^2}. \tag{4.59}$$

To summarize, the boundary conditions for the thermal–hydrodynamic problem in the melt are as follows.

1. Symmetry axis ($u_n = 0$, $F_\tau = 0$):

$$\frac{\partial T}{\partial r} = 0, \quad u_\varphi = 0, \quad \psi = 0, \quad \omega = 0. \tag{4.60}$$

2. Crystallization and melting interfaces ($u_n = 0$, $u_\tau = 0$):

$$T = T_0, \quad u_\varphi = 2\pi r\, \Omega_{\mathrm{Cr,F}}, \quad \psi = 0, \quad \omega = -\frac{2}{r}\, \frac{\psi(n_*)}{n_*^2} \tag{4.61}$$

   with T_0 denoting the melting point temperature, $\Omega_{\mathrm{Cr,F}}$, the rotation rate of the crystal (Cr) or feed rod (F), r, the radial coordinate of the considered boundary point, and $\psi(n_*)$, the value of the stream function at as small as possible distance n_* from the boundary (in practice this distance is determined by the locations of the nearest nodes).

3. Free melt surface ($u_n = 0$, $F_\tau =$ (4.58)):

$$\lambda_\mathrm{l} \frac{\partial T}{\partial n} = q^{\mathrm{EM}} - q^{\mathrm{rad}}, \quad \frac{\partial u_\varphi}{\partial n} = \frac{u_\varphi}{r}\frac{\partial r}{\partial n}, \quad \psi = 0, \quad \omega = \frac{F_\tau}{\eta}, \tag{4.62}$$

where q^{rad} is calculated as described in Section 4.7 and q^{EM} is calculated by (3.14) or (4.37) based on a previously calculated distribution of surface currents (the calculation of the surface currents see in Section 4.2). For the free melt surface in the vicinity of ITP, the $q_{\mathrm{M}}^{\mathrm{EM}}$ must be used instead of q^{EM}, as pointed out in Section 4.5.1. The boundary condition for the azimuthal velocity u_φ comes from (3.35) by setting $F_\varphi = 0$ due to the axial symmetry of the model. For the sake of the numerical method described below, the following equivalent form of the free surface boundary condition for the azimuthal velocity is used:

$$\frac{\partial(r u_\varphi)}{\partial n} = 2 u_\varphi \frac{\partial r}{\partial n}. \tag{4.63}$$

4.6.3 The numerical method: SUPG-stabilized FEM

For the numerical solving of the flow and heat transport problem, the Finite Element Method (FEM) is used. Let us shortly consider the principles of the method for application to a flow problem like that one formulated above.

The equations (4.51), (4.52), (4.53) and (4.54) have the general form

$$\underbrace{\mathfrak{L}_t \mathfrak{u}}_{\text{time change}} + \underbrace{\mathfrak{L}_{\mathrm{conv}} \mathfrak{u}}_{\text{convection}} = \underbrace{\mathfrak{L}_{\mathrm{diff}}^{(2)} \mathfrak{u}}_{\text{diffusion}} + \underbrace{\mathfrak{s}_*^{(1)} \mathfrak{u} + \mathfrak{s}_*^{(0)}}_{\text{source terms}}$$

where $\mathfrak{L}_x$ are the differential operators corresponding to different parts of the equation, $\mathfrak{u} = \mathfrak{u}(\mathbf{x})$ is the unknown field over the calculation domain $\mathbf{x} \in \Xi$, the source term $(\mathfrak{s}_*^{(1)} \mathfrak{u})$ is the part proportional to $\mathfrak{u}$, and $\mathfrak{s}_*^{(0)}$ is the $\mathfrak{u}$-independent part of sources. Because the solution of the above equation is, in general, time dependent, we calculate the instantaneous field $\mathfrak{u}$ at time t by taking in account the "old" field distribution $\mathfrak{u}^{\mathrm{old}}$ at time $t - \Delta t$. The field $\mathfrak{u}^{\mathrm{old}}$ has been calculated or predefined previously. For the sake of numerical robustness at large time steps Δt, the implicit scheme is used: the field $\mathfrak{u}^{\mathrm{old}}$ appears only in the time-derivative term while the actual field $\mathfrak{u}$ is placed in the rest part of equation. The time derivative is approximated by

$$\mathfrak{L}_t \mathfrak{u} \approx \frac{\mathfrak{u} - \mathfrak{u}^{\mathrm{old}}}{\Delta t} = -\mathfrak{s}_t^{(1)} \mathfrak{u} - \mathfrak{s}_t^{(0)}$$

where $\mathfrak{s}_t^{(1)} = -1/\Delta t$ and $\mathfrak{s}_t^{(0)} = \mathfrak{u}^{\mathrm{old}}/\Delta t$. This way the form of the general equation can be simplified by including the time derivative in the source terms:

$$\mathfrak{L}_{\mathrm{conv}} \mathfrak{u} = \mathfrak{L}_{\mathrm{diff}}^{(2)} \mathfrak{u} + \mathfrak{s}^{(1)} \mathfrak{u} + \mathfrak{s}^{(0)} \tag{4.64}$$

with $\mathfrak{s}^{(1)} = \mathfrak{s}_*^{(1)} + \mathfrak{s}_t^{(1)}$ and $\mathfrak{s}^{(0)} = \mathfrak{s}_*^{(0)} + \mathfrak{s}_t^{(0)}$.

We have discretized the calculation domain Ξ and look for the approximate solution in the form of a linear combination of predefined basis functions $N_\imath$ (called also shape functions or trial functions):

$$\mathfrak{u}(\mathbf{x}) = \sum_{\imath \in \{\text{nodes}\}} N_\imath(\mathbf{x}) \mathfrak{u}_\imath, \tag{4.65}$$

where $\mathfrak{u}_\imath$ are the unknown coefficients. The number of the basis functions and the number of the coefficients are here both equal to the number of nodes. In FEM, only the weak form of equation (4.64) is solved:

$$\int_\Xi W_\imath \left(\mathfrak{L}_{\text{conv}} \mathfrak{u} - \mathfrak{L}_{\text{diff}}^{(2)} \mathfrak{u} - \mathfrak{s}^{(1)} \mathfrak{u} - \mathfrak{s}^{(0)} \right) \mathrm{d}\Xi = 0, \qquad \imath \in \{\text{nodes}\}, \tag{4.66}$$

where $W_\imath = W_\imath(\mathbf{x})$ are the weight functions (or test functions). The number of weight functions is also equal to the number of nodes. The idea in FEM is to substitute (4.65) into (4.66) to get the system of equations for the unknown coefficients $\mathfrak{u}_\imath$. A typical problem is however the diffusion term $\mathfrak{L}_{\text{diff}}^{(2)}$, which has second order derivatives and creates singularities if the first derivative of the basis functions $N_\imath$ (and hence that of the approximate solution (4.65)) is discontinuous. This takes place if the chosen basis functions are piecewise linear, which is typical. The approach used in FEM is reducing the order of derivatives from 2 to 1 with help of partial integration or the divergence theorem. In general form:

$$\int_\Xi W_\imath \, \mathfrak{L}_{\text{diff}}^{(2)} \mathfrak{u} \, \mathrm{d}\Xi = \int_\Xi \mathfrak{L}_{\text{diff}}(W_\imath, \mathfrak{u}) \, \mathrm{d}\Xi + \oint_{\partial\Xi} W_\imath \mathfrak{D}\mathfrak{u} \, \mathrm{d}\partial\Xi \tag{4.67}$$

where $\mathfrak{L}_{\text{diff}}(\cdot,\cdot)$ is a bilinear differential operator with first order derivatives only. The last term on the right hand side integrates over the boundary $\partial\Xi$ of the domain Ξ and the operator $\mathfrak{D}$ is a differential operator of first order as well (it is typically proportional to the normal gradient at the boundary).

The boundary integral in (4.67) is evaluated by means of boundary conditions of the second or third kind, which can be written in the general form as

$$r^\zeta \, \mathfrak{D}\mathfrak{u} + \mathfrak{q}^{(1)} \mathfrak{u} = \mathfrak{q}^{(0)} \qquad \text{at part of } \partial\Xi \text{ with 2nd or 3rd kind BCs}, \tag{4.68}$$

where $\mathfrak{q}^{(0)}$ and $\mathfrak{q}^{(1)}$ are prescribed fields at the boundary and ζ equals 0 or 1 (dependent on the specific form of the boundary condition). In case of the second kind boundary conditions, $\mathfrak{q}^{(1)}$ equals zero.

Consequently, the equation system (4.66) transforms to:

$$\int_{\Xi} \mathfrak{L}(W_\imath, \mathfrak{u})\,\mathrm{d}\Xi + \oint_{\partial\Xi} W_\imath \frac{\mathfrak{q}^{(1)}}{r^\zeta}\mathfrak{u}\,\mathrm{d}\partial\Xi = \int_{\Xi} W_\imath \mathfrak{s}^{(0)}\,\mathrm{d}\Xi + \oint_{\partial\Xi} W_\imath \frac{\mathfrak{q}^{(0)}}{r^\zeta}\,\mathrm{d}\partial\Xi, \quad \imath \in \{\text{nodes}\},$$

where the bilinear operator

$$\mathfrak{L}(\mathfrak{v}, \mathfrak{u}) \equiv \mathfrak{v}\mathfrak{L}_{\text{conv}}\mathfrak{u} - \mathfrak{L}_{\text{diff}}(\mathfrak{v}, \mathfrak{u}) - \mathfrak{v}\mathfrak{s}^{(1)}\mathfrak{u}$$

has been introduced for briefness. Substitution (4.65) yields a system of linear algebraic equations with respect to the unknown coefficients $\mathfrak{u}_\imath$:

$$\sum_{\jmath\in\{\text{nodes}\}} \mathfrak{u}_\jmath \left\{ \int_{\Xi} \mathfrak{L}(W_\imath, N_\jmath)\,\mathrm{d}\Xi + \oint_{\partial\Xi} W_\imath \frac{\mathfrak{q}^{(1)}}{r^\zeta} N_\jmath\,\mathrm{d}\partial\Xi \right\} = \int_{\Xi} W_\imath \mathfrak{s}^{(0)}\,\mathrm{d}\Xi + \oint_{\partial\Xi} W_\imath \frac{\mathfrak{q}^{(0)}}{r^\zeta}\,\mathrm{d}\partial\Xi, \qquad \imath \in \{\text{nodes}\}. \quad (4.69)$$

The solution of the problem reduces hence to: 1) choosing appropriate basis and weight functions and calculating the integrals, 2) solving the particular linear (or linearized) system of equations (4.69) for one of the flow variables, and 3) iterating over the whole (nonlinear) system of equations for all flow variables.

Choosing the weight functions equal to the basis functions, $W_\imath = N_\imath$, leads to the standard Bubnov-Galerkin weak formulation. With convection-dominated problems, i.e., when the nonlinearity is strong enough, the standard Bubnov-Galerkin FEM fails if no stabilization is added to avoid non-physical oscillation of the solution. Artificial addition of stabilization while using the Bubnov-Galerkin weight functions, however, makes the problem statement inconsistent. Therefore it is preferable to introduce the stabilization by changing the weight functions themselves, which is known as the Petrov-Galerkin weak formulation. The Petrov-Galerkin weight functions $W_\imath \neq N_\imath$ can be viewed as perturbed Bubnov-Galerkin weight functions and the several possible Petrov-Galerkin approaches differ by the kind of perturbation used. One of the most popular applications is the *streamline upwind/Petrov-Galerkin* stabilization (SUPG), which is constructed by adding streamline-upwind perturbations to the Bubnov-Galerkin weight functions (see e.g. [83], [84]):

$$W_\imath = N_\imath + \tau\mathfrak{L}_{\text{conv}} N_\imath, \quad (4.70)$$

where τ is a stabilization parameter that weights the perturbation. Since according to the weak problem formulation the perturbation is multiplied with the residual of the

differential equation, the consistency is fulfilled in that the exact solution also satisfies the stabilized form exactly.

The stabilization parameter τ (denoted in what follows by $\tau_\imath$, since it is, in general, different for each weight function) determines the actual amount of stabilization and is calculated with help of the coth-formula (also called the *optimal* stabilization formula), which is derived from a simplified (1D) convection–diffusion model, see Section 4.6.7.

4.6.4 Basis functions and system matrix

When calculating the integrals in (4.69), it has to be taken into account that we work with cylindrical coordinates in a 3D domain Ξ. Often, however, the term "calculation domain" is also used to indicate the cross-section of the domain Ξ with one half-plane (r, z) with $r \geq 0$. Let us denote here this cross-section by S and its boundary by Γ. The domain S is discretized i.e. subdivided in triangular elements S_e such that $\sum_e S_e = S$, as described in Section 4.5.2. Each element has three nodes and each node belongs to several elements. The nodes are connected by edges. Hence the boundary Γ is subdivided in edges that connect the boundary nodes. The elements e that are placed near the boundary Γ have got edges[4] Γ_e on the boundary, such that $\sum_e \Gamma_e = \Gamma$. For elements having no edges on the boundary, the Γ_e is an empty set (or zero).

According to the approach of linear FEM, we choose piecewise linear and localized basis functions $N_\imath$, i.e., basis functions that are linear inside every element and have a value 1 just at one node, with zero at all other nodes:

$$N_\imath\,(\text{node}\,\jmath) = \begin{cases} 1 \;\text{ if }\; \jmath = \imath \\ 0 \;\text{ if }\; \jmath \neq \imath. \end{cases} \tag{4.71}$$

This choice of basis functions implies that the coefficients $\mathfrak{u}_\imath$ in (4.65) receive the meaning of nodal values of $\mathfrak{u}$.

Inside element e with nodes $\imath$, $\jmath$ and k, the basis function $N_\imath$ equals:

$$N_\imath(r, z) = \frac{c_\imath + b_\imath r + a_\imath z}{2A}, \tag{4.72}$$

where A is the area of element e and the element-specific coefficients $a_\imath$, $b_\imath$ and $c_\imath$ are

[4] We assume here for simplicity of notation that there are no elements with more than one edge lying on the boundary.

defined based on coordinates $(r_\imath, z_\imath)$ of the three nodes of the same element by

$$\begin{cases} a_\imath = r_k - r_\jmath \\ b_\imath = z_\jmath - z_k \\ c_\imath = r_\jmath z_k - r_k z_\jmath \\ \imath \neq k \neq \jmath \\ \frac{1}{2}(b_\imath a_\jmath - b_\jmath a_\imath) = A > 0. \end{cases}$$

A consequence of the choice of basis functions $N_\imath$ as local functions is that the weight functions $W_\imath$ (4.70) are local as well. Hence if splitting the integrals of (4.69) into separate element integrals, the $\imath$-th equation will only include non-zero integrals over elements e that contain the node $\imath$. Let us designate the set of such elements by $e \ni \imath$. Equation (4.69) can be rewritten:

$$\sum_{e\ni\imath}\sum_{\jmath\in\{\text{nodes}\}} \mathfrak{u}_\jmath \left\{ \int_{S_e} \mathfrak{L}(W_\imath, N_\jmath)\, r\mathrm{d}r\mathrm{d}z + \int_{\Gamma_e} W_\imath \mathfrak{q}^{(1)} N_\jmath\, r^{1-\zeta}\mathrm{d}\Gamma \right\} = \sum_{e\ni\imath} \left\{ \int_{S_e} W_\imath \mathfrak{s}^{(0)}\, r\mathrm{d}r\mathrm{d}z + \int_{\Gamma_e} W_\imath \mathfrak{q}^{(0)}\, r^{1-\zeta}\mathrm{d}\Gamma \right\}, \qquad \imath \in \{\text{nodes}\}.$$

Another consequence of the locality of $N_\jmath$ is that $\mathfrak{L}(\cdot, N_\jmath)$ is local too. Hence the integral over S_e on the left hand side equals zero if the $\jmath$-th node does not belong to the same element. The boundary integral on the left hand side behaves, of course, similarly due to $N_\jmath$ in the integral. Concerning the weight functions (4.70), we follow [84] and define the stabilization contributions only inside element interiors, setting them to zero on the boundaries. Hence we replace $W_\imath$ by $N_\imath$ in the boundary integrals and find the final reduced form of the equation (4.69):

$$\sum_{e\ni\imath}\sum_{\jmath\in e} \mathfrak{u}_\jmath \left\{ \int_{S_e} \mathfrak{L}(W_\imath, N_\jmath)\, r\mathrm{d}r\mathrm{d}z + \int_{\Gamma_e} N_\imath \mathfrak{q}^{(1)} N_\jmath\, r^{1-\zeta}\mathrm{d}\Gamma \right\} = \sum_{e\ni\imath} \left\{ \int_{S_e} W_\imath \mathfrak{s}^{(0)}\, r\mathrm{d}r\mathrm{d}z + \int_{\Gamma_e} N_\imath \mathfrak{q}^{(0)}\, r^{1-\zeta}\mathrm{d}\Gamma \right\}, \qquad \imath \in \{\text{nodes}\}, \quad (4.73)$$

or in matrix form:

$$\sum_{e\ni\imath}\sum_{\jmath\in e} M^{(e)}_{\imath\jmath}\mathfrak{u}_\jmath = \sum_{e\ni\imath} B^{(e)}_\imath, \qquad \imath \in \{\text{nodes}\}. \quad (4.74)$$

The matrices $M^{(e)}$ and $B^{(e)}$ are called the local (or element) matrices because the indices are running over the three nodes of the element e only. Building the global

matrix of the system of linear algebraic equations includes thus calculating 9 matrix elements $M_{ij}^{(e)}$ and 3 matrix elements $B_i^{(e)}$ for each element e.

4.6.5 Integration of diffusion terms and boundary conditions

In order to perform the integration, let us write down explicitly the diffusion terms obtained by the transformation (4.67). For the temperature we have:

$$\int_S \left[\frac{1}{r}\frac{\partial}{\partial r}\left(\chi\, r\frac{\partial T}{\partial r}\right) + \frac{\partial}{\partial z}\left(\chi\frac{\partial T}{\partial z}\right)\right] W_\imath\, r\mathrm{d}r\mathrm{d}z = \\ -\int_S \chi\, r\left[\frac{\partial T}{\partial r}\frac{\partial N_\imath}{\partial r} + \frac{\partial T}{\partial z}\frac{\partial N_\imath}{\partial z}\right]\mathrm{d}r\mathrm{d}z + \oint_\Gamma \chi r\frac{\partial T}{\partial n}N_\imath\,\mathrm{d}\Gamma, \quad (4.75)$$

where the weight function $W_\imath$ (cf. (4.70)) has been taken equal to:

$$W_\imath = N_\imath + \tau_\imath\left(u_{r\imath}\frac{\partial N_\imath}{\partial r} + u_{z\imath}\frac{\partial N_\imath}{\partial z}\right). \quad (4.76)$$

Here $u_{r\imath}$ and $u_{z\imath}$ are the values of velocity components at the node $\imath$. Such weight function implies that the stabilization contribution is constant in each element and: $\frac{\partial W_\imath}{\partial r} = \frac{\partial N_\imath}{\partial r}$.

For the vorticity and azimuthal velocity the diffusion term is slightly different because of the nature of these variables as φ-components of vectorial fields:

$$\int_S \left[\frac{\partial}{\partial r}\left(\frac{\nu}{r}\frac{\partial(ru_\varphi)}{\partial r}\right) + \frac{\partial}{\partial z}\left(\nu\frac{\partial u_\varphi}{\partial z}\right)\right] W_\imath\, r\mathrm{d}r\mathrm{d}z = \\ -\int_S \frac{\nu}{r}\left[\frac{\partial(ru_\varphi)}{\partial r}\frac{\partial(rN_\imath)}{\partial r} + \frac{\partial(ru_\varphi)}{\partial z}\frac{\partial(rN_\imath)}{\partial z}\right]\mathrm{d}r\mathrm{d}z + \oint_\Gamma \nu\frac{\partial(ru_\varphi)}{\partial n}N_\imath\,\mathrm{d}\Gamma, \quad (4.77)$$

where, in order to eliminate the stabilization contribution from the diffusion term as successfully as for the T-equation above, the following slightly modified weight function has been chosen for the ω- and u_φ-equations ($r_\imath$ stands for the node value of r):

$$W_\imath = N_\imath + \tau_\imath\frac{r_\imath}{r}\left(u_{r\imath}\frac{\partial N_\imath}{\partial r} + u_{z\imath}\frac{\partial N_\imath}{\partial z}\right), \quad (4.78)$$

which implies that $\frac{\partial(rW_\imath)}{\partial r} = \frac{\partial(rN_\imath)}{\partial r}$ in each element.

The first integral on the right hand side of (4.77) can be transformed further to:

$$-\int_S \nu r\left[\frac{\partial u_\varphi}{\partial r}\frac{\partial N_\imath}{\partial r} + \frac{\partial u_\varphi}{\partial z}\frac{\partial N_\imath}{\partial z}\right]\mathrm{d}r\mathrm{d}z - \int_S \nu\left(\frac{\partial u_\varphi}{\partial r}N_\imath + u_\varphi\frac{\partial N_\imath}{\partial r} + \frac{u_\varphi}{r}N_\imath\right)\mathrm{d}r\mathrm{d}z. \quad (4.79)$$

In the stream function equation, there is no convection term and hence no streamline-upwind correction to the weight function: $W_\imath = N_\imath$. Consequently the diffusion term becomes:

$$\int_S \left[\frac{\partial}{\partial r}\left(\frac{1}{r}\frac{\partial\psi}{\partial r}\right) + \frac{\partial}{\partial z}\left(\frac{1}{r}\frac{\partial\psi}{\partial z}\right)\right] N_\imath \, r\mathrm{d}r\mathrm{d}z = \\ -\int_S \left[\frac{1}{r}\frac{\partial\psi}{\partial r}\frac{\partial(rN_\imath)}{\partial r} + \frac{\partial\psi}{\partial z}\frac{\partial N_\imath}{\partial z}\right] \mathrm{d}r\mathrm{d}z + \oint_\Gamma \frac{\partial\psi}{\partial n} N_\imath \, \mathrm{d}\Gamma, \quad (4.80)$$

where the first integral on the right hand side can be transformed further to:

$$-\int_S \left[\frac{\partial\psi}{\partial r}\frac{\partial N_\imath}{\partial r} + \frac{\partial\psi}{\partial z}\frac{\partial N_\imath}{\partial z}\right] \mathrm{d}r\mathrm{d}z - \int_S \frac{1}{r}\frac{\partial\psi}{\partial r} N_\imath \, \mathrm{d}r\mathrm{d}z. \quad (4.81)$$

Taking into account the form (4.72) of the basis functions $N_\imath$, the following approximations for the diffusion integrals in elements are obtained:

$$\begin{aligned}
T \quad &: \quad -\int_{S_e} \mathfrak{L}_{\mathrm{diff}}(W_\imath, N_\jmath)\, r\mathrm{d}r\mathrm{d}z = \chi\overline{r}\frac{a_\imath a_\jmath + b_\imath b_\jmath}{4A} \\
\omega, u_\varphi \quad &: \quad -\int_{S_e} \mathfrak{L}_{\mathrm{diff}}(W_\imath, N_\jmath)\, r\mathrm{d}r\mathrm{d}z = \nu\left(\overline{r}\frac{a_\imath a_\jmath + b_\imath b_\jmath}{4A} + \frac{b_\imath + b_\jmath}{6} + \frac{A}{12\overline{r}}(1+\delta_{\imath\jmath})\right) \\
\psi \quad &: \quad -\int_{S_e} \mathfrak{L}_{\mathrm{diff}}(W_\imath, N_\jmath)\, r\mathrm{d}r\mathrm{d}z = \frac{a_\imath a_\jmath + b_\imath b_\jmath}{4A} + \frac{b_\jmath}{6\overline{r}},
\end{aligned}$$

where a bar above a variable stands for the *average nodal value* of the variable in the chosen element (it coincides with the average value over the element area only for variables that are linear coordinate functions):

$$\text{in element } S_e: \quad \overline{X} \equiv \frac{1}{3}\sum_{\imath\in e} X_\imath.$$

The boundary integrals like in equations (4.75) and (4.77) are calculated with help of the second or third kind boundary conditions. As seen at the end of Section 4.6.2, we have 2nd kind boundary conditions for the temperature and both 2nd and 3rd kind boundary conditions for the azimuthal velocity. With using the denotation of (4.68), the respective edge integrals are then written as follows:

$$\begin{aligned}
T \quad &: \quad \mathfrak{D}T = \chi\frac{\partial T}{\partial n}, \quad \zeta = 0, \quad \mathfrak{q}^{(1)} = 0 \\
&\qquad \int_{\Gamma_e} N_\imath \mathfrak{q}^{(0)}\, r\mathrm{d}\Gamma = \frac{L}{6}\left(r_\imath\overline{\mathfrak{q}^{(0)}} + \overline{r}\mathfrak{q}_\imath^{(0)} + \overline{r\mathfrak{q}^{(0)}}\right) \\
u_\varphi \quad &: \quad \mathfrak{D}u_\varphi = \frac{\nu}{r}\frac{\partial(ru_\varphi)}{\partial n}, \quad \zeta = 1 \\
&\qquad \int_{\Gamma_e} N_\imath \mathfrak{q}^{(0)}\, \mathrm{d}\Gamma = \frac{L}{6}\left(\mathfrak{q}_\imath^{(0)} + 2\overline{\mathfrak{q}^{(0)}}\right) \\
&\qquad \int_{\Gamma_e} N_\imath \mathfrak{q}^{(1)} N_\jmath\, \mathrm{d}\Gamma = \frac{L}{12}\left(\mathfrak{q}_\imath^{(1)} + \mathfrak{q}_\jmath^{(1)} + 2\delta_{\imath\jmath}\overline{\mathfrak{q}^{(1)}}\right),
\end{aligned}$$

where L is the length of the edge Γ_e and a bar above a variable stands this time for the average nodal value of the variable on this edge (hence averaging over two nodes only):

$$\text{on edge } \Gamma_e: \quad \overline{X} \equiv \frac{1}{2}\sum_{\imath\in\Gamma_e} X_\imath.$$

Both temperature and azimuthal velocity have also first kind boundary conditions. For the vorticity and stream function, according to the introduced problem formulation, the first kind boundary conditions even are the only ones existent. The treatment of these boundary conditions is different from that above: the equations of (4.73) that correspond to the boundary nodes $\imath$ with first kind boundary conditions are simply rewritten with using explicitly the boundary value $\mathfrak{u}_\imath^{\mathrm{BC}}$:

$$\mathfrak{u}_\imath = \mathfrak{u}_\imath^{\mathrm{BC}}, \qquad \imath \in \{\text{nodes with 1st kind BC}\} \tag{4.82}$$

(the matrix elements for all $\mathfrak{u}_{\jmath\neq\imath}$ are set to zero).

4.6.6 Integration of convection and source terms

Since there is no convection term in the stream function equation, the weight function for this variable is taken equal to the basis function. For the other variables, however, we use the stabilized version of the weight function as shown above in (4.76) and (4.78):

$$W_\imath = N_\imath + \tau_\imath \left(\frac{r_\imath}{r}\right)^\zeta \left(u_{r\imath}\frac{\partial N_\imath}{\partial r} + u_{z\imath}\frac{\partial N_\imath}{\partial z}\right),$$

where $\zeta = 0$ for temperature and $\zeta = 1$ for the vorticity and azimuthal velocity. After integration, taking into account (4.72), the convection terms have hence the form:

$$\begin{aligned}
&\int_{S_e} W_\imath \mathfrak{L}_{\mathrm{conv}} N_\jmath \, r\mathrm{d}r\mathrm{d}z = \\
&\qquad \int_{S_e} N_\imath \mathfrak{L}_{\mathrm{conv}} N_\jmath \, r\mathrm{d}r\mathrm{d}z \;+\; \tau_\imath r_\imath^\zeta \int_{S_e} \left(u_{r\imath}\frac{\partial N_\imath}{\partial r} + u_{z\imath}\frac{\partial N_\imath}{\partial z}\right) \mathfrak{L}_{\mathrm{conv}} N_\jmath \, r^{1-\zeta}\mathrm{d}r\mathrm{d}z = \\
&\qquad\qquad \frac{3 + r_\imath/\overline{r}}{24}\left(a_\jmath\frac{\partial\psi}{\partial r} - b_\jmath\frac{\partial\psi}{\partial z}\right) \;+\; \tau_\imath\left(\frac{r_\imath}{\overline{r}}\right)^\zeta \overline{r}\,\frac{(u_{r\imath}b_\imath + u_{z\imath}a_\imath)(u_{r\imath}b_\jmath + u_{z\imath}a_\jmath)}{4A}.
\end{aligned}$$

The elements near the symmetry axis need special treatment. In the elements whose at least one node lies on the axis, the first part of the above expression is replaced by

$$\int_{S_e} N_\imath \mathfrak{L}_{\mathrm{conv}} N_\jmath \, r\mathrm{d}r\mathrm{d}z\bigg|_{r\to 0} = \frac{3 + r_\imath/\overline{r}}{24}\, a_\jmath\frac{\partial\psi}{\partial r} - \frac{9 + 3\overline{r^2}/\overline{r}^2 + 6r_\imath/\overline{r} + 2(r_\imath/\overline{r})^2}{120}\, b_\jmath\frac{\partial\psi}{\partial z}.$$

The derivatives of ψ in the above expressions are assumed constant inside every element and are obtained from the three node values of ψ of that element, according to (4.65) and (4.72), in the following way:

$$\frac{\partial\psi}{\partial r} = \frac{1}{2A}\sum_{\imath\in e} b_\imath\psi_\imath \ , \quad \frac{\partial\psi}{\partial z} = \frac{1}{2A}\sum_{\imath\in e} a_\imath\psi_\imath. \tag{4.83}$$

The node values of the radial and axial velocity components are obtained after each calculation of the stream function field by averaging the stream function derivatives in the neighbouring elements:

$$u_{r\imath} = -\sum_{e\ni\imath}\left(\frac{1}{\overline{r}_e}\frac{\partial\psi}{\partial z}\bigg|_e A_e\right)\Bigg/\sum_{e\ni\imath} A_e \ , \quad u_{z\imath} = \sum_{e\ni\imath}\left(\frac{1}{\overline{r}_e}\frac{\partial\psi}{\partial r}\bigg|_e A_e\right)\Bigg/\sum_{e\ni\imath} A_e.$$

Let us now consider the source terms $\mathfrak{s}^{(1)} = \mathfrak{s}^{(1)}_* + \mathfrak{s}^{(1)}_t$. For the azimuthal velocity, $\mathfrak{s}^{(1)}_* = -u_r/r$. The respective contribution to the system matrix is as follows:

$$-\int_{S_e} W_\imath \mathfrak{s}^{(1)}_* N_\jmath \, r\mathrm{d}r\mathrm{d}z = -\frac{A}{12\,\overline{r}}\frac{\partial\psi}{\partial z}(1+\delta_{\imath\jmath}) \ + \ \tau_\imath \frac{r_\imath u_{r\imath}(u_{r\imath}b_\imath + u_{z\imath}a_\imath)}{6\overline{r}}.$$

For elements near the symmetry axis, the first term on the right hand side of the above expression is replaced by

$$-\frac{(3\overline{r} + r_\imath + r_\jmath)A}{60\,\overline{r}^2}\ \frac{\partial\psi}{\partial z}(1+\delta_{\imath\jmath}).$$

For the vorticity, there is a similar source term, $\mathfrak{s}^{(1)}_* = u_r/r$, and consequently the expressions of the integrals are analogous to the ones above but with the opposite sign.

The inertial part of source term, $\mathfrak{s}^{(1)}_t$, is present for all variables excepting ψ. For the azimuthal velocity and vorticity we have:

$$-\int_{S_e} W_\imath \mathfrak{s}^{(1)}_t N_\jmath \, r\mathrm{d}r\mathrm{d}z = \frac{(3\overline{r} + r_\imath + r_\jmath)A}{60\,\Delta t}(1+\delta_{\imath\jmath}) \ + \ \tau_\imath \frac{r_\imath(u_{r\imath}b_\imath + u_{z\imath}a_\imath)}{6\,\Delta t}.$$

For temperature, the same expression is used but the stabilization part is replaced by

$$\tau_\imath \frac{(3\overline{r} + r_\jmath)(u_{r\imath}b_\imath + u_{z\imath}a_\imath)}{24\,\Delta t}.$$

And finally, we write down the contributions to the left side of the linear equation system arising due to the source terms $\mathfrak{s}^{(0)} = \mathfrak{s}^{(0)}_* + \mathfrak{s}^{(0)}_t$.

For the stream function ψ we have $\mathfrak{s}^{(0)} = \mathfrak{s}_*^{(0)} = \omega$ and the respective integral equals:

$$\int_{S_e} W_\imath \mathfrak{s}_*^{(0)} \, r\mathrm{d}r\mathrm{d}z = \frac{A}{60} \left[3(3\overline{r} + r_\imath)\overline{\omega} + (3\overline{r} + 2r_\imath)\omega_\imath + 3\overline{r\omega} \right].$$

For the vorticity ω, the $\mathfrak{s}_*^{(0)}$-part of the source term is more complicated and equal to $\mathfrak{s}_*^{(0)} = \frac{2u_\varphi}{r}\frac{\partial u_\varphi}{\partial z} - g\beta\frac{\partial T}{\partial r}$. The respective integral is expressed as follows:

$$\int_{S_e} W_\imath \mathfrak{s}_*^{(0)} \, r\mathrm{d}r\mathrm{d}z = \frac{A}{6} \left[(3\overline{u_\varphi} + u_{\varphi\imath})\frac{\partial u_\varphi}{\partial z} - \frac{g\beta}{2}(3\overline{r} + r_\imath)\frac{\partial T}{\partial r} \right] + \tau_\imath \, r_\imath (u_{r\imath} b_\imath + u_{z\imath} a_\imath) \left(\frac{\overline{u_\varphi}}{\overline{r}}\frac{\partial u_\varphi}{\partial z} - \frac{g\beta}{2}\frac{\partial T}{\partial r} \right).$$

The derivatives of azimuthal velocity and temperature are assumed constant in elements and are calculated in an analogous way as the derivatives of ψ, see (4.83). For elements near the symmetry axis, the first term on the right hand side of the above expression is replaced by

$$\frac{A}{6} \left[\frac{(3\overline{r} + r_\imath)\overline{u_\varphi}}{\overline{r}}\frac{\partial u_\varphi}{\partial z} - \frac{g\beta}{10} \left(3(3\overline{r} + 2r_\imath) + \frac{3\overline{r^2} + 2r_\imath^2}{\overline{r}} \right) \frac{\partial T}{\partial r} \right].$$

For the temperature and azimuthal velocity, there are no sources $\mathfrak{s}_*^{(0)}$.

The inertial part of the source term, written in the general form as $\mathfrak{s}_t^{(0)} = \mathfrak{u}^{\mathrm{old}}/\Delta t$, yields the following integral for the temperature T:

$$\int_{S_e} W_\imath \mathfrak{s}_t^{(0)} \, r\mathrm{d}r\mathrm{d}z = \frac{A}{60\Delta t} \left[3(3\overline{r} + r_\imath)\overline{T^{\mathrm{old}}} + (3\overline{r} + 2r_\imath)T_\imath^{\mathrm{old}} + 3\overline{rT^{\mathrm{old}}} \right] + \tau_\imath \, \frac{u_{r\imath} b_\imath + u_{z\imath} a_\imath}{8\,\Delta t} \left(3\overline{r}\,\overline{T^{\mathrm{old}}} + \overline{rT^{\mathrm{old}}} \right).$$

For the azimuthal velocity u_φ and vorticity ω, the expressions of the integral are similar but T^{old} is replaced by u_φ^{old} or ω^{old}, respectively, and the stabilization term is modified:

$$\tau_\imath \, \frac{u_{r\imath} b_\imath + u_{z\imath} a_\imath}{2\,\Delta t} \, r_\imath \overline{u_\varphi^{\mathrm{old}}}$$

(or with ω^{old} instead of u_φ^{old}, for the vorticity).

4.6.7 Stabilization parameter τ

The stabilization parameter τ, which is responsible for the appropriate weighting of the amount of stabilization, is calculated in each element based on a formula derived

from a simplified equation in one dimension. Let us consider the one-dimensional convection–diffusion equation for the scalar field $y(x)$,

$$u\frac{\partial y}{\partial x} = D\frac{\partial^2 y}{\partial x^2},$$

which has the exact solution

$$y^{\mathrm{ex}}(x) = C_1 \exp\frac{ux}{D} + C_2,$$

where the constants C_1 and C_2 depend on the boundary conditions. Then it can be shown (see e.g. [84]) that using the linear FEM and a uniform distribution of nodes along x brings the *nodally exact* solution of the above equation if the following stabilization parameter is applied:

$$\tau = \frac{\Delta x}{2|u|}\left[\coth(\mathrm{Pe}) - \frac{1}{\mathrm{Pe}}\right],$$

where Δx is the distance between nodes and Pe is the Peclet number defined by

$$\mathrm{Pe} = \frac{|u|\,\Delta x}{2D}.$$

Such definition of τ is often called the "optimal" in the literature. A more complicated formula can be written for an irregular node distribution as well, the usage of the above simple coth-law can, however, be well justified also in this case, since most important part of the stabilization effect (the stabilization of the downstream node) will be in both cases equal [84]. Noteworthy, the stabilization parameter depends always only on the relative positions of the next two nodes and is independent on the boundary conditions, hence the definition of τ is local.

The above formula is used as approximation for the general case of more than one dimension and arbitrary node or element distributions. For our specific case, the stabilization parameter is introduced in the triangle elements:

$$\tau_e = \frac{h_e}{2|u_e|}\left[\coth(\mathrm{Pe}_e) - \frac{1}{\mathrm{Pe}_e}\right],$$

where the element length in streamline direction, h_e, is used instead of Δx, and the Peclet number of element e is defined by

$$\mathrm{Pe}_e = \frac{|u_e|\,h_e}{2D}.$$

Here D stands for the respective diffusion coefficient, i.e., ν or χ, and the elemental velocity u_e comprises only the radial and azimuthal components:

$$|u_e| = \sqrt{u_{re}^2 + u_{ze}^2}\,, \quad u_{re} = -\frac{1}{\overline{r}_e}\frac{\partial \psi}{\partial z}\,, \quad u_{ze} = \frac{1}{\overline{r}_e}\frac{\partial \psi}{\partial r},$$

where the derivatives of ψ are obtained according to (4.83).

The element length in streamline direction, h_e, can be calculated by using the functions $N_\imath$ (see (4.72)) of the three nodes of the element e:

$$h_e = 2\left(\sum_{\imath\in e}\frac{1}{|u_e|}\left|u_{re}\frac{\partial N_\imath}{\partial r}+u_{ze}\frac{\partial N_\imath}{\partial z}\right|\right)^{-1}.$$

In order to ensure that one constant stabilization parameter is used throughout the $\imath$-th equation, we define the nodal value of stabilization parameter, $\tau_\imath$, as the maximum of the values of τ_e in the elements containing the considered node:

$$\tau_\imath = \max_{e\ni\imath}\tau_e\,.$$

4.6.8 Numerical solution and coupling of all flow variables

The equation systems are build for each of the flow variables (ψ, T, u_φ and ω) as shown above. Since each node interacts only with the neighbouring nodes and itself, the matrices of the linear systems are sparse and the diagonal elements are nonzero. No preconditioning is needed and the sparsity is used to speed up the process of iterative solution and reduce the storage memory by introducing arrays of neighbouring node indices for each node. These arrays define hence the positions of the nonzero matrix elements at each row of the system matrix and allow skipping the large amount of non-necessary arithmetic operations with zero elements.

The full solution of the axisymmetric fluid flow at a given time step includes a cyclic recalculation of the four systems of equations: first we calculate the stream function, which yields the radial and axial velocity components, then the azimuthal velocity and temperature. At this point also the boundary conditions for the vorticity are modified. At the last step, the vorticity itself is solved. The cycle is repeated until the convergence is reached. Normally, with a small enough time step (typically 0.002 s), only one such cycle per time step is needed, due to the good initial conditions (the change of solution from one time step to another is small), and the calculation proceeds for the next time step.

4.6.9 Test of the flow solver

The developed axisymmetric HD solver of FZONE was tested by comparing to another axisymmetric HD solver FZHD (which uses also the $\psi - \omega$ formulation) developed in the nineties by Prof. Muižnieks. The code FZHD solves hydrodynamics in the melt with prescribed shape of boundaries and uses a somewhat different approximation and numerical implementation as FZONE. Instead of the streamline upwind/Petrov-Galerkin scheme, a simpler upwind approximation scheme with empirically chosen weighting factor for the stabilization of the convective terms is used in FZHD. The test calculations with FZONE and FZHD have shown [85]:

- If calculating on similar triangular grids, the calculation results between FZONE and FZHD differ. If refining the grid for FZHD, the results get equal. This is explained by a higher numerical viscosity in FZHD, hence the choice of the stabilization parameter in FZONE is better.
- FZONE is more stable than FZHD if the grid is bad (i.e., the triangles are somewhere too stretched): the solution with FZHD diverges whereas FZONE just may get a worse convergence. That FZONE does not diverge is explained by a better approximation of the integrals. This advantage of FZONE is important for successful calculation of fluid flow with permanently deforming grid due to the change of the shape of the floating zone.

Since the code FZHD has been compared earlier to the well-known commercial CFD package FLUENT and the agreement was well, i.e., FZHD showed even better behaviour than FLUENT[5], the above comparison between FZONE and FZHD was enough to conclude that FZONE is in agreement with FLUENT as well.

[5] FLUENT needed finer grid than FZHD to get the same solution, hence FLUENT had a higher numerical viscosity, which could be related to the fact that FLUENT solves in the natural velocity–pressure variables.

4.7 Radiation modelling with view factors

The surface-to-surface radiation model with view factors is modelled in `FZONE` mainly following the recipes by Dupret et al. in [86] (the publication considers the Czochralski growth) and including additionally a formalism in terms of "space node" for the case of a non-closed radiative surface system, i.e., when the enclosing surfaces are left outside the model, as preferred for floating zone modelling. Also the numerical implementation of the radiation model is different from that described in [86].

4.7.1 Equations for an open radiative system

Introductory assumptions and relations

The following assumptions are used:

- Radiation is only diffuse. This approximation is supposed to work satisfactory well because real solid surfaces are generally non-smooth.
- Surfaces are opaque. Emission, absorption and reflection of radiating waves only occur at the surfaces of the bodies and not within the bodies themselves.
- Bodies are optically gray. The optical material properties are assumed temperature and wavelength independent in the whole spectrum.

According to the Planck's law, the spectral emissive power $e_{\mathrm{b}\lambda}(T)$ of a black body (or a perfect absorber) at the given temperature T and wavelength λ equals

$$e_{\mathrm{b}\lambda}(T) = \frac{2\pi C_1}{\lambda^5 \left(\mathrm{e}^{C_2/\lambda T} - 1\right)},$$

where $C_1 = 0.595448 \cdot 10^8$ W μm^4 m^{-2} and $C_2 = 14388$ μm K. Integrating over the whole spectrum yields the total power $q_{\mathrm{b}}(T)$ emitted by the black body per unit area,

$$q_{\mathrm{b}}(T) = \int_0^\infty e_{\mathrm{b}\lambda}(T)\,\mathrm{d}\lambda = \sigma_{\mathrm{SB}} T^4,$$

where $\sigma_{\mathrm{SB}} = 5.67 \cdot 10^{-8}$ W m^{-2} K^{-4} is the Stefan-Boltzmann constant. The total power q_{e} emitted by a non-black body per unit area is given by the expression

$$q_{\mathrm{e}}(\mathbf{x}) = \epsilon(\mathbf{x})\, q_{\mathrm{b}}(T(\mathbf{x})) = \epsilon(\mathbf{x})\, \sigma_{\mathrm{SB}} T^4(\mathbf{x}), \tag{4.84}$$

where $\epsilon(\mathbf{x}) \leqslant 1$ is the surface emissivity at a generic point $\mathbf{x}$ on the radiating surface.

Any surface element is emitting itself and meanwhile bombarded by waves coming from the other surface elements. The incident heat flux $q_{\mathrm{i}}(\mathbf{x})$ can either penetrate the body or be reflected. The penetrating waves are totally absorbed by the opaque surfaces. The absorbed heat flux equals

$$q_{\mathrm{a}}(\mathbf{x}) = \alpha(\mathbf{x})\, q_{\mathrm{i}}(\mathbf{x}),$$

where α is the surface absorptivity. According to the Kirchhoff's law for thermodynamic equilibrium in isothermal enclosure, the absorptivity and emissivity are equal. Hence, the absorbed and reflected heat fluxes, q_{a} and q_{r}, are given by

$$q_{\mathrm{a}}(\mathbf{x}) = \epsilon(\mathbf{x})\, q_{\mathrm{i}}(\mathbf{x}), \tag{4.85}$$

$$q_{\mathrm{r}}(\mathbf{x}) = (1 - \epsilon(\mathbf{x}))\, q_{\mathrm{i}}(\mathbf{x}). \tag{4.86}$$

The total outgoing heat flux q_{o} is the sum of the emitted and reflected fluxes:

$$q_{\mathrm{o}}(\mathbf{x}) = q_{\mathrm{e}}(\mathbf{x}) + q_{\mathrm{r}}(\mathbf{x}) \quad = \epsilon(\mathbf{x})\, \sigma_{\mathrm{SB}} T^4(\mathbf{x}) + (1 - \epsilon(\mathbf{x}))\, q_{\mathrm{i}}(\mathbf{x}). \tag{4.87}$$

What one actually needs for the global heat exchange calculation is the net radiation-caused heat flux from the radiating surfaces, i.e., the difference between the outgoing and incident fluxes:

$$q^{\mathrm{rad}}(\mathbf{x}) = q_{\mathrm{o}}(\mathbf{x}) - q_{\mathrm{i}}(\mathbf{x}). \tag{4.88}$$

Using equations (4.87) and (4.88), the incident and outgoing fluxes at $\mathbf{x}$ are expressed in terms of the net flux $q^{\mathrm{rad}}(\mathbf{x})$:

$$\begin{cases} q_{\mathrm{i}}(\mathbf{x}) = \sigma_{\mathrm{SB}} T^4(\mathbf{x}) - \frac{1}{\epsilon(\mathbf{x})}\, q^{\mathrm{rad}}(\mathbf{x}), \\ q_{\mathrm{o}}(\mathbf{x}) = \sigma_{\mathrm{SB}} T^4(\mathbf{x}) - \frac{1-\epsilon(\mathbf{x})}{\epsilon(\mathbf{x})}\, q^{\mathrm{rad}}(\mathbf{x}). \end{cases} \tag{4.89}$$

View factors

The total incident heat flux $q_{\mathrm{i}}(\mathbf{x})$ is the sum of the contributions of the outgoing fluxes $q_{\mathrm{o}}(\mathbf{x}^*)$ from all other points $\mathbf{x}^*$ on the enclosure. If the system of surfaces is not closed, the incident heat flux contains also the contribution from the space node.

Let $\mathrm{d}S$ and $\mathrm{d}S^*$ be infinitesimal areas at points $\mathbf{x}$ and $\mathbf{x}^*$. The fraction of the incident flux on $\mathrm{d}S$ that leaves $\mathrm{d}S^*$ is calculated by

$$\mathrm{d}q_{\mathrm{i}}(\mathbf{x}) = K(\mathbf{x}, \mathbf{x}^*) \cdot q_{\mathrm{o}}(\mathbf{x}^*)\, \mathrm{d}S^*, \tag{4.90}$$

where $K(\mathbf{x}, \mathbf{x}^*)$ is the surface view factor between $\mathbf{x}$ and $\mathbf{x}^*$. According to the Lambert's cosine law for diffuse radiation, whenever $\mathrm{d}S$ and $\mathrm{d}S^*$ see each other, $K(\mathbf{x}, \mathbf{x}^*)$ is given by the formula

$$K(\mathbf{x}, \mathbf{x}^*) = -\frac{[(\mathbf{x}^* - \mathbf{x}) \cdot \mathbf{n}][(\mathbf{x}^* - \mathbf{x}) \cdot \mathbf{n}^*]}{\pi[(\mathbf{x}^* - \mathbf{x}) \cdot (\mathbf{x}^* - \mathbf{x})]^2}, \tag{4.91}$$

where $\mathbf{n}$ and $\mathbf{n}^*$ are the unit normals to $\mathrm{d}S$ and $\mathrm{d}S^*$ (these are outer normals on the surface of the radiating body). On the other hand, when $\mathrm{d}S$ and $\mathrm{d}S^*$ do not see each other, $K(\mathbf{x}, \mathbf{x}^*)$ vanishes:

$$K(\mathbf{x}, \mathbf{x}^*) = 0. \tag{4.92}$$

Hence the view factor $K(\mathbf{x}, \mathbf{x}^*)$ is always symmetrical:

$$K(\mathbf{x}, \mathbf{x}^*) = K(\mathbf{x}^*, \mathbf{x}). \tag{4.93}$$

Space node

Since Dupret et al. [86] consider the Czochralski process with full casing, a modification has been made here by including additionally a formalism in terms of the so-called space node in order to reduce the task and avoid calculating a fully closed radiating surface system of the floating zone process. The space node characterizes the influence of the surrounding space. It accumulates all the radiative heat flux not incident on the explicit surfaces and does not reflect anything but radiates back as a black body with an effective temperature, the ambient temperature T_{amb}. Hence, for the space node, the outgoing radiation heat flux (4.87) reduces to

$$q_{\mathrm{o}}(\mathrm{space}) = \sigma_{\mathrm{SB}} T_{\mathrm{amb}}^4. \tag{4.94}$$

It is also assumed that a space view factor $K^{\mathrm{space}}(\mathbf{x})$ may be defined so that it fulfills two equations:

- The part of incident flux at point $\mathbf{x}$ that is supplied by the space node equals

  $$K^{\mathrm{space}}(\mathbf{x}) \cdot q_{\mathrm{o}}(\mathrm{space}).$$

  This leads, if using (4.90), to the following total incident heat flux at $\mathbf{x}$:

  $$q_{\mathrm{i}}(\mathbf{x}) = \int_{\mathbf{x}^* \in S} K(\mathbf{x}, \mathbf{x}^*) \cdot q_{\mathrm{o}}(\mathbf{x}^*)\, \mathrm{d}S^* \; + \; K^{\mathrm{space}}(\mathbf{x}) \cdot q_{\mathrm{o}}(\mathrm{space}), \tag{4.95}$$

  where S designates the whole radiating surface.

- On the other hand, the integral incident flux onto the space node contributed by a radiating surface element $\mathrm{d}S^*$ positioned at point $\mathbf{x}^*$ equals

$$K^{\mathrm{space}}(\mathbf{x}^*) \cdot q_{\mathrm{o}}(\mathbf{x}^*)\,\mathrm{d}S^*,$$

  where $q_{\mathrm{o}}(\mathbf{x}^*)$ is the outgoing flux at $\mathbf{x}^*$. Adding the integrated contribution of the same surface element $\mathrm{d}S^*$ over the whole surface S leads to the total outgoing power from $\mathrm{d}S^*$:

$$q_{\mathrm{o}}(\mathbf{x}^*)\,\mathrm{d}S^* = \int_{\mathbf{x}\in S} [K(\mathbf{x},\mathbf{x}^*) \cdot q_{\mathrm{o}}(\mathbf{x}^*)\,\mathrm{d}S^*]\,\mathrm{d}S + K^{\mathrm{space}}(\mathbf{x}^*) \cdot q_{\mathrm{o}}(\mathbf{x}^*)\,\mathrm{d}S^*.$$

Dividing both sides of the last equation by $q_{\mathrm{o}}(\mathbf{x}^*)\,\mathrm{d}S^*$ leads to an integral relation the view factors satisfy:

$$\int_{\mathbf{x}\in S} K(\mathbf{x},\mathbf{x}^*)\,\mathrm{d}S + K^{\mathrm{space}}(\mathbf{x}^*) = 1. \tag{4.96}$$

The obtained equation (4.96) yields $K^{\mathrm{space}}(\mathbf{x}^*)$ for each $\mathbf{x}^* \in S$ if the calculation procedure of $K(\mathbf{x},\mathbf{x}^*)$ is known.

Radiative integral equation

To write the integral equation for the net heat fluxes $q^{\mathrm{rad}}(\mathbf{x})$, the expressions (4.89) and (4.94) are substituted into (4.95):

$$\frac{q^{\mathrm{rad}}(\mathbf{x})}{\epsilon(\mathbf{x})} - \int_{\mathbf{x}^*\in S} \frac{1-\epsilon(\mathbf{x}^*)}{\epsilon(\mathbf{x}^*)}\,K(\mathbf{x},\mathbf{x}^*)\,q^{\mathrm{rad}}(\mathbf{x}^*)\,\mathrm{d}S^* = \sigma_{\mathrm{SB}}T^4(\mathbf{x}) - \sigma_{\mathrm{SB}}T^4_{\mathrm{amb}}K^{\mathrm{space}}(\mathbf{x}) - \int_{\mathbf{x}^*\in S} \sigma_{\mathrm{SB}}T^4(\mathbf{x}^*)\,K(\mathbf{x},\mathbf{x}^*)\,\mathrm{d}S^*.$$

In the special case of a closed system, i.e., without free surrounding space, we have $K^{\mathrm{space}}(\mathbf{x}) \equiv 0$ and the above equation reduces to the 3D integral equation in [86].

Using (4.96) and (4.93), we obtain the final form of the 3D integral equation for an open set of radiating surfaces:

$$\frac{q^{\mathrm{rad}}(\mathbf{x})}{\epsilon(\mathbf{x})} - \int_{\mathbf{x}^*\in S} \frac{1-\epsilon(\mathbf{x}^*)}{\epsilon(\mathbf{x}^*)}\,K(\mathbf{x},\mathbf{x}^*)\,q^{\mathrm{rad}}(\mathbf{x}^*)\,\mathrm{d}S^* = \sigma_{\mathrm{SB}}\left[T^4(\mathbf{x}) - T^4_{\mathrm{amb}}\right] - \int_{\mathbf{x}^*\in S} \sigma_{\mathrm{SB}}\left[T^4(\mathbf{x}^*) - T^4_{\mathrm{amb}}\right]\,K(\mathbf{x},\mathbf{x}^*)\,\mathrm{d}S^*. \tag{4.97}$$

2D radiative integral equation and the axisymmetric view factor $K_\mathbf{c}$

The next step is to take into account the axial symmetry of the radiating surface S. Let r, θ and z denote the cylindrical coordinates of the point $\mathbf{x}$ and let $p(S)$ stand for the intersection of the axisymmetric surface S and the half-plane $\theta = 0$. The "axisymmetric view factor" $K_\mathrm{c}(\mathbf{x}, \mathbf{x}')$ is defined then by the integral

$$K_\mathrm{c}(\mathbf{x}, \mathbf{x}') = 2 \int_0^\pi K(\mathbf{x}, \mathbf{x}^*)\, \mathrm{d}\theta^* \tag{4.98}$$

with the following $\mathbf{x}$, $\mathbf{x}'$ and $\mathbf{x}^*$ given in Cartesian components:

$$\begin{cases} \mathbf{x} &= (r,\, 0,\, z) \in p(S) \\ \mathbf{x}' &= (r',\, 0,\, z') \in p(S) \\ \mathbf{x}^* &= (r' \cos\theta^*,\, r' \sin\theta^*,\, z') \in S. \end{cases} \tag{4.99}$$

For each $\mathbf{x} \in p(S)$ we rewrite the integral equation (4.97) in the 2D form

$$\begin{aligned} &\frac{q^\mathrm{rad}(\mathbf{x})}{\epsilon(\mathbf{x})} - \int_{\mathbf{x}' \in p(S)} \frac{1 - \epsilon(\mathbf{x}')}{\epsilon(\mathbf{x}')}\, r' K_\mathrm{c}(\mathbf{x}, \mathbf{x}')\, q^\mathrm{rad}(\mathbf{x}')\, \mathrm{d}s' \\ &\qquad = \sigma_\mathrm{SB} \left[T^4(\mathbf{x}) - T_\mathrm{amb}^4\right] - \int_{\mathbf{x}' \in p(S)} \sigma_\mathrm{SB} \left[T^4(\mathbf{x}') - T_\mathrm{amb}^4\right]\, r' K_\mathrm{c}(\mathbf{x}, \mathbf{x}')\, \mathrm{d}s', \end{aligned} \tag{4.100}$$

where s is the curvilinear abscissa on $p(S)$.

According to equations (4.93), (4.98), (4.99) and keeping in mind the invariance of the system with respect to rotational transformations, it is easy to proof that the axisymmetric view factors $K_\mathrm{c}(\mathbf{x}, \mathbf{x}')$ obey the same symmetry rule as the 3D view factors $K(\mathbf{x}, \mathbf{x}^*)$:

$$K_\mathrm{c}(\mathbf{x}, \mathbf{x}') = K_\mathrm{c}(\mathbf{x}', \mathbf{x}). \tag{4.101}$$

Considering the relation (4.96), there is an analogous rule for the axisymmetric view factor, too. By using the equations (4.93), (4.96), (4.98), (4.99) and the identity $\int_{\mathbf{x}^* \in S} K(\mathbf{x}, \mathbf{x}^*)\, \mathrm{d}S^* \equiv \int_{\mathbf{x}' \in p(S)} \left[\int_0^{2\pi} K(\mathbf{x}, \mathbf{x}^*) \mathrm{d}\theta^*\right]\, r' \mathrm{d}s'$, we obtain

$$\int_{\mathbf{x}' \in p(S)} r'\, K_\mathrm{c}(\mathbf{x}, \mathbf{x}')\, \mathrm{d}s' + K^\mathrm{space}(\mathbf{x}) = 1. \tag{4.102}$$

Calculation of the axisymmetric view factor

In what follows, we keep the designations (4.99) considering $\mathbf{x}$, $\mathbf{x}'$, $\mathbf{x}^*$ and also introduce the following expressions in Cartesian components for the respective unit normals $\mathbf{n}$,

$\mathbf{n}'$ and $\mathbf{n}^*$ (outer normals on the surface of the radiating bodies):

$$\begin{cases} \mathbf{n} &= (\cos\phi,\ 0,\ \sin\phi) \\ \mathbf{n}' &= (\cos\phi',\ 0,\ \sin\phi') \\ \mathbf{n}^* &= (\cos\phi'\cos\theta^*,\ \cos\phi'\sin\theta^*,\ \sin\phi'), \end{cases} \tag{4.103}$$

where ϕ and ϕ' stand for the polar angles of the vectors $\mathbf{n}$ and $\mathbf{n}'$, respectively, in the plane $\theta = 0$.

Introducing the vectors (4.99) and (4.103) into the equation (4.91), we can express the dependence of $K(\mathbf{x}, \mathbf{x}^*)$ on θ^*:

$$K(\mathbf{x}, \mathbf{x}^*) = \hat{K}(\theta^*) = \frac{(a' + b'\,\cos\theta^*)(a'' + b''\,\cos\theta^*)}{\pi\,(a + b\,\cos\theta^*)^2}, \tag{4.104}$$

where a, b, a', b', a'', b'' only depend on $r, z, r', z', \phi, \phi'$ (which are fixed) but not on θ^*. The explicit expressions are:

$$\begin{cases} a &= r^2 + r'^2 + (z' - z)^2 \\ b &= -2rr' \\ a' &= r\,\cos\phi - (z' - z)\,\sin\phi \\ b' &= -r'\,\cos\phi \\ a'' &= r'\,\cos\phi' + (z' - z)\,\sin\phi' \\ b'' &= -r\,\cos\phi' \end{cases}$$

Integrating equation (4.104) with respect to θ^* and taking into account that $a^2 > b^2$ leads to the primitive function $I(\theta)$ of $\hat{K}(\theta^*)$:

$$\begin{aligned} I(\theta) &= \int_0^\theta \hat{K}(\theta^*)\,\mathrm{d}\theta^* \\ &= A\,\theta + B\ \arctan\left(\sqrt{\frac{a-b}{a+b}}\,\tan\theta/2\right) + C\,\frac{\sin\theta}{a + b\,\cos\theta}, \end{aligned} \tag{4.105}$$

where coefficients A, B and C are functions of a, b, a', b', a'', b''. The expressions of the coefficients (not given explicitly in [86]) have been obtained as follows.

If $r \neq 0$, $r' \neq 0$ and $\mathbf{x} \neq \mathbf{x}'$, then

$$\begin{cases} A &= \dfrac{b'\,b''}{\pi\,b^2} \\ B &= 2\,\dfrac{-a^3\,b'\,b'' + 2\,a\,b^2\,b'\,b'' + a\,b^2\,a'\,a'' - b^3\,a''\,b' - b^3\,a'\,b''}{\pi\,b^2\,\sqrt{(a+b)\,(a-b)}\,(a+b)\,(a-b)} \\ C &= -\dfrac{(a\,b' - b\,a')\,(a\,b'' - b\,a'')}{\pi\,b\,(a+b)\,(a-b)} \end{cases}$$

If $r' \neq 0$ and $\mathbf{x} \neq \mathbf{x}'$ but $r = 0$ (which implies $b = b'' = 0$), then

$$\begin{cases} A &= \dfrac{a'\,a''}{\pi\,a^2} \\ B &= 0 \\ C &= \dfrac{a''\,b'}{\pi\,a} \end{cases}$$

If $r \neq 0$ and $\mathbf{x} \neq \mathbf{x}'$ but $r' = 0$ (which implies $b = b' = 0$), then

$$\begin{cases} A &= \dfrac{a'\,a''}{\pi\,a^2} \\ B &= 0 \\ C &= \dfrac{a'\,b''}{\pi\,a} \end{cases}$$

If $\mathbf{x} = \mathbf{x}'$ (which implies $a + b = a' + b' = a'' + b'' = 0$) or $r = r' = 0$, then

$$\begin{cases} A &= \dfrac{a'\,a''}{\pi\,a^2} \\ B &= 0 \\ C &= 0 \end{cases}$$

To calculate the axisymmetric view factor $K_{\mathrm{c}}(\mathbf{x}, \mathbf{x}')$ we need to know the range Θ of values of θ^* for which $K(\mathbf{x}, \mathbf{x}^*)$ does not vanish:

$$\hat{K}(\theta^*) > 0 \quad \Leftrightarrow \quad \theta^* \in \Theta. \tag{4.106}$$

It is possible to characterize Θ as a set of intervals $(\theta_{\mathrm{m}\imath}, \theta_{\mathrm{M}\imath})$:

$$\Theta = \bigcup_{\imath} (\theta_{\mathrm{m}\imath}, \theta_{\mathrm{M}\imath}), \quad 0 \leqslant \theta_{\mathrm{m}\imath} < \theta_{\mathrm{M}\imath} \leqslant \pi. \tag{4.107}$$

According to (4.98), (4.104) and (4.105), knowledge of Θ allows to calculate the expected result:

$$K_{\mathrm{c}}(\mathbf{x},\mathbf{x}') = 2\sum_{\imath}\big(I(\theta_{\mathrm{M}\imath}) - I(\theta_{\mathrm{m}\imath})\big). \tag{4.108}$$

In order to obtain Θ, the values of $\theta_{\mathrm{m}\imath}$ and $\theta_{\mathrm{M}\imath}$ must be detected considering the viewed and hidden parts of the radiating surfaces. It is done following closely the analytical approach described in [86], which is based on the cylindrical symmetry of the system. Since the procedure is complex and described well in the reference, the details are omitted here.

4.7.2 Numerical implementation of the radiation model

Discretization of the integral equation

In order to obtain the distribution of the net radiation heat fluxes $q^{\mathrm{rad}}(\mathbf{x})$ along the radiating surface S with fixed distribution of temperature $T(\mathbf{x})$, the equation (4.100) is discretized and solved numerically as a system of linear equations by means of the Gauss procedure.

The surface S is discretized to coaxial ring-type elements $S_\imath$, where $\imath$ represents the element index. For the corresponding line segments $p(S_\imath)$, the length $L_\imath$ and the midpoint $\mathbf{x}_\imath^{\mathrm{m}} = (r_\imath^{\mathrm{m}}, 0, z_\imath^{\mathrm{m}}) \in p(S_\imath)$ is considered. Inside the $\imath$-th element, the emissivity ϵ, the temperature T and the net radiation heat flux q^{rad} are assumed constant and are denoted by $\epsilon_\imath$, $T_\imath$ and $q_\imath^{\mathrm{rad}}$, respectively. The quantities $q_\imath^{\mathrm{rad}}$ are the ones to be found via the solution of the radiation equation (4.100), which is discretized by splitting the integrals $\int_{\mathbf{x}'\in p(S)}$ into sums $\sum_\imath \int_{\mathbf{x}'\in p(S_\imath)}$. By writing the equation at each element midpoint, a system of linear algebraic equations with respect to $q_\imath^{\mathrm{rad}}$ is built up (index $\imath$ runs over all elements):

$$\sum_{\jmath}\frac{1}{\epsilon_\jmath}[\delta_{\imath\jmath} - (1-\epsilon_\jmath)\,V_{\imath\jmath}]\cdot q_\jmath^{\mathrm{rad}} = \sigma_{\mathrm{SB}}\sum_k(\delta_{\imath k} - V_{\imath k})(T_k^4 - T_{\mathrm{amb}}^4), \tag{4.109}$$

where $\delta_{\imath\jmath}$ is the Kronecker symbol and $V_{\imath\jmath}$ is the designation for the integral over the $\jmath$-th element:

$$V_{\imath\jmath} = \int_{\mathbf{x}'\in p(S_\jmath)} r' K_{\mathrm{c}}(\mathbf{x}_\imath^{\mathrm{m}},\mathbf{x}')\,\mathrm{d}s'. \tag{4.110}$$

Approximation of integrals and speed optimization

The building of matrix for the system of equations (4.109) includes calculation of the axisymmetric view factors $K_c(\mathbf{x}, \mathbf{x}')$. Each calculation of a view factor contains a run through all surface elements to detect the visible and hidden parts (see [86]). Thus there is a threefold run through all surface elements, which makes the matrix building time-critical.

To reduce the necessary computational resources, the simplest approximation for the integrals (4.110) is used, which is justified by a small size of the elements:

$$V_{ij} \approx L_j \cdot r_j^m \cdot K_c(\mathbf{x}_i^m, \mathbf{x}_j^m). \tag{4.111}$$

Due to the symmetry property (4.101) of the axisymmetric view factors, we actually need to calculate only those view factors $K_c(\mathbf{x}_i^m, \mathbf{x}_j^m)$ with $i \leqslant j$. To reduce the amount of necessary calculations to obtain the values of the view factors, different tricks related to the algorithm detecting the visible and hidden parts have been used. So, during calculation of a certain $K_c(\mathbf{x}_i^m, \mathbf{x}_j^m)$, we have to run through all the surface elements and check if they are the "hiding elements", i.e., if they partly or fully hide element i from element j. It is possible, however, to use different strategies to decrease the number of elements that have to undergo the control. For example, we exclude from consideration as an eventual hiding element the elements whose z-coordinate is higher or lower than both z_i and z_j. We stop the control run after the first detection of a fully hiding element. In this context much helps also a prior control of the elements i and j, because they often are oriented in a way that one of them is a fully hiding element itself.

The result of the used algorithm optimizations was a considerable reduction (about a factor of 20) in the necessary computational resources for the view factors calculation and building of the radiation matrix.

Test of precision

According to equations (4.102) and (4.110), the following equality holds:

$$\sum_j V_{ij} + K_i^{\text{space}} = 1, \tag{4.112}$$

where

$$K_i^{\mathrm{space}} \equiv K^{\mathrm{space}}(\mathbf{x}_i^{\mathrm{m}}).$$

Using the identity (4.112), we can check the accuracy of the approximated integration (4.111) by a similar method as done by Dupret et al. in [86]. We verify the deflection from 1 of the left-hand side of (4.112) in locations from which the surface element dS may not see the space. In these locations the space view factor K^{space} is zero. We have detected the error level 3–4%, which can be regarded as very good in the context of the reference work [86], where the authors notice errors even about 70–80%. They have solved this problem by subdividing selected surface elements. Our good success without the additional measures is obviously a consequence of the relatively small sizes of the surface elements we use.

4.8 Coupling of all models in FZONE

4.8.1 Temperature – radiation coupling

The radiating surfaces include the surfaces of the inductor, which is kept cold by means of cooling, and, eventually, one or several reflectors. In the present implementation, however, the temperature field in these bodies is not calculated explicitly but the inductor surface temperature T_{ind} and the reflector surface temperature T_{refl} are taken as fixed model parameters and applied for the radiation calculation, together with the respective emissivity values $\varepsilon_{\mathrm{ind}}$ and $\varepsilon_{\mathrm{refl}}$. Also the temperature of the open melting front is fixed and equals the melting point temperature of silicon. The temperature on the rest of the radiating surfaces has to be calculated by taking into account the radiation.

The previous description of the calculation of the net heat fluxes $q^{\mathrm{rad}}(\mathbf{x})$ (see Section 4.7) included the distribution of the temperature $T(\mathbf{x})$ at the radiating surfaces as fixed parameters in the equations. To obtain the actual temperature distribution on the surfaces where it is variable, the temperature calculation inside the silicon parts and the radiation calculation have to be repeated several times. The view factors for a constant geometry need meanwhile to be calculated only once.

Each of the separate temperature calculations in crystal, melt and feed rod is performed iteratively. The calculation of temperature inside the melt in presence of convection

was described in details in Section 4.6. The calculation of the temperature in crystal and feed rod is also performed with FEM but is simpler than the calculation in melt since no fluid flow has to be calculated parallel to temperature and no stabilization is needed (hence a simple Bubnov-Galerkin formulation can be used). Nevertheless, the convection term due to the constant downwards movement of the crystal and feed rod is taken into account. Also taken into account is the temperature dependence of the thermal conductivity of solid silicon, which makes the temperature equation non-linear. Another source of non-linearity (at the global level though) is the radiation heat exchange, which is taken into account as heat flux $q^{\mathrm{rad}}(\mathbf{x})$ via boundary conditions in each of the separate temperature calculation procedures. The coupling of the temperature calculations in the separate parts of silicon and the global heat exchange via radiation is performed in an outer iteration cycle where the last calculated temperature distribution is the input for the next radiation calculation and vice versa:

$$\ldots \rightarrow T_{(n)} \rightarrow q^{\mathrm{rad}}_{(n)} \rightarrow T_{(n+1)} \rightarrow q^{\mathrm{rad}}_{(n+1)} \rightarrow \ldots$$

If the intermediate results for temperature, $T_{(n)}$, are calculated till a full convergence of the temperature iterations in crystal and feed rod, then the outer iteration sweep diverges due to the non-linearity of the global heat exchange. To avoid that, we couple closer the temperature with the radiation fluxes by finishing the intermediate calculation of $T_{(n+1)}$ in the crystal and feed rod as soon as the maximum allowed change in temperature with the respective iteration process is reached, i.e., when $\max|T_{(n+1)} - T_{(n)}| \approx \Delta_{\max}T_{(n)}$. The value of parameter $\Delta_{\max}T_{(n)}$ is dependent on the actual outer iteration. The starting value, $\Delta_{\max}T_{(0)}$, is a chosen constant, for example 5 K. In course of the outer temperature–radiation iterations the parameter $\Delta_{\max}T$ is modified automatically in order to get a convergence. The following simple rule is used: if the sign of $\max\{T_{(n+1)} - T_{(n)}\}$ is opposite to the sign of $\max\{T_{(n)} - T_{(n-1)}\}$, then let $\Delta_{\max}T_{(n+1)} = \frac{1}{2}\Delta_{\max}T_{(n)}$, otherwise let $\Delta_{\max}T_{(n+1)} = \Delta_{\max}T_{(n)}$. Such a treatment avoids divergence and amplifying of the oscillations around the solution during the temperature–radiation iterations, which is particularly important at the beginning stages of calculation with the initial guess of temperature distribution strongly different from the sought solution.

4.8.2 Total calculation algorithm

The quasi-transient calculation algorithm leading to a steady-state (with respect to the laboratory reference system) solution of phase boundaries is depicted in a simplified way in Fig. 4.15. The choice of a time step (called also the geometry time step and having the typical order of magnitude 1 second) and moving of the fronts (see Section 4.1) is followed by finding the new ITP location, which is coupled to the EM field (Section 4.2) and the free surface shape (see Section 4.4). The new ITP is found by minimization of D_{ITP}, the pressure imbalance at ITP. The following coupled calculation of the temperature and radiation (see Section 4.8.1) yields the necessary temperature gradients for the determination of the new front velocities. In the melt, the temperature calculation includes also the calculation of the melt flow as described in Section 4.6. The geometry time step is subdivided in smaller time steps (the hydrodynamics time step is typically only some milliseconds large) and a time dependent flow is calculated. The relevant heat fluxes at the fronts are averaged over all hydrodynamics time steps in frame of the current geometry time step. Sometimes reasonable studies of the phase boundaries can also be performed by neglecting the effect of the melt flow in order to reduce the computational recourses needed (see one such study in Section 5.2). For more accurate comparisons to measurements, however, the flow effect can occur being important, as it is shown in Section 5.3.

If the new front velocities are very different from the old ones, the precision might be low due to the geometry time step chosen and the calculation is repeated with a smaller time step. Otherwise, the next step is made and the calculation proceeds. Such repeating of the last geometry step is, however, only reasonable in case the hydrodynamics is neglected.

As the solution approaches a steady state, the front velocities diminish. We assume that the stationary solution is found when all velocity values fall below a predefined convergence level. In case the melt flow has strong effect, it can though occur that there is no real steady state at all, due to the time-dependent character of the flow, and the shape of fronts will be oscillating about some average shape.

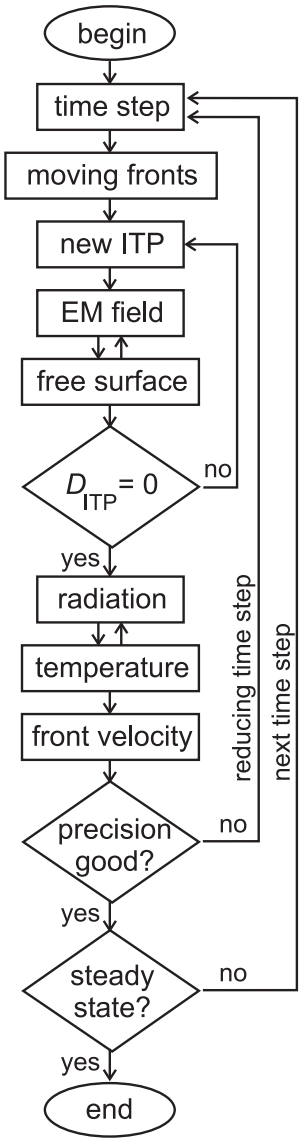

Figure 4.15: Simplified calculation scheme. The temperature calculation includes the calculation of the melt motion in the floating zone.

4.8.3 Zone height targeting by adjusting inductor current

It will be seen below in Sections 5.2– 5.3 that the most floating zone calculations have as input parameter the zone height H_{Z}, instead of the inductor current I. For targeting the needed zone height, the following simple algorithm for the change of the inductor current has been implemented in FZONE.

Before the calculation, the initial step of change of the electric current, $\Delta I_{(0)}$, has to be chosen (a typical value could be 16 A). The adjustment of I during the calculation is then performed along with the convergence check (cf. the control box "steady state?" in Fig. 4.15) before going to the next time step.

Let us assume we have finished the n-th time step ($n \geq 1$). Prior to modifying I, the actual step of change $\Delta I_{(n)}$ is calculated from the previous value, $\Delta I_{(n-1)}$. In doing so, the values of the zone height at the actual moment, $H_{\mathrm{Z}(n)}$, and time step back, $H_{\mathrm{Z}(n-1)}$, are taken into account and compared to the target value $H_{\mathrm{Z}}^{\mathrm{targ}}$. If

$$(H_{\mathrm{Z}}^{\mathrm{targ}} - H_{\mathrm{Z}(n)}) \cdot (H_{\mathrm{Z}}^{\mathrm{targ}} - H_{\mathrm{Z}(n-1)}) < 0$$

then the zone height (as a function of time) is crossing the target. In this case the step of change of I is reduced:

$$\Delta I_{(n)} = \max\left(\frac{\Delta I_{(n-1)}}{2},\, \Delta_{\min} I\right),$$

where the value of $\Delta_{\min} I$ is a predefined constant (e.g., 1 A). In all other cases the old step of change of I is kept: $\Delta I_{(n)} = \Delta I_{(n-1)}$. Hence: $\Delta I_{(n)} \in [\Delta_{\min} I,\ \Delta I_{(0)}]$ for all n.

The current I is only changed if the zone height is going away from the target:

$$|H_{\mathrm{Z}}^{\mathrm{targ}} - H_{\mathrm{Z}(n)}| > |H_{\mathrm{Z}}^{\mathrm{targ}} - H_{\mathrm{Z}(n-1)}|.$$

In this case the new value of the inductor current is calculated by

$$I_{(n+1)} = I_{(n)} + \mathrm{sign}(H_{\mathrm{Z}}^{\mathrm{targ}} - H_{\mathrm{Z}}) \cdot \Delta I_{(n)},$$

where it has been taken into account that an increase in current is needed to augment the zone height. If the above condition is not fulfilled, the old value of current is kept: $I_{(n+1)} = I_{(n)}$.

Despite the simplicity, the targeting algorithm showed a very good performance.

5 Calculation of phase boundaries

The models for the axisymmetric calculation of FZ phase boundaries and their implementation in the computation code `FZONE` were described in Chapter 4. In the present chapter, actual calculations with `FZONE` are undertaken in order to study the phase boundaries in an 8 inch FZ growth process and to make a comparison of the results to experimental data.

5.1 Calculation example

To illustrate the way of functioning of the phase boundary calculation, let us consider as example an 8 inch FZ crystal growth process and neglect, for simplicity, the melt flow. The silicon properties are taken from Table 3.1. The emissivity of the open melting front is assumed equal to $\varepsilon_{\mathrm{s}}(T_0)$. The chosen inductor current I, crystal radius R_{Cr}, feed rod radius R_{F} and other process parameters are summarized in Table 5.1. The reflector is positioned like in Fig. 4.1, the main slit and three additional slits for the HF inductor are considered as well like in Fig. 4.1. The effective width of each slit is set 2 mm. The modelling parameter I_{mslit} is assumed equal to 0.5.

The initial rectilinear geometry used is shown in Fig. 5.1 together with three successive stages of the convergence illustrating a typical calculation progress. The vectors of the front velocities in the reference system of inductor, v_n, are vanishing as the solution approaches the steady state. The initial melt, crystal and feed domains are triangulated as needed for the FEM calculation. In the course of calculation, the finite element mesh is adapted in every step and the triangulation is repeated time by time due to the strong changes in shapes of the domains. The final mesh and the obtained steady-state phase boundaries and the temperature field are shown in Figs. 5.2–5.3.

The lines of magnetic field of the HF inductor are depicted in Fig. 5.2. Most of them are crossing the inductor due to accounting of slits in frame of the axisymmetric approximation. The vertical separator drawn inside the cross-section of the inductor

Parameter	Symbol	Value
Inductor current	I	1500 A
EM field frequency	f	2.8 MHz
Single crystal radius	R_{Cr}	102.0 mm
Feed rod radius	R_{F}	77.5 mm
Single crystal pull rate	V_{Cr}	1.80 mm/min
Feed rod push rate	V_{F}	3.12 mm/min
Crystal rotation rate	Ω_{Cr}	5 rpm
Emissivity of inductor	$\varepsilon_{\mathrm{ind}}$	0.3
Emissivity of reflector	$\varepsilon_{\mathrm{refl}}$	0.3
Temperature of inductor	T_{ind}	400 K
Temperature of reflector	T_{refl}	1000 K
Ambient temperature	T_{amb}	600 K

Table 5.1: Calculation example: FZ process parameters and other input parameters.

marks the end of the additional slits. At larger distances from the center, the few field lines still going through the inductor are due to the main slit. The influence of the end of the additional slits on the shape of the open front can be observed.

The distribution of the net radiation heat flux density q^{rad} at the silicon surfaces is shown by the varying length of the vectors in Fig. 5.3. Steep change in q^{rad} takes place at the inner and exterior triple points due to the different emissivity of the liquid and solid phases. A slight influence of the reflector may be observed in the net radiation flux from the crystal and the temperature field inside the crystal.

The numerical solution of the ITP region and the respective finite element mesh in the melt and feed are in view in Fig. 5.4. The inner edge of the inductor shows the scale in Fig. 5.4(a). An even closer view of the finite element meshes in the ITP vicinity is demonstrated in Fig. 5.4(b). These two pictures display the smooth transition “melting interface—open front”, which, however, does not seem smooth in large scale, e.g. in Fig. 5.2. Since we use approximate model of ITP, the large-scale image (like Fig. 5.2) should be considered as the result of the ITP calculation while Figs. 5.4(a) and 5.4(b) mostly reflect the numerical approach.

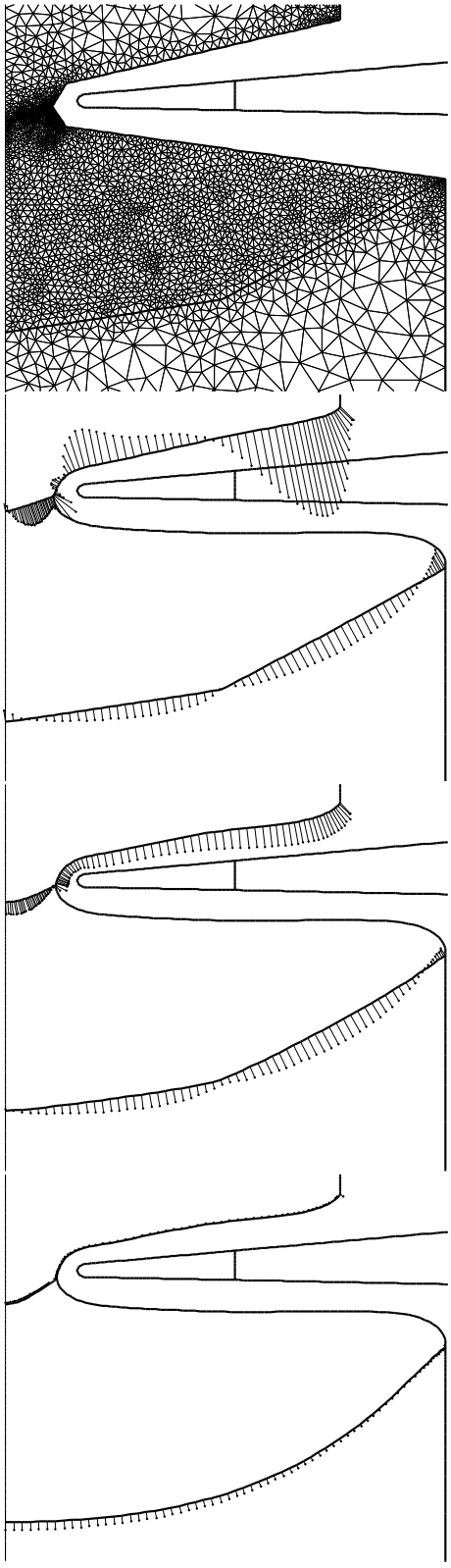

Figure 5.1: Calculation progress: the triangulated starting geometry and 3 successive stages of the convergence to a steady state. Shown are also the vectors of the front velocities v_n.

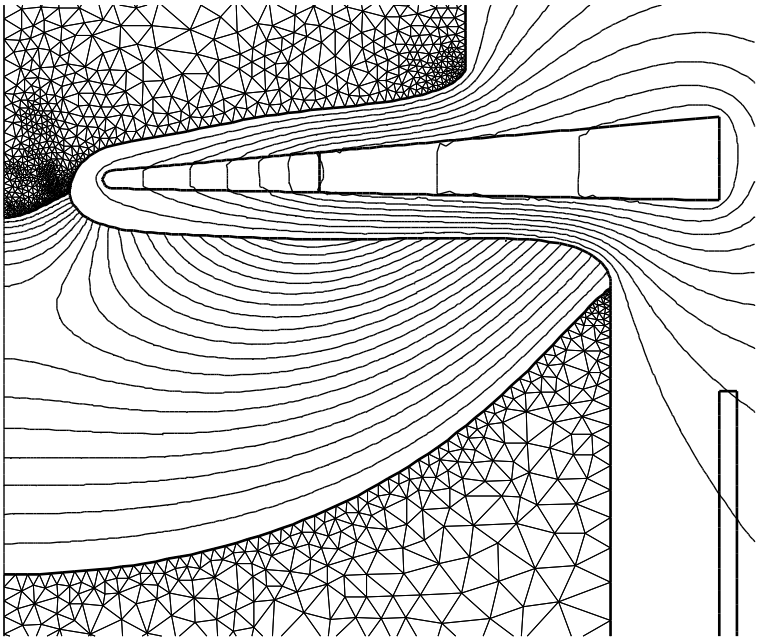

Figure 5.2: Steady state solution: the temperature isolines in the melt with step 2.9 K (maximum 1745 K) and the magnetic field lines. Shown is also the finite element mesh in the crystal and feed rod.

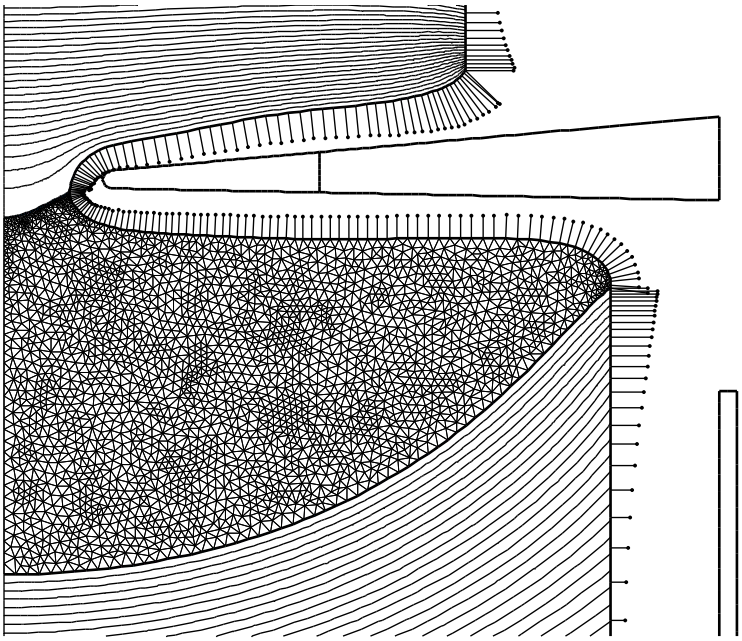

Figure 5.3: Steady state solution: the temperature isolines with step 10 K in the crystal and feed and the vectors showing the magnitude of q^{rad} at the silicon surfaces. Shown is also the finite element mesh in the melt.

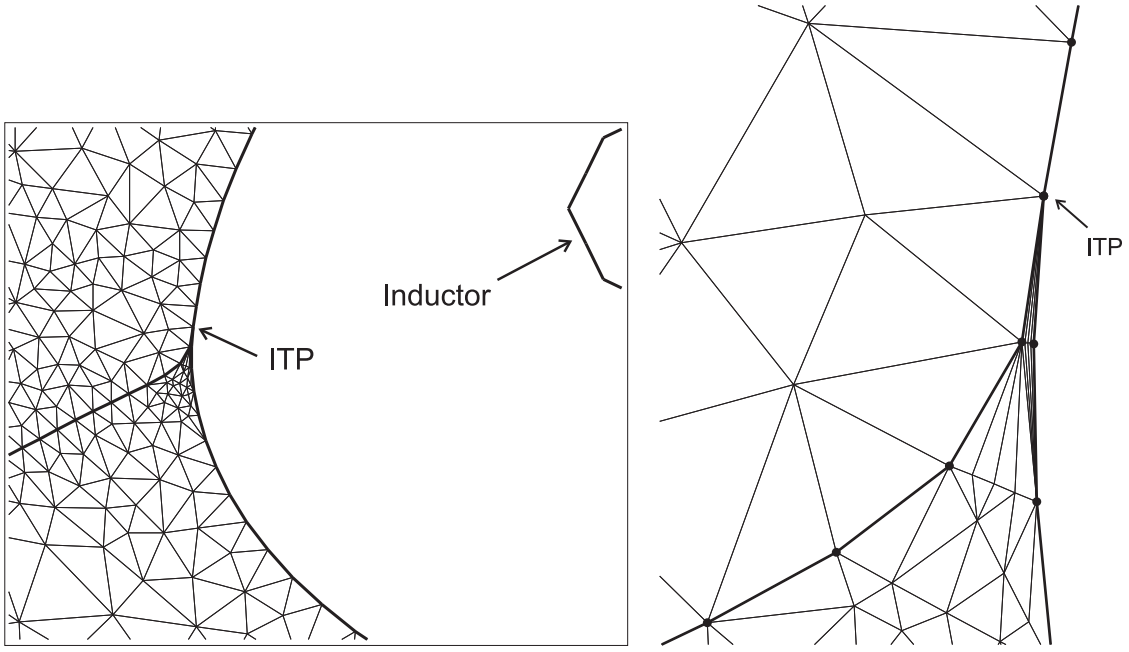

(a) (b)

Figure 5.4: The inner triple point and its triangulated vicinity in the melt and feed rod.

5.2 Numerical study without melt flow

In this section, we use `FZONE` to study numerically the qualitative and quantitative relationships between the various growth process characteristics as well as explore the limits of the process parameters allowing the existence of a steady-state floating zone. The existence of the floating zone is considered with the focus on having a permanent liquid bridge between the feed melting front and the crystallization front. It is ensured by a sufficient melting of the feed rod, especially of the central part of it, and by avoiding a breakdown of the neck of the liquid zone, i.e., by the existence of a stationary free melt surface.

We neglect at this stage the convective heat transfer due to the melt motion in the molten zone and concentrate our attention on the other factors forming the zone shape. This approximation is justified by the existence of many flow structures of practical relevance (which can be created, e.g., by different ways of crystal rotation) that influence the phase boundaries negligibly. Consideration of the influence of flow on the zone shape and comparison with concrete measurement data is the subject of Section 5.3.

We consider 8 inch FZ silicon crystal growth. The reflector position as well as the main slit and the three additional slits of the HF inductor are considered like in Fig. 4.1. The most relevant process parameters for the reference configuration are listed in Table 5.2, for the rest of parameters see Section 5.1. The material properties of silicon used in the calculations were given in Section 3.1. The chosen growth system configuration is taken as the starting-point for the study of the influence of different modifications.

The steady-state phase boundaries, the temperature field and the lines of magnetic field of the high-frequency inductor for the reference configuration are shown in Fig. 5.5.

5.2.1 Zone height and inductor current

A significant FZ process parameter is the height of the zone, H_Z, i.e., the distance along the vertical between the edge of the feed rod and the exterior triple point (ETP), at which the exterior surface of the single crystal is adjoined by the free surface of the melt. In the example in Fig. 5.5, the zone height is $H_Z = 37$ mm. It is possible to adjust the zone height by changing the inductor power and keeping all other process parameters constant. That is illustrated in Fig. 5.6 showing the phase boundaries

Parameter	Symbol	Value
Inductor current	I	1510 A
EM frequency	f	2.8 MHz
Needle-eye hole radius of inductor	R_{H}	16.5 mm
Length of the additional slits	L_{slit}	36 mm
Radius of the additional slits	R_{slit}	52.5 mm
		$= R_{\mathrm{H}} + L_{\mathrm{slit}}$
Single crystal radius	R_{Cr}	102.0 mm
Feed rod radius	R_{F}	77.5 mm
Single crystal pull rate	V_{Cr}	1.80 mm/min
Feed rod push rate	V_{F}	3.12 mm/min

Table 5.2: Parameters of the chosen reference configuration (some other model parameters see also in Section 5.1).

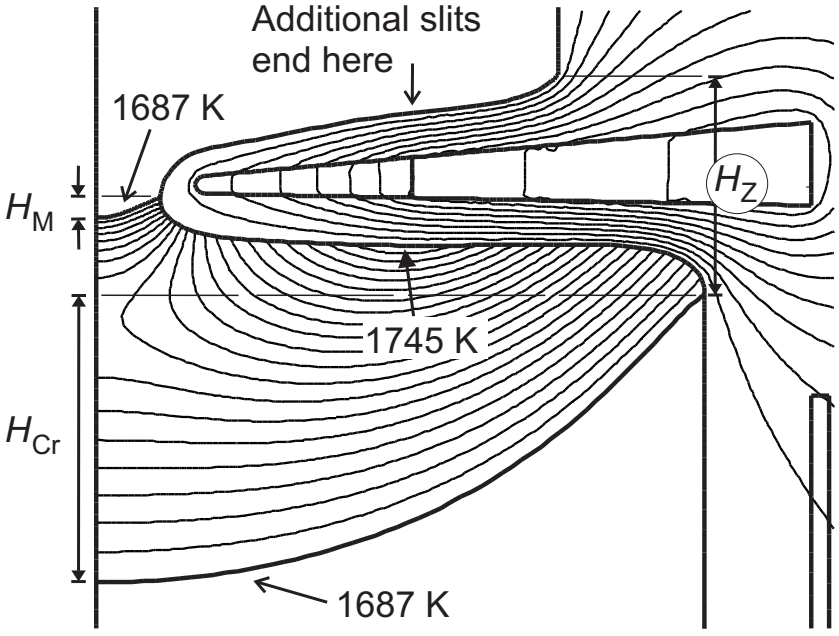

Figure 5.5: The temperature isolines in the melt ($\Delta T = 58$ K) and the magnetic field lines for the reference configuration. The zone height $H_{\mathrm{Z}} = 37$ mm, the crystallization interface deflection $H_{\mathrm{Cr}} = 48$ mm and the melting interface deflection $H_{\mathrm{M}} = 4$ mm.

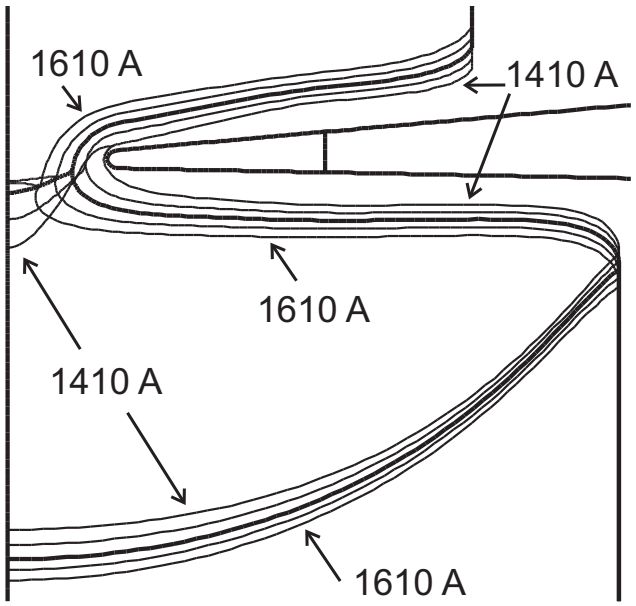

Figure 5.6: Phase boundaries with different zone heights corresponding to inductor current values from 1410 till 1610 A with step 50 A. The thick phase boundary lines correspond to the reference case with 1510 A and $H_{\mathrm{Z}} = 37$ mm.

calculated for different inductor current values. The reference case with the current 1510 A and zone height 37 mm is shown with a thick line. The inductor current has been changed up to 1610 A and down to 1410 A, i.e., only ± 100 A or $\pm 7\%$ of the reference current value. On both ends of the change area, the further change was limited by physical reasons. So a further lifting of the current above 1610 A (say to 1660 A) leads to a cutting of the liquid zone neck. The disconnection of the upper and lower part of the growth system prohibits a stable growth process. On the other hand, if the inductor current falls below 1410 A, then the distance of the inductor to the open melting front and meniscus becomes critical. This is seen also in Fig. 5.7. The zone neck radius R_{N} of the liquid floating zone approaches the inductor hole radius R_{H} as the current value diminishes. The other curve on Fig. 5.7 shows the zone height as a function of the inductor current I. The curve $H_{\mathrm{Z}}(I)$ is linear and it is explained by the relatively small change of I.

The calculated region around the inner triple point in three cases with very high values of I, implying large zone heights, is treated in more detail in Fig. 5.8. Despite the numerical algorithm of the triple point calculation, which smoothes the angle between the melting interface and open melting front, a sharp solid rim can be seen at ITP. Although these modelling limitations hinder obtaining a more precise picture of ITP, the calculation result agrees well with the tendency known in practice: uncontrolled

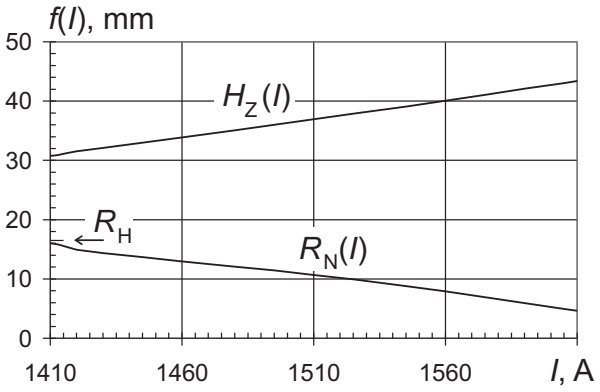

Figure 5.7: The zone height $H_\mathrm{Z}/\mathrm{mm} = 62.3 \cdot I/\mathrm{kA} + 56.9$ and the zone neck radius R_N as function of the inductor current I. The inductor hole radius R_H is shown too.

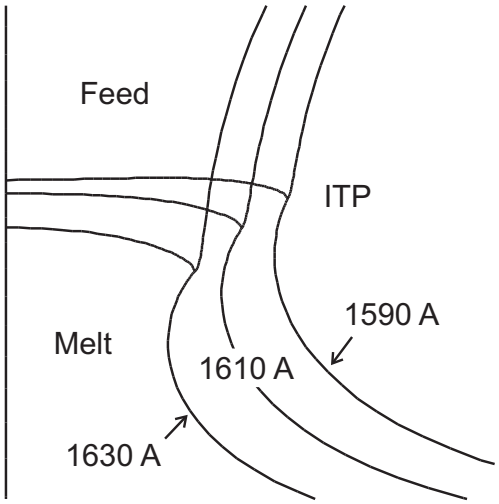

Figure 5.8: The calculated inner triple point in case of very high inductor current: $I =$ 1590 A, 1610 A, 1630 A.

growth of sharp pikes ("noses") occurs at ITP in case of the zone height being too large [87].

As discussed above, the change area of the inductor current allowing the existence of a steady-state floating zone constitutes only about ±7% of the absolute current value. Although the power supply from the vacuum tube HF generator to the inductor and the corresponding current value can be altered monotonically, e.g. with the power supply from DC circuit, the spatial distribution of the HF current density on the surfaces of current suppliers and other parts of the oscillation circuit makes it difficult in praxis to measure the absolute value of the HF electric current precisely enough concerning that high growth system sensibility. Hence it is reasonable to use the zone

height H_Z as the control parameter of the process by relative changing of inductor current to meet the target value of H_Z. In the following numerical studies, we adjust appropriately the inductor current I to keep the zone height constantly at 37 mm.

5.2.2 Reflector

A side reflector (see the example in Fig. 4.1) is used in praxis to reduce the temperature gradient and thermal stress in the crystal where high temperature differences arise, particularly due to the large diameter of the crystal. In our calculation model, we assume the silver reflector being slitted to avoid eddy currents, hence the magnetic field lines are freely crossing the reflector as shown in Fig. 5.5. The comparison of the phase boundaries with and without reflector is given in Fig. 5.9. The case with reflector positioned low is the reference configuration as shown in Figs. 4.1 and 5.5 with inductor current 1510 A. In case with reflector positioned high, the reflector has been shifted upwards so that the top edge of the reflector is approximately at the height of the exterior triple point (ETP). In this case the inductor current is only 1460 A. Without any reflector a much higher current (1600 A) is necessary in order to maintain the same zone height. It is explained by the action of the reflector as a passive heater. Another effect of the reflector is seen on the temperature field in the crystal center where the heat flux from the crystallization interface has to find a long way down to the lower edge of the reflector in order to radiate away through the free end of the mono-crystalline ingot. Hence the presence of a reflector reduces not only the radial- but also the axial gradient of temperature in the crystal. Consequently, the deflection of the crystallization front, H_{Cr}, becomes larger to ensure the balance of heat fluxes at the phase interface. The calculation shows that without reflector the axial temperature gradient on the crystal axis near the phase boundary is about 8.7 K/mm whereas with the low reflector, 7.3 K/mm only. Obviously the change in the temperature gradient has not been fully compensated by the deflection of the crystallization interface, because the lowering of the inductor power to preserve the zone height diminishes the necessary augmentation of the crystallization interface deflection by reducing the heat flux from the melt. Indeed, the axial temperature gradient in the melt center near the phase boundary is about 1.0 K/mm and 0.56 K/mm without reflector and with the low reflector, respectively. The maximum temperature difference in the melt is reduced from 71 K (without reflector) to 58 K (with the low reflector) or even to 45 K (with the high reflector). Also the increase in the deflection of the melting interface,

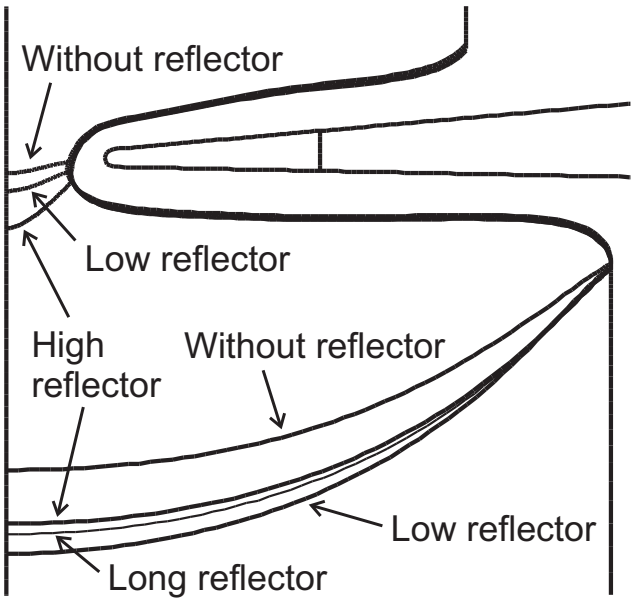

Figure 5.9: Phase boundaries with the reflector positioned low or high, without the reflector or with a prolonged reflector.

Reflector	I, A	ΔT, K	H_{Cr}, mm	H_{M}, mm
no	1600	71	35	2.2
low	1510	58	48	3.8
long	1460	45	45	8.6
high	1460	45	43	8.9

Table 5.3: Different reflectors ($H_{\mathrm{Z}} = 37$ mm).

H_{M}, is explained by the reduction of the inductor power when applying a reflector.

Beside the low and high reflectors, a third example considered in Fig. 5.9 is a prolonged reflector whose top edge coincides to that of the high reflector while the lower edge, to that of the low reflector. Since the local action of the long reflector in the vicinity of ETP is similar to that of the high reflector, the inductor power and the melting interface are not changed significantly by replacing the high reflector by the long one. The crystallization front, however, gets deflected slightly more than with the shorter reflector (see Fig. 5.9). Hereby we see the pure effect of the reflector's lower edge height, without change of the inductor power.

The calculation results with different reflectors are summarized in Table 5.3: ΔT stands for the maximum temperature difference in the melt, H_{Cr}, for the crystallization interface deflection and H_{M}, for the melting interface deflection (as defined in Fig. 5.5).

5.2.3 Pull rate

The pull rate of crystal is one of the most important FZ process parameters. During the study of the zone shape at different growth rates the feed push rate was adjusted to satisfy the steady-state FZ process condition:

$$V_{\mathrm{F}} R_{\mathrm{F}}^2 = V_{\mathrm{Cr}} R_{\mathrm{Cr}}^2. \tag{5.1}$$

The phase boundaries corresponding to the reference case with $V_{\mathrm{Cr}} = 1.8$ mm/min are shown with the thick line in Fig. 5.10, the other lines correspond to different growth rates. Table 5.4 shows the change of some parameters including the floating zone neck radius, R_{N}, and the height of the free bulk liquid surface, H_{L}, which is defined as the vertical distance between ETP and ITP. The inner triple point, which delimits the melting interface from the open melting front, has no exactly defined location in frame of the fluid film model and the values of H_{L} have an accuracy threshold below 0.5 mm. Since H_{L} depends strongly on the free surface angle at ITP, we also use another characteristic quantity, the height of the zone neck, H_{N}, which is defined as the vertical distance between ETP and the zone neck's thinnest place, where the free surface is vertical. H_{N} is dependent on the physical properties of the melt as well as on the crystal size and neck radius determined by the inductor and feed.

The smaller the pull rate, the smaller the deflection of the crystallization front and the higher the position of the melting interface. There exists a lower limit between 0.6 and 0.8 mm/min below which no steady-state floating zone for the considered 8 inch process with the fixed zone height is possible. At that small pull rates, the melting front stays above the inner edge of the inductor and enlarges the height of the free bulk liquid surface, H_{L}. If a critical value of H_{L} (slightly above 18.5 mm) is exceeded, the zone neck collapses due to the effect of surface tension. Nevertheless, the lower limit of the pull rate depends substantially on the inductor and zone height. For example, a stable free melt surface at a pull rate of only 0.1 mm/min can be made possible, according to calculations, by means of enlarging the inductor hole diameter by 20 mm and reducing the zone height to 33 mm, which helps to diminish the increase in H_{L}. Although H_{L} reaches 19.5 mm (and H_{N} reaches 16.5 mm) in that case, the free melt surface stays stable due to a large neck radius (R_{N} exceeding 22 mm), which heightens considerably the critical value of H_{L}.

With high pull rates, the deflection of both the crystallization and melting interfaces increases. Especially the melting interface becomes steep. Despite the shape of the

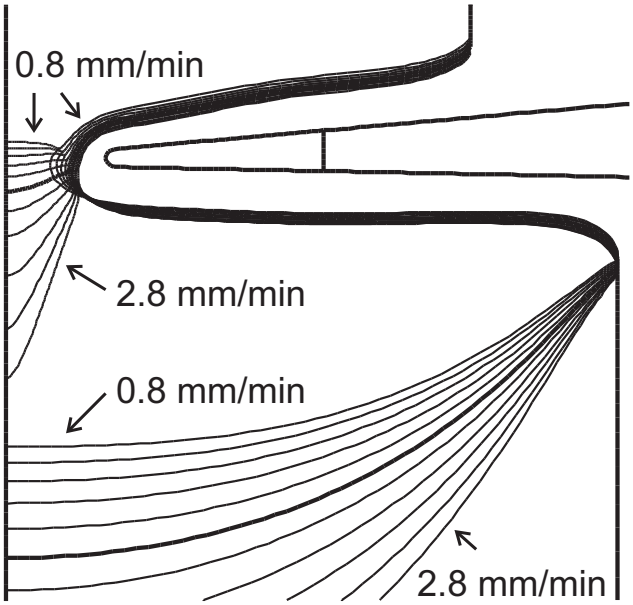

Figure 5.10: Phase boundaries at different crystal pull rates from 0.8 till 2.8 mm/min with step of 0.2 mm/min.

$V_{\mathrm{Cr}}\,(V_{\mathrm{F}})$, $\frac{\mathrm{mm}}{\mathrm{min}}$	I, A	ΔT, K	H_{Cr}, mm	H_{M}, mm	R_{N}, mm	$H_{\mathrm{L}}\,(H_{\mathrm{N}})$, mm
0.8 (1.39)	1510	80	31	-1.1	7.3	18.5 (15.9)
1.2 (2.08)	1510	71	36	0.2	9.2	18.1 (16.0)
1.6 (2.77)	1510	62	44	2.1	10.3	17.1 (16.1)
1.8 (3.12)	1510	58	48	3.8	10.7	16.6 (16.1)
2.0 (3.46)	1510	54	54	6.3	11.0	16.1 (16.1)
2.4 (4.16)	1515	46	67	15	11.5	16.2 (16.2)
2.8 (4.85)	1525	40	84	33	11.9	15.9 (15.9)

Table 5.4: Different crystal pull rates ($H_{\mathrm{Z}} = 37$ mm).

melting interface, the distance between the deepest point of the melting interface and that of the crystallization interface is increasing with pull rate, in the considered area of pull rates. Apart from the practical issues leading to crystal dislocation and cracking if grown at too high speed with too steep crystallization front (as happens already above 2 mm/min), the limiting factor would be here the approaching of the open melting front to the inductor, which does not melt the feed rod fast enough if the zone height is fixed (see Fig. 5.10 showing the distance between the feed rod and inductor decreasing with growth rate). The problem could be overcome by heightening the inductor power and zone height appropriately. Another and unavoidable upper limit of the pull rate is set by the total ability of the crystal surface to radiate the heat away. The maximum growth rate can be achieved and the maximum heat can be emitted by the solid crystal surface at the melting point temperature, i.e., when the crystallization interface nearly coincides with the exterior surface of the crystal (a thin "nutshell" of crystal is left over).

It is interesting that the zone height stays practically constant when reducing the pull rate (and the feed push rate) at a constant inductor power. Hence the calculations with fixed zone height for the pull rates about and below 2 mm/min correspond to the inductor current 1510 A (see Table 5.4). At higher pull rates, a slightly heightened inductor power was necessary, e.g., the case of 2.8 mm/min corresponds to $I = 1525$ A.

5.2.4 Single crystal diameter

FZ process development toward a larger single crystal size usually requires serious modifications of the whole growth system including the HF inductor. Nevertheless, for the purpose of illustration, we can consider here the zone shape with different crystal diameters from 4 to 8 inches by keeping the inductor, the zone height and the pull rate of the 8 inch process configuration. The reflector is removed to avoid interference of different effects. We change the feed push rate, to satisfy the condition (5.1), as well as the inductor power, to fuse the feed at the respective rate and keep the zone height constant.

As seen in Fig. 5.11, the deflection of the crystallization interface is changing most dramatically. The untypical convex crystallization front about the center of the 4 inch zone is explained by the effect of the relatively long additional slits of the actual inductor reducing the ratio of the heat supply in the central part to the heat supply in

R_{Cr}, mm	V_F, $\frac{mm}{min}$	I, A	ΔT, K	H_{Cr}, mm	R_N, mm	H_L (H_N), mm
51	0.78	1060	26	0	9.0	17.6 (16.7)
76	1.73	1305	44	13	9.8	17.2 (16.3)
102	3.12	1600	71	35	10.3	17.5 (16.1)

Table 5.5: Different single crystal sizes ($V_{Cr} = 1.8$ mm/min, $H_Z = 37$ mm, no reflector).

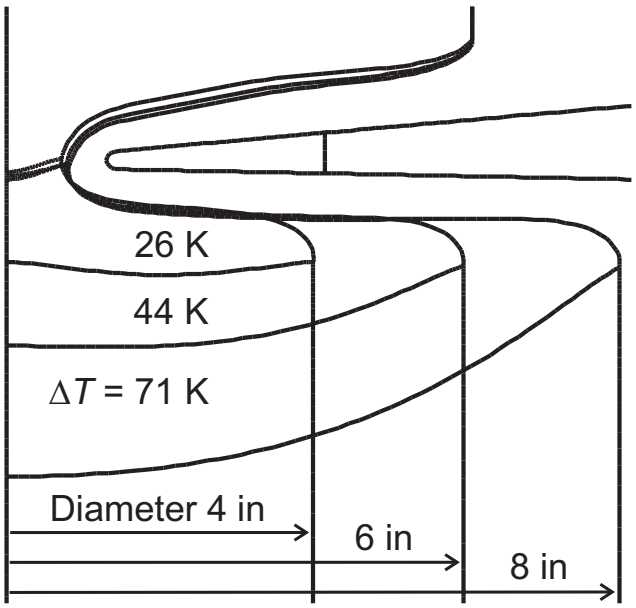

Figure 5.11: Phase boundaries and the maximum temperature difference ΔT in the melt for FZ processes with different crystal diameters (in all cases the zone height is 37 mm, the inductor is the same and no reflector is applied).

the periphery of the molten zone. Beside the deflection of the crystallization front, as a consequence also the maximum temperature difference in the melt, ΔT, increases rapidly with crystal diameter: the heat flux from the free melt surface has to be conducted through a larger molten zone. Table 5.5 summarizes some calculation results obtained with different crystal radii, R_{Cr}, including the total height of the free melt surface, H_L, and the height of the zone neck relative to ETP, H_N, as defined previously. We see that H_N, which was practically independent on the pull rate (see back Table 5.4), decreases monotonically with crystal radius, whereas H_L changes in a more complicated way and is, for 8 inch zone, higher than in the case with reflector. The value of H_L stays however always (according to Tables 5.4 and 5.5) below the Heywang limit for crystal and feed of strongly different diameters (see Section 2.2).

R_F, mm	V_F, $\frac{mm}{min}$	I, A	ΔT, K	H_M, mm
93.0	2.17	1580	58	1.4
77.5	3.12	1510	58	3.8
62.0	4.87	1440	58	12
46.5	8.66	1395	56	39

Table 5.6: Different feed rod sizes ($H_Z = 37$ mm, $V_{Cr} = 1.8$ mm/min).

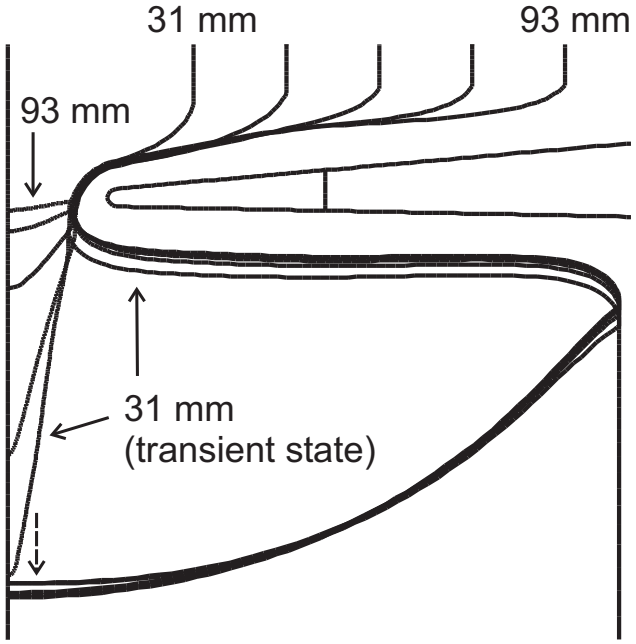

Figure 5.12: Phase boundaries with feed rod radii form 93 mm till 31 mm. No stationary melting interface is possible with a feed rod radius of only 31 mm.

5.2.5 Feed rod diameter

The size of the feed rod enters the relation (5.1) and determines the feed supply speed needed to grow the fixed-diameter single crystal with a given pull rate. In Fig. 5.12, a series of calculation results with different poly silicon rods is shown. The feed diameter has been changed from 186 mm down to 62 mm with a step of 31 mm. The pull rate $V_{Cr} = 1.8$ mm/min is kept unchanged. The smaller the feed rod diameter, the larger the feed push rate V_F and the deeper the melting interface deflection (see also Table 5.6). It is seen that a too small feed rod size makes the steady state growth impossible and a solid bridge is built between the feed and the grown crystal. The reason is the high (about 19.5 mm/min for $R_F = 31$ mm) supply rate of the feed, which can not be fused fast enough in the central part.

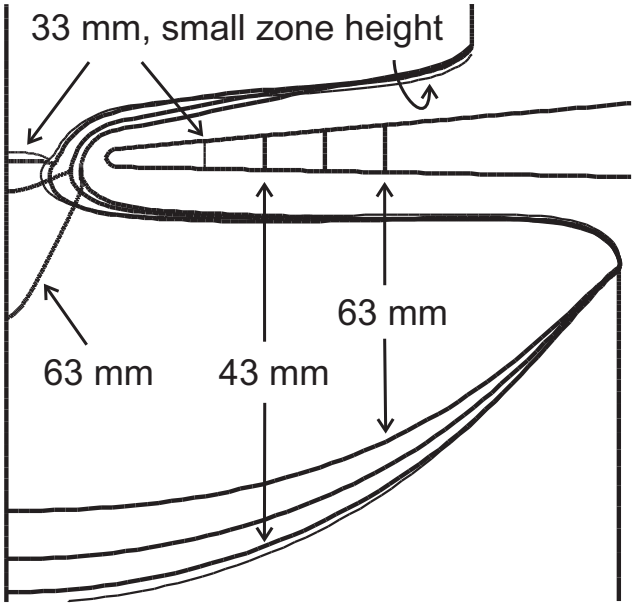

Figure 5.13: Phase boundaries obtained with varied length of the additional slits: $R_{\mathrm{slit}} = 62.5; 52.5; 42.5$ mm ($H_{\mathrm{Z}} = 37$ mm) and $R_{\mathrm{slit}} = 32.5$ mm ($H_{\mathrm{Z}} = 35$ mm).

R_{H}, mm	L_{slit}, mm	R_{slit}, mm $= R_{\mathrm{H}} + L_{\mathrm{slit}}$	I, A	ΔT, K	H_{Cr}, mm	H_{M}, mm	R_{N}, mm
16.5	26	42.5	1600	73	53.7	-0.4	7.1
16.5	36	52.5	1510	58	48.4	3.8	10.7
16.5	46	62.5	1435	46	40.3	25	12.3

Table 5.7: Different inductor slit lengths ($H_{\mathrm{Z}} = 37$ mm).

The upper limit of the feed rod diameter is determined by the ability of the inductor to ensure a sufficient slope everywhere at the open melting front so that the melt flows constantly to the center and no accumulation and dropping of the melt occurs.

5.2.6 Inductor modifications

The dimensions and shape of the inductor have a crucial role in the performance of the FZ growth process. Here we consider the effect of the inductor hole size and the length of the additional slits. Both the increase of the inductor hole and the lengthening of the slits reduce the induced power around the central part and shift the power maximum on the free melt surface further outwards.

The phase boundaries shown in Fig. 5.13 demonstrate the effect of varied length of

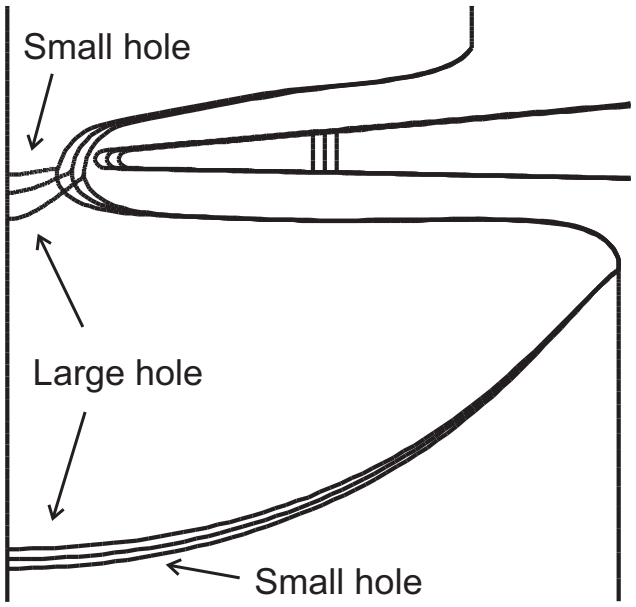

Figure 5.14: Phase boundaries obtained with varied radius of the hole of inductor: $R_{\mathrm{H}} = 14.0; 16.5; 19.0$ mm. To simplify the figure, the case $R_{\mathrm{H}} = 21.5$ mm of Table 5.8 is not shown here.

R_{H}, mm	L_{slit}, mm	R_{slit}, mm $= R_{\mathrm{H}} + L_{\mathrm{slit}}$	I, A	ΔT, K	H_{Cr}, mm	H_{M}, mm	R_{N}, mm
14.0	36	50.0	1560	63	50.4	0.8	7.6
16.5	36	52.5	1510	58	48.4	3.8	10.7
19.0	36	55.0	1465	54	46.0	9.2	13.3
21.5	36	57.5	1420	50	42.9	22	15.9

Table 5.8: Different inductor hole sizes ($H_{\mathrm{Z}} = 37$ mm).

the additional slits (see also Table 5.7). The slit length is reduced from $L_{\mathrm{slit}} = 36$ mm, which is the reference configuration ($R_{\mathrm{slit}} \approx 53$ mm), to $L_{\mathrm{slit}} = 26$ mm ($R_{\mathrm{slit}} \approx 43$ mm) and a steady-state solution is obtained. Another reduction of the slit length by 10 mm leads to cutting of the zone neck at the defined zone height of 37 mm. It is, however, possible to obtain a steady-state zone with that short slits at a smaller zone height of 35 mm (see the thin phase boundary lines in Fig. 5.13). It is theoretically possible to remove the additional slits at all and to compensate the decrease of the zone neck radius by a further reduction of the zone height (cf. Fig. 5.6) but it leads to a substantial change of the open front's slope, which may cause dropping of the liquid onto the inductor from the insufficiently sloped surface.

Increasing the length of the additional slits till $L_{\text{slit}} = 46$ mm ($R_{\text{slit}} \approx 63$ mm) leads to a strongly deflected melting interface as well as reduced crystallization interface deflection, due to the reduced inductor power. A further increase of the slit length by 10 mm does not yield any stationary solution, as the melting front meets the crystallization front.

Another possibility to change the power distribution and the neck radius considerably is the variation of the inductor hole size (see Fig. 5.14 and Table 5.8), which, however, does not impact remarkably the open melting front, excepting the neck region. The length of the additional slits has been left unchanged. Like in case of the slit length variation, the lower and upper limits of the inductor hole size are determined by cutting of the zone neck and the melting interface deflection, respectively. That demonstrates the necessity for a needle-eye inductor.

5.2.7 Frequency

According to the equations (3.1) and (3.14), the EM field frequency f influences directly the integral surface density of the induced power:

$$q^{\text{EM}} \propto \sqrt{\frac{f}{\sigma}}\, i_{\text{ef}}^2, \tag{5.2}$$

where σ is the electrical conductivity of the solid or liquid silicon and i_{ef}, the local effective surface current, which depends on the inductor current I. Hence increasing f results in higher q^{EM} if not compensated by a reduction of I. A more complicated effect of the frequency takes place at the open melting front, which is covered, according to the assumed model, by a thin fluid film. The higher the frequency, the larger the part of the electric current induced inside the liquid film. Due to the different electrical conductivities of the liquid and solid silicon, the total heat amount depends on the ratio of the fluid film thickness and the EM skin layer depth. These effects are taken into account in the mathematical model and produce the results illustrated in Fig. 5.15 where the phase boundaries corresponding to the reference frequency and a 4 times higher frequency are shown. In order to keep the zone height unchanged, the inductor current is reduced from 1510 A in the reference case to 1160 A in the high-frequency case. We see that due to the change of the placement of the open melting front and the subsequent redistribution of the surface currents i_{ef}^2, the necessary decrease of the inductor current I could not be estimated precisely enough by the expression (5.2).

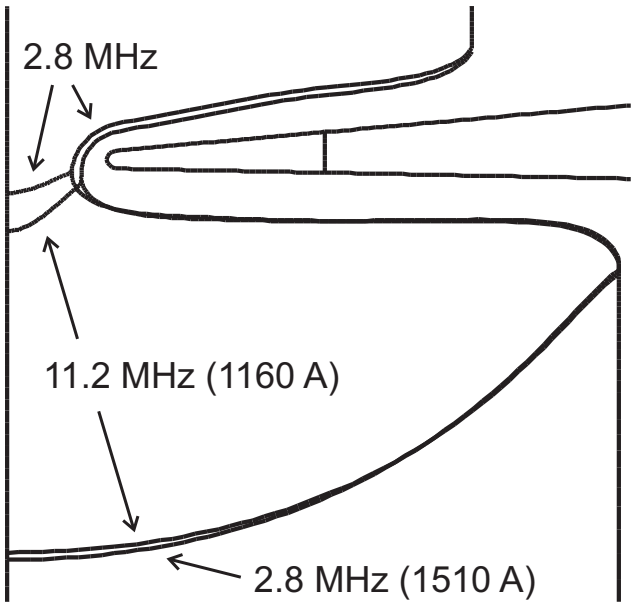

Figure 5.15: Influence of a 4 times higher EM frequency on the phase boundaries.

If not counting the strong changes in the inductor current, the influence of the EM frequency on the phase boundaries is weak and the frequency change considered in Fig. 5.15 has been chosen very large in order to see that influence good enough. For real FZ growth, however, the frequency might not be changed in a so wide range without disturbing the process performance. A high frequency necessitates a high voltage at the inductor and increases the risk of arcing with subsequent EM field breakdown. On the other hand, the frequency must stay high enough to ensure a small field penetration depth into silicon (i.e., the skin effect) and consequently a stable melting of the feed rod. A too low frequency leads to heat generation deep in the solid, leaving the surface cold and deteriorating the melting process.

5.3 Influence of melt flow and its verification

The above study in Section 5.2 was performed without taking into account the melt flow. This was justified by the wish to focus attention on the pure effect of other parameters, whereas the effect of melt flow can vary depending on the rotation of the crystal, which would make due to the additional degrees of freedom (the art of crystal rotation) the above parameter study too immense and resources consuming. In some cases, it can even be justified to neglect the effect of melt flow at all (e.g., it was stated in [45] that the melt flow has only little influence on the phase boundaries). The present axisymmetric flow calculations with `FZONE` show, however, that the flow can

Figure 5.16: The photo-scanning resistivity measurement in the vertical cross-section of an 8 inch FZ crystal (Siltronic AG) has been performed at the Institute of Crystal Growth [88].

also have a significant influence on the phase boundaries, particularly on the shape of the crystallization front, which is characterized, for simplicity, by its deflection H_C.

The melt flow effect is illustrated here for two cases, in which the calculations without hydrodynamics yield a crystallization interface deflection significantly different from the measured one, and for one case where the hydrodynamic influence is small. The respective interface forms have been determined from the photo-scanning resistivity measurements in the vertical cross-section of the grown crystal [88].

5.3.1 FZ 8 inch process

The first example is an 8 inch floating zone. The measured (see Fig. 5.16) deflection of the crystallization interface is about 44 mm, whereas the calculation without account of hydrodynamics yields a deflection of about 50 mm. Hence the flow calculation was used to explain the difference. The flow showed a time-dependent character, see Fig. 5.17 for the fluctuations of the maximum and minimum values of the stream function, characterizing the intensity of the flow vortices in one or the opposite direction, respectively, and the maximum of the melt temperature. Due to the mixing of the fluid, the latter is significantly lower than the characteristic temperature maximum in calculation without hydrodynamics (see, e.g., the value of $\Delta T = 58$ K in Fig. 5.5).

As can be observed from the frames shown in Fig. 5.18, the time dependence of the distributions of the stream function and temperature is particularly strong in the peripheral part of the molten zone, i.e., in the region near the exterior triple point,

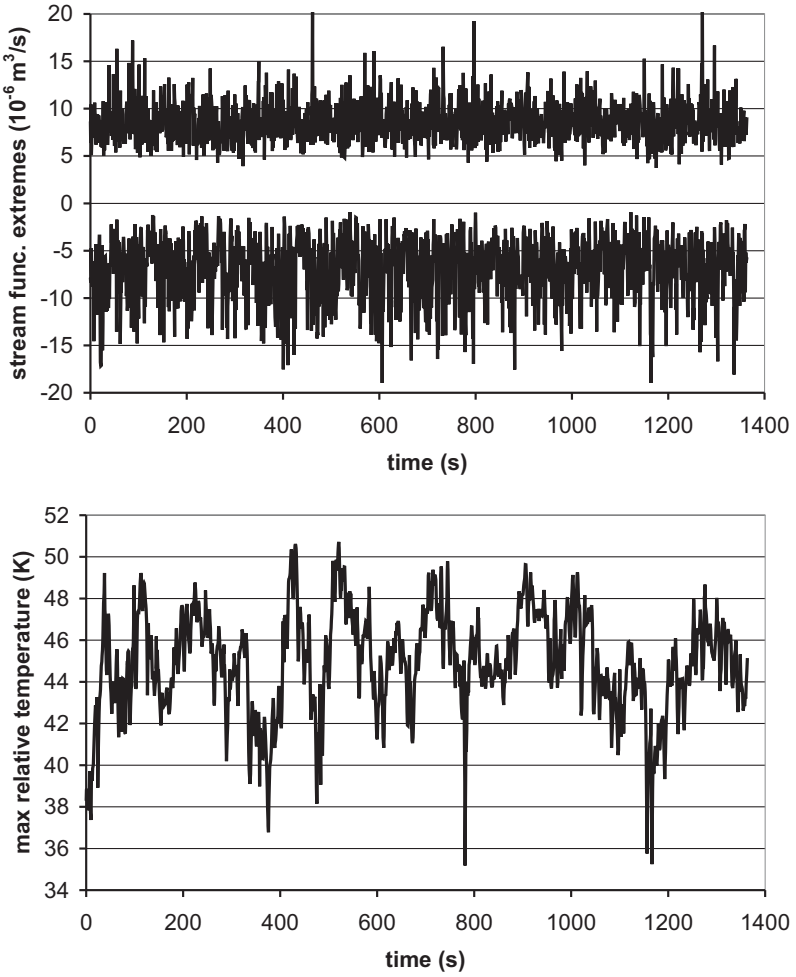

Figure 5.17: The calculated fluctuations of the maximum and minimum values of the stream function (the upper figure) and the maximum of melt temperature relative to the melting point, ΔT (the lower figure).

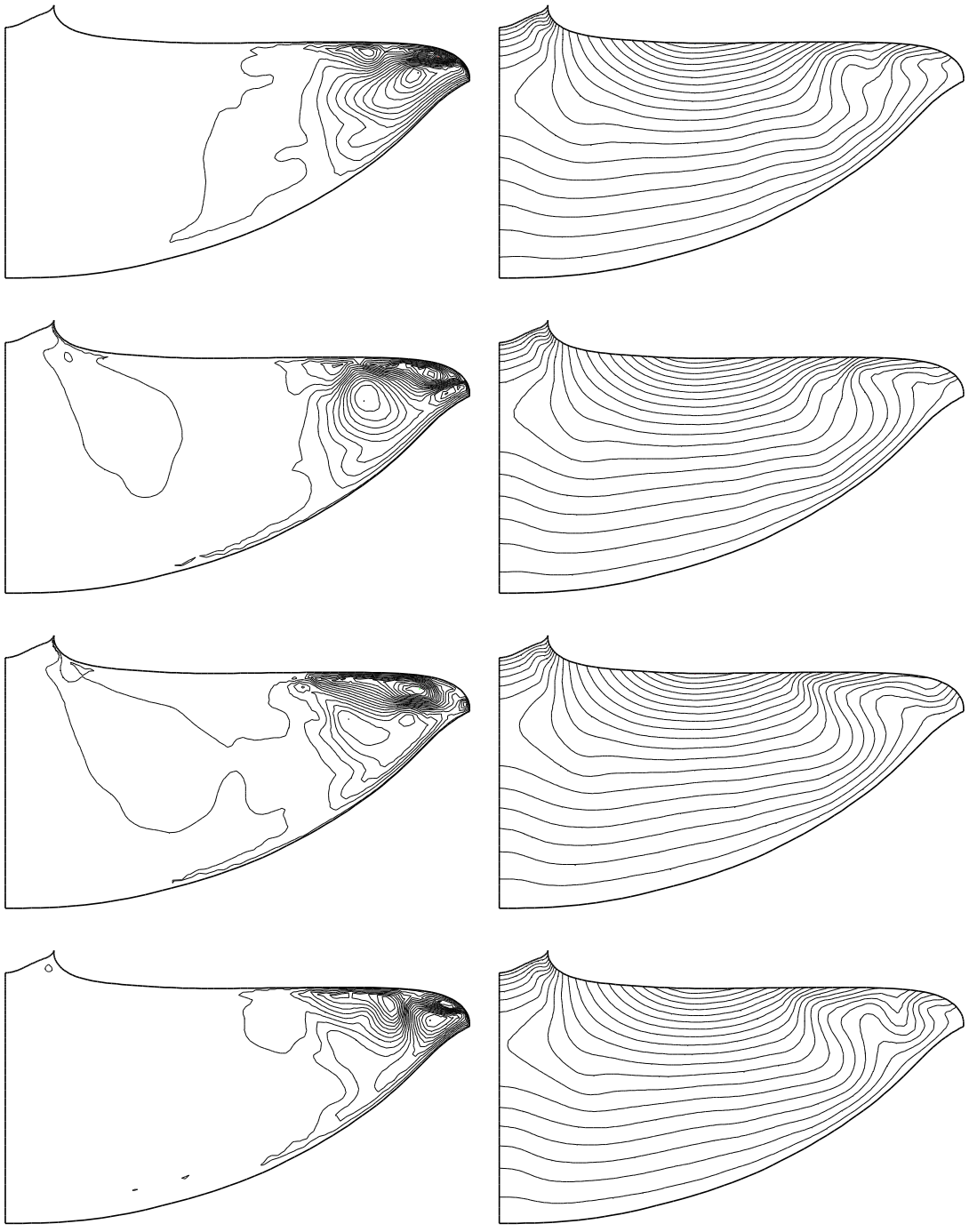

Figure 5.18: Isolines of the stream function (left) and temperature (right) in the melt in four successive time instants with interval of 0.5 s. (The transient flow calculation was performed with a much smaller time step of 2 ms.)

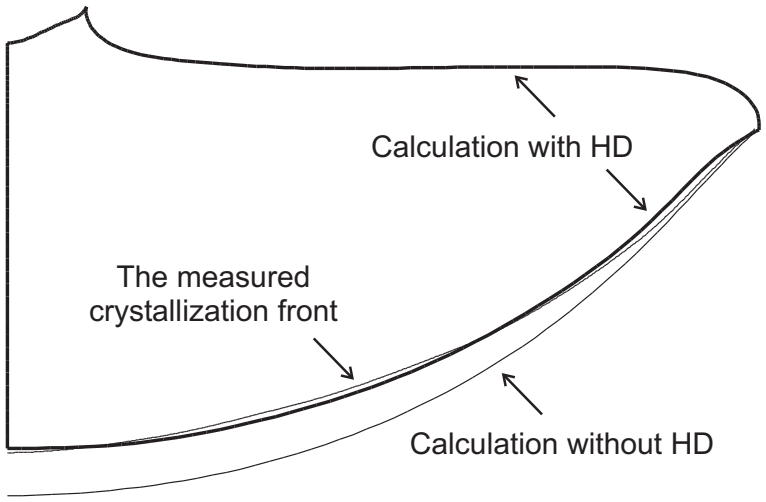

Figure 5.19: Comparison of the FZ 8 inch phase boundaries calculated with hydrodynamics (thick lines) to the measured crystallization interface (thin line) and to the calculated interface without taking into account the melt flow (the thin line with larger deflection).

where the Marangoni force tries to build a vortex with a movement towards ETP along the free melt surface, whereas the electromagnetic force acts in the opposite direction. This unstable vortex structure in the peripheral part of the zone has an influence on the deflection of the crystallization interface, which consequently shows a fluctuating character too. Since the melting/crystallization processes are relatively slow in comparison to the melt flow fluctuations, the changes of the front deflection take also relatively much time and long calculations of the time dependence of the flow are needed to bring the crystallization interface to a steady-state position[1], if started from a bad initial guess. In Fig. 5.20, calculations with 3 different initial guesses are considered: 40, 46 and 43 mm front deflection. It can be seen that in the first two cases the interface showed clear tendency to move to a larger or smaller deflection, respectively. Only for the third initial guess it stayed at the level slightly above 43 mm, which is hence the found value of the interface deflection under the influence of melt motion.

The picture showing the calculated zone shape and a comparison to the calculated interface without accounting melt hydrodynamics, as well as the curve of the interface drawn from the photo-scanning measurement is shown in Fig. 5.19.

[1] Steady-state position for the crystallization interface means that the fluctuations take place around a stable average shape. Ideal steady state, i.e., without fluctuations, is not possible if taking into account the time-dependent melt motion.

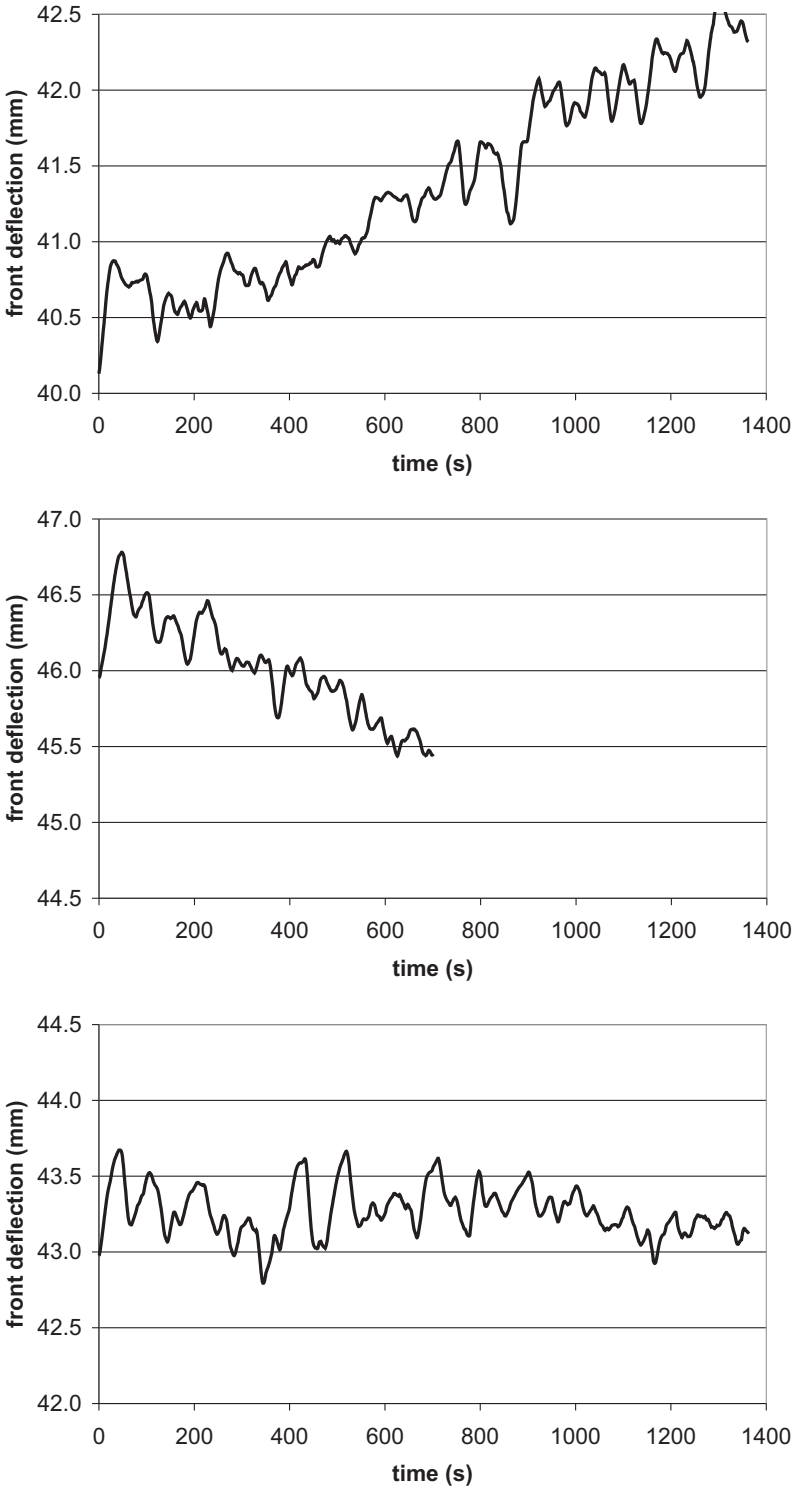

Figure 5.20: Calculation of the FZ 8 inch phase boundaries taking into account melt flow: convergence of the deflection of the crystallization interface to a steady-state value slightly above 43 mm.

Parameter	Symbol	Value
Zone height	H_{C}	22.7 mm
EM frequency	f	3 MHz
Needle-eye hole radius of inductor	R_{H}	15 mm
Single crystal radius	R_{Cr}	25 mm
Feed rod radius	R_{F}	25 mm
Single crystal pull rate	V_{Cr}	2.8 mm/min
Feed rod push rate	V_{F}	2.8 mm/min
Crystal rotation rate	Ω_{Cr}	6 rpm

Table 5.9: Parameters of the 2 inch process.

5.3.2 FZ 2 inch process

The second example is a 2 inch floating zone with inductor placed relatively close to the free melt surface (Fig. 5.21). The main process parameters are listed in Table 5.9. The measured deflection of the interface is about 7 mm [88], the calculation without hydrodynamics yields, however, a much smaller deflection of 1.8 mm. Like in case of the 8 inch example, this difference can be explained by the effect of the melt motion: the interface deflection fluctuates due to the unstable flow around 6–7 mm, depending on the calculation approach used (see Fig. 5.24). In the following we discuss it in more detail.

Due to the proximity of the inductor to the free melt surface, the EM forces in the melt create a very strong flow with a permanently changing pattern (see Fig. 5.25). With the Reynolds number of the flow sometimes exceeding 10000, the calculation by an axisymmetric model is not reliable, because the non-axisymmetric modes of the flow instability are not taken into account. Since the goal of the calculation was, however, just to demonstrate that the large difference between the thermal calculation without HD and the measured interface deflection can be explained by the effect of melt motion, the demands to DNS[2] were relaxed and the melt flow was calculated

[2] DNS stands for Direct Numerical Simulation, i.e., the direct calculation of turbulent flows by the Navier-Stokes equations. Differently from the turbulence modelling, where the mean-flow equations instead of the Navier-Stokes equations are solved, the DNS calculation has to be able to resolve all the scales of motion, hence the computational cost of such a calculation is immense (some estimations are given in [89]).

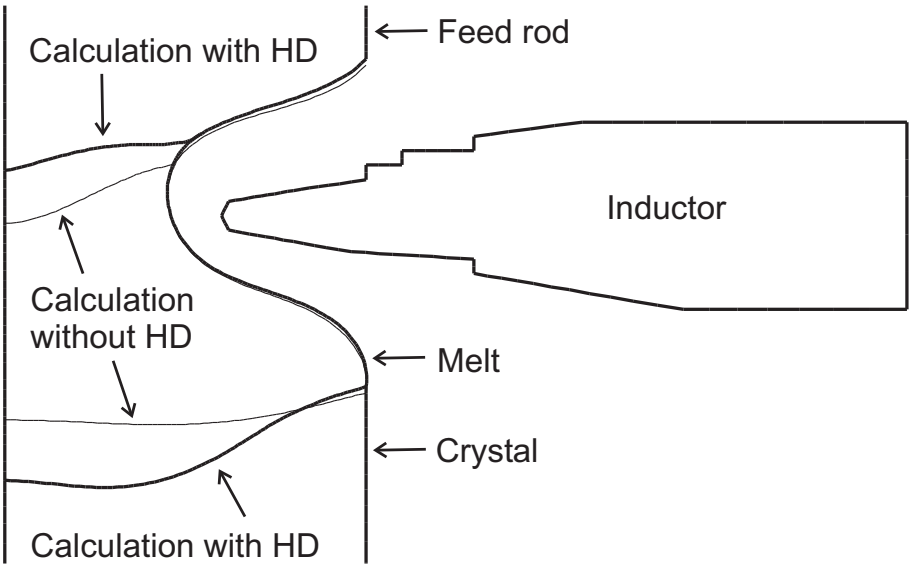

Figure 5.21: Comparison of the FZ 2 inch phase boundaries calculated with hydrodynamics (thick lines) to the calculated interface without taking into account the melt flow (thin lines).

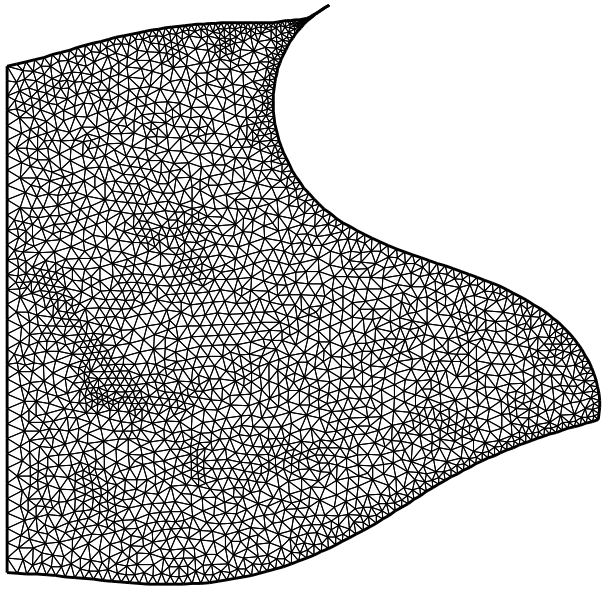

Figure 5.22: Finite element grid in the melt as used for the calculation of the 2 inch floating zone. Because the phase boundaries move, the grid is regenerated from time to time during the calculation.

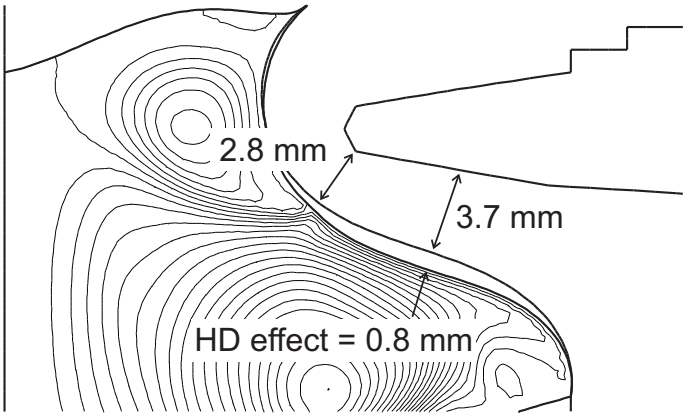

Figure 5.23: Example of the direct effect of HD on the free surface shape: due to instantaneous strong melt flow along the free surface, its distance to the inductor increases by up to 0.8 mm in comparison to a calculation without accounting for this effect.

with the axisymmetric solver of `FZONE` on the grid shown in Fig. 5.22 by using a time step of 2 ms.

First a calculation for 3900 seconds was done by starting from an initial guess of crystallization interface with deflection of 7 mm (i.e., the experimental value). This part of calculation is shown on the top graph in Fig. 5.24. It should be taken into account when interpreting these results that, as usually in FZ calculations, the zone height was kept constant by changing the inductor current. The targeting of the zone height was done by using the algorithm described in Sec. 4.8.3 (with the parameter $\Delta_{\min} I = 1$ A). The continuation of the calculations from $t = 3900$ s to 5600 s was done with different approaches as shown in the middle and bottom graphs of Fig. 5.24. So some calculations were made with keeping the inductor current constant at $I = 488.9$ A, which was the average value of the previous 3900 s (see the thin curves in the graphs).

Because of the strong flow in contrast to typical 4–8 inch floating zone processes, the 2 inch example was calculated by accounting for the direct effect of the melt flow on the shape of the free surface, which was considered in Sections 3.5 and 3.6. It was observed that although important at the time instants with strong flow along the free surface (see Fig. 5.23), this effect did change the average value of the interface deflection just slightly, as seen if comparing the curves in the middle graph to those in the bottom graph of Fig. 5.24, the latter having this effect turned off. These differences seem to be below the numerical level of accuracy of the calculations.

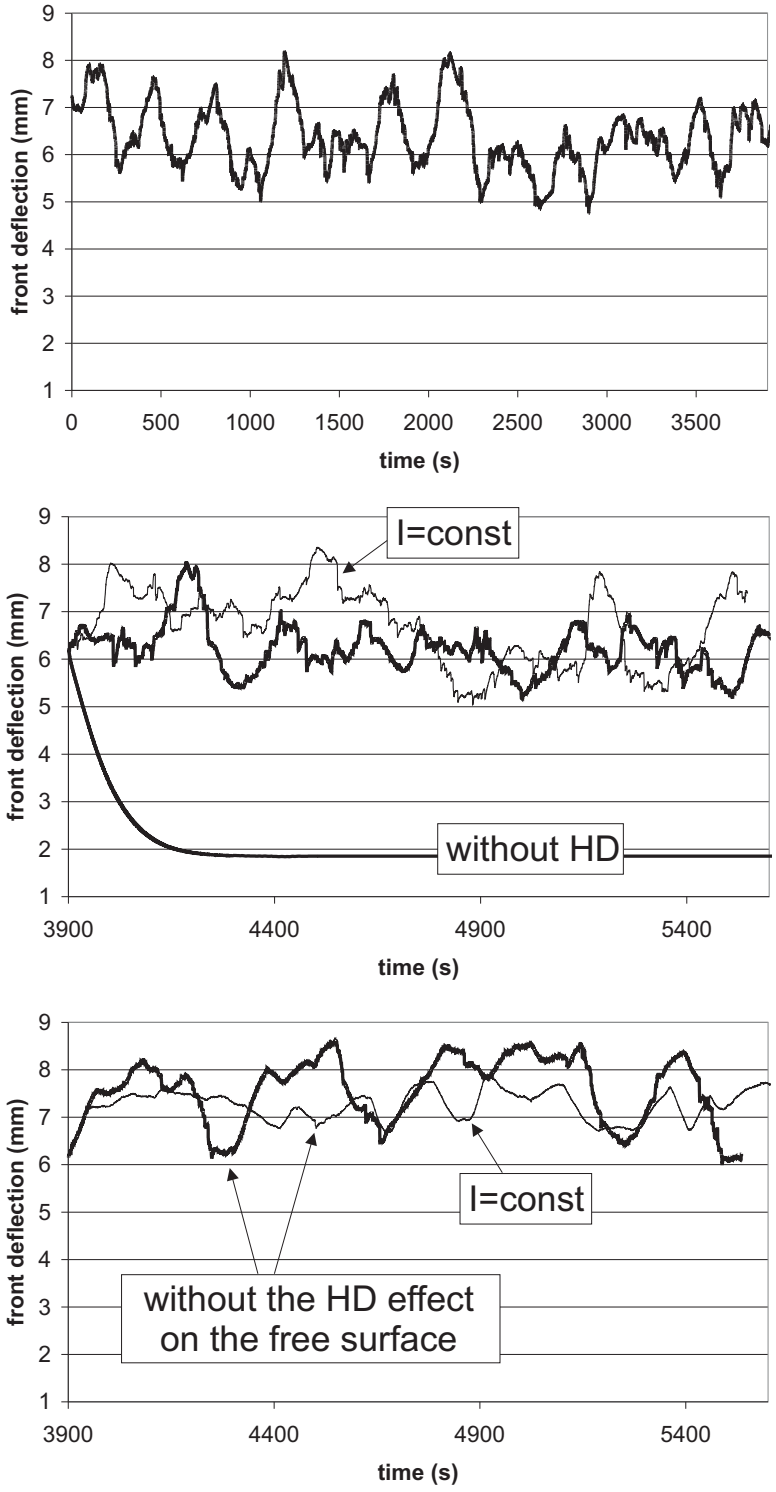

Figure 5.24: Calculation of the FZ 2 inch phase boundaries: fluctuation of the deflection of the crystallization interface about 7 or 6 mm with hydrodynamics (HD), and the convergence to 1.8 mm if HD is turned off.

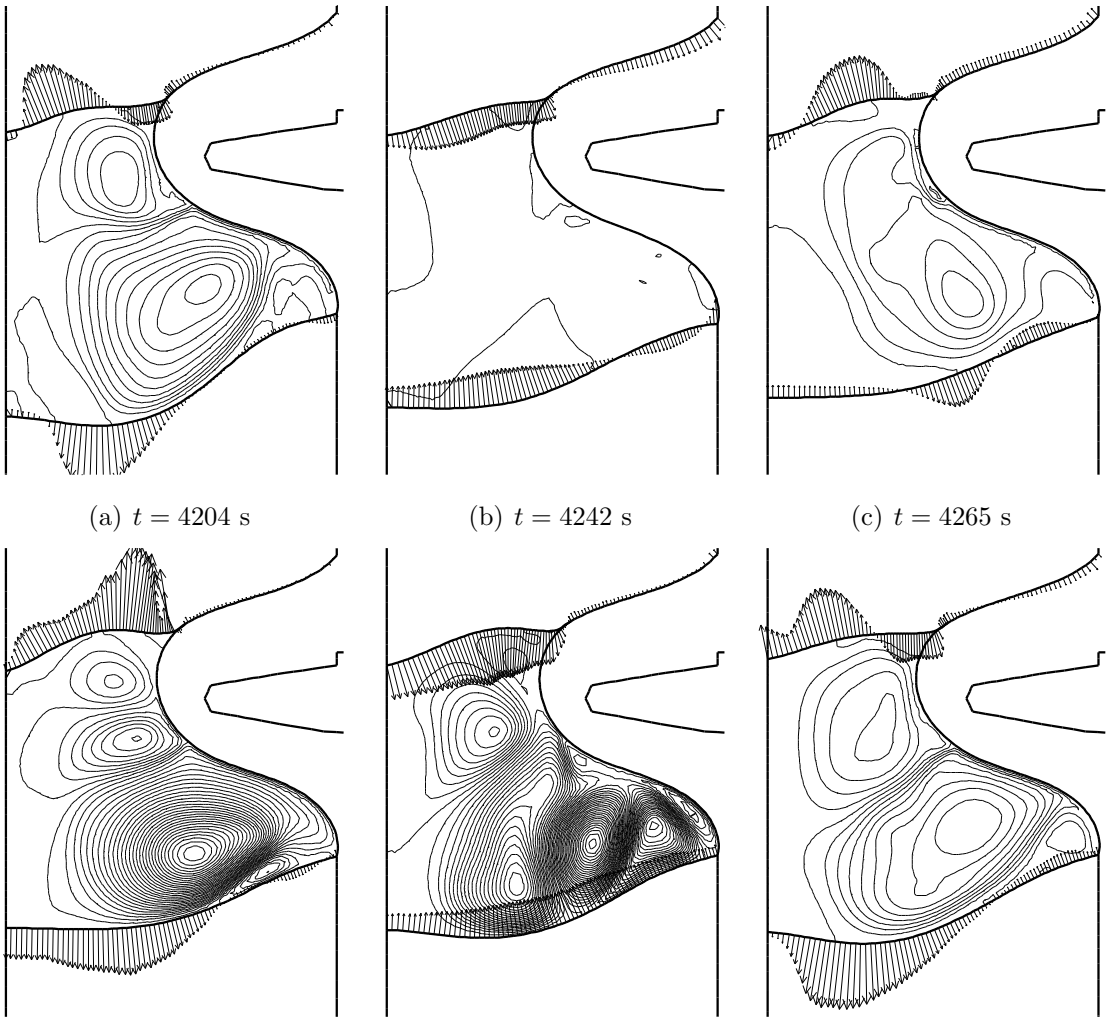

(a) $t = 4204$ s (b) $t = 4242$ s (c) $t = 4265$ s

(d) $t = 4304$ s (e) $t = 4350$ s (f) $t = 4375$ s

Figure 5.25: Some typical stream function pictures of the very dynamical melt flow in the calculated 2 inch floating zone. The arrows show the instantaneous moving velocities of the solid–liquid phase boundaries. For the time instants t, cf. Fig. 5.24.

The proper result of the 2 inch floating zone study is shown in the middle graph of Fig. 5.24: turning the hydrodynamics off lets the crystallization interface assume a flat form very far from the measured one, while the calculation with hydrodynamics shows fluctuations about a large value of deflection. Hence the measurement result with the surprisingly large deflection can be explained by the convective heat transport in the melt.

The convection effect reduced the maximum relative melt temperature from $\Delta T = 53$ K (without HD) to $\Delta T = 31$ K, i.e., by 22 K, which is more than in case of the 8 inch floating zone with only 13 K reduction.

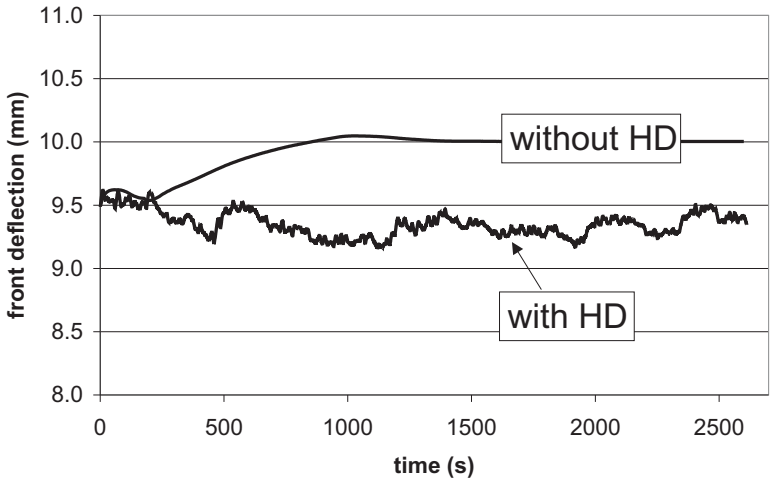

Figure 5.26: Calculation of the FZ 4 inch phase boundaries: fluctuation of the deflection of the crystallization interface about 9.3 mm with HD, and the convergence to 10.0 mm if HD is turned off. Both values agree well with the experimental value of ca. 10 mm. Both calculations have been started from an initial guess calculated without HD on a coarser grid.

5.3.3 FZ 4 inch process

Let us shortly mention another calculation example, a 4 inch floating zone process with pull rate 2.8 mm/min, where the influence of the melt flow did not bring much change in the thermal field: the convection effect reduced the maximum relative melt temperature from $\Delta T = 31$ K (without HD) to $\Delta T = 27$ K, i.e., by only 4 K. The corresponding changes of crystallization interface were negligible. As seen in Fig. 5.26, the difference between the interface deflections calculated with and without hydrodynamics is about 0.7 mm, which can be considered being below the level of achievable accuracy if accounting the approximations used in the calculation model, e.g., the axisymmetric approximation of the EM field of the slitted inductor, and if the calculation is not tuned by empirical parameters. Hence in this case, both calculations show a good agreement to the measured interface deflection, which was ca. 10 mm [88].

6 3D Melt flow and rotational striations

6.1 Introduction

The kind of axisymmetric modelling of floating zone growth like described in the previous chapter yields, typically, a good approximation for the shape of the phase boundaries that can be further used for the modelling of dopant incorporation or defect distribution in the grown crystal. There are numerous works by other authors (see Section 2.2) using the axisymmetric approximation for the dopant transport study in the floating zone, while the question about the influence of the three-dimensional effects even in an axisymmetric floating zone can be posed as well.

The needle-eye inductors for FZ processes are designed to stand strong electric currents at high frequencies, which implies a high voltage between the current suppliers and a danger of electrical breakdowns. Consequently, the needle-eye inductors are pancake-shaped and have just one turn. The EM field created by such an inductor and the corresponding distribution of the heat sources and forces at the silicon surface are only roughly axisymmetric. The non-symmetry influences the melt flow and generates micro-inhomogeneities of resistivity in the grown crystal rod, which are known as the so-called rotational striations. The unwanted rotational striations arise due to the rotation of the crystal relative to the inductor under the conditions of disturbed symmetry and repeat periodically in the longitudinal direction of the crystal with the wave length being determined by the growth rate and single crystal rotation speed. Since the rotational striations are originated by 3D effects, they cannot be calculated within limits of a 2D model.

There are two main objectives of the present chapter: 1) to see the effects of the non-symmetry of the inductor on the structure of the three-dimensional melt flow and 2) to examine the rotational striations. The three-dimensionality of the flow is created in our model by the non-symmetric shape of the inductor only: we make here an approximation by assuming that the shape of the free melt surface stays axisymmetric.

In what follows, a series of publications[1] where the 3D flow and the rotational striations have been calculated numerically is included. The software used for these calculations was the commercial computational fluid dynamics package `FLUENT` ([90, 91]). Unlike the self-developed code `FZONE`, which calculates the flow in terms of the $\psi - \omega$ variables by the Finite Element Method (see Section 4.6), `FLUENT` is working with the velocity−pressure variables on basis of the Control Volume Method (known also as the Finite Volume Method), which is described e.g. in [92]. A comparison between the two approaches for a 2D flow was mentioned in Section 4.6.9. The approach used in the own-made code `FZONE` was more effective in 2D computations, the present study, however, deals primarily with 3D phenomena. Due to practical reasons, the numerical approach in the 3D calculations is coarser and fine effects like influence of the fluid flow on the zone shape are neglected.

6.2 Included paper 1: Effect of EM and Marangoni forces

The first of the papers is mostly devoted to the analysis of the influence of the different forces on the melt surface. Due to the high frequency of the EM field, the EM forces act in a thin boundary layer of the melt and, as quasi-surface forces, counteract the surface forces created by the gradient of the temperature-dependent surface tension, i.e., the Marangoni forces. A schematic illustration of the action of forces in a cross-section of the molten zone is shown in Fig. 3.1. The EM- and Marangoni forces have also minor azimuthal components due to a non-axisymmetric distribution of the EM power density and temperature along the free melt surface.

In order to distinctly see the individual impact by EM- and Marangoni forces on the melt flow and rotational striations, studies have been carried out with neglecting either EM forces or Marangoni forces (or both of them) while buoyancy forces stay always accounted. Physically, the results with neglecting Marangoni force may be interpreted as a model of a case with lower frequency of EM field of inductor (domination of EM force) while the results with neglecting EM force, as a model with higher frequency of the field (domination of Marangoni force).

The results of the studies have been published as included below in the article [63] in the journal *Magnetohydrodynamics*.

---

[1] The author of thesis acknowledges gratefully the contribution of about 10% by the coauthors of the included publications. The text of the publications has been written by the author of thesis.

МАГНИТНАЯ ГИДРОДИНАМИКА. – 1999. – Т. 35, № 3. – С. 278 – 293

G. Ratnieks[1], A. Muižnieks[1,2], L. Buligins[1], G. Raming[2], A. Mühlbauer[2]

[1]Department of Physics, University of Latvia, Zeļļu str. 8, LV-1002, Riga, Latvia
[2]Institute for Electroheat, University of Hanover,
Wilhelm-Busch-Str. 4, D-30167, Hanover, Germany

3D NUMERICAL ANALYSIS OF THE INFLUENCE OF EM AND MARANGONI FORCES ON MELT HYDRODYNAMICS AND MASS TRANSPORT DURING FZ SILICON CRYSTAL GROWTH

Г. Ратниекс, А. Муйжниекс, Л. Булыгинс, Г. Раминг, А. Мюльбауэр

3D ЧИСЛЕННЫЙ АНАЛИЗ ВЛИЯНИЯ ЭЛЕКТРОМАГНИТНЫХ СИЛ И СИЛ МАРАНГОНИ НА ГИДРОДИНАМИКУ РАСПЛАВА И ПЕРЕНОС МАССЫ ПРИ ВЫРАЩИВАНИИ КРИСТАЛЛОВ КРЕМНИЯ МЕТОДОМ ЗОННОЙ ПЛАВКИ

С помощью трехмерного численного моделирования проведен анализ влияния ЭМ сил и сил Марангони на гидродинамику расплава и процесс массопереноса при выращивании кристаллов методом зонной плавки с методикой игольного ушка, используемой в производстве высококачественных кристаллов кремния большого диаметра (> 100 мм). Поскольку плоский индуктор имеет только один виток, распределения электромагнитного поля, источников теплоты и ЭМ сил являются осесимметричными только приближенно. Эта несимметрия совместно с вращением кристалла отражается на гидродинамическом и термическом полях, а также на поле концентрации примесей в расплавленной зоне и вызывает в выращиваемом кристалле флуктуации удельного электрического сопротивления, которые известны под названием ротационных полос роста. Несимметричное высокочастотное ЭМ поле плоского индуктора вычисляется методом граничных элементов. Полученное несимметричное распределение источников теплоты на свободной поверхности расплава и соответствующие ЭМ силы используются для вычисления трехмерных гидродинамических и температурных полей в расплаве на криволинейной трехмерной сетке коммерческим программным пакетом (метод контрольных объемов). Рассчитывается также трехмерное поле концентрации примесей, затем используемое для расчета флуктуаций сопротивления в продольном сечении выращиваемого кристалла. Рассматривается влияние несимметричных ЭМ, Марангони и сил плавучести на характер течения расплава и на флуктуации сопротивления в выращиваемом кристалле кремния.

Introduction. Floating zone (FZ) crystal growth with the needle-eye technique is used nowadays for the production of high quality silicon single crystals with large diameters (>100mm) [1], Fig. 1. To enable melting and growing of large-diameter silicon rods, the heater is a concentric pancake induction coil with the inner radius smaller and outer radius larger than the radii of feed rod and single crystal. The high-frequency electromagnetic (HF EM) field of the coil induces electric currents on the surface of silicon material. This results in: (1) Joulean heat sources, which are responsible for melting, and (2) EM forces, being decisive factor in the formation of the free surface shape of the molten zone. The heat sources and the EM forces, along with the crystal rotation, applied during the growth process, significantly change the fluid flow in the volume of the melt. For demands of applications, boron, phosphorus, or other group III or group V dopants are added to silicon crystal to adjust its electrical resistivity. It is very desirable to get the resistivity in crystal as uniform as possible. The resistivity distribution in the grown crystal is determined by the dopant concentration field in melt near the crystallisation interface while the dopant concentration distribution is strongly influenced by the fluid flow patterns in the molten zone. As it is rather difficult to investigate and optimise the many-parameter FZ-process experimentally, numerical simulations are necessary.

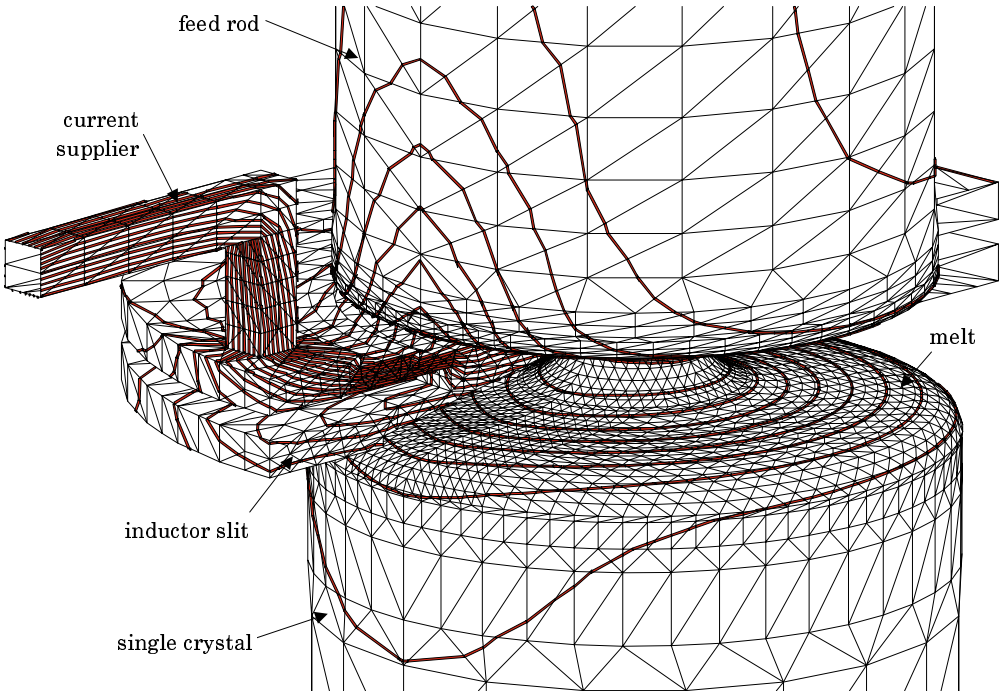

Fig. 1. 3D view of the EM model for the FZ-growth system (only a half of the inductor is shown), triangular boundary elements and calculated lines of HF electric current stream function.

The axisymmetric (2D) mathematical model and the calculation method for the shape of the molten zone and hydrodynamics during FZ crystal growth are described in [1]. In [2], the calculation of the averaged-in-time dopant concentration fields and macroscopic resistivity distributions are given. The transient axisymmetric numerical calculation of the hydrodynamic, temperature and dopant concentration fields is performed in [3] and microscopic inhomogeneities are analysed. Some three-dimensional (3D) aspects of non-industrial FZ-processes are considered in [4]. However, 3D analysis of the industrial FZ-process has not been carried out before.

Since the pancake inductor has only one turn (in order to avoid electrical breakdown) and current suppliers (Fig. 1), the EM field and the distribution of heat sources are only roughly axisymmetric. The non-symmetry generates micro-inhomogeneities of resistivity in the grown crystal rod, which are known as so-called rotational striations. The unwanted rotational striations are caused by the rotation of single crystal in the non-symmetric EM field and repeat periodically in the longitudinal direction of the crystal (the period being given by the growth rate and single crystal rotation speed). Since three-dimensional effects originate the rotational striations, they cannot be calculated within limits of a two-dimensional model. In the present work, 3D numerical modelling is undertaken to analyse the floating zone crystal growth with one-turn HF inductor used for the production of high quality silicon single crystals with large diameters. From the calculated 3D dopant concentration field in the melt, the longitudinal variations of resistivity are derived in the grown crystal and the influence of the non-symmetric EM, Marangoni and buoyancy forces is studied.

1. General scheme of solution. The general sequence of models, approximations and methods used for solving of the three-dimensional floating zone silicon problem consists of several steps described below.

1) Axisymmetric shape of the molten zone of silicon is obtained by solving a two-dimensional thermal-electromagnetic problem numerically by assuming that the inductor-coil is strictly axisymmetric. The mathematical model and calculation procedure based on 2D finite element and 2D boundary element methods are described in [1].

2) The 3D distribution of high-frequency electric currents induced in the skin-layer of the molten silicon and the Joulean heat sources density are obtained via 3D EM field calculations by using 3D boundary element method as described in [5]. The previously calculated 2D geometry of the molten zone is used to get an axisymmetric 3D geometry for the silicon molten zone and solid parts. The deviations of the shape of the molten zone from axial symmetry due to more or less non-symmetrically distributed EM forces are assumed to be small and are neglected. For the inductor, the real non-symmetric 3D shape is considered. This information about the FZ-system geometry is used to generate the triangular boundary element grid on the surfaces of the silicon and the inductor (Fig. 1).

3) The 3D calculations of the coupled hydrodynamic, temperature, and dopant concentration fields are carried out with the computational fluid dynamics program package FLUENT by using control volume method as described in [6] and [7]. Power density of heat sources and EM forces, previously calculated on the triangular 3D boundary element mesh, are transferred to the structured 3D grid on the free melt surface for hydrodynamic calculations. For heat sources and EM forces, the high-frequency approximation is kept (replacing the detailed description of the exponential decay of power and force density in the skin-layer depth by an integral 'surface value'). The Marangoni forces are calculated simultaneously from the temperature distribution by means of a user-defined subroutine. A steady-state hydrodynamic–thermal problem is considered.

4) The 3D dopant concentration field in the melt is calculated using FLUENT with additionally compiled user-defined subroutines (including treatment of the segregation condition on the crystallisation and melting interfaces; see [2]). Finally, the normalised distribution of resistivity at the crystallisation interface is derived by assuming that it is inversely proportional to the dopant concentration. The resistivity variations in the grown crystal (rotational striations) are calculated by accounting for the vertical movement and rotation of the crystal and for the curvature of the crystallisation interface.

2. Characteristics of the chosen FZ-system. The presented results, calculated for floating zone growth of 4" silicon crystals, are based on the laboratory experiment at the Institute of Crystal Growth, Berlin [8]. The used physical properties of silicon are given in [1] and [2]. The main growth process parameters are as follows: EM field frequency $f = 2.8$ MHz, effective value of the electric current in inductor $I_0 = 1000$ A, single crystal rotation rate $W_{Cr} = 5$ rpm (rounds per minute), feed rod rotation rate $W_F = -20$ rpm, crystal growth rate $V_{Cr} = 3.4$ mm/min, crystal radius $R_{Cr} = 52.5$ mm, feed rod radius $R_F = 48.6$ mm, radius of the central hole (inner radius) of the inductor $R_H = 17.5$ mm, outer (maximum) radius of the inductor $R_I = 82.4$ mm, radius of the zone neck $R_N = 10.9$ mm, supply velocity of molten silicon from feed rod $V_M = 78.8$ mm/min (this is an averaged value for the feed–melt interface). The parameters R_N and V_M are taken from 2D model [1] as results of axisymmetric calculation of liquid phase's boundaries.

3. Results with EM and Marangoni forces. The calculation of the coupled 3D hydrodynamic and thermal fields in the molten zone for the considered FZ-system is performed on a structured (hexahedral) cylindrical grid. The grid is illustrated in Fig. 2, where the vertical cross-section and the melting and crystallisation interfaces are shown. For the main calculation variant, both the Marangoni and EM forces at the melt free surface as well as

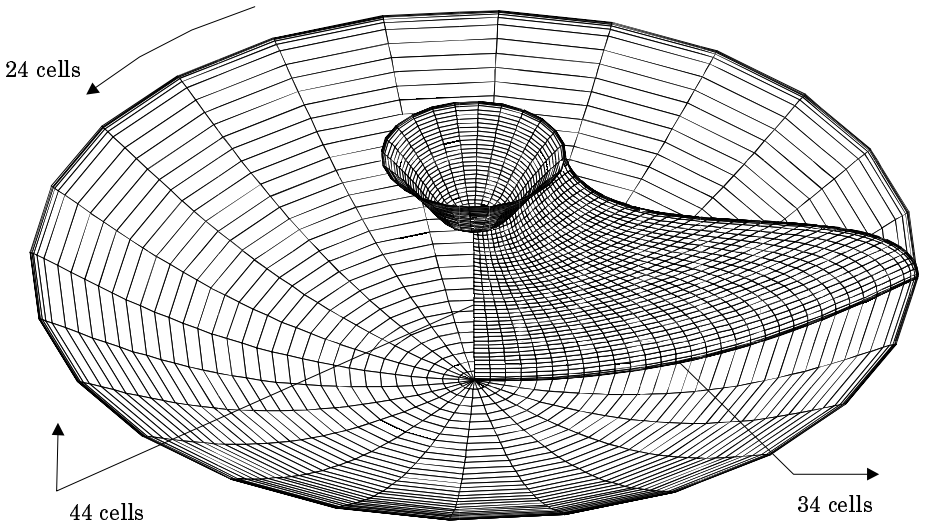

Fig. 2. 3D grid used for hydrodynamic-thermal and concentration calculations in the melt.

the buoyancy forces in the melt volume and rotation of single crystal and feed rod are considered. From the 3D EM calculations (Fig. 1), distributions of heat sources and electromagnetic surface forces that are caused by an inductor with slit width 1 mm are used. In Fig. 2, and in other figures considering the molten zone, the inductor slit comes from the left-hand side.

The 3D hydrodynamic-thermal calculations lead to the coupled velocity and temperature fields in the molten zone. The calculated 3D temperature distribution is illustrated in Fig. 3. In Fig. 3*a*, the temperature distribution on the melt free surface with a distinct asymmetry of the thermal field is shown from the top. The region of maximum temperature corresponds to the opposite-to-slit side of the inductor but is shifted in the direction of single crystal rotation because of the influence of convective heat transfer. Fig. 3*b* shows the temperature distribution in the volume of the molten zone in the vertical cross-section that corresponds to the plane of inductor slit. It can be seen that the temperature distribution strongly deviates from the axial symmetry, especially near the free melt surface.

The calculated 3D velocity distribution is illustrated in Figs 4 and 5*a*, *b*. In Fig. 4, the velocity vectors on the free melt surface can be seen. Fig. 5a shows the velocities in the vertical cross-section in the plane of inductor slit (only the radial and axial components of the velocity vectors are shown). The maximum of velocity magnitude is reached at the free surface near the melting interface due to a steep temperature gradient and, consequently, a strong Marangoni force at this location. Another but smaller maximum exists at the peripheral part of the free surface, where EM force dominates over Marangoni force. The following features of non-symmetry of the velocity field are observed: 1) velocity maxima at the free surface are different comparing the slit side and the opposite-to-slit side; characteristically the maxima at the opposite-to-slit side are stronger (on the right-hand side in Fig. 5*a*); 2) structure of vortices differs qualitatively (especially in the regions of high velocity) comparing the slit side and the opposite-to-slit side; 3) fluid flow is going through the geometrical axis of symmetry of the molten zone; it takes place also at the vicinity of the centre of the crystallisation front, where a non-zero horizontal velocity component can be observed. These properties of fluid flow are caused

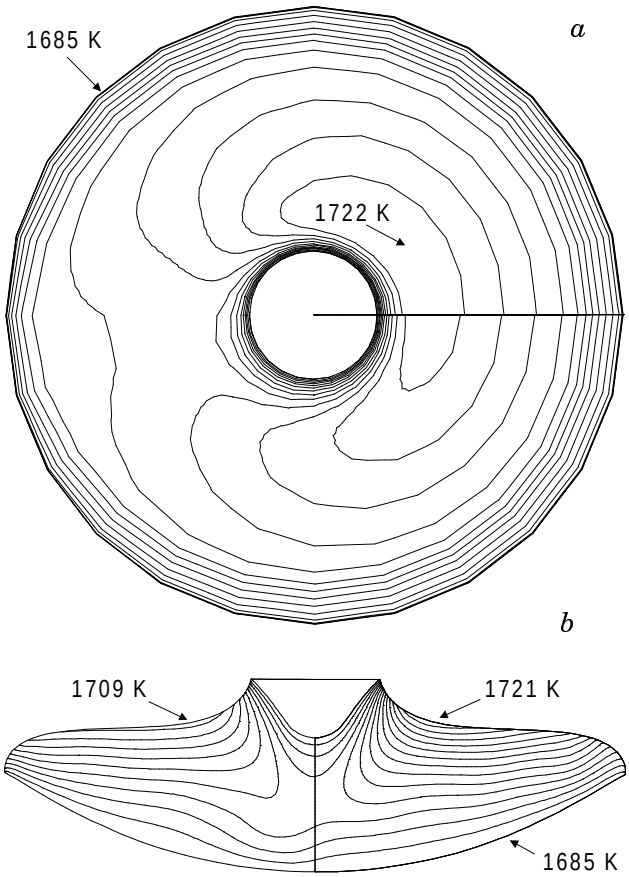

Fig. 3. Temperature field: *a* – temperature on the free melt surface (view from top), and *b* – in the vertical cross-section corresponding to the plane of inductor slit.

by the asymmetry of EM and Marangoni forces, which mostly are acting in mutually opposite directions. In Fig. 5*b*, we see the distribution of magnitude of the azimuthal velocity component, which is also non-symmetric correspondingly to the non-symmetric convective momentum transport in the vertical cross-section of the molten zone.

As Figs 4, 5*a*, *b* show, the non-symmetry of EM, Marangoni and buoyancy forces does not destroy fully the quasi-axial-symmetry of the velocity field. It is due to the influence of crystal rotation on hydrodynamics in the molten zone.

The fluid velocity distribution is used to calculate the dopant concentration field. Fig. 5*c* illustrates the normalised concentration distribution in the vertical cross-section of the molten zone. A distinct concentration boundary layer in the vicinity of the growth interface can be observed. The influence of the main fluid flow vortices (see Fig. 5*a*) gives rise to the maximum of concentration in the region where fluid flow is going away from the crystallisation interface. In Fig. 6, the distribution of concentration in the melt near the growth interface is shown. This distribution has significant asymmetry in the central region. At the periphery, the deviations from axial symmetry are rather small.

The dopant distribution along the crystallisation interface is the one responsible for the dopant incorporation in the growing crystal. Since the steady-state solution, described above, concerns the laboratory reference system (i.e. the reference system of inductor) while the crystal is rotating and moving downwards, the deviations from axial symmetry (like in Fig. 6) cause

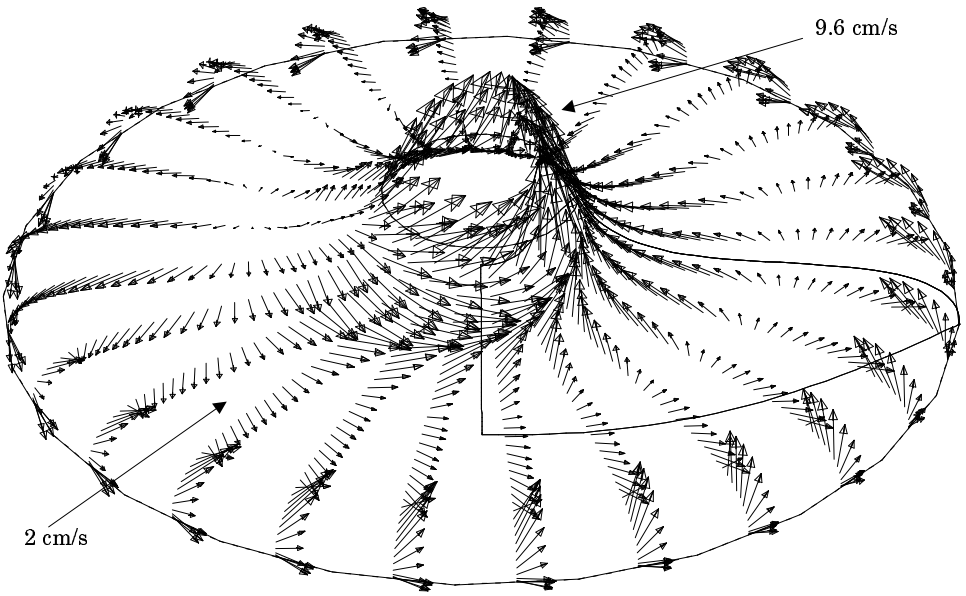

Fig. 4. Velocity vectors on the free surface of the melt.

generation of resistivity inhomogeneities (rotational striations) in the crystal. The resulting normalised resistivity distribution along 10 mm long part of the longitudinal cut of the grown crystal rod is shown in Fig. 7*a*. The picture displays an alternating crest-trough pattern, which is the proper pattern of rotational striations. At the crystal axis, the crests from one side meet troughs from the opposite side (half wavelength phase shift). Besides the longitudinal rotational striations, which are represented by the resistivity variations along the axial direction of the crystal, also the radial rotational striations take place. They are represented by the small-wavelength resistivity variations along the radial direction. (Remark: the macroscopic variations along crystal radius represent the 'axisymmetric part' of the influence of the steady-state fluid flow.) The radial rotational striations are caused by the curved shape of the crystallisation interface. The curvature of the interface reflects itself in the herringbone-form of the crest-trough pattern.

The calculated resistivity distribution shows that the largest rotational striations (reaching almost 30%, see Fig. 7*b*) are present near the central part of the crystal. Small variations can be seen also near the outer rim of the rod. Such radial distribution of the relative amplitudes of rotational striations agrees qualitatively with experimental measurements [8]. Detailed comparison with experimental data is a subject of a separate paper.

Since the calculated are steady-state flows, the corresponding resistivity variations do not include the oscillations caused by hydrodynamic instabilities. It has been shown that the real-life flow in the considered FZ-system is time-dependent and the steady-state solution is only an approximation, which can be obtained due to the sufficiently high numerical viscosity of the finite difference scheme (relatively coarse calculation grid, see Fig. 2).

4. Study of the influence of forces. In order to study the individual influence of forces on melt hydrodynamics and mass transport in floating zone, calculations with neglecting either EM forces or Marangoni forces (or both of them) have been carried out. Buoyancy forces are always kept. The results are illustrated in Figs. 8–13.

Neglecting both EM and Marangoni forces (when only the buoyancy and rotation are driving the fluid motion) yields a comparatively simple flow structure consisting of two toroidal vortices (Fig. 8*a*). The character of dopant

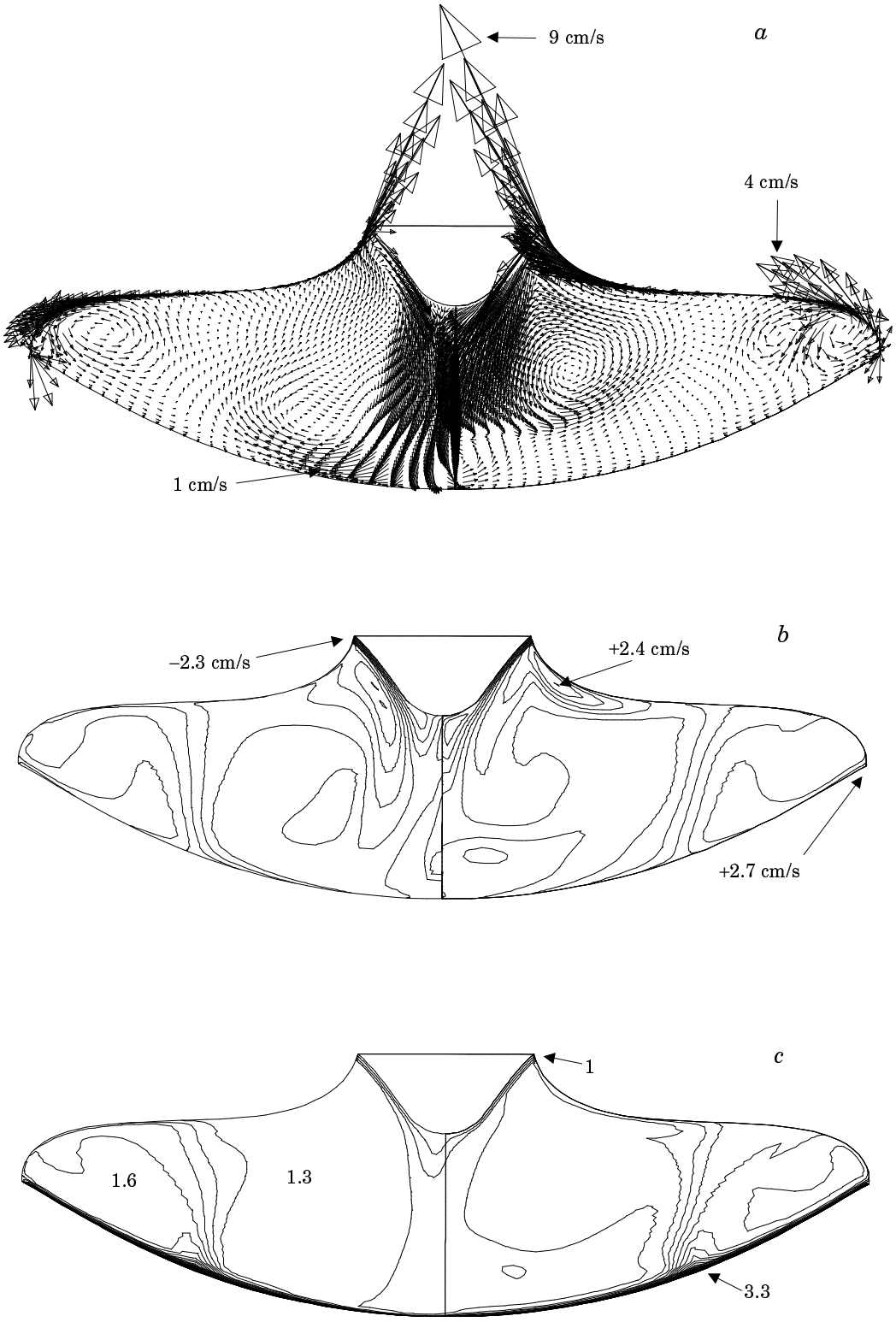

Fig. 5. Velocity and concentration fields in the vertical cross-section in the plane of inductor slit: *a* – velocity vectors projected to the plane of the cross-section, *b* – azimuthal velocity component, and *c* – dopant concentration.

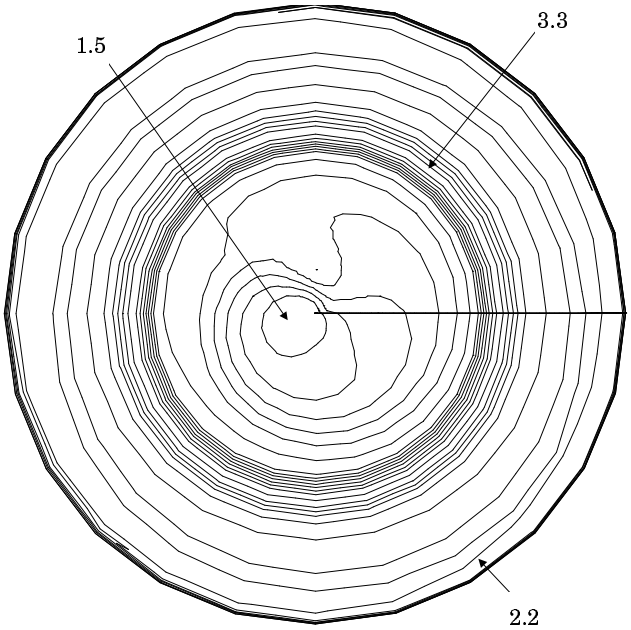

Fig. 6. Dopant concentration in the melt near the crystal growth interface.

concentration distribution (Fig. 8*c*) resembles qualitatively the case with all forces accounted. It is explained by partial compensation of EM and Marangoni forces, which results in a similar position of the flow separation point at crystallisation interface. Consequently, also the resistivity distribution in Fig. 9 is similar to that in Fig. 7. The main obvious difference is in the amplitude of rotational striations. It is small in the case of neglecting EM and Marangoni forces because of small asymmetry of the calculated hydrodynamic and thermal fields and concentration distribution.

If one of both forces is applied neglecting the other one, high velocity maxima arise near the free surface of the melt (see Figs 10*a*, 12*a*). We see that Marangoni forces mostly intensify the buoyancy-driven vortices and do not act against them while EM forces, on the contrary, do. This feature of EM forces evokes appearing of a distinct stretched vortex near the free surface of the melt and the flow becomes relatively unstable resulting in a slower convergence to the steady state. In both the case of EM forces and the case of Marangoni forces, also the distribution of the azimuthal velocity component gets complicated (Figs 10*b*, 12*b*). The maximum of the azimuthal velocity is reached somewhere in the melt volume and not more on the outer rim of the crystallisation interface. The resulting concentration distributions, as shown in Figs 10*c* and 12*c*, differ strongly from the one in Fig. 5*c*. As a consequence, also the resistivity distributions in Figs. 11 and 13 are very different from the one in Fig. 7.

Comparing Figs 7*b*, 9*b*, 11*b*, and 13*b* shows that the amplitude of rotational striations becomes relevant only in the case when both EM and Marangoni forces are accounted. Excluding only one of them leads to drastic changes in the result. That demonstrates the effect of the mutual counteraction and partial compensation of EM and Marangoni forces. Therefore, the concentration distribution is very sensitive to both of them and it is important to take into account the involved EM and Marangoni forces as carefully as possible. Further studies are necessary to check the accuracy of the used approximations for the forces near the free surface. Retaining the axisymmetric shape for the floating zone (from 2D calculations) and introducing the non-

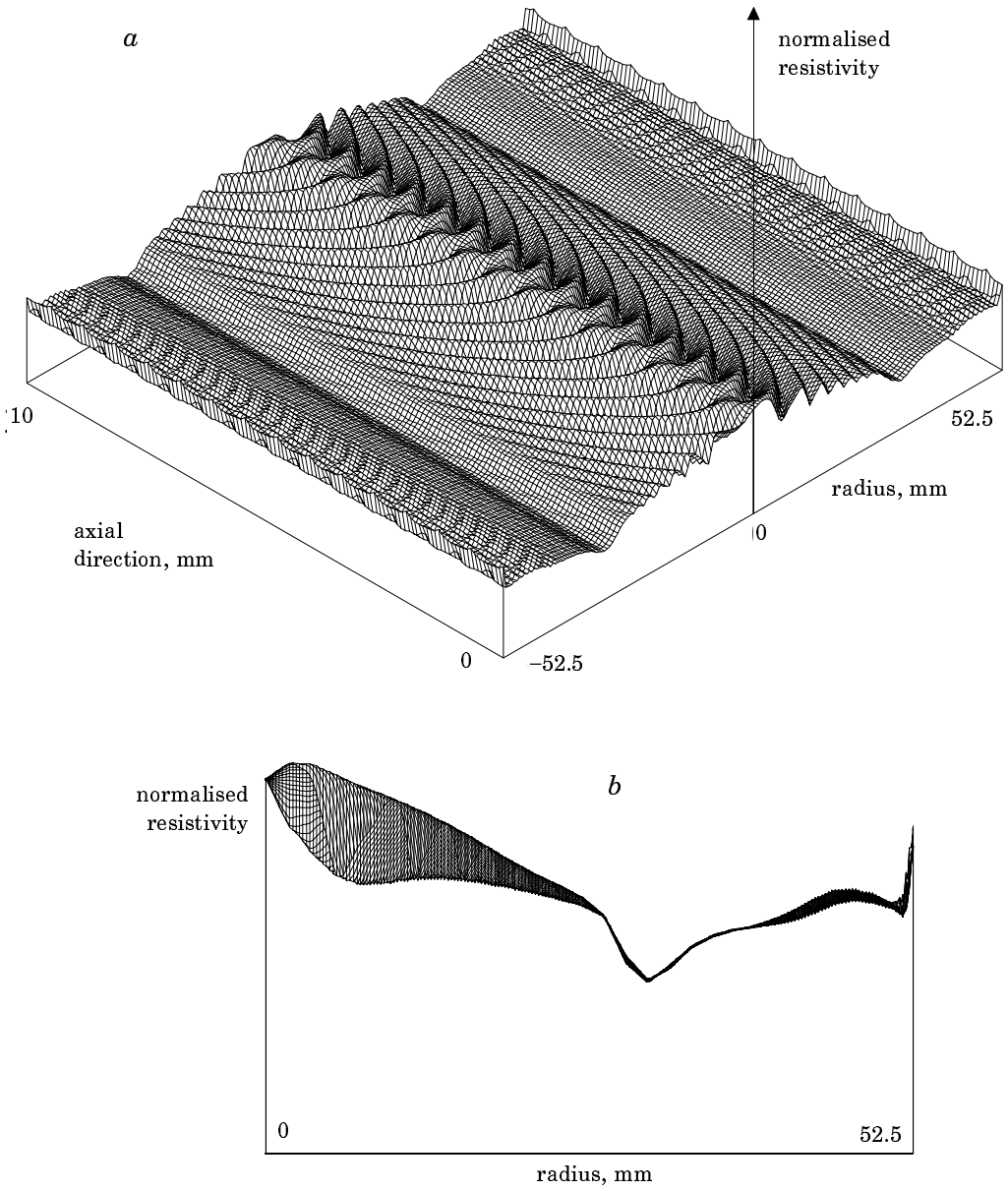

Fig. 7. Resistivity distribution with rotational striations in the vertical cross-section of the rotating crystal.

symmetry only through EM field constitute one of the possible sources of deviance of the present results (with all forces) from reality.

The studies of the influence of EM and Marangoni forces show the role of both of them and give impression how the system will behave if one of the forces becomes negligibly small in comparison with the other one. Such conditions may form up with special choice of EM field frequency. If the frequency is higher, the impact of EM force on the melt hydrodynamics becomes smaller, if it is lower, EM force becomes stronger while Marangoni force keeps about the same magnitude because the total Joulean power (adjusted by a proper choice of inductor current) should be the same for maintaining the melting rate of silicon rod. In this sense, the case of excluding Marangoni force corresponds to low-frequency model while the case of excluding EM force, to high-frequency model.

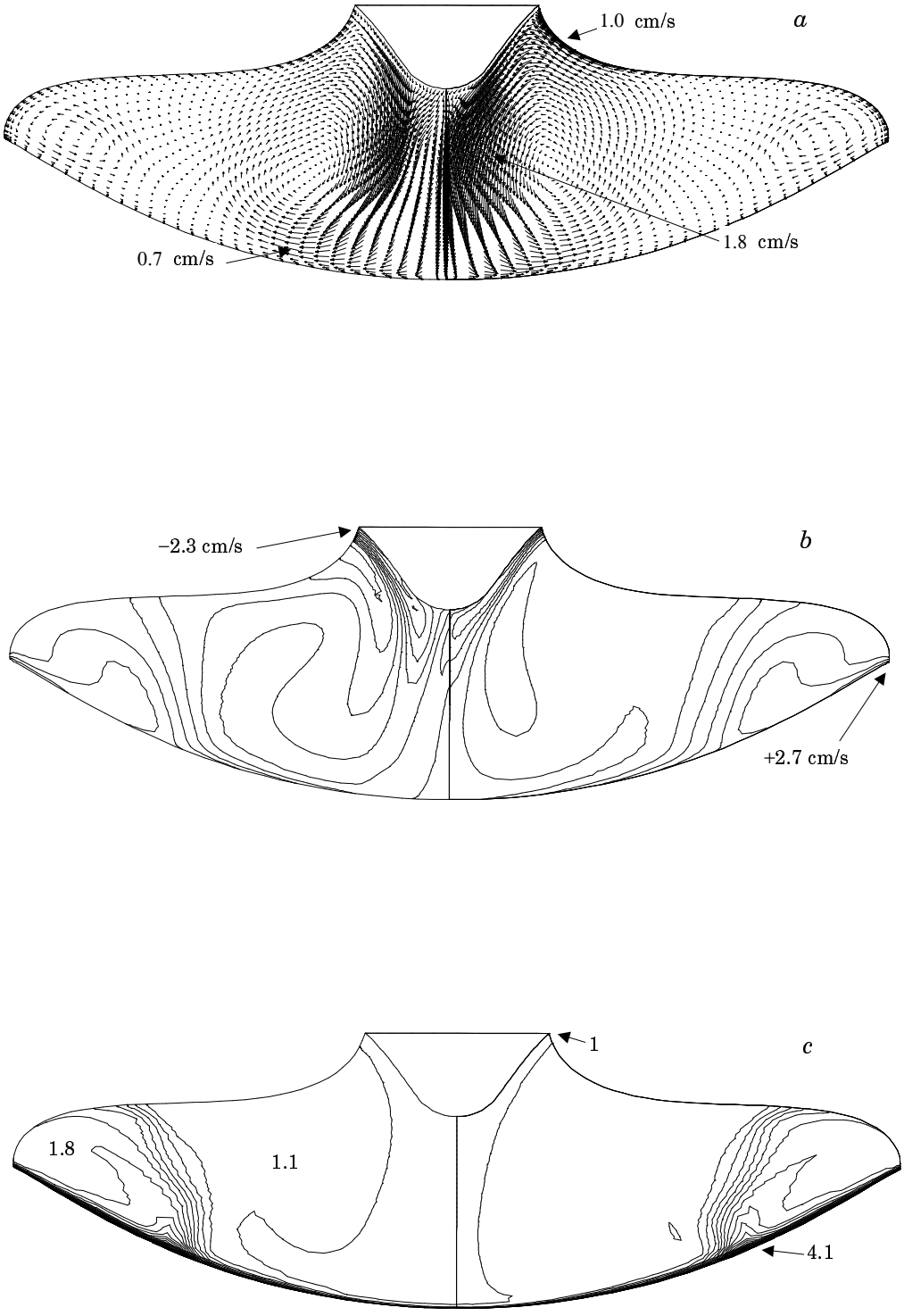

Fig. 8. Neglecting both EM and Marangoni forces: Velocity and concentration fields in the vertical cross-section in the plane of inductor slit: *a* – velocity vectors, projected to the plane of the cross-section, *b* – azimuthal velocity component, and *c* – dopant concentration.

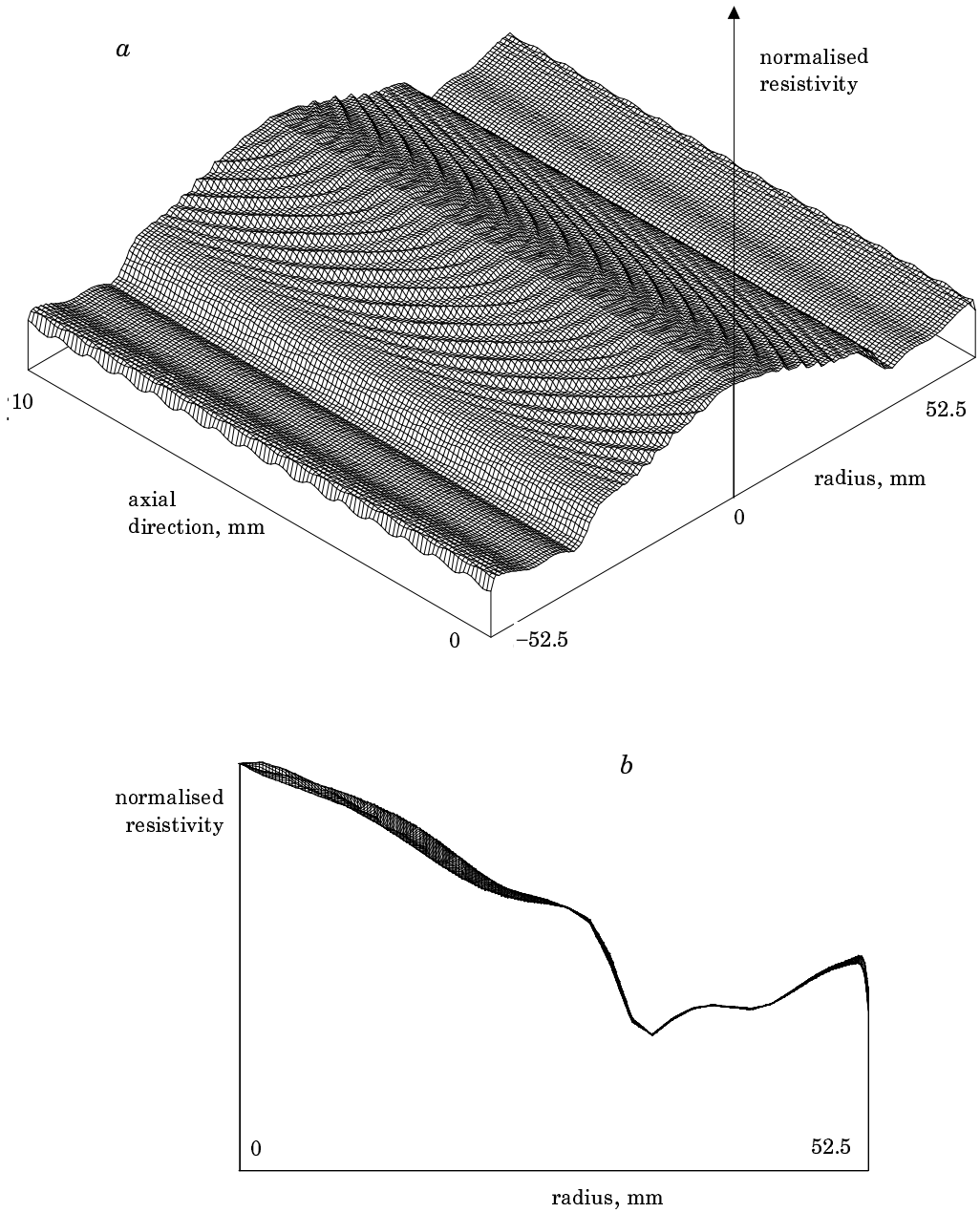

Fig. 9 Neglecting both EM and Marangoni forces: Resistivity distribution with rotational striations in the vertical cross-section of the rotating crystal.

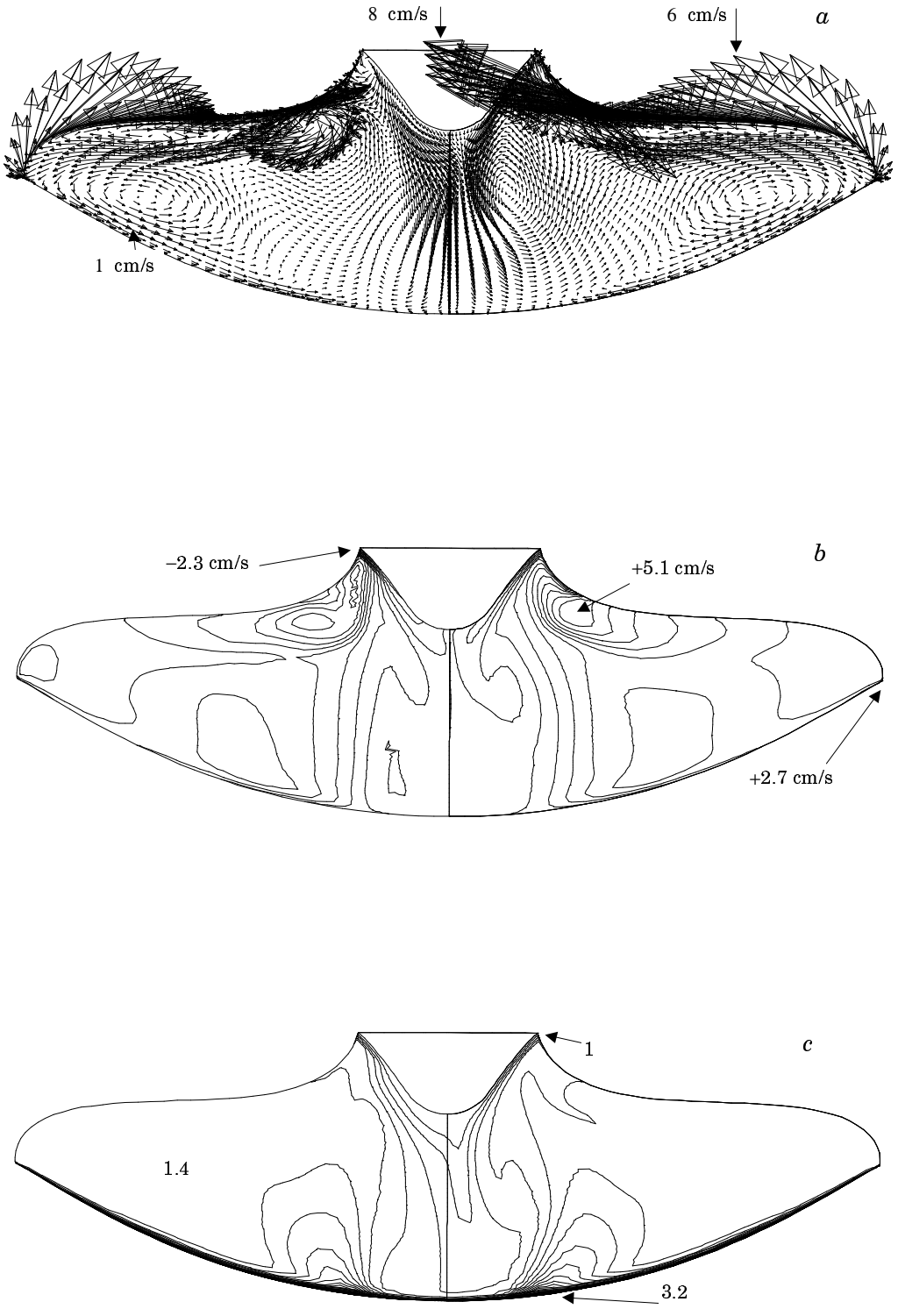

Fig. 10. Influence of EM force (neglecting Marangoni force): Velocity and concentration fields in the vertical cross-section in the plane of inductor slit: a – velocity vectors, projected to the plane of the cross-section, b – azimuthal velocity component, and c – dopant concentration.

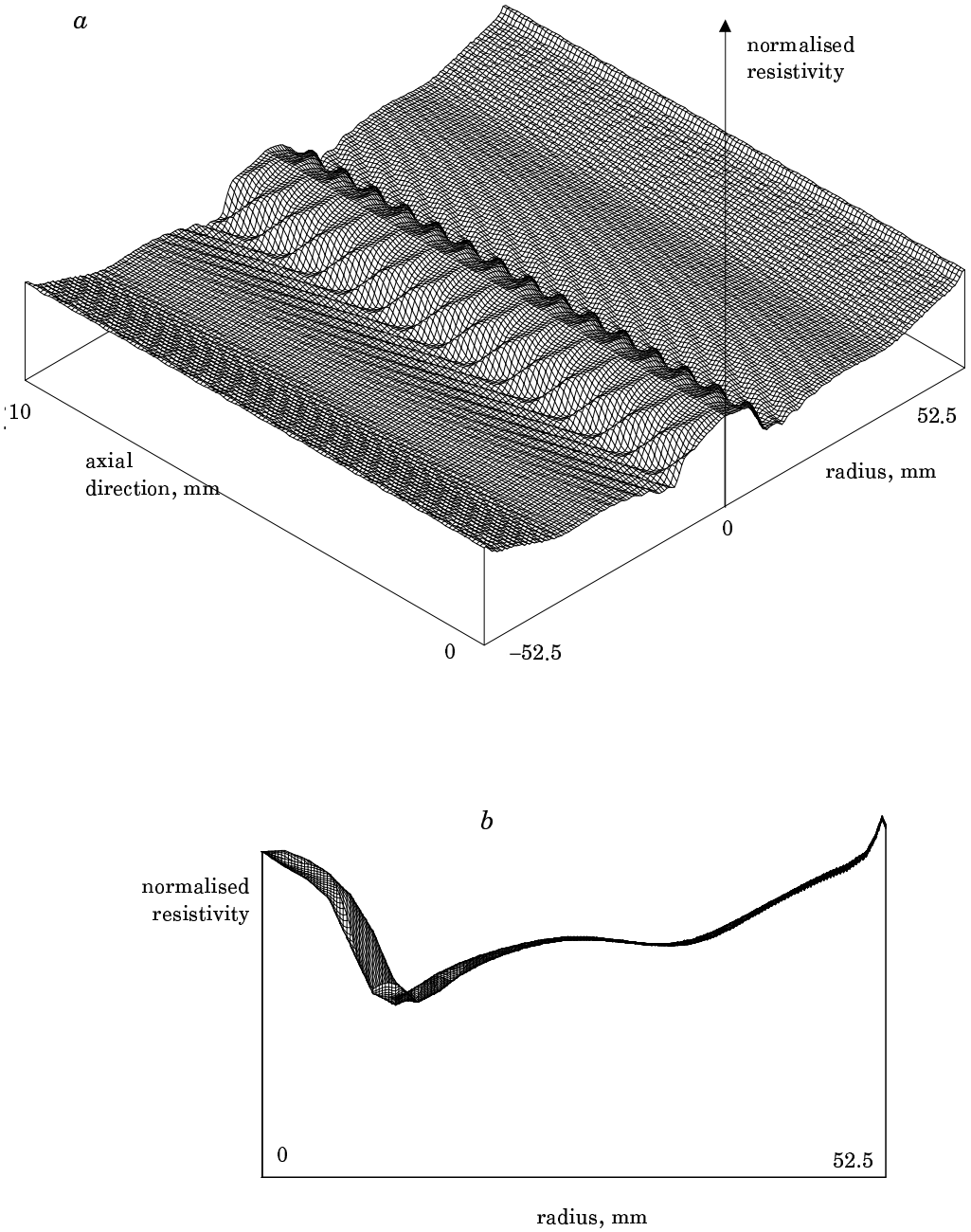

Fig. 11. Influence of EM force (neglecting Marangoni force): Resistivity distribution with rotational striations in the vertical cross-section of the rotating crystal.

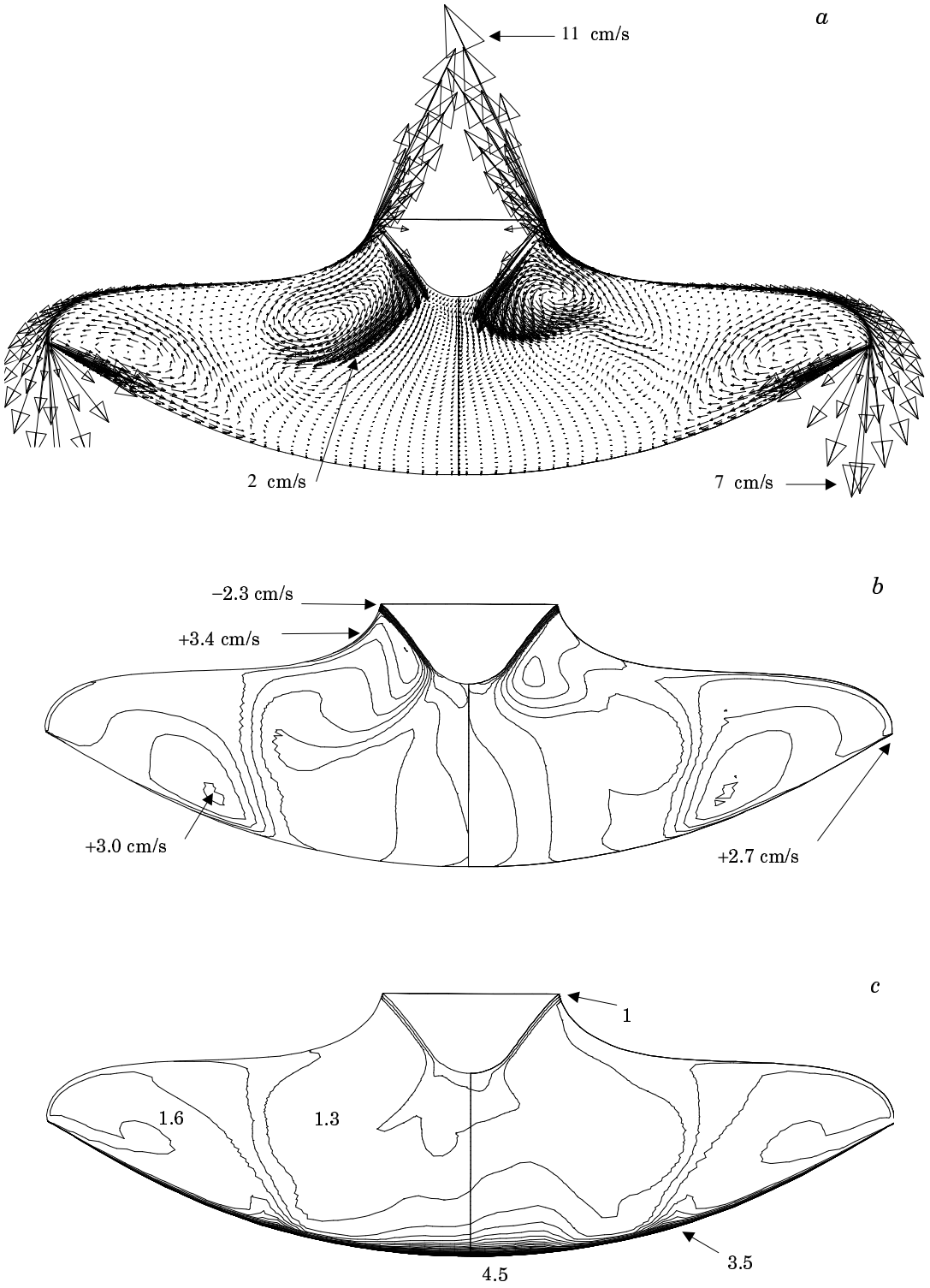

Fig. 12. Influence of Marangoni force (neglecting EM force): Velocity and concentration fields in the vertical cross-section in the plane of inductor slit: *a* – velocity vectors, projected to the plane of the cross-section, *b* – azimuthal velocity component, and *c* – dopant concentration.

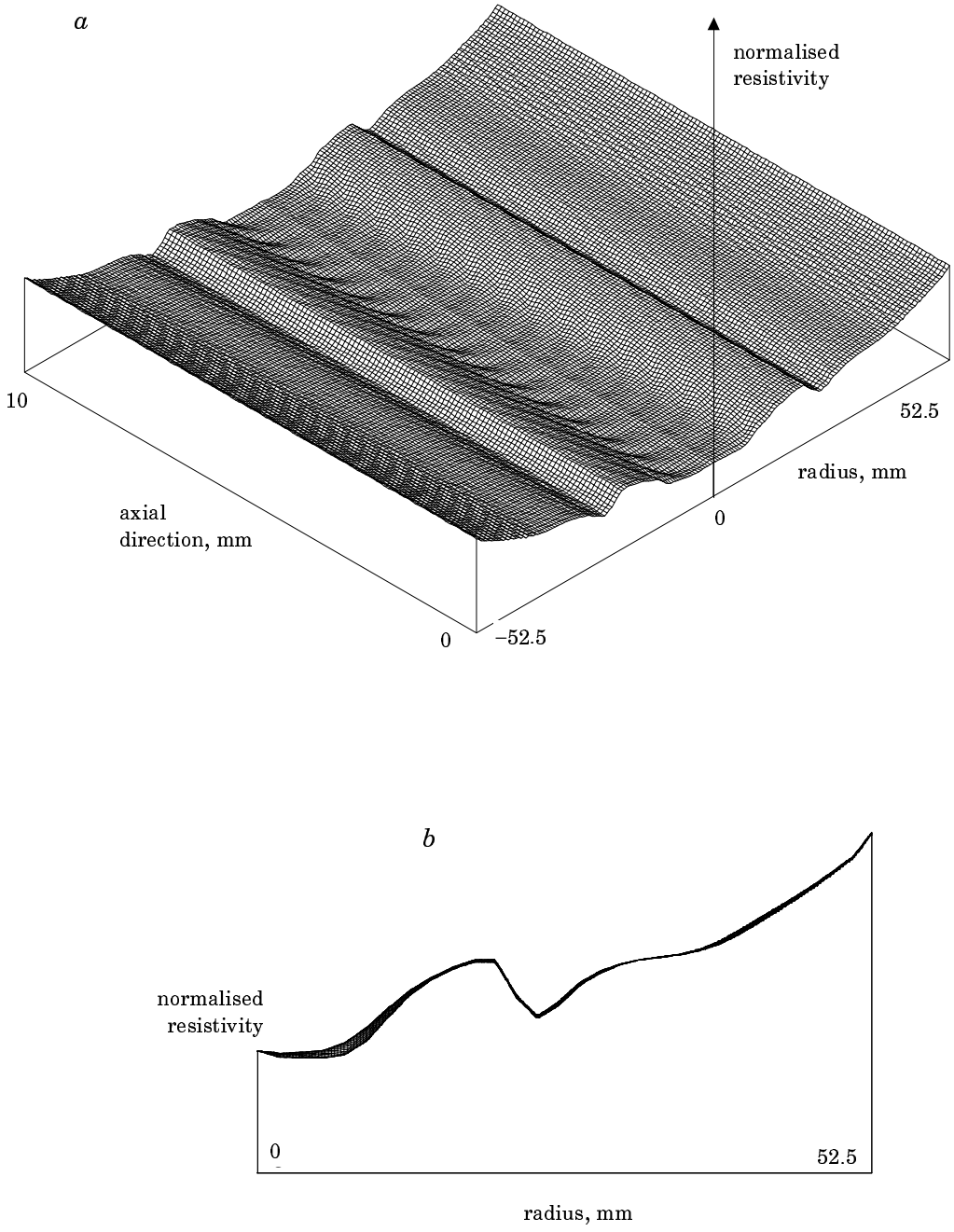

Fig. 13. Influence of Marangoni force (neglecting EM force): Resistivity distribution with rotational striations in the vertical cross-section of the rotating crystal.

Conclusions. (1) 3D numerical modelling is carried out to analyse the influence of EM and Marangoni forces on melt hydrodynamics and mass transport during the floating zone growth of large diameter crystals with the needle-eye technique. A non-symmetric HF electromagnetic field of the pancake inductor is calculated. The obtained non-symmetrical power distribution on the free melt surface and the corresponding EM forces are used for the calculation of the coupled 3D hydrodynamic and temperature fields in the molten zone. The buoyancy, Marangoni and EM forces are considered and a steady-state non-symmetric flow structure is obtained.

(2) The 3D hydrodynamic field is used to calculate the corresponding non-symmetric dopant concentration field in the melt. Accounting effect of the non-symmetry and crystal rotation, the variations of resistivity in the grown single crystal (rotational striations) are obtained. Longitudinal resistivity oscillations near crystal axis (almost 30%) are found to be considerably higher than at the periphery.

(3) Studies of the individual influence of forces on melt hydrodynamics and mass transport in floating zone and on the resulting resistivity variations in crystal are performed. Neglecting both EM and Marangoni forces yields rather even and symmetrical flow structure. Neglecting only one of them leads to intense melt motion near the free surface. If Marangoni force is turned off, EM force evokes high degree of asymmetry of fluid flow in the major part of melt volume, however it does not create strong asymmetry near the growth interface. If EM force is turned off and Marangoni force is acting, the melt motion does not deviate very much from symmetric pattern even at the free surface. As a result, the calculations with neglecting at least one of the forces show comparatively small amplitude of rotational striations. The distributions of dopant concentration and resistivity in crystal are very sensitive to both EM and Marangoni forces, whose mutual counteraction and partial compensation play an important role in amplifying the rotational striations. The results with neglecting Marangoni force may be interpreted as a model of a case with lower frequency of EM field of inductor while the results with neglecting EM force, as a model with higher frequency of EM field.

This paper presents results obtained within the frame of a cooperation project between Institute for Electroheat (University of Hanover) and Department of Physics (University of Latvia). The project has been sponsored by VW foundation (Hanover, Germany), and it is gratefully acknowledged.

REFERENCES

1. *Mühlbauer A., Muižnieks A., Virbulis J., Lüdge A., Riemann H.* Interface shape, heat transfer and fluid flow in the floating zone growth of large silicon crystals with the needle-eye technique // J. Crystal Growth. – 1995. – Vol. 151. – P. 66–79.

2. *Mühlbauer A., Muižnieks A., Virbulis J.* Analysis of the dopant segregation effects at the floating zone growth of large silicon crystals // J. Crystal Growth. – 1997. – Vol. 180. – P. 372–380.

3. *Mühlbauer A., Muižnieks A., Raming G., Riemann H., Lüdge A.* Numerical modelling of the microscopic inhomogeneities during FZ silicon growth // J. Crystal Growth. – 1999. – Vol. 198/199. – P. 107–113.

4. *Kaiser T.* Magnetohydrodynamische Effekte bei der Halbleiterkristallzüchtung // Diss., Geowissenschaftliche Fakultät der Albert-Ludwigs-Univ. Freiburg i. Br. (1998).

5. *Mühlbauer A., Muižnieks A., Leßmann H.-J.* Berechnung von dreidimensionalen elektromagnetischen Feldern bei der induktiven Erwärmung // Archiv für Elektrotechnik. – 1994. – Vol. 77. – P. 157–168.

6. *Patankar S.* Numerical heat transfer and fluid flow // Hemisphere Publ. Corp., Washington DC, 1980.

7. Fluent User's Guide (Version 4.3, Version 4.4), Fluent Inc.

8. *Lüdge A., Riemann H.* (Institute of Crystal Growth, Berlin): personal commun.

Поступила в редакцию 9.08.99

6.3 Included paper 2: Steady-state 3D flow

The second included paper presents a study of rotational striations by means of steady-state 3D flow calculations and Fourier analysis of the calculated resistivity variations along the longitudinal cross-section of the crystal. Photo-scanning measurements from the Institute of Crystal Growth (Berlin) are used for verification of the results. The Fourier analysis of the measurement data shows a reasonable agreement with that of the calculated data: the frequency of the rotation of crystal is seen clearly and the radial distribution of the Fourier amplitudes is similar. The most important difference is, as expected, the lack of the frequencies due to the flow instability in the Fourier spectrum created from calculation results. Hence additional 2D time-dependent flow calculations are done for a comparison, showing no rotational frequency but the spectrum due to the flow fluctuations.

The results of the studies have been published as included further in the article [64] in *Journal of Crystal Growth*. The considered inductor has a slit width 1 mm. Figure 6.1 shows a supplemental illustration of the effect of slit width on the induced power distribution at the free melt surface: two power distributions are compared by displaying only one half of each, taking into account the plane symmetry of the inductor. These distributions imply the perturbations of the temperature field and EM force, which are considered here as the only sources of deviation from the axial symmetry.

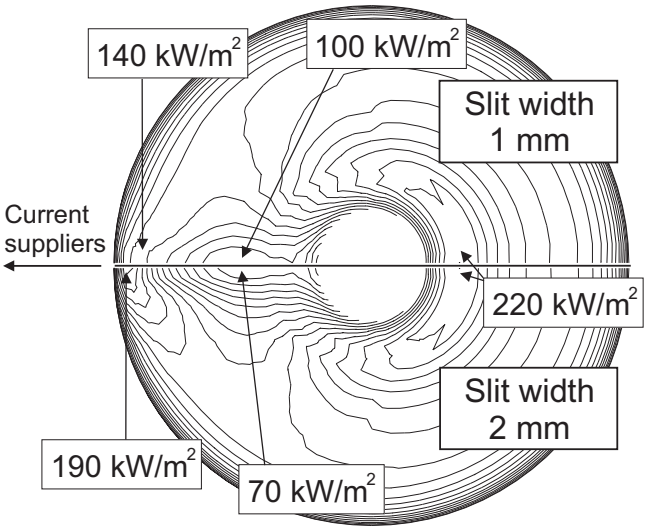

Figure 6.1: Isolines of the Joulean power density on the free melt surface created by inductor with a 1 mm slit (upper half) and 2 mm slit (lower half).

ELSEVIER

Journal of Crystal Growth 216 (2000) 204–219

JOURNAL OF CRYSTAL GROWTH

www.elsevier.nl/locate/jcrysgro

Influence of the three dimensionality of the HF electromagnetic field on resistivity variations in Si single crystals during FZ growth☆

G. Ratnieks[a], A. Muiznieks[a,b], L. Buligins[a], G. Raming[b], A. Mühlbauer[b,*], A. Lüdge[c], H. Riemann[c]

[a]*Department of Physics, University of Latvia, Zellu str. 8, LV-1002 Riga, Latvia*
[b]*Institute for Electroheat, University of Hanover, Wilhelm-Busch-Strasse 4, D-30167 Hanover, Germany*
[c]*Institute of Crystal Growth, Rudower Chaussee 6, D-12489 Berlin, Germany*

Received 10 December 1999; accepted 16 February 2000
Communicated by K.W. Benz

Abstract

Three-dimensional numerical modelling is carried out to analyse the floating zone crystal growth with the needle-eye technique used for the production of high-quality silicon single crystals with large diameters ($\geqslant 100$ mm). Since the pancake inductor has only one turn, the EM field and the distribution of heat sources and EM forces are only roughly axisymmetric. The non-symmetry together with crystal rotation reflects itself on the hydrodynamic, thermal and dopant concentration fields in the molten zone and causes variations of resistivity in the grown single crystal, which are known as the so-called rotational striations. The non-symmetric high-frequency electromagnetic field of the pancake inductor is calculated by boundary element method. The obtained non-symmetric power distribution on the free melt surface and the corresponding EM forces are used for the coupled calculation of the 3D steady-state hydrodynamic and temperature fields in the molten zone on a body fitted structured 3D grid by a commercial program package with control volume approach. The buoyancy, Marangoni and EM forces are considered. The afterwards calculated corresponding 3D dopant concentration field is used to derive the variations of resistivity in a longitudinal cut of the grown crystal. The results are compared with experimental measurements (photo-scanning method) and with results of 2D transient flow calculations. Rotational striations are found in both 3D-calculated and experimental resistivity distributions and show a qualitative agreement. A Fourier analysis for the resistivity variations is performed and the observed differences are explained by modelling limitations.

PACS: 81.10; 81.10.A; 02.60; 47.65

Keywords: Floating zone growth; Rotational striations; Numerical modelling

☆This paper presents results obtained within the frame of a cooperation project that is sponsored by VW foundation, Hanover, Germany. Cooperation partners of this project are Institute for Electroheat, University of Hanover, Germany and Department of Physics, University of Latvia, Latvia.

*Corresponding author. Tel.: + 45-511-762-2872; fax: + 49-511-762-3275.
E-mail address: mbr@ewh.uni-hannover.de (A. Mühlbauer).

1. Introduction

For the floating zone (FZ) growth of large-diameter ($\geqslant 100$ mm) silicon rods, the heater is a concentric pancake induction coil with the inner radius smaller and outer radius larger than the radii of feed rod and single crystal (the needle-eye technique). The high-frequency electromagnetic (HF EM) field of the coil induces electric currents on the surface of silicon material. This results in: (1) Joulean heat sources, responsible for melting, and (2) EM forces, decisive factor in the formation of the free surface shape of the molten zone. The heat sources and the EM forces, along with the crystal rotation, applied during the growth process, determine the fluid flow in the volume of the melt. When boron, phosphorus or other group III or group V dopants are added to the melt, the resistivity distribution in the grown crystal is determined by the dopant concentration field in melt near the crystallisation interface while the dopant concentration distribution is strongly influenced by the fluid flow patterns in the molten zone. It is rather difficult to investigate and optimise the many-parameter FZ-process experimentally. Therefore numerical simulations are necessary.

Various aspects of the axisymmetric (2D) mathematical modelling and the calculation methods for the shape of the molten zone and hydrodynamics during radio-frequency needle-eye FZ growth of large crystals are described in Refs. [1–4]. The case of small crystals ($\leqslant 10$ mm) is considered, e.g. in Ref. [5]. In Refs. [4–6], the calculation of the time-averaged dopant concentration fields and macroscopic resistivity distributions are given. Lüdge et al. [7] compare the results for macroscopic resistivity distributions calculated by the model in Ref. [6] with spreading resistance and 4-point measurements. Some transient axisymmetric numerical calculations of the hydrodynamic and temperature fields are described in Ref. [8], considering 100 mm crystals, and in Ref. [9], where 10 mm crystals are considered. Transient dopant concentration fields are calculated in Ref. [8] and microscopic inhomogeneities are analysed.

Since the pancake inductor has only one turn and current suppliers (Fig. 1), the EM field and the distribution of heat sources are only roughly axisymmetric. The non-symmetry generates micro-inhomogeneities of resistivity in the grown crystal rod, which are known as the so-called rotational striations. They are caused by the rotation of single crystal in the non-symmetric EM field and repeat periodically in the longitudinal direction of the crystal with the period being given by the growth rate and single-crystal rotation speed. Since rotational striations are always originated by three-dimensional (3D) effects, they cannot be calculated within limits of a two-dimensional model. Some 3D aspects of non-industrial FZ-processes (small crystal diameters) are considered in Ref. [10]. 3D calculations of an industrial FZ-process have been carried out only recently in Ref. [14], where the influence of the three-dimensional EM and Marangoni forces is studied numerically but a more detailed analysis of rotational striations and a comparison with experiment is still lacking.

Therefore, the 3D numerical analysis of the industrial floating zone growth of large-diameter silicon single crystals is developed and presented here. Steady-state melt flow is considered and normalised resistivity distribution in the grown crystal is calculated and analysed. Photo-scanning measurements of resistivity are performed and the experimental data is compared to the calculation results. A comparison with axisymmetric transient flow calculations is also done.

2. General scheme of solution

The general sequence of models, approximations and methods used for solving the three-dimensional floating zone silicon problem consists of several steps described below.

(1) The axisymmetric shape of the molten zone of silicon is obtained by solving a two-dimensional thermal–electromagnetic problem numerically by assuming that the inductor–coil is strictly axisymmetric. The mathematical model and calculation procedure based on 2D finite element and 2D boundary element methods are described in Ref. [2]. Three-dimensional effects in this step are neglected and phase boundaries are calculated disregarding the part

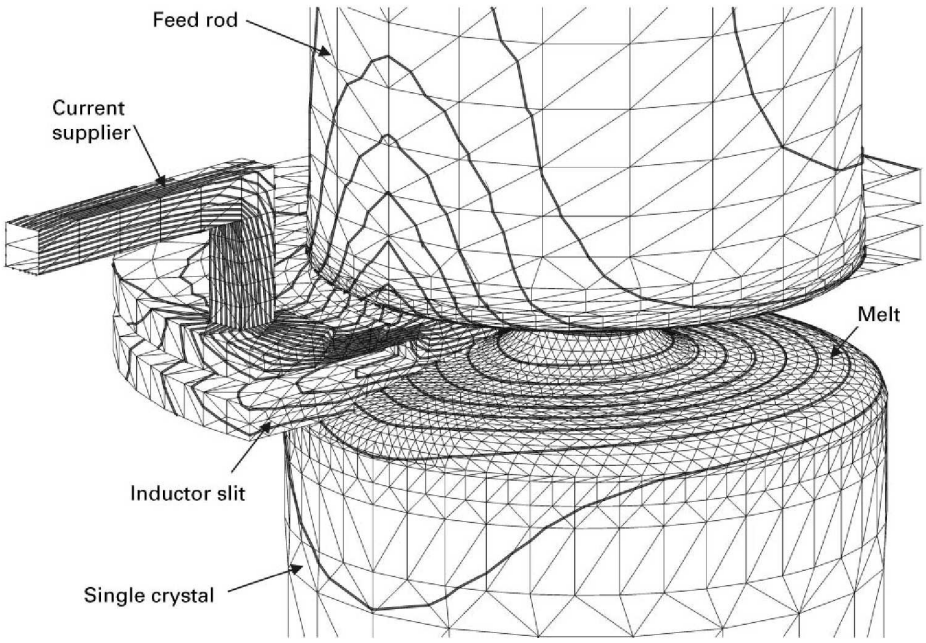

Fig. 1. 3D view of the EM model for the FZ-growth system with only a half of the inductor shown, triangular boundary elements and calculated lines of HF electric current stream function.

of the heat transfer caused by convection in the liquid zone.

(2) The 3D distribution of high-frequency electric currents induced in the skin-layer of the molten silicon and the Joulean heat sources density are obtained via 3D EM field calculations by using 3D boundary element method as described in Ref. [11]. The previously calculated 2D geometry of the molten zone is used to get an axisymmetric 3D geometry for the silicon molten zone and solid parts. The deviation of the shape of the molten zone from axial symmetry due to more or less non-symmetrically distributed EM forces is assumed to be small and is neglected. For the inductor, the real non-symmetric 3D shape is considered. This information about the FZ-system geometry is used to generate the triangular boundary element grid on the surfaces of the silicon and the inductor.

(3) The steady-state 3D calculations of the coupled hydrodynamic, temperature, and dopant concentration fields are carried out with the computational fluid dynamics program package FLUENT, version 4.32, by using control volume method as described in Refs. [12,13]. Power density of heat sources and EM forces, previously calculated on the triangular 3D boundary element mesh, are transferred to the structured 3D grid on the free melt surface for hydrodynamic calculations. For heat sources and EM forces, the high-frequency approximation is kept, which means replacing the detailed description of the exponential decay of power and force density in the skin-layer depth by an integral "surface value". The Marangoni forces are considered by means of a user-defined subroutine.

(4) The 3D dopant concentration field in the melt is calculated using FLUENT with additionally compiled user-defined subroutines including treatment of the segregation conditions at the crystallisation and melting interfaces. Finally, the normalised distribution of resistivity at the crystallisation interface is derived by assuming that it is inversely proportional to the dopant concentration. The resistivity variations in the

grown crystal (rotational striations) are calculated by accounting for the vertical movement and rotation of the crystal and for the curvature of the crystallisation interface.

3. 3D modelling and calculation of EM field

The high-frequency electromagnetic field in the FZ-system is essentially three-dimensional because of the non-symmetric HF inductor, even in the case of the axisymmetric approximation of the shape of silicon parts (feed rod, single crystal, and molten zone, whose vertical cross-section can be seen, e.g. in Fig. 3b). Due to the small penetration depth $\delta = 1/\sqrt{\pi\mu_0 f\kappa}$ of the 3D HF EM field ($f \approx 3$ MHz) in the copper inductor and in the silicon (κ being the conductivity of silicon or copper, respectively), the current distribution in the system can be described by a surface current density $\boldsymbol{i}$. When neglecting displacement currents, a scalar function defined on the surfaces and called electric stream function, ψ, can be introduced:

$$\boldsymbol{i} = \frac{\partial\psi}{\partial\xi_2}\boldsymbol{e}_1 - \frac{\partial\psi}{\partial\xi_1}\boldsymbol{e}_2, \tag{1}$$

where ξ_1 and ξ_2 are local orthogonal coordinates along the surface of the silicon or inductor with coordinate ξ_3 directed into the material and normal to the surface. $\boldsymbol{e}_1, \boldsymbol{e}_2$ and $\boldsymbol{e}_3$ are the corresponding unity vectors. The Bio–Savart law and the condition that in case of very high frequency the magnetic flux density normal to the surface is zero are used for the calculation of ψ. The surfaces of the conducting bodies are discretised using triangular boundary elements (Fig. 1). The values of the stream function are calculated in all nodes of the grid.

An example of the calculated distribution of the function ψ is shown in Fig. 1 as isolines with a constant step. The density of lines is related to the value of surface current density and the direction of lines corresponds to the direction of the current. From the value of $\boldsymbol{i}$, the respective surface power density q_{EM} on the free melt surface can be derived:

$$q_{EM} = \frac{i_{ef}^2}{\delta\kappa_M}, \tag{2}$$

where i_{ef} denotes the effective value of $\boldsymbol{i}$.

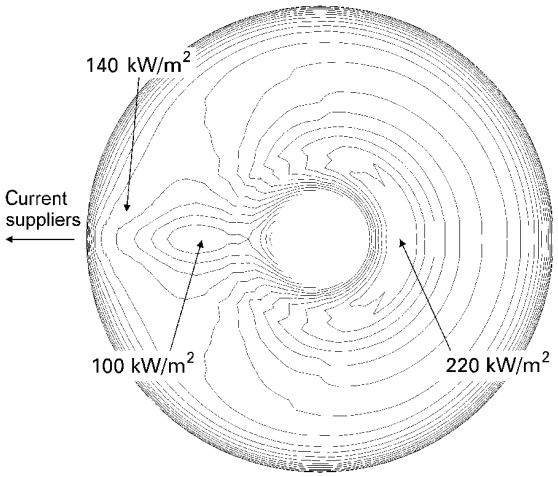

Fig. 2. Joulean power density q_{EM} on the free surface of the melt.

The calculated non-symmetric distribution of q_{EM} on the free surface of the molten zone (see an example in Fig. 2) is used as a boundary condition for the temperature calculation in the melt (Section 4).

Because of the non-symmetric distribution of the current density on the free melt surface, the electromagnetic force is also non-symmetric and should be taken into account in hydrodynamic calculations. From the expression for the force volume density $\boldsymbol{f}$,

$$\boldsymbol{f} = \boldsymbol{j} \times \boldsymbol{B} \tag{3}$$

and the Maxwell's equation for the specific case,

$$\mu_0 \boldsymbol{j} = \mathrm{rot}\,\boldsymbol{B}, \tag{4}$$

it follows that

$$\boldsymbol{f} = -\frac{1}{2\mu_0}\mathrm{grad}(B^2) + \frac{1}{\mu_0}(\boldsymbol{B}\nabla)\boldsymbol{B}. \tag{5}$$

The gradient part in Eq. (5) does not influence the velocity field directly because it is a potential force and can be compensated by pressure gradient in the melt. The second part of Eq. (5), in the case of distinct skin-effect, can be analysed under the assumption that the magnetic field $\boldsymbol{B}$ and the current volume density $\boldsymbol{j}$ in the skin-layer are parallel to the

surface (the local coordinates ξ_1, ξ_2, and ξ_3 are used again), i.e.

$$\boldsymbol{B} = \boldsymbol{e}_1 B_1 + \boldsymbol{e}_2 B_2, \quad B_3 = 0, \tag{6}$$

$$\boldsymbol{j} = \boldsymbol{e}_1 j_1 + \boldsymbol{e}_2 j_2, \quad j_3 = 0. \tag{7}$$

From the second part of Eq. (5) by using Eqs. (6), (7) and (4), we get the tangential force volume density in the skin-layer as a function of ξ_3:

$$\boldsymbol{f} = \frac{1}{2\mu_0}\left(\boldsymbol{e}_1 \frac{\partial B^2}{\partial \xi_1} + \boldsymbol{e}_2 \frac{\partial B^2}{\partial \xi_2}\right) = \frac{1}{2\mu_0}\mathrm{grad}_{1,2}(B^2). \tag{8}$$

In the considered case of a small penetration depth of electric current, the force volume density may be integrated over the skin-layer to get the tangential force surface density and the influence of $\boldsymbol{f}$ on melt hydrodynamics may be replaced by influence of the corresponding surface force. For hydrodynamics, only the time-averaged surface force value $\boldsymbol{F}_{\mathrm{EM}}$ is of interest:

$$\boldsymbol{F}_{\mathrm{EM}} = \int_0^\infty \bar{\boldsymbol{f}}\,\mathrm{d}\xi_3 = \frac{1}{2\mu_0}\mathrm{grad}_{1,2}\left[\int_0^\infty \bar{B}^2\,\mathrm{d}\xi_3\right], \tag{9}$$

where a line above the variable means averaging in time.

Because of the distinct skin-effect, it can be assumed that

$$\bar{B}^2 = \mu_0^2 i_{\mathrm{ef}}^2 \exp(-2\xi_3/\delta). \tag{10}$$

It follows from Eqs. (9) and (10) that

$$\boldsymbol{F}_{\mathrm{EM}} = \frac{1}{4}\mu_0 \delta\,\mathrm{grad}_{1,2}(i_{\mathrm{ef}}^2). \tag{11}$$

This surface force is used as a part of the boundary condition on the free melt surface in the hydrodynamic calculation (see below).

4. 3D modelling of HD, thermal, concentration fields and crystal resistivity

The 3D calculations of the coupled hydrodynamic, thermal, and dopant concentration fields are carried out with FLUENT [13] on a structured hexahedral 3D mesh over the axisymmetrical melt volume. The grid size is: 34 cells in radial direction, 44 cells in axial direction, and 24 cells in azimuthal direction. The non-symmetric distributions of heat sources (Fig. 2) and EM forces, calculated on the triangular 3D boundary element mesh, are transferred to the structured 3D grid. The hydrodynamic–thermal problem is assumed to be steady state. The investigation of hydrodynamic instabilities (i.e. transient calculation) with the 3D model needs a finer grid and more computer power and is not considered in this paper.

The melt flow is calculated as an incompressible laminar flow. The buoyancy force is considered with Boussinesq approximation. The corresponding 3D hydrodynamic equations are written as follows:

$$b_0(\boldsymbol{v}\nabla)\boldsymbol{v} = -\mathrm{grad}\,p + \eta\Delta\boldsymbol{v} - b_0\boldsymbol{g}\beta(T - T_0), \tag{12}$$

$$\nabla\boldsymbol{v} = 0, \tag{13}$$

where $\boldsymbol{v}$, p, and T are the velocity, pressure, and temperature fields, respectively, η, the viscosity, $\boldsymbol{g}$, the gravity, b_0, the density at melting point, and β, the linear thermal expansion coefficient. For the velocity vector $\boldsymbol{v}$, the cylindrical components $v_r(r,\alpha,z)$, $v_\alpha(r,\alpha,z)$, $v_z(r,\alpha,z)$ are used in calculations.

The boundary conditions for the velocity field consider the rotation of the feed rod and melting process at the melting interface:

$$v_r = 0, \quad v_z = -V_{\mathrm{M}}, \quad v_\alpha = 2\pi W_{\mathrm{F}} r, \tag{14}$$

where V_{M} is the supply velocity of molten silicon from feed rod and W_{F}, the rotation rate of feed rod. It is assumed that V_{M} is constant over the melting interface. On the growth interface, the crystallisation process and the rotation of the crystal are considered:

$$v_{\mathrm{r}} = 0, \quad v_z = -V_{\mathrm{Cr}}, \quad v_\alpha = 2\pi W_{\mathrm{Cr}} r, \tag{15}$$

where V_{Cr} is the growth rate of the single crystal and W_{Cr}, its rotation rate.

The free melt surface is considered as a frictionless boundary, and the momentum sources due to the surface force $\boldsymbol{F}$ are involved near the surface. For the total value of $\boldsymbol{F}$, both the electromagnetic force (11) and Marangoni force are accounted:

$$\boldsymbol{F} = \boldsymbol{F}_{\mathrm{EM}} + \frac{\partial\gamma}{\partial T}\mathrm{grad}_{1,2}\,T. \tag{16}$$

The steady-state temperature field $T(r,\alpha,z)$ is calculated simultaneously with velocity field as follows:

$$b_0 c_p(\boldsymbol{v}\nabla)T = \lambda\Delta T, \tag{17}$$

where λ is the thermal conductivity and c_p, the specific heat. As boundary condition on the melting and crystallisation interfaces, the melting temperature is used. On the free melt surface, the heat flux corresponding to the electromagnetic power surface density (2) is applied.

The steady-state concentration field $C(r,\alpha,z)$ is obtained from the calculated velocity field by using the 3D equation of diffusion:

$$(\boldsymbol{v}\nabla)C = D\Delta C, \tag{18}$$

where D is the binary diffusion coefficient of the dopant in silicon and $\boldsymbol{v}(r,\alpha,z)$, the calculated velocity field. The following boundary condition at the growth interface describing the segregation effect is used:

$$D\frac{\partial C}{\partial n} = V_{Cr}(1-k_0)C\cos(\theta), \tag{19}$$

where n refers to the inner normal direction of the molten zone, θ denotes the local angle between the growth interface and radial direction, and k_0 is the equilibrium segregation coefficient. At the melting interface, the boundary condition is again coupled with the value of concentration C on this boundary:

$$D\frac{\partial C}{\partial n} = -V_M(C_F - C)\cos(\theta), \tag{20}$$

where C_F is the dopant concentration in the feed rod (concentration values are normalised by setting $C_F = 1$). In practice, because of the relatively high value of V_M, it is a sufficiently good approximation to take a simpler boundary condition for the melting interface:

$$C = C_F. \tag{21}$$

To obtain the rotational striations (i.e. the resistivity oscillations along the axis of the grown crystal), it is necessary to switch from the fixed coordinates, (r,α,z), to the reference system of the rotating and downwards moving single crystal, (r,α',z'). If the shape of the curved axisymmetric crystallisation interface is given by $z = z_{Cr}(r)$ and the concentration at this interface is described by the function $C_{Cr}(r,\alpha) = C(r,\alpha,z_{Cr}(r))$, then the corresponding normalised resistivity distribution $\rho(r,\alpha',z')$ in the grown crystal equals

$$\rho(r,\alpha',z') = [k_0 C_{Cr}(r,\alpha_{Cr})]^{-1} \tag{22}$$

with

$$\alpha_{Cr}(r,\alpha',z') = 2\pi\frac{z'-z_{Cr}(r)}{V_{Cr}}W_{Cr} + \alpha'. \tag{23}$$

Formulas (22) and (23) are used to calculate the resistivity distribution in the grown crystal from a given steady-state distribution of dopant concentration at crystallisation interface in the laboratory reference system (r,α,z), in which the position of the inductor is fixed.

5. Characteristics of the chosen FZ-system

The results below, calculated for floating zone growth of 4″ silicon crystals, are based on the laboratory experiment at the Institute of Crystal Growth, Berlin. The used physical properties of silicon and main growth parameters are given in Table 1. The shape of the modelled HF inductor can be seen in Fig. 1. The slit width of 1 mm is used in calculations.

6. Results of 3D calculations

The surface currents and the corresponding surface density of heat sources from 3D EM calculations are shown in Figs. 1 and 2, for the specific FZ-system (Section 5, Table 1). In Fig. 2 and in the following figures considering the molten zone, the inductor slit is on the left side.

The 3D hydrodynamic–thermal calculations with the finite difference grid described in Section 4 lead to the coupled temperature and velocity fields in the molten zone. In Fig. 3a, the temperature distribution on the free melt surface with a distinct asymmetry of the thermal field is shown from the top. The region of maximum temperature corresponds to the opposite-to-slit side of the

Table 1
Physical properties of silicon and process parameters

Melting temperature, T_0	1685 K
Melt density at melting point, b_0	2530 kg/m^3
Linear thermal expansion coefficient, β	1.4×10^{-4} K^{-1}
Viscosity, η	8.6×10^{-4} kg/m s
Specific heat, c_p	1000 J/kg K
Thermal conductivity of the melt, λ_M	67 W/m K
Thermal conductivity of solid silicon, $\lambda_{F,Cr}(T)$	$(4.495–7.222\ (T/T_0) + 3.728\ (T/T_0)^2)\times 22$ W/m K
Emissivity of the melt, ε_M	0.27
Emissivity of solid silicon, $\varepsilon_{F,Cr}(T)$	$0.46\times\{1.39$, if $T/T_0 < 0.593; 1.96–0.96\ (T/T_0)$, if $T/T_0 \geqslant 0.593\}$
Latent heat of fusion, q_0	1.8×10^6 J/kg
Electrical conductivity of the melt, κ_M	1.2×10^6 1/Ω m
Electrical conductivity of solid silicon, $\kappa_{F,Cr}$	5.0×10^4 1/Ω m
Surface tension at melting point, γ	0.74 N/m
Thermal gradient of surface tension, $d\gamma/dT$	-1.0×10^{-4} N/m K
Diffusion coefficient of phosphorous, D	3.4×10^{-8} m^2/s
Equilibrium segregation coefficient of phosphorous, k_0	0.35
EM field frequency, f	2.8 MHz
Electric current in inductor (effective value), I_0	1000 A
Single-crystal rotation rate, W_{Cr}	5 rpm
Feed rod rotation rate, W_F	-20 rpm
Growth rate (i.e. single crystal pull rate), V_{Cr}	3.4 mm/min
Single-crystal radius, R_{Cr}	52.5 mm
Feed rod radius, R_F	48.6 mm
Central hole (inner) radius of the inductor, R_H	17.5 mm
Maximum (outer) radius of the inductor, R_I	82.4 mm
Melt–feed–gas triple point radial coordinate, R_N	10.9 mm
Melt supply velocity from feed rod, V_M (averaged along the feed–melt interface)	78.8 mm/min

inductor but is shifted in the direction of single crystal rotation because of the influence of convective heat transfer. Fig. 3b shows the temperature distribution in the volume of the molten zone in the vertical cross-section that corresponds to the plane of the inductor slit. It can be seen that the temperature distribution strongly deviates from the axial symmetry, especially near the free melt surface.

The calculated 3D velocity distribution is illustrated in Figs. 4, 5a and b. In Fig. 4, the velocity vectors on the free melt surface can be seen. Fig. 5a shows the velocity in the vertical cross-section in the plane of the inductor slit with only the radial and axial components of the velocity vectors shown. The maximum of the velocity magnitude is reached at the free surface near the melting interface due to a steep temperature gradient and, consequently, a strong Marangoni force at this location. Another but smaller maximum exists at the peripheral part of the free surface, where EM force dominates over Marangoni force. Due to asymmetry of EM and Marangoni forces, which mostly are acting in opposite directions, the following features of non-symmetry of the velocity field are observed: (1) the velocity maxima at the free surface are different comparing the slit side and the opposite-to-slit side; characteristically the maxima at the opposite-to-slit side are stronger, as it can be seen on the right-hand side in Fig. 5a; (2) the structure of vortices differs qualitatively, especially in the regions of high velocity, comparing the slit side and the opposite-to-slit side; (3) fluid flow is going through the geometrical symmetry-axis of the molten zone; this takes place also in the vicinity of the centre of the crystallisation front, where a non-zero horizontal velocity component can be observed.

In Fig. 5b, we see the distribution of the magnitude of the azimuthal velocity component, which is also non-symmetric due to the non-symmetric convective momentum transport in the vertical

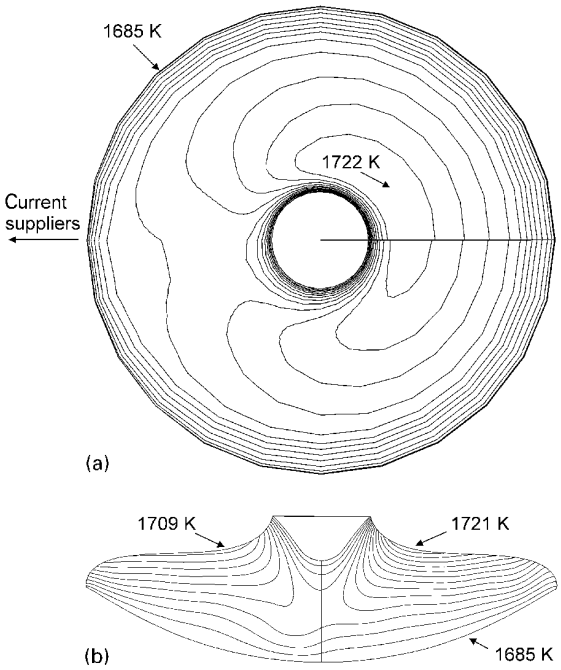

Fig. 3. Temperature field: (a) temperature on the free melt surface (view from top) and (b) in the vertical cross-section corresponding to the plane of inductor slit.

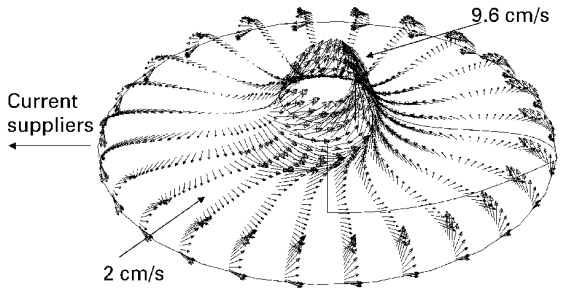

Fig. 4. Velocity vectors on the free surface of the melt.

cross-section of the molten zone. As Figs. 4, 5a and b show, the non-symmetry of EM, Marangoni and buoyancy forces does not fully destroy the quasi-axial-symmetry of the velocity field. The crystal rotation makes the hydrodynamics in the molten zone remaining roughly axisymmetric.

The fluid velocity distribution is used to calculate the dopant concentration field. Fig. 5c illustrates

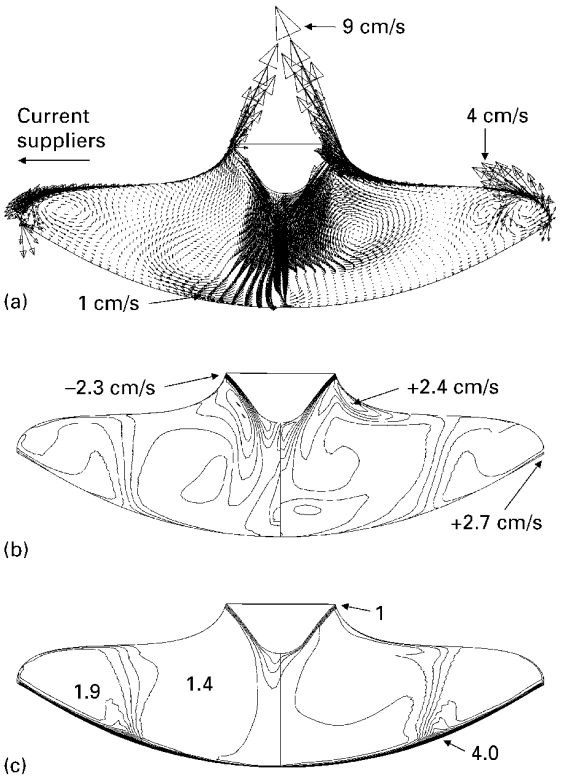

Fig. 5. Velocity and concentration fields in the vertical cross-section in the plane of inductor slit: (a) velocity vectors projected to the plane of the cross-section, (b) azimuthal velocity component and (c) dopant concentration.

the normalised concentration distribution in the vertical cross-section of the molten zone. A distinct concentration boundary layer in the vicinity of the growth interface can be observed. The influence of the main fluid flow vortices (see Fig. 5a) gives rise to the maximum of concentration in the region where fluid flow is going away from the crystallisation interface. In Fig. 6, the distribution of concentration in the melt at the growth interface, $C_{Cr}(r, \alpha)$, is shown. This distribution has significant asymmetry in the central region. At the periphery, the deviations from axial symmetry are rather small.

The dopant distribution along the crystallisation interface is responsible for the dopant incorporation in the growing crystal. Since the solution, described above, concerns the laboratory reference

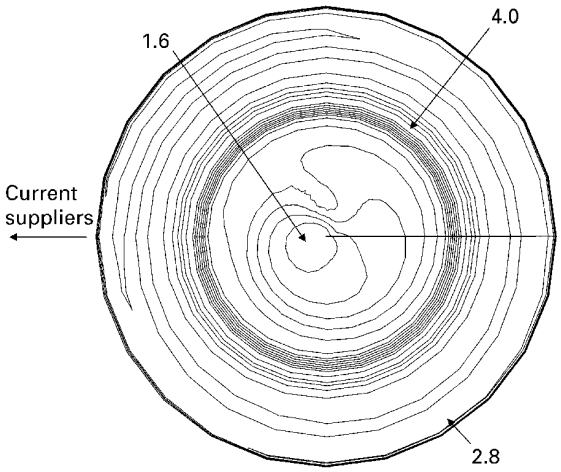

Fig. 6. Dopant concentration $C_{Cr}(r,\alpha)$ in the melt at the crystal growth interface.

system, where the crystal is rotating and moving downwards, the deviation from axial symmetry of the distribution of $C_{Cr}(r,\alpha)$ causes generation of resistivity inhomogeneities (rotational striations) in the crystal (see Eqs. (22) and (23)). The resulting normalised resistivity distribution, $\rho(r,\alpha',z')$, along a 10 mm long part of a longitudinal cut ($\alpha' = \text{const}$) of the grown crystal rod is shown in Fig. 7, where rotational striations with the typical alternating crest-trough pattern can be seen. At the crystal axis, the crests from one side meet troughs from the opposite side (half wavelength phase shift). Besides the longitudinal resistivity variations, also the small-wavelength variations along the radial direction of the crystal are observed. These radial variations are caused by the curvature of the crystallisation interface, which reflects itself in the herringbone-form of the crest-trough pattern. The calculated resistivity distribution shows that the largest rotational striations (reaching almost 30%) are present near the central part of the crystal. Small variations can be seen also near the outer rim of the rod. The overall distribution of resistivity contains also large-scale resistivity variations along the crystal radius. These macroscopic variations represent the axisymmetric part of the concentration distribution at the growth interface.

For comparison with photo-scanning measurements (see Section 8), the distribution of the axial derivative of the resistivity, $\partial\rho/\partial z'$, is calculated. To analyse the longitudinal variations of resistivity in the grown crystal, a Fourier analysis of $\partial\rho/\partial z'$ in axial direction is done. Instead of wave-numbers,

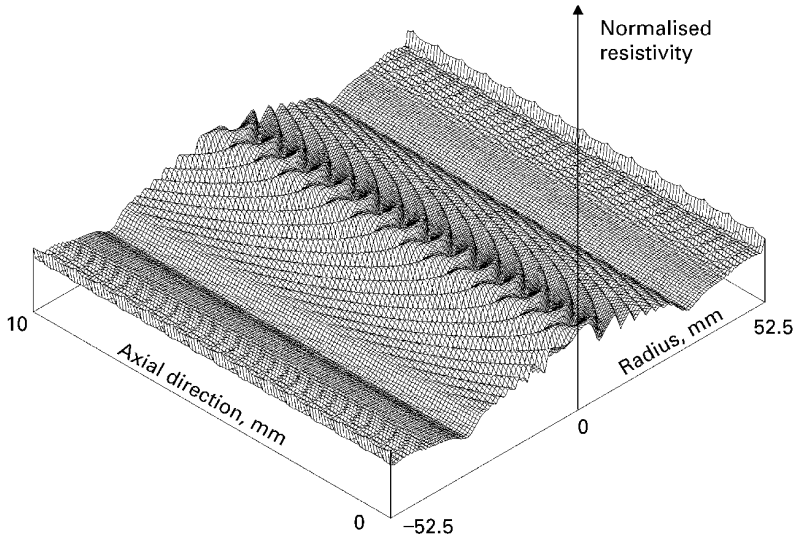

Fig. 7. From 3D steady-state calculations: distribution of resistivity $\rho(r,\alpha',z')$ in the vertical cross-section ($\alpha' = \text{const}$) of the rotating crystal.

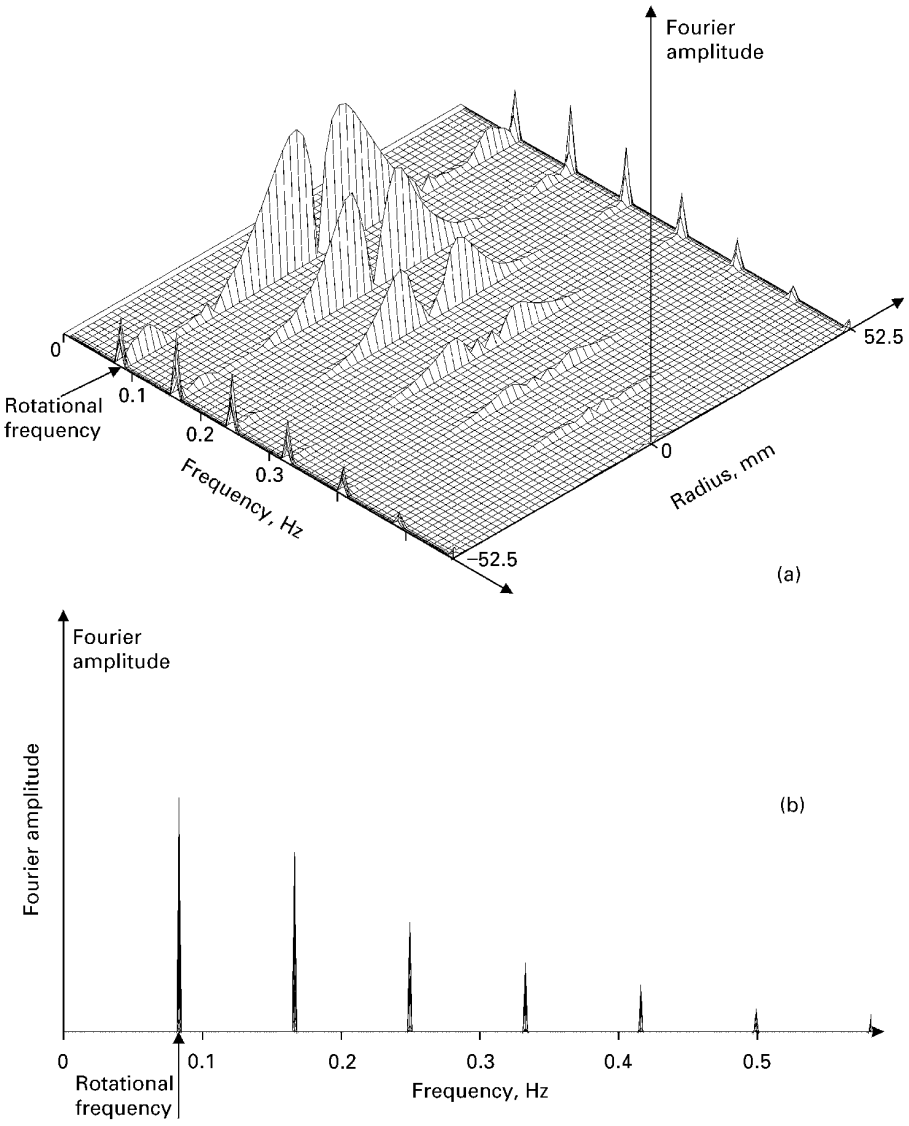

Fig. 8. From 3D steady-state calculations: Fourier analysis of $\partial\rho/\partial z'$ in axial direction.

we consider henceforth the frequencies of the local temporal variations of dopant incorporation at the rotating crystal's growth interface, which are directly related to the wave-numbers through the crystal growth velocity. The obtained distribution of Fourier amplitudes along the diameter of the crystal rod is shown in Fig. 8. The 3D calculations are steady-state, therefore, the corresponding spectrum is essentially discrete and has the lowest frequency, i.e. "first harmonic", equal to that of crystal rotation ($W_{Cr} = 5\,\text{rpm} \approx 0.083\,\text{Hz}$). The wavelength of the first harmonic of the longitudinal striations is 0.68 mm in crystal's axial direction at the used growth parameters (Table 1). Two symmetric regions of high Fourier amplitudes near the central part of the crystal can be observed (Fig. 8a).

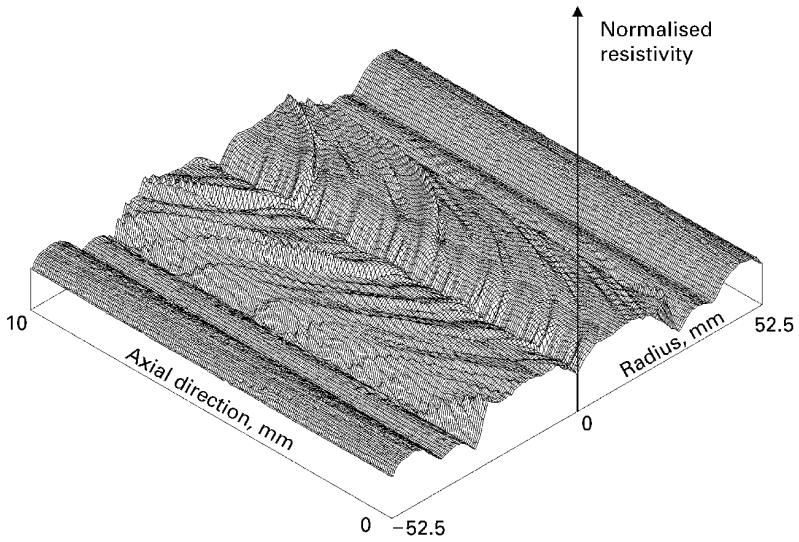

Fig. 9. From 2D transient calculations: axisymmetric distribution of resistivity $\rho_{2D}(r, z')$ in the vertical cross-section of the crystal.

Although the crystal rotation frequency dominates in the resistivity oscillations, the attenuation of amplitudes of higher harmonics is rather slow as shown in the sideview in Fig. 8b. Regarding Fig. 6, it is obvious that the first harmonic in the central part of crystal arises due to the shifting of the concentration minimum from the centre of the growth interface. The mechanism for the second harmonic is most easy imagined as originating from elliptical shape of the concentration minimum.

Since the calculated 3D flow is steady-state, the corresponding resistivity variations do not include the oscillations caused by hydrodynamic instabilities. It has been shown that the real-life flow in the considered FZ-system is time-dependent and the steady-state solution is an approximation to a certain degree of accuracy.

7. 2D transient calculations

The size of the 3D control volume grid makes it difficult to investigate the unstable fluid flow modes via transient calculations, and normally, only steady-state flow is calculated; it can be done due to sufficiently high numerical viscosity of the finite difference scheme in 3D calculations on a comparatively coarse grid. Therefore, the contribution in resistivity variations of the hydrodynamic instabilities is analysed on the basis of 2D transient calculations. The axisymmetric coupled hydrodynamic–thermal calculations for the system described in Table 1 are performed on a very fine 2D finite element grid. The corresponding numerical viscosity is low and therefore a time-dependent fluid flow can be obtained. The oscillating hydrodynamic fields are stored for the total time period of 800 s and used for the calculation of the transient concentration field $C_{2D}(r, z, t)$.

The time-dependent distribution of concentration at the growth interface, $C_{2D\,Cr}(r, t)$, is used to derive the axisymmetric resistivity distribution $\rho_{2D}(r, z')$. For a 10 mm long part of a longitudinal cut of the crystal, it is shown in Fig. 9 and displays more distinct resistivity oscillations in the central part than at the periphery. It can be seen that the crest-trough pattern is symmetric: at the axis, a crest from one side meets an equal crest from the opposite side, and not a trough, as in the case of 3D calculations. The Fourier analysis of $\partial\rho_{2D}/\partial z'$ in axial direction is illustrated in Fig. 10. The spectrum is discrete because a finite time period or, equivalently, a finite crystal length is analysed. For

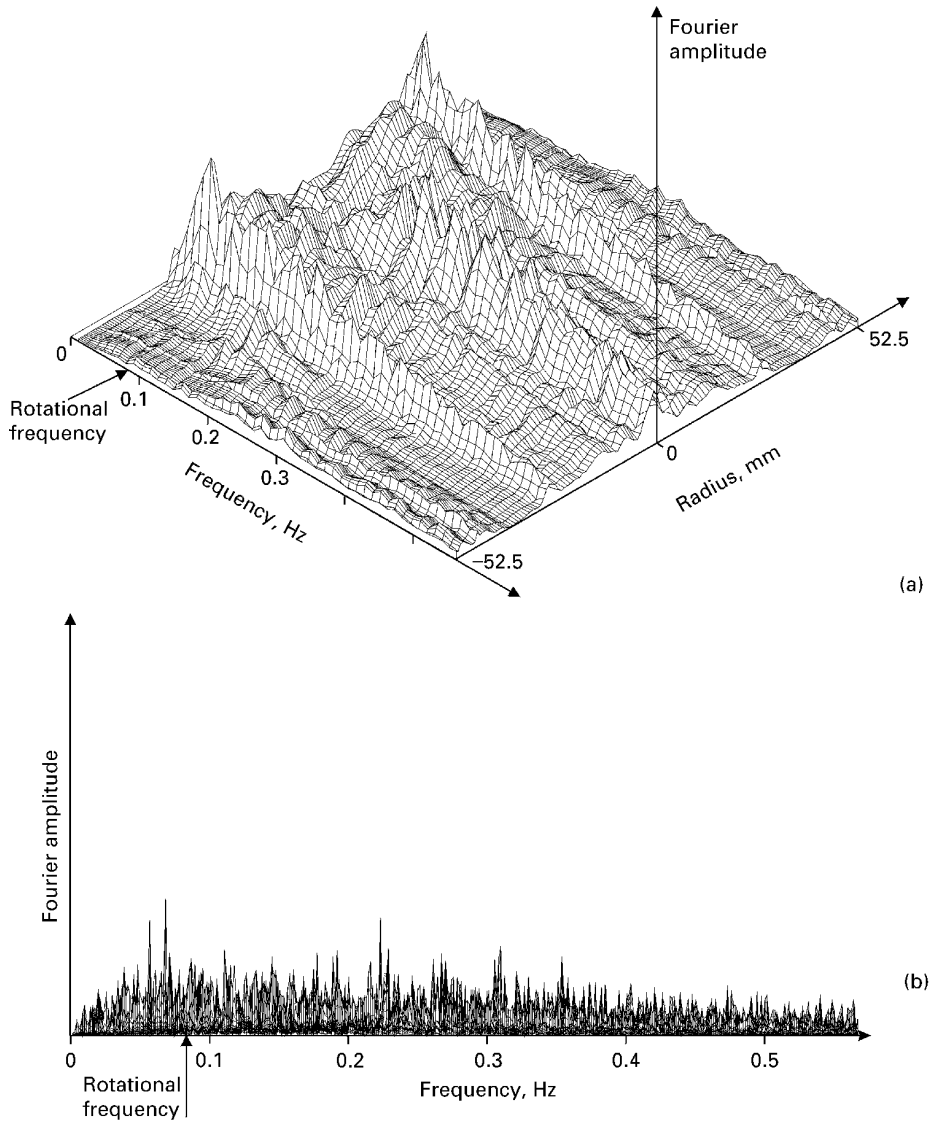

Fig. 10. From 2D transient calculations: Fourier analysis of $\partial\rho_{2D}/\partial z'$ in axial direction.

a 40 mm long crystal part, the spectral resolution threshold is about 0.0014 Hz, at the used growth parameters. In general, spectrum may depend on the sample length, which determines the values of the allowed discrete frequencies. Analysis of 40, 30, 20 and 10 mm long samples has been performed. The spectra have been compared after taking sums over the squares of some neighbouring Fourier amplitudes to impose a common artificially low spectral resolution of 0.0112 Hz (in order to enable comparison of the different spectra). A good agreement has been found between the cases of 40, 30 and 20 mm, which means that the spectrum, for these lengths, is not essentially dependent on the length of the chosen sample. The amplitudes distribution in Fig. 10a is based on the imposed

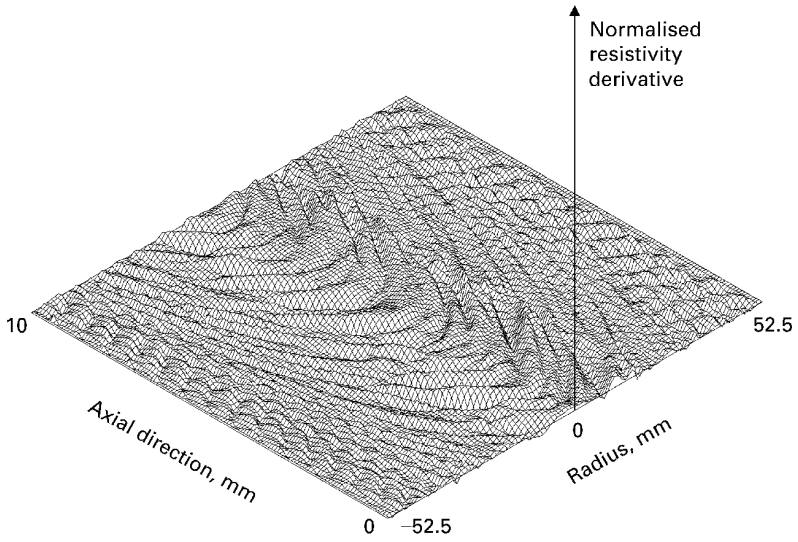

Fig. 11. Experimental data: Distribution of the axial derivative of resistivity, $\partial\rho_{exp}/\partial z'(r,\alpha',z')$, in the vertical cross-section ($\alpha' = \text{const}$) of the crystal.

resolution of 0.0112 Hz, while the sideview in Fig. 10b illustrates the spectrum of a 40 mm long sample with the threshold resolution of 0.0014 Hz.

It can be seen that higher and lower frequencies than the crystal rotation frequency W_{Cr} exist in the resistivity oscillations. That is a significant difference from 3D case, where frequencies lower than W_{Cr} cannot be obtained in principle. Thus, the low frequencies in Fig. 10 are originated exclusively due to the transient character of the flow.

Comparison of Figs. 9 and 7 show also some differences in the macroscopic variations of resistivity along the radius of the crystal. Namely, the axisymmetric flow gives rise to a local concentration maximum and resistivity minimum at the centre of the crystallisation interface because the axial symmetry induces a flow separation point at this location. The 3D calculations do not show such effect because the flow is passing the geometrical symmetry-axis.

8. Experimental measurements

For comparison of the calculation results with experiment, the FZ-grown silicon crystal is cut vertically and the resistivity derivative $\partial\rho_{exp}/\partial z'$ in the longitudinal cross-section of the crystal is measured by the photo-scanning method. The measured distribution, $\partial\rho_{exp}/\partial z'(r,\alpha',z')$ with $\alpha' = \text{const}$, is shown in Fig. 11. The corresponding Fourier analysis in axial direction is illustrated in Fig. 12. Similarly as it was in Fig. 10 for 2D case (see above), Fig. 12b shows a spectrum with the threshold resolution of 0.0014 Hz, which is obtained from analysing the data of a 40 mm long crystal part, while the distribution in Fig. 12a is based on the low resolution of 0.0112 Hz obtained after taking sums over the neighbouring Fourier amplitudes.

In general, there is a qualitative agreement between the experimental and calculated 3D results: similar alternating crest–trough patterns with the same wavelength can be observed (compare Fig. 11 with Fig. 7). The crests from one side meet the troughs from the opposite side, although it cannot be seen very distinctly in Fig. 11 because of somewhat smoothened distribution. The spectra are also similar in the sense that both 3D calculation and experiment give the two characteristic regions of maximum Fourier amplitude near the central part of crystal and smaller amplitude maximums near the outer rim, as comparison of Fig. 12a with Fig. 8a shows.

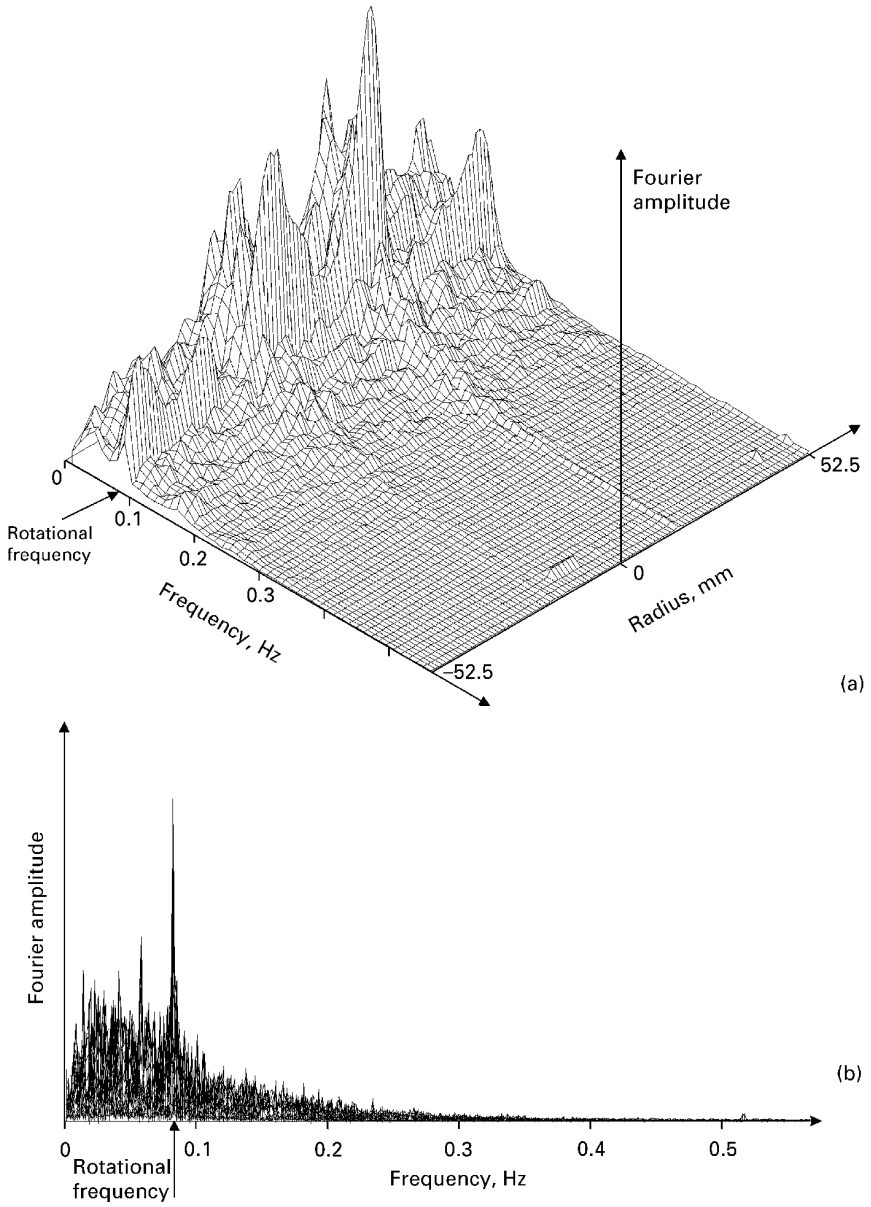

Fig. 12. Experimental data: Fourier analysis of $\partial\rho_{exp}/\partial z'$ in axial direction.

There are some differences between the experimental and the 3D calculation results. The first difference is obvious: the presence of oscillation frequencies lower than the rotational one in the distribution of experimental Fourier amplitudes and its absence in the three-dimensionally calculated spectrum. As shown by 2D transient calculations, the low frequencies can arise due to hydrodynamic instabilities.

Another difference is that the experiment exhibits a very distinct peak of Fourier amplitudes at the rotation frequency and the amplitudes diminish

fast with increasing frequencies, while we see a rather long tail of relatively high frequencies in the results of 3D and 2D calculations. It has been estimated that the resolution of the photo-scanning measurements is good enough to allow to measure frequencies up to about the seventh harmonic of the rotational frequency. Although a clear answer can be given only after additional studies, the following reason of the mentioned difference is assumed at this stage: the presented 3D calculations do not include all of the sources of non-symmetry, because the shape of the free melt surface has been kept axisymmetric. It could be expected that, with accounting for the real-life non-symmetry of the melt free surface, the 3D calculations would give a more asymmetric result and, consequently, relatively higher normalised Fourier amplitude for the rotational frequency.

9. Conclusions

(1) Three-dimensional numerical modelling is carried out to analyse the floating zone crystal growth with the needle-eye technique used for the production of high-quality silicon crystals with large diameters. The shape of the molten zone is taken from 2D calculations and kept axisymmetric. A non-symmetric HF electromagnetic field of the pancake inductor is calculated. The obtained non-symmetrical power distribution on the free melt surface and the corresponding EM forces are used for the calculation of the coupled 3D hydrodynamic and temperature fields in the molten zone. The buoyancy, Marangoni and EM forces are considered and a steady-state non-symmetric flow structure is obtained.

(2) The 3D hydrodynamic field is used to calculate the corresponding non-symmetric dopant concentration field in the melt. Accounting for the effect of non-symmetry and crystal rotation, the variations of resistivity (rotational striations) in the grown single crystal are obtained. Longitudinal resistivity oscillations near the crystal axis of almost 30% are found to be considerably higher than at the periphery.

(3) The results of 3D calculations are compared with experimental data of photo-scanning measurements of the resistivity variations in the longitudinal cut of the crystal and with results of unsteady 2D calculations. A Fourier analysis of the resistivity variations is done. The 2D results show the influence of hydrodynamic instability on the crystal resistivity like low-frequency resistivity variations due to flow unsteadiness. In the experimental resistivity distribution, both the influence of rotation (rotational striations) and of hydrodynamic instability are observed. The rotation frequency dominates over other frequencies of resistivity variations. The 3D calculation results show certain qualitative agreement with experiment. The major difference is in the relative weight of the amplitude of rotational frequency among the other frequencies. It is explained by the suppressed asymmetry of the system, i.e. the approximation of axisymmetric molten zone shape.

(4) A further increase of accuracy of the 3D calculations could be achieved by accounting for the asymmetry of the shape of the molten zone and considering the time-dependence of the three-dimensional flow.

Acknowledgements

The authors are grateful for the support received from VW foundation, Hanover, Germany.

References

[1] K.H. Lie, J.S. Walker, D.N. Riahi, J. Crystal Growth 100 (1990) 450.
[2] A. Mühlbauer, A. Muiznieks, J. Virbulis, A. Lüdge, H. Riemann, J. Crystal Growth 151 (1995) 66.
[3] Z. Guo, S. Maruyama, S. Togawa, J. Crystal Growth 194 (1998) 321.
[4] S. Togawa, Y. Nishi, M. Kobayashi, Electrochem. Soc. Proc. 98–13 (1998) 67.
[5] C.W. Lan, S. Kou, J. Crystal Growth 108 (1991) 351.
[6] A. Mühlbauer, A. Muiznieks, J. Virbulis, J. Crystal Growth 180 (1997) 372.

[7] A.Lüdge, H. Riemann, W. Schröder, A. Muiznieks, G. Raming, Experimental confirmation of a numerical model of doping distribution for floating-zone silicon growth with the needle eye technique, Proceedings of the Eighth International Symposium on Silicon Materials Science and Technology, San Diego, May 3–8, 1998, p. 2.
[8] A. Mühlbauer, A. Muiznieks, G. Raming, H. Riemann, A. Lüdge, J. Crystal Growth 198/199 (1999) 107.
[9] T. Munakata, I. Tanasawa, J. Crystal Growth 206 (1999) 27.
[10] T. Kaiser, Magnetohydrodynamische Effekte bei der Halbleiterkristallzüchtung, Dissertation, Geowissenschaftliche Fakultät der Albert-Ludwigs-Universität Freiburg i. Br. 1998.
[11] A. Mühlbauer, A. Muiznieks, H.-J. Leßmann, Arch. Elektrotech. 77 (1994) 157.
[12] S. Patankar, Numerical Heat Transfer and Fluid Flow, Hemisphere Publishing Corp., Washington DC, 1980.
[13] Fluent User's Guide (Version 4.3), Fluent Inc.
[14] G. Ratnieks, A. Muiznieks, L. Buligins, G. Raming, A. Mühlbauer, Magn. Gidrodinamika 35 (3) (1999) 278.

6.4 Included paper 3: Unsteadiness and parametric study

The third paper complements the previous study of rotational striations in two ways. First the numerical model of the 3D flow is revisited and the numerical approach is refined in order to resolve the unsteadiness of the flow. Indeed, the flow shows considerable time-dependence and the spectrum of resistivity fluctuations in the crystal gets filled by the frequencies of the hydrodynamic oscillations. The effect of the flow unsteadiness on the rotational striations is, however, not large, which justifies the steady-state approach. The second key aspect of the paper is the dependence of the rotational striations on a couple of parameters: the crystal rotation rate and width of the inductor slit.

The results of the studies have been published as included below in the article [66] in *Journal of Crystal Growth*. Additionally, some results are summarized in a graphical form in Fig. 6.2.

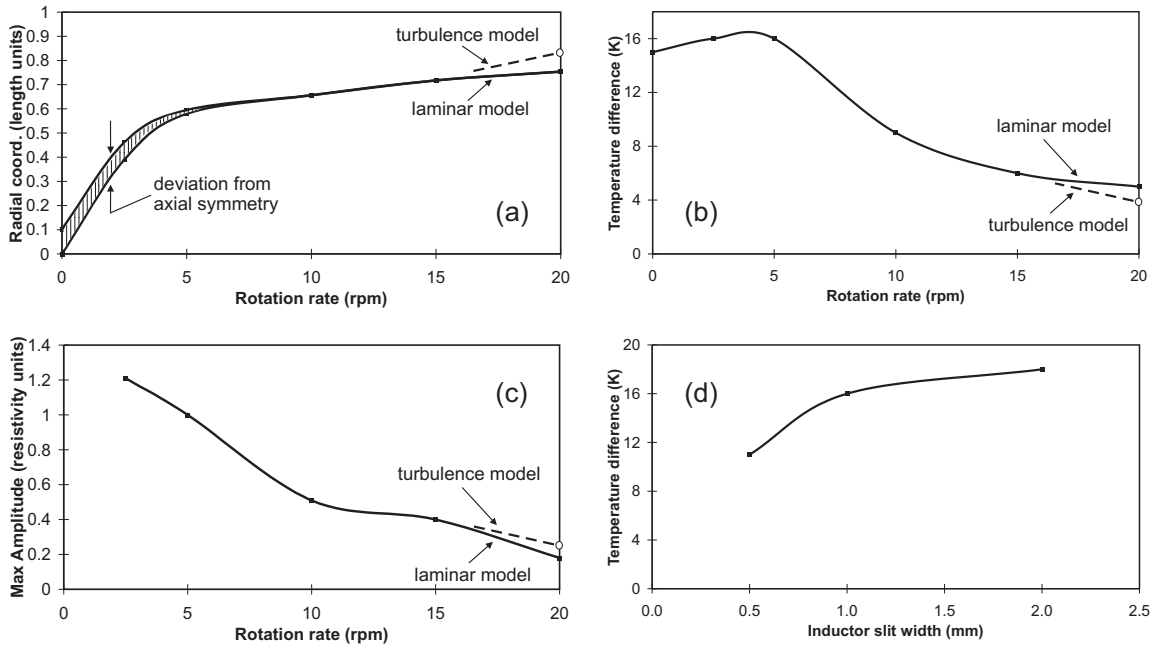

Figure 6.2: Dependence on crystal rotation rate or inductor slit width of: (a) the radial position of the dopant concentration maximum; (b,d) the characteristic temperature difference at the free surface; and (c) the maximum Fourier amplitude of rotational striations.

ELSEVIER

Journal of Crystal Growth 230 (2001) 48–56

JOURNAL OF CRYSTAL GROWTH

www.elsevier.com/locate/jcrysgro

Numerical 3D study of FZ growth: dependence on growth parameters and melt instability☆

G. Ratnieks[a], A. Muižnieks[a,b,*], A. Mühlbauer[b], G. Raming[b]

[a] *Department of Physics, University of Latvia, Zellu str. 8, LV-1002 Riga, Latvia*
[b] *Institute for Electroheat, University of Hanover, Wilhelm-Busch-Str. 4, D-30167 Hanover, Germany*

Abstract

Three-dimensional modelling of the floating zone (needle-eye) crystal growth process is carried out to analyse numerically the stability of the melt flow and the influence of the crystal rotation rate and inductor slit width on the 3D flow field and on the grown crystal resistivity. The unsteadiness of the melt is simulated and it is found that for the considered growth parameters a steady-state flow can be a reasonable approximation to the unsteady melt motion. The parametric studies have shown that increasing the rotation rate essentially changes the flow pattern and weakens the rotational striations, while the inductor slit width has a more local influence on these characteristics.

Keywords: A1. Computer simulation; A1. Fluid flows; A1. Mass transfer; A2. Floating zone technique; B2. Semiconducting silicon

1. Introduction

For the floating zone (FZ) growth of large-diameter ($\geqslant 100$ mm) silicon rods, the needle-eye technique and a high frequency electromagnetic field (≈ 3 MHz) are used. Two-dimensional (i.e. axisymmetric) models and the calculation methods of the processes during FZ growth have been considered in numerous studies, e.g. Refs. [1–8]. In fact, the pancake inductor has only one turn and current suppliers with a slit between them (see the sketch of one half of the system in Fig. 1), therefore the EM field and the distribution of heat sources are only roughly axisymmetric even if the rest of the system arrangement can be assumed as axisymmetric. The non-symmetry together with crystal rotation generates the small-scale inhomogeneities of resistivity in the grown crystal rod that are called rotational striations. Some three-dimensional (3D) aspects of non-industrial FZ processes with small crystal diameters have been considered in Ref. [9]. Also 3D calculations of an industrial FZ process have been carried out [10–12]. In Ref. [11], the influence of the 3D electromagnetic, Marangoni and buoyancy forces is studied, while in Ref. [12] the rotational striations are analysed

☆This paper presents results obtained within the frame of a cooperation project sponsored by VW foundation, Hanover, Germany. Cooperation partners of this project: Institute for Electroheat, University of Hanover, Germany and Department of Physics, University of Latvia, Latvia.

*Corresponding author. Institute for Electroheat, University of Hannover, Wilhelm-Busch-Str. 4, D-30167, Hannover, Germany. Tel.: +49-511-762-2872; fax: +49-511-762-3275.

E-mail address: muizniek@ewh.uni-hannover.de (A. Muižnieks).

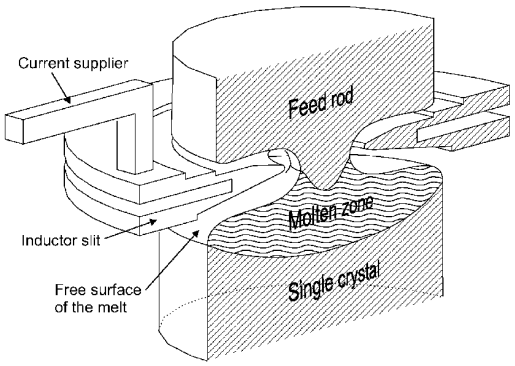

Fig. 1. 3D view of the FZ-growth system (half cut).

and compared with experiment. However, a 3D study of dependence of the process on the various growth parameters has been still lacking.

In the present paper, the 3D studies are continued in order to analyse the influence of the crystal rotation rate and the width of inductor slit on the 3D flow field and on the grown crystal resistivity as well as to check the validity of the steady-state laminar flow model, which is done by performing the transient flow analysis.

2. Modelling methods

Since a more complete information about the used modelling methods can be found in Ref. [12], only a short summary is given here. An axisymmetric shape of the molten zone is obtained by solving 2D thermal–electromagnetic problem and assuming axial symmetry of the inductor (2D finite element and boundary element methods). The distribution of the high-frequency electric current in the skin-layer of the melt is obtained via 3D EM field calculations (3D boundary element method). The previous axisymmetric geometry of silicon parts is retained and the three-dimensionality of EM forces and heat sources follows from the asymmetry of the inductor. The 3D calculations of the coupled hydrodynamic, temperature, and dopant concentration fields in the molten zone are carried out with the finite volume method using the commercial CFD-code FLUENT [13] (version 4.48, with user-defined subroutines). The non-symmetric distributions of heat sources and EM forces as well as the buoyancy and Marangoni forces are considered. The resistivity variations in the grown crystal, i.e., rotational striations are calculated from the (transient) dopant concentration at the crystallisation interface.

3. Unsteadiness

For the considered FZ-Si process (2.8 MHz EM field, 5 rpm rotation of crystal, $\varnothing$ 100 mm; see Ref. [12] for a complete list of parameters), the characteristic Reynolds number reaches a relatively high value ($\approx$ 4000), which may lead to unstable flow conditions.

If using a computational grid in the molten zone of about 40,000 cells, i.e., control volumes (the number of cells in radial, axial and azimuthal directions being 34, 44 and 24, respectively), then normally a converged result for the steady-state flow is obtained. However, when refining the grid two times in each direction, which leads to ca. 300,000 cells (with the respective number of cells in radial, axial and azimuthal directions being 66, 92 and 48, respectively) it is observed that no steady-state convergence may be obtained more. This is interpreted so that, with refining mesh, the numerical viscosity of the discretisation scheme has been lowered enough to resolve the physical unsteadiness of the flow. Therefore, the fine grid calculations have been performed in the time-dependent manner with a time step of 2.5 ms. Calculations have been done for about 77 s starting from a partly converged result of a steady-state calculation.

The results of the transient flow and dopant field calculations are illustrated in Fig. 2. The frames, arranged in columns, show the fields at three sequential time instants with increment of 2.5 s. In the cross-section of the melt, the characteristic vortex shedding at the left part (underneath the inductor slit) is observed. Although the flow field behaviour is rather complicated and lacks a strong periodicity, the flow tends to change with time periodically with a characteristic period of 7–8 s. The main stages of the vortex shedding can be seen

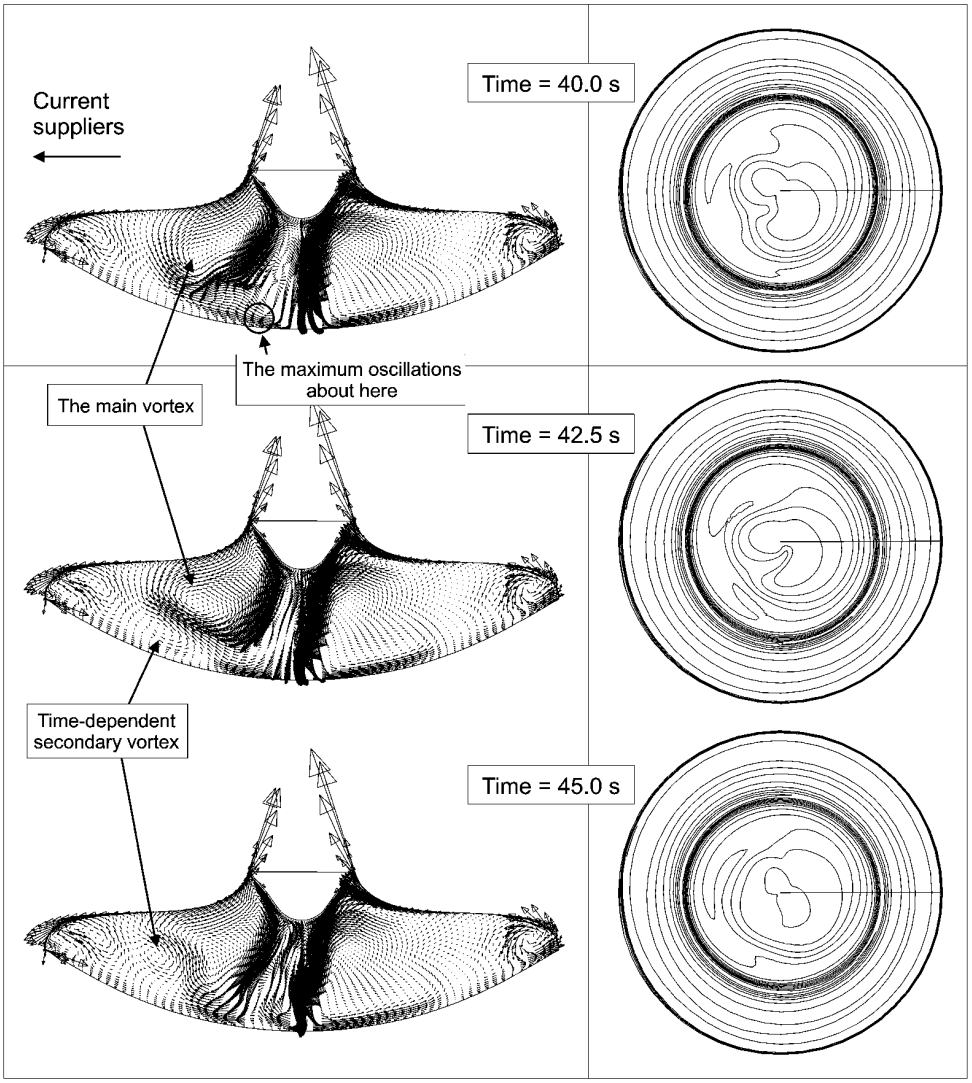

Fig. 2. Transient flow field: velocity in the vertical cross-section (on the left), and dopant concentration in the melt at the crystal growth interface (on the right).

in the three frames: (1) at the first step, one large vortex is dominating in the central region on the left side; (2) then a secondary vortex is arising below the main one and near the growth interface; and (3) finally, the secondary vortex moves up towards the free surface of the molten zone and the main vortex tends to occupy again the central region on the left. After that all gets repeated from the beginning. It is interesting to note that the flow at the right side (opposite to the inductor slit) stays practically unchanged with time.

The region with the largest amplitudes of temperature and velocity oscillations is found near the centre of the molten zone and directly below the inductor slit, as indicated in Fig. 2. Velocity oscillations have an amplitude of nearly 1 cm/s,

and the axial and azimuthal velocity components are changing their directions periodically. The radial velocity component is behaving most irregularly. The temperature is changing with time in the limits of about 1 K.

The instantaneous flow and dopant fields in Fig. 2 are to be compared to the respective steady-state calculation results obtained on a coarser grid (see Fig. 4 below). The main differences between the steady-state and the transient results occur in the central region of the molten zone on the left side from the axis, where the issue of the discrepancies is, of course, the transient character of the flow, which could not be resolved on the coarser grid. Nevertheless, the general flow patterns keep close similarity. For the dopant concentration along the growth interface, there is also analogy between the transient and steady-state results except the central region, where for the transient case the concentration isolines have a much more complicated shape because of the high sensitivity of the dopant distribution to the changes in the fluid flow near the growth interface.

Similar to Ref. [12], resistivity distribution in the grown crystal is obtained by switching from the fixed cylindrical coordinates, (r, α, z), to the reference system of the rotating and downward moving single crystal, (r, α', z'). The shape of the curved axisymmetric crystallisation interface is given by $z = z_{Cr}(r)$ and the concentration at this interface is described by the time-dependent function $C_{Cr}(r, \alpha, t) = C(r, \alpha, z_{Cr}(r), t)$, where $C(r, \alpha, z, t)$ is the calculated distribution of dopant concentration in the melt volume. The corresponding normalised resistivity distribution $\rho(r, \alpha', z')$ in the grown crystal then equals

$$\rho(r, \alpha', z') = [k_0\, C_{Cr}(r, \alpha_{Cr}, t_{Cr})]^{-1} \quad (1)$$

with k_0 being the equilibrium segregation coefficient. The functions α_{Cr} and t_{Cr} describe the proper angular coordinate and the time instant at which the crystallisation of the solid point in crystal has occurred

$$\alpha_{Cr}(r, \alpha', z') = 2\pi \frac{z' - z_{Cr}(r)}{V_{Cr}} W_{Cr} + \alpha', \quad (2)$$

$$t_{Cr}(r, z') = \frac{z' - z_{Cr}(r)}{V_{Cr}}, \quad (3)$$

where V_{Cr} is the growth rate of the single crystal and W_{Cr}, its rotation rate (compare (1), (2) and (3) to the respective formulas in Ref. [12]).

The calculated resistivity distribution for one longitudinal cross-section of the grown crystal rod (at angle $\alpha' = 0^\circ$) is shown in Fig. 3a. Similar to the corresponding figure in Ref. [12], where a steady-state flow was considered, an alternating crest-trough pattern with the typical herringbone form is observed. However, in the present case, the pattern has lost the exact harmonic periodicity and is more complex because of the overlaying effect of unsteadiness. Meantime, the general shape of the resistivity distribution, i.e., the large-scale variations along the crystal radius are equal in both cases.

Just as described in Ref. [12], the Fourier analysis of $\partial\rho/\partial z'$ in the axial direction is done and the obtained distribution of Fourier ampli-

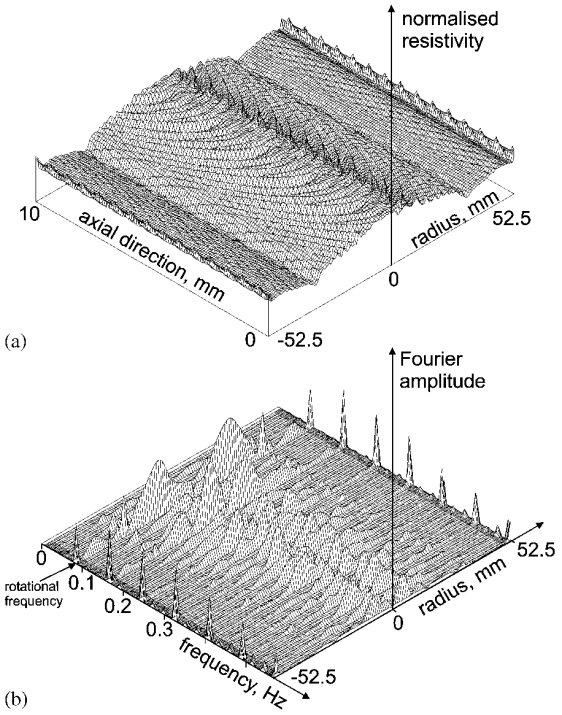

Fig. 3. From 3D transient calculations: (a) distribution of resistivity $\rho(r, \alpha', z')$ in the vertical cross-section $\alpha' = \text{const.}$ of the rotating crystal, and (b) Fourier analysis of $\partial\rho/\partial z'$ in axial direction.

tudes along the diameter of the crystal rod is shown in Fig. 3b for the same angle $\alpha' = 0°$. The principal difference between the present spectrum and the spectrum in Ref. [12] is that the spectrum describing the transient results is, in general, continuous while the spectrum for steady-state results was essentially discrete and had the lowest frequency equal to that of crystal rotation. Now, the not-exactly-periodic transient behaviour of the flow and concentration field is described during a finite time interval (36 s is chosen in the specific case) corresponding to a finite grown crystal length, 2.04 mm, which determines the resolution threshold of the continuous spectrum. Therefore in this case, the smallest frequency is 3 times lower than the rotation frequency of the crystal, which corresponds to a wavelength of 0.68 mm. However, it can be seen that the rotation frequency and its higher harmonics still prevail over the intermediate frequencies of unsteadiness. This is seen clearly at the rim of the crystal, where like in the steady-state case in Fig. 4 distinct rotational striations appear due to the non-symmetric action of EM forces in the periphery.

It should be noted that the case of unsteady melt flow yields, in principle, the resistivity distribution changing with the angle α' not only by a phase shift. The dependence of the present results on the angle can be observed in Fig. 3b as the lack of exact symmetry between the Fourier amplitude distributions in the positive and negative directions along the radius axis. This effect, however, is small and an approximate symmetry is retained.

It is concluded that a steady-state flow can be considered as a reasonable approximation to the unsteady melt motion, therefore we have used the steady-state model with the coarser grid for the 3D parametric studies below.

4. Parametric studies: crystal rotation rate

The crystal rotation rate is one of the main process parameters because the rotation is essen-

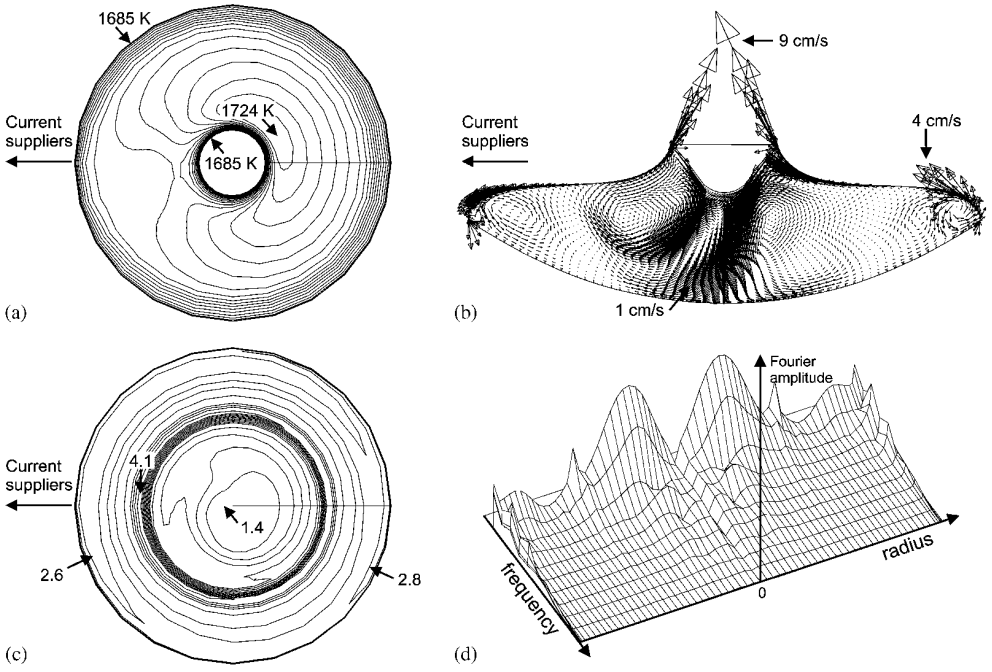

Fig. 4. Results for crystal rotation rate 5 rpm and inductor slit 1 mm: (a) temperature at the free surface, (b) velocity in the vertical cross-section, (c) dopant concentration in melt at the growth interface, and (d) Fourier analysis of $\partial\rho/\partial z'$ in axial direction (see footnote 1 and footnote 2).

tial for the growth process and any changes in the rotation rate influence directly the melt hydrodynamics and as a consequence the resistivity distribution in the crystal. The previous results (those above and in Refs. [11,12]) have been obtained for a crystal rotation rate of 5 rpm. In the present study, also rates of 0, 2.5, 10, 15 and 20 rpm are considered. The other growth parameters are kept unchanged.

In Figs. 4 and 5, the results for the temperature, velocity, dopant concentration fields and the Fourier analysis[1] for two different rotation rates (5 and 15 rpm) can be compared[2].

It is observed from the flow patterns in the cross-section of the molten zone and from the dopant distributions at the growth interface that higher rotation rates make the velocity and concentration fields more axisymmetric and also suppress the fluid motion in the radial and axial directions. For example, in the case of the 15 rpm rotation in Fig. 5b, larger areas of small velocity in the vertical cross-section can be seen (compare with the 5 rpm case in Fig. 4b), particularly it concerns the lower part of the molten zone, which is the most directly influenced by the crystal rotation. The higher the rotation rate, the more the fluid rotation resembles rotation of a solid body.

The flow and dopant field calculation with zero rotation rate has shown that in the limit of a very slow rotation there is not only the most expressed deviation from axial symmetry but also a very different dopant distribution with a maximum near the centre of the growth interface, while in the case of higher rotation there is always a ring of concentration maximum around the centre and a minimum takes place in the centre itself. The higher the rotation rate, the bigger the radius of the ring of maximum concentration (cf. Figs. 4c, 5c). The location of the maximum near the centre for the 0 rpm case is explained by a distinct flow structure, where the flow separation takes place at the centre of the growth interface and the flow is directed towards the central axis all along the interface. The higher the rotation rate, the farther from the centre the flow separation point is located (cf. Figs. 4b, 5b). The concentration minimum and maximum values are approximately equal for all of the rotation rates except the 0 rpm case, in which the maximum value is about two times higher.

With non-zero rotation of crystal, the temperature maximum at the free melt surface is shifted in the counter-clockwise direction, which is the direction of crystal rotation (see Figs. 4a, 5a). To characterize the non-symmetry of the temperature distribution at the free surface, one can consider the difference between the maximum temperature at the free surface and minimum temperature at another point located at the free surface at the same distance from rotation axis as the first point. This characteristic temperature difference for different rotation rates is found as follows: 15 K for 0 rpm, 16 K for 2.5–5 rpm, 9 K for 10 rpm, 6 K for 15 rpm, and 5 K for 20 rpm, i.e., for faster rotation the temperature distribution becomes noticeably more even and symmetric.

Comparison of the rotational striations (i.e., of the respective Fourier amplitudes for resistivity variations) in crystal grown with different rotation rates shows that they diminish with increasing rotation rate. Considering the maximum Fourier amplitude for the rotation frequency of the resistivity variations the following relative values normalised to the amplitude for the case of 5 rpm are found: 1.2 for 2.5 rpm, 0.5 for 10 rpm, 0.4 for 15 rpm, and 0.2 for 20 rpm.

5. Parametric studies: inductor slit width

Another parametric study includes changing the slit width of the inductor while keeping the 5 rpm

[1] The amplitude is depicted as a function of the frequency and the radial coordinate of the crystal. It should be considered that the spectrum is strictly discrete (as shown in Fig. 3b) and, along the frequency axis, the amplitudes are joined for convenience only. The smallest non-zero frequency corresponds to the rotational frequency of the crystal.

[2] Note that for different crystal rotation rates frequency scales differ because the smallest frequency is different. Also, for comparison purposes, the Fourier amplitudes of the axial derivative of resistivity have been divided by the rotation frequency, which means that the displayed amplitudes for different rotation rates allow to compare the variations in the resistivity itself, not in the derivative. The Fourier analysis is still done for derivatives to make the amplitudes for higher frequencies seen better.

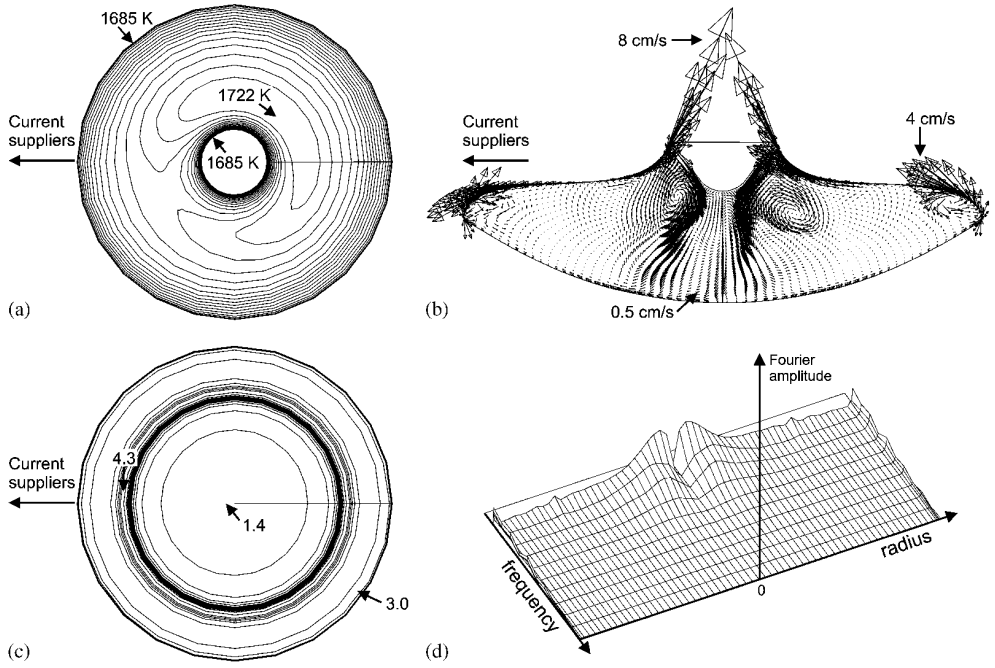

Fig. 5. Results for crystal rotation rate 15 rpm: (a) temperature at the free surface, (b) velocity in the vertical cross-section, (c) dopant concentration in melt at the growth interface, and (d) Fourier analysis of $\partial\rho/\partial z'$ in axial direction (see footnote 1 and footnote 2).

rotation rate and the other parameters unchanged. The slit width is an important parameter of the inductor. A too small width may lead to electrical breakdown, whereas a wider slit produces a more non-symmetric EM field. In our case when regarding the steady-state flow model, the slit is of special importance because it is the only reason for the system to deviate from the axial symmetry.

Normally, in this article and in Refs. [11,12], a slit of 1 mm has been assumed. In the present study, calculations have been done also with slits of width 0.5 and 2 mm. This leads to different distributions of EM forces and heat sources along the free melt surface. The temperature, velocity and concentration fields, as well as the Fourier analysis of the resulting resistivity distribution for the 2 mm slit are illus-trated in Fig. 6, which is to be compared to the 1 mm case shown before in Fig. 4.

Comparing the flow patterns in the cross-section of the molten zone and the dopant distributions at the growth interface (Figs. 6 and 4), it is observed that although the flow and dopant distributions are not fully equal, they are very similar. The main influence of the change in EM force and power distribution is observed in the vicinity of the free surface of the melt, including the peripheral region underneath the slit, which is the closest to the growth interface. The rest volume of the flow and, consequently, the dopant distribution in the central region are less influenced.

Similar as in Section 4, to characterize the non-symmetry of the temperature distribution at the free melt surface, one can consider the characteristic temperature difference defined in Section 4. This temperature difference is found to be 11 K for 0.5 mm, 16 K for 1.0 mm, and 18 K for 2.0 mm slit. It can be seen that the 0.5 mm slit results in considerably reduced temperature field asymmetry compared with the case of 1 mm. Meanwhile, although for the broad slit (2 mm) the temperature difference reaches a maximum value, it is not much higher than that for the 1 mm slit. The explanation is that with the 2 mm slit there is not only a deeper

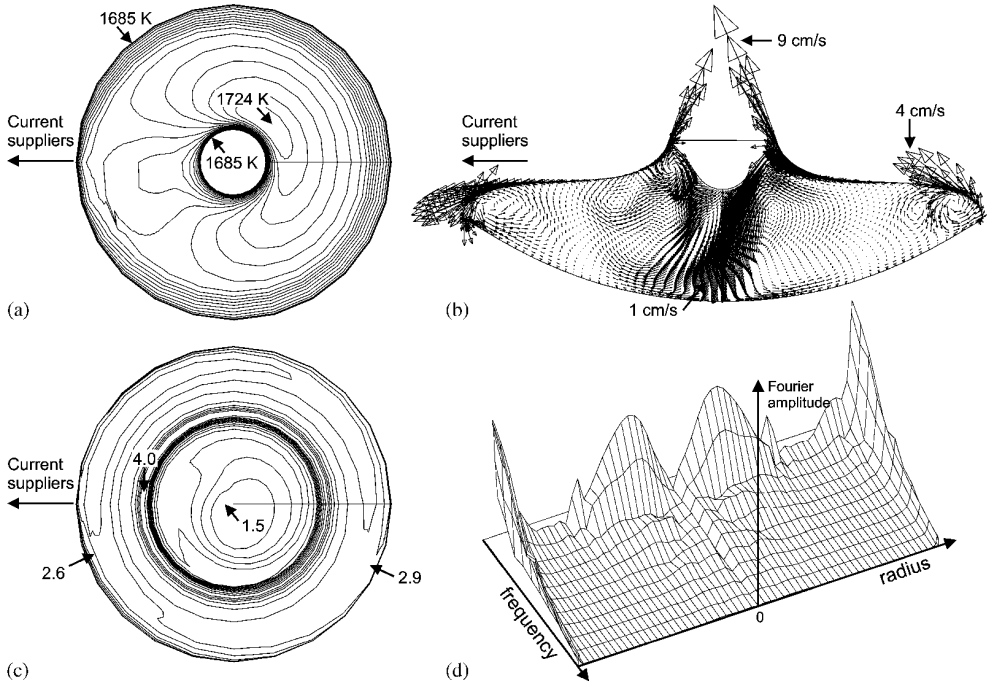

Fig. 6. Results for inductor slit 2 mm: (a) temperature at the free surface, (b) velocity in the vertical cross-section, (c) dopant concentration in melt at the growth interface, and (d) Fourier analysis of $\partial\rho/\partial z'$ in axial direction (see footnote 1).

minimum of power density at about middle radius of the free melt surface underneath the slit, but also a distinct local maximum near the crystal rim underneath the slit.

Near the rim of the grown crystal, the case with 2 mm slit shows higher Fourier amplitudes than in case of a smaller slit width (cf. Figs. 6d and 4d). Apparently, this fact is caused by the influence of the higher non-symmetry of EM forces. The effect of EM forces is indicated by the altered velocity field in the periphery at the side of the inductor slit (see Figs. 6b and 4b). Due to the large slit size, the EM forces have made a stronger flow velocity towards the periphery along the free surface of the melt and the small counter-vortex has disappeared. This has led to a more non-symmetric dopant transport in the periphery of the molten zone and, consequently, the dopant concentration isolines have deviated more from the concentric shape at the rim of the crystallisation interface (Fig. 6c).

It must be emphasized that the used one-way analysis does not consider the influence of the non-symmetric power distribution on the shape of interfaces. Therefore, the crystallisation front remains axisymmetric and e.g. the remelting under the inductor slit is not analysed. On the other hand, the remelting acts only locally in the vicinity of the crystal rim and should not disturb the flow structure in the whole zone.

6. Conclusions

Numerical three-dimensional modelling of the floating zone (needle-eye) crystal growth process has been carried out to analyse the influence of the crystal rotation rate and of the width of the inductor slit on the 3D flow field and on the grown crystal resistivity. Comparison of the transient results, obtained on a relatively fine computational grid, with steady-state results on a coarser grid,

not resolving the unsteadiness, shows that local differences appear in the most unsteady flow region near the centre of the molten zone while a good agreement is found in the rest of the melt volume. The parametric studies have shown that increasing the rotation rate essentially changes the flow pattern and weakens the rotational striations, while the inductor slit width has a more local influence on these characteristics.

References

[1] K.H. Lie, J.S. Walker, D.N. Riahi, J. Crystal Growth 100 (1990) 450.
[2] A. Mühlbauer, A. Muižnieks, J. Virbulis, A. Lüdge, H. Riemann, J. Crystal Growth 151 (1995) 66.
[3] Z. Guo, S. Maruyama, S. Togawa, J. Crystal Growth 194 (1998) 321.
[4] S. Togawa, Y. Nishi, M. Kobayashi, Electrochem. Soc. Proc. 98–13 (1998) 67.
[5] C.W. Lan, S. Kou, J. Crystal Growth 108 (1991) 351.
[6] A. Mühlbauer, A. Muižnieks, J. Virbulis, A. Lüdge, H. Riemann, J. Crystal Growth 180 (1997) 372.
[7] A. Mühlbauer, A. Muižnieks, G. Raming, H. Riemann, A. Lüdge, J. Crystal Growth 198/199 (1999) 107.
[8] T. Munakata, I. Tanasawa, J. Crystal Growth 206 (1999) 27.
[9] T. Kaiser, Magnetohydrodynamische Effekte bei der Halbleiterkristallzüchtung, Dissertation, Geowissenschaftliche Fakultät der Albert-Ludwigs-Universität Freiburg i. Br. 1998.
[10] G. Ratnieks, A. Muižnieks, G. Raming, A. Mühlbauer, L. Buligins, 3D modelling of magnetic, temperature, hydrodynamic and dopant concentration fields during FZ-silicon crystal growth, Proceedings of International Colloquium on Modeling of Material Processing, Riga, May 28–29, 1999, pp. 30–35.
[11] G. Ratnieks, A. Muižnieks, L. Buligins, G. Raming, A. Mühlbauer, Magn. Gidrodin. 35 (3) (1999) 278.
[12] G. Ratnieks, A. Muižnieks, L. Buligins, G. Raming, A. Mühlbauer, A. Lüdge, H. Riemann, J. Crystal Growth 216 (2000) 204.
[13] Fluent User's Guide (Version 4.4), Fluent Inc.

7 Summary and conclusions

Axisymmetric phase boundaries

For the first time, a closed system of mathematical models for steady-state FZ crystal growth has been proposed: the shape of the inductor, the process parameters and material properties determine the location and shape of the phase boundaries. A computation code `FZONE` that solves the phase boundaries in a partly transient way and implements many important updates to the models published earlier has been made and found applicable for calculation of floating zones with large crystal diameters (e.g., about 8 inch). The following main improvements in comparison to the most advanced one of the previous models (i.e., the model by Virbulis and Mühlbauer et al. [45, 46], where the authors were focusing on 4 inch floating zone) have been introduced:

- A model of the open melting front structure has been proposed in order to take into account the tangential change in the average melt quantity (i.e., the thickness of the "fluid film") and to calculate the corresponding Joulean heat flux due to the penetrating magnetic field. The resulting open melting front form agrees now better to the reality.

- A special calculation method for the position of the inner triple point has been developed in order to ensure an automated procedure, which was absent in the previous model.

- The free surface calculation algorithm with fitting of the angle at the crystal rim has been strongly improved in order to function well when applied to large floating zones.

- The view factors model has been implemented for the radiation heat transfer calculation, whose better performance over the T^4-boundary conditions is of particular importance for large floating zones because of larger temperature differences at the radiating surfaces.

- A better method of accounting for the approximate influence of the inductor slits has been implemented. It allows calculation of effectively axisymmetric EM fields created by multiple-slit inductors (as typical for large crystal growth) and accounts also for the main slit, which was neglected in the previous model.

- Axisymmetric time-dependent flow calculation with SUPG-stabilized Finite Element Method has been implemented in order to take into account the melt flow effect onto the temperature field and shape of the floating zone. The stabilization approach was essential to successfully deal with both: 1) the strong convection inside the floating zone and 2) the deformation of the finite element grid near the inner triple point as the zone boundaries move during the calculation procedure. The implemented model includes also the direct effect of the melt flow on the shape of the free melt surface (in sense of Section 3.6), which has not been studied for floating zone before.

- The used partly transient modelling approach with finding the positions of the crystallization and melting fronts by imitating their movements in time has allowed to study the time dependent interaction of the interface form and melt flow. Beside that, it also facilitated a further development of the model toward a fully transient description of the growth process, which is not considered in the present work.

By using the new code `FZONE`, for the first time parametric studies of phase boundaries for an 8 inch floating zone have been performed, by neglecting the melt flow. The following conclusions are drawn from the numerical calculations:

- The calculations affirmed that the FZ process is very sensitive to changes in the inductor current: for the considered 8 inch process the zone height changed linearly with $\mathrm{d}H_\mathrm{Z}/\mathrm{d}I = 0.0623$ mm/A. With a chosen realistic zone height of 37 mm and inductor current of 1510 A, the change limits of inductor current allowing the existence of a steady-state floating zone constitute only $\pm 7\%$, which corresponds to zone height change by $\pm 17\%$. The lower limit is determined by the reducing distance between the inductor and the melt, the upper limit, by the electromagnetic cutting of the zone neck. Also the experimentally observed sharp edge building at the inner triple point in case of a too large inductor current (and zone height) could be demonstrated. Because the inductor current in an

FZ process is never precisely known, the following studies were made by fixing the zone height.

- The usage of a reflector in 8 inch FZ process, especially in the proximity of the exterior triple point, has a significant influence: on the one hand, it reduces considerably the current that is needed to keep the prescribed zone height and hence also the danger of arcing and, on the other hand, it reduces the temperature gradients in the crystal and the danger of crystal cracking.

- With a given inductor shape and prescribed zone height, there exist limitations on the possible crystal pull rates. The lower limit at ca. 0.7 mm/min is determined by the surface tension: the zone neck collapses after the free melt surface exceeds a critical height above 18.5 mm. The upper limit is reached at ca. 2 mm/min because the crystallization front gets unrealistic steep. Between these limits, the inductor current stays constant but the vertical placement of the whole zone is shifted relative to inductor.

- A too small feed rod diameter causes formation of a solid bridge between the feed rod and the grown crystal whereas the upper feed rod size limit is determined by the ability of inductor to ensure a sloped open melting front.

- Geometry of the inductor is an influential means of FZ process design. The lower and upper limits of the inductor hole size are determined by cutting of the zone neck by a too small hole and solid bridge formation as the melting interface goes down if the hole is too large, which illustrates the necessity for a needle-eye inductor. To additionally have a sufficient slope of the open melting front, the additional slits are indispensable too.

- Comparing the 8 inch floating zone to smaller floating zones (6 and 4 inches) shows that the typical deflection of the crystallization interface grows rapidly with crystal size. This can be explained by a slower increase in the area of (and radiation from) the crystal's cylindrical surface than in the crystal's cross-sectional area (and heat supplied from the inductor onto the free melt surface) with crystal diameter.

Further calculations of the phase boundaries for 8 inch, 4 inch and 2 inch floating zones have been performed with account for the melt flow. The results have been compared to those of calculations neglecting melt flow and the following conclusions are drawn:

- For the 8 inch floating zone, the effect of melt convection reduced the overheating of the melt from $\Delta T = 58$ K by 13 K and reduced the crystallization interface deflection by 6 mm. This reduced deflection agrees well with experimental measurements.

- For the 4 inch floating zone, the effect of melt convection reduced the overheating of the melt from $\Delta T = 31$ K by only 4 K and did not change the crystallization interface deflection significantly. This deflection agrees well with experimental measurements.

- For the 2 inch floating zone, the effect of melt convection reduced the overheating of the melt from $\Delta T = 53$ K by 22 K and increased the crystallization interface deflection by 5 mm. This increased deflection agrees well with experimental measurements. The large effect of convection despite the small melt volume is explained by the strong EM forces due to the proximity of the inductor to the free melt surface.

- The direct influence of the melt flow on the free surface shape (in sense of Section 3.6) was negligible for 8 and 4 inch floating zones. For the 2 inch floating zone, due to the temporary strong melt flow, a considerable effect on the free surface fluctuations was found (the distance between the free melt surface and the inductor changed sometimes due to the flow effect by more than 20%). Despite that, the time-average effect on the crystallization interface deflection was insignificant.

To summarize: Calculations neglecting the melt motion yield a first approximation of the phase boundaries. For more precise predictions, the convective heat transfer has to be accounted. The direct influence of the melt flow on the free melt surface shape is normally irrelevant.

3D aspects and rotational striations

Another part of the work has been devoted to the effect of the three-dimensionality of the inductor on the melt flow in the floating zone and on the resistivity distribution in the grown crystal, the latter being derived from the dopant distribution in the vicinity of the crystallization interface. The shape of the 4 inch molten zone is taken from axisymmetric phase boundary calculations and the three-dimensional flow and

dopant distribution in the melt is calculated by the commercial CFD program package FLUENT. For the first time, the phenomenon of rotational striations in FZ crystals has been examined numerically.

Due to the non-axisymmetric Joulean power distribution on the free melt surface, the temperature distribution in the melt and all acting forces under consideration (buoyancy, EM- and Marangoni forces) show a non-symmetric distribution as well. Studies of the individual influence of these forces have shown that the distribution of dopant concentration and resistivity in crystal are very sensitive to both EM- and Marangoni forces, whose mutual counteraction and partial compensation play an important role in amplifying the rotational striations.

The rotational striations, i.e., the resistivity variations created by the non-symmetry and crystal rotation during the growth, have been obtained numerically and subjected to Fourier analysis. The following conclusions are drawn:

- Parametric studies of the rotational striations show that increasing the rotation rate essentially changes the flow pattern and weakens the striations, whereas the inductor slit width has a more local influence on these characteristics.
- The amplitude of rotational striations near the central axis of crystal is found to be considerably higher than at the periphery, which agrees very well to measurement data and is explained by the flow structure.
- A difference from measurements has been found in the relative weight of the Fourier amplitude of rotational frequency among other frequencies, which could be explained by suppressed asymmetry of the system due to the approximation of axisymmetric floating zone shape.

Although it was possible to obtain the rotational striations by accounting only the non-axisymmetric shape of the inductor, in reality other sources of non-symmetry (like non-axisymmetric shape of the free melt surface) join and can possibly make the non-symmetry of melt flow and the striations stronger.

Bibliography

[1] H. C. Theuerer. *US Patent 3.060.123*, filed 1952, issued 1962.

[2] W. Zulehner. Historical overview of silicon crystal pulling development. *Mat. Science and Engineering*, B73:7, 2000.

[3] W. v. Ammon. Silicon crystal growth. In G. Müller, J.-J. Métois, and P. Rudolph, editors, *Crystal Growth — from Fundamentals to Technology*, pages 239–270. Elsevier B. V., 2004.

[4] W. C. Dash. *J. Appl. Phys.*, 29:736, 1958.

[5] W. C. Dash. *J. Appl. Phys.*, 30:459, 1959.

[6] W. C. Dash. *J. Appl. Phys.*, 31:736, 1960.

[7] G. Raming. *Modellierung des industriellen FZ-Verfahrens zur Züchtung von Siliziumeinkristallen.* PhD thesis, Institut für Elektrowärme, Universität Hannover, Hannover, 2000.

[8] V. V. Voronkov. *J. Crystal Growth*, 59:625, 1982.

[9] W. Keller. *BRD Patent 1.148.525*, filed 1959, issued 1963.

[10] L. R. Crosby and H. M. Stewart. *US Patent 3.249.406*, filed 1963, issued 1966.

[11] W. G. Pfann. *Trans. AIME*, 194:747, 1952.

[12] P. H. Keck and M. J. E. Golay. *Phys. Rev.*, 89:1297, 1953.

[13] R. Emeis. *Z. Naturforsch.*, 9a:67, 1954.

[14] S. Müller. *Z. Naturforsch.*, 9b:504, 1954.

[15] P. H. Keck, W. van Horn, J. Soled, and A. MacDonald. *Rev. Sci. Instrum.*, 25:331, 1954.

[16] W. Keller and A. Mühlbauer. *Floating-Zone Silicon*. Marcel Dekker, New York, 1981.

[17] G. Ziegler. *Z. Naturforsch.*, 16a:219, 1961.

[18] W. Heywang. *Z. Naturforsch.*, 11a:238, 1956.

[19] S. R. Coriell and M. R. Cordes. Theory of molten zone shape and stability. *J. Crystal Growth*, 42:466, 1977.

[20] D. N. Riahi and J. S. Walker. *J. Crystal Growth*, 94:635, 1989.

[21] K. H. Lie, D. N. Riahi, and J. S. Walker. Free surface shape and AC electric current distribution for float zone silicon growth with a radio frequency induction coil. *J. Crystal Growth*, 100:450, 1990.

[22] J. L. Duranceau and R. A. Brown. *J. Crystal Growth*, 75:367, 1986.

[23] C. W. Lan, Y. J. Kim, and S. Kou. *J. Crystal Growth*, 104:801, 1990.

[24] C. W. Lan and S. Kou. Heat transfer, fluid flow and interface shapes in floating-zone crystal growth. *J. Crystal Growth*, 108:351, 1991.

[25] C. W. Lan and S. Kou. Effects of rotation on heat transfer, fluid flow and interfaces in normal gravity float-zone crystal growth. *J. Crystal Growth*, 114:517, 1991.

[26] C. W. Lan and S. Kou. Shortened floating zone crystal growth under normal gravity. *J. Crystal Growth*, 119:281, 1992.

[27] C. W. Lan and S. Kou. Radial dopant segregation in zero-gravity floating-zone crystal growth. *J. Crystal Growth*, 132:578, 1993.

[28] B. Xiong and W. R. Hu. *J. Crystal Growth*, 133:155, 1993.

[29] C. W. Lan. *J. Crystal Growth*, 169:269, 1996.

[30] C. W. Lan and M. C. Liang. *Int. J. Numer. Methods Eng.*, 40:621, 1997.

[31] C. W. Lan and C. H. Tsai. *J. Crystal Growth*, 173:561, 1997.

[32] Z. M. Tang and W. R. Hu. Influence of liquid bridge volume on the onset of oscillation in floating zone convection III. Three-dimensional model. *J. Crystal Growth*, 207:239, 1999.

[33] C. W. Lan and M. C. Liang. Three-dimensional simulation of vertical zone-melting crystal growth: symmetry breaking to multiple states. *J. Crystal Growth*, 208:327, 2000.

[34] C. W. Lan and C. H. Chian. *J. Crystal Growth*, 230:172, 2001.

[35] C. W. Lan. Three-dimensional simulation of floating-zone crystal growth of oxide crystals. *J. Crystal Growth*, 247:597, 2003.

[36] Th. Kaiser and K. W. Benz. Floating zone growth of silicon in magnetic fields: III. Numerical calculations. *J. Crystal Growth*, 183:564, 1998.

[37] Th. Kaiser. *Magnetohydrodynamische Effekte bei der Halbleiterkristallzüchtung*. PhD thesis, Geowissenschaftliche Fakultät der Albert-Ludwigs-Universität Freiburg i. Br., 1998.

[38] P. Dold, A. Cröll, M. Lichtensteiger, Th. Kaiser, and K. W. Benz. Floating zone growth of silicon in magnetic fields: IV. Rotating magnetic fields. *J. Crystal Growth*, 231:95, 2001.

[39] T. P. Lyubimova, R. V. Scuridin, A. Cröll, and P. Dold. Influence of high frequency vibrations on fluid flow and heat transfer in a floating zone. *Crys. Res. Technol.*, 38(7-8):635, 2003.

[40] T. Munakata and I. Tanasawa. Study on silicon melt convection during the RF-FZ crystal growth process II. numerical investigation. *J. Crystal Growth*, 206:27, 1999.

[41] A. Mühlbauer, W. Erdmann, and W. Keller. Electrodynamic convection in silicon floating zones. *J. Crystal Growth*, 64:529, 1983.

[42] K. H. Lie, J. S. Walker, and D. N. Riahi. Melt motion in the float zone process with an axial magnetic field. *J. Crystal Growth*, 109:167, 1991.

[43] A. Mühlbauer, A. Muižnieks, A. Jakowitsch, and J. Virbulis. The Calculation of the 3D High Frequency Current Distribution During Silicon FZ Growth. *Latvian J. Phys. and Techn. Sc.*, 4:5, 1992.

[44] A. Mühlbauer, A. Muižnieks, A. Jakowitsch, and J. Virbulis. Berechnung des dreidimensionalen Hochfrequenzfeldes beim Zonenschmelzen von Silizium. *Archiv für Elektrotechnik*, 76:161, 1993.

[45] A. Mühlbauer, A. Muižnieks, J. Virbulis, A. Lüdge, and H. Riemann. Interface shape, heat transfer and fluid flow in the floating zone growth of large silicon crystals with the needle-eye technique. *J. Crystal Growth*, 151:66, 1995.

[46] J. Virbulis. *Numerische Simulation der Phasengrenzen und Schmelzenströmung bei der Züchtung von Siliziumeinkristallen mit dem Floating-Zone Verfahren*. PhD thesis, Faculty of Physics and Mathematics, University of Latvia, Rīga, 1997.

[47] H. Riemann, A. Lüdge, K. Böttcher, H.-J. Rost, B. Hallmann, W. Schröder, W. Hensel, and B. Schleusener. Silicon Floating Zone Process: Numerical Modeling of RF Field, Heat Transfer, Thermal Stress, and Experimental Proof for 4 Inch Crystals. *J. Electrochem. Soc.*, 142(3):1007, 1995.

[48] A. Mühlbauer, A. Muižnieks, and J. Virbulis. Analysis of the dopant segregation effects at the floating zone growth of large silicon crystals. *J. Crystal Growth*, 180:372, 1997.

[49] A. Mühlbauer, A. Muižnieks, G. Raming, H. Riemann, and A. Lüdge. Numerical modelling of the microscopic inhomogeneities during FZ silicon growth. *J. Crystal Growth*, 198/199:107, 1999.

[50] A. Mühlbauer, A. Muižnieks, and G. Raming. System of mathematical models for the analysis of industrial FZ-Si-crystal growth processes. *Crys. Res. Technol.*, 34:217, 1999.

[51] G. Raming, A. Muižnieks, and A. Mühlbauer. Numerical modelling of the influence of different types of magnetic fields on fluid motion and resistivity profiles during FZ-silicon crystal growth. In *Proc. International Colloquium "Modelling of Material Processing"*, pages 24–29, Rīga, May 1999.

[52] S. Togawa, Y. Nishi, and M. Kobayashi. Estimation of radial resistivity profile of FZ-Si crystals by numerical simulation. *Electrochem. Soc. Proc.*, 98(13):67, 1998.

[53] Z. Guo, S. Maruyama, and S. Togawa. Combined heat transfer in floating zone growth of large silicon crystals with radiation on diffuse and specular surfaces. *J. Crystal Growth*, 194:321, 1998.

[54] M. Kimura, H. Arai, T. Mori, and H. Yamagishi. Facet formation in silicon single crystals grown by VMFZ method. *J. Crystal Growth*, 128:282, 1993.

[55] M. Kimura, K. Yoshizawa, and H. Yamagishi. In *Proc. 4^{th} International Symposium on High Purity Silicon*, 96-13, page 58, 1996.

[56] J. Virbulis. Private communication, 2000.

[57] G. Ratnieks, A. Muižnieks, and A. Mühlbauer. Modelling of phase boundaries for large industrial FZ silicon crystal growth with the needle-eye technique. *J. Crystal Growth*, 255:227, 2003.

[58] G. Ratnieks, A. Muižnieks, and A. Mühlbauer. Mathematical modelling of industrial FZ process for large (200 mm) silicon crystal growth. In *Proc. International Colloquium "Modelling of Electromagnetic Processing"*, pages 205–210, Hanover, March 2003.

[59] A. Rudevičs, A. Muižnieks, G. Ratnieks, A. Mühlbauer, and Th. Wetzel. Numerical study of transient behaviour of molten zone during industrial FZ process for large silicon crystal growth. *J. Crystal Growth*, 266:54, 2004.

[60] A. Rudevičs, A. Muižnieks, H. Riemann, A. Lüdge, G. Ratnieks, and W. von Ammon. Numerical study and comparison with experimantal data for transient behaviour of phase boundaries during industrial FZ process for silicon crystal growth. *J. Crystal Growth*, 275:e561, 2005.

[61] A. Rudevičs, A. Muižnieks, and G. Ratnieks. Transient modelling of FZ crystal growth process and automatic adjusting of the HF inductor current and feed rod velocity. In *Proc. Joint 15th Riga and 6th PAMIR Conference on Fundamental and Applied MHD*, volume 2, pages 229–232, Rīga, June 2005.

[62] G. Ratnieks, A. Muižnieks, G. Raming, A. Mühlbauer, and L. Buligins. 3D modelling of magnetic, temperature, hydrodynamic and dopant concentration fields during FZ-silicon crystal growth. In *Proc. International Colloquium "Modelling of Material Processing"*, pages 30–35, Rīga, May 1999.

[63] G. Ratnieks, A. Muižnieks, L. Buligins, G. Raming, and A. Mühlbauer. 3D numerical analysis of the influence of EM and Marangoni forces on melt hydrodynamics. *Magnetohydrodynamics*, 35(3):278, 1999.

[64] G. Ratnieks, A. Muižnieks, L. Buligins, G. Raming, A. Mühlbauer, A. Lüdge, and H. Riemann. Influence of the three dimensionality of the HF electromagnetic field

on resistivity variations in Si single crystal during FZ growth. *J. Crystal Growth*, 216:204, 2000.

[65] A. Mühlbauer, A. Muižnieks, G. Raming, and G. Ratnieks. 2D and 3D numerical modelling of FZ large silicon single crystal growth: Relation between growth process and crystal quality. In *Proc. International Colloquium "Modelling of Saving Resources"*, pages 17–22, Rīga, May 2001.

[66] G. Ratnieks, A. Muižnieks, A. Mühlbauer, and G. Raming. Numerical 3D study of FZ growth: dependence on growth parameters and melt instability. *J. Crystal Growth*, 230:48, 2001.

[67] A. Mühlbauer, A. Muižnieks, G. Ratnieks, and G. Raming. Influence of the three-dimensionality of the electromagnetic field on the rotation-caused resistivity variations in Si single crystal during FZ-growth / Department of Physics (University of Latvia, Rīga) and Institute for Electroheat (University of Hanover). Scientific report on the cooperative research project supported by VW foundation, 2000.

[68] A. Mühlbauer, A. Muižnieks, G. Ratnieks, A. Krauze, G. Raming, and Th. Wetzel. Using of EM fields during industrial CZ and FZ large silicon crystal growth. *The International Journal for Computation and Mathematics in Electrical and Electronic Engeneering*, 22(1):123, 2003.

[69] A. Mühlbauer, A. Muižnieks, G. Ratnieks, A. Krauze, G. Raming, and Th. Wetzel. Mathematical modelling of the industrial growth of large silicon crystals by CZ and FZ process. *The International Journal for Computation and Mathematics in Electrical and Electronic Engeneering*, 22(1):158, 2003.

[70] R. Hull, editor. *Properties of Crystalline Silicon*. EMIS Datareviews Series 20. INSPEC, The Institution of Electrical Engenieers, London, 1999.

[71] S. C. Hardy. The surface tension of liquid silicon. *J. Crystal Growth*, 69:456, 1984.

[72] W. K. Rhim, S. K. Chung, A. J. Rulison, and R. E. Spjut. *Int. J. Thermophys.*, 18(2):459, 1997.

[73] A. Tegetmeier. *Oberflächenspannung und Wachstumswinkel: zwei wichtige Parameter der Schmelzzonenzüchtung*. PhD thesis, Geowissenschaftliche Fakultät der Albert-Ludwigs-Universität Freiburg i. Br., 1995.

[74] E. Šilters, G. Sermons, and J. Miķelsons. *Electrodynamics*. Zvaigzne, Rīga, 1986. In Latvian.

[75] A. Mühlbauer, A. Muižnieks, and A. Jakowitsch. Modellierung des elektromagnetischen Feldes in Induktionsöfen mit kaltem Tiegel. *Elektrowärme International*, 49(B3):B130, August 1991.

[76] G. K. Batchelor. *An introduction to fluid dynamics*. Cambridge University Press, Cambridge, 2000.

[77] L. D. Landau and E. M. Lifshitz. *Hydrodynamics*, volume 6 of *Course of Theoretical Physics*. Nauka, Moscow, 1986. In Russian.

[78] A. Muižnieks, E. Westphal, and A. Mühlbauer. Modellierung des elektromagnetischen Feldes in Induktionsöfen mit einem dickwandigen metallischen Tiegel. *Elektrowärme International*, 50(B3):B286–B294, Oktober 1992.

[79] J. R. Shewchuk. http://www.cs.cmu.edu/∼quake/triangle.html. In internet.

[80] J. R. Shewchuk. Triangle: Engineering a 2D Quality Mesh Generator and Delaunay Triangulator. In M. C. Lin and D. Manocha, editors, *Applied Computational Geometry: Towards Geometric Engineering*, volume 1148 of *Lecture Notes in Computer Science*, pages 203–222. Springer-Verlag, Berlin, May 1996. From the First ACM Workshop on Applied Computational Geometry.

[81] J. R. Shewchuk. Delaunay refinement algorithms for triangular mesh generation. *Computational Geometry: Theory and Applications*, 22(1-3):21, May 2002.

[82] C. A. J. Fletcher. *Computational techniques for fluid dynamics*, volume 2. Springer-Verlag, Berlin, 1991.

[83] A. N. Brooks and T. J. R. Hughes. Streamline upwind/Petrov-Galerkin formulations for convection dominated flows with particular emphasis on the incompressible Navier-Stokes equations. *Comp. Methods Appl. Mech. Engrg.*, 32:199–259, 1982.

[84] T.-P. Fries and H. G. Matthies. A review of Petrov-Galerkin stabilization approaches and an extension to meshfree methods. Technical report, Institute of Scientific Computing, Technical University Braunschweig, Brunswick, Germany, March 2004.

[85] A. Muižnieks. University of Latvia. Private communication, 2007.

[86] F. Dupret, P. Nicodème, Y. Ryckmans, P. Wouters, and M. J. Crochet. Global modelling of heat transfer in crystal growth furnaces. *Int. J. Heat Mass Transfer*, 33(9):1849, 1990.

[87] L. Altmannshofer. Siltronic AG. Private communication, 2004.

[88] A. Lüdge and H. Riemann. Institute of Crystal Growth, Berlin. Private communication.

[89] S. B. Pope. *Turbulent Flows*. Cambridge University Press, Cambridge, 2000.

[90] Fluent Inc. *FLUENT User's Guide, Version 4.3*, January 1995.

[91] Fluent Inc. *FLUENT User's Guide, Release 4.4*, August 1996.

[92] S. Patankar. *Numerical Heat Transfer and Fluid Flow*. Hemisphere Publishing Corp., Washington, DC, 1980.